

# UC Berkeley

## UC Berkeley Electronic Theses and Dissertations

**Title**

Post-earthquake Traffic Capacity of Modern Bridges in California

**Permalink**

<https://escholarship.org/uc/item/27p8r8mq>

**Author**

Terzic, Vesna

**Publication Date**

2009

Peer reviewed|Thesis/dissertation

# **Post-earthquake Traffic Capacity of Modern Bridges in California**

by

Vesna Terzić

A dissertation submitted in partial satisfaction of the

requirements for the degree of

Doctor of Philosophy

in

Engineering – Civil and Environmental Engineering

in the

Graduate Division

of the

University of California, Berkeley

Committee in charge:

Professor Božidar Stojadinović, Chair

Professor Stephen A. Mahin

Associate Professor Douglas Dreger

Fall 2009

# **Post-earthquake Traffic Capacity of Modern Bridges in California**

Copyright © 2009

by

Vesna Terzić

All rights reserved

# Abstract

Post-earthquake Traffic Capacity of Modern Bridges in California

by

Vesna Terzić

Doctor of Philosophy in Engineering – Civil and Environmental Engineering

University of California, Berkeley

Professor Božidar Stojadinović, Chair

Evaluation of the post-earthquake capacity of a bridge to carry self-weight and traffic loads is essential for a safe and timely re-opening of the bridge after an earthquake. Although modern highway bridges in California designed using the Caltrans Seismic Design Criteria are expected to maintain at minimum a gravity load-carrying capacity during both frequent and extreme seismic events, as of now, there are no validated, quantitative guidelines for estimating the remaining load carrying capacity of the bridges after an earthquake event.

In this study, experimental and analytical methods were combined to evaluate the post-earthquake traffic load carrying capacity of a modern California highway overpass bridge. An experimental study on models of circular reinforced concrete bridge columns was performed first to investigate the relationship between earthquake-induced damage in bridge columns and the capacity of the columns to carry axial load in a damaged condition. The earthquake-like damage was induced in the column specimens in bi-lateral quasi-static lateral load tests. The damaged column specimens were then tested in compression to failure to evaluate their remaining axial load strength. It was found that well-confined modern bridge columns lose approximately 20% of their axial load capacity after sustaining displacement ductility demands of 4.5 in both principal directions of the bridge. Typical California highway overpass bridges are designed such that they are not expected to develop displacement ductility demands larger than 4.0 in design-basis earthquake events. These test results were used to calibrate a finite element model of a bridge column. This bridge column model was incorporated into a hybrid model of a typical

California overpass bridge and tested using the hybrid simulation technique. This typical bridge is a straight 5-span overpass with single-column bents. During these hybrid simulations a heavy truck load was applied on the bridge immediately after the earthquake to study the behavior of the damaged bridge under such truck load. The hybrid bridge model safely carried the applied truck load after surviving an earthquake that induced displacement ductility demands of 4.7 and 6.7 in the longitudinal and transverse direction of the bridge, respectively. The finite element model of the typical California overpass bridge was validated using the data from hybrid simulations. The validated model of the typical bridge was used to evaluate its post-earthquake truck load capacity in an extensive parametric study that examined the effect of different ground motions and bridge modeling parameters such as the boundary conditions imposed by the bridge abutments, location of the truck on the bridge, and amount of bridge column residual drift.

The principal outcomes of this study are the following findings. A typical modern California highway bridge overpass is safe for traffic use after an earthquake if none of its columns failed, i.e. none of the column main reinforcing bars fractured, and if its abutments are still capable for restraining torsion of the bridge deck about its longitudinal axis. If any of the columns failed, i.e. if broken column reinforcing bars were discovered in a post-earthquake inspection, the bridge should be closed for regular traffic. Emergency traffic with weight, lane and speed restrictions may be allowed on a bridge whose columns failed if the abutments can restrain torsion of the bridge deck. These findings pertain to the bridge configuration investigated in this study. Additional research on the post-earthquake traffic load capacity of different bridge configurations is strongly recommended.

**To my husband Uglješa and  
our daughter Tara**

# TABLE OF CONTENTS

<b>TABLE OF CONTENTS .....</b>	<b>ii</b>
<b>LIST OF FIGURES .....</b>	<b>iv</b>
<b>LIST OF TABLES .....</b>	<b>ix</b>
<b>ACKNOWLEDGMENT .....</b>	<b>x</b>
<b>1 INTRODUCTION .....</b>	<b>1</b>
1.1 Motivation .....	1
1.2 Background .....	1
1.3 Research Objective and Scope .....	2
1.4 Organization of Report .....	4
<b>2 EXPERIMENTAL INVESTIGATION: QUASI-STATIC TESTS .....</b>	<b>5</b>
2.1 Introduction .....	5
2.2 Experimental Setup and Test Program .....	5
2.2.1 Prototype and Model .....	6
2.2.2 Test Matrix .....	9
2.2.3 Geometry and Reinforcement .....	9
2.2.4 Material Properties .....	11
2.2.5 Loading Pattern: Quasi-Static Tests .....	12
2.2.6 Test Setup .....	15
2.2.7 Instrumentation .....	17
2.3 Test Results .....	20
2.3.1 Test Results for the Base Column Specimens .....	20
2.3.2 Test Results for the Shear-Short Column Specimen .....	36
2.3.3 Comparison of the Test Results from the Base45 and ShearShort45 Tests .....	39
<b>3 EXPERIMENTAL INVESTIGATION: HYBRID SIMULATION TESTS .....</b>	<b>41</b>
3.1 Introduction .....	41
3.2 Components and Procedure of a Hybrid Simulation .....	42
3.3 Experimental Setup and Test Program .....	43
3.3.1 Test Matrix .....	44
3.3.2 Hybrid Modeling and Loading .....	45

3.3.3	Integration Algorithm.....	54
3.3.4	Test Setup.....	54
3.3.5	Geometric Transformations .....	57
3.3.6	Instrumentation .....	62
3.4	Overview of Experimental Observations.....	63
3.4.1	Results of the HSM Test .....	63
3.4.2	Results of the HSH Test.....	72
<b>4</b>	<b>ANALYTICAL MODELING.....</b>	<b>82</b>
4.1	Model of a Bridge Column .....	82
4.2	Pre-test Calibration of the Analytical Model .....	85
4.3	Calibration of Analytical Model Based on Quasi-Static and Axial Test Results .....	87
4.4	Validation of Analytical Model Based on Hybrid Simulations and Axial Test Results .....	100
<b>5</b>	<b>POST-EARTHQUAKE BRIDGE TRUCK LOAD CAPACITY.....</b>	<b>103</b>
5.1	Bridge Model and Loading Regime.....	103
5.1.1	Bridge Geometry and Reinforcement .....	103
5.1.2	Analytical Modeling .....	103
5.1.3	Loading .....	105
5.2	Parametric Study .....	109
5.2.1	Choice of Parameters .....	110
5.2.2	Matrix of Analyzed Cases.....	115
5.2.3	Post-earthquake Bridge Truck Load Capacity .....	116
<b>6</b>	<b>CONCLUSIONS AND FUTURE WORK.....</b>	<b>128</b>
6.1	Conclusions.....	130
6.2	Future Work .....	131
	<b>REFERENCES.....</b>	<b>132</b>
	<b>APPENDIX A: MATERIALS AND CONSTRUCTION .....</b>	<b>165</b>
	<b>APPENDIX B: SELECTION OF LOADING PATTERN FOR QUASI-STATIC TEST ..</b>	<b>180</b>
	<b>APPENDIX C: EXPERIMENTAL SETUP AND INSTRUMENTATION .....</b>	<b>187</b>
	<b>APPENDIX D: GROUND MOTION RECORDS .....</b>	<b>204</b>



## LIST OF FIGURES

Fig. 1.1	Methodology for evaluation of the remaining capacity of a bridge to carry traffic load after an earthquake event.....	3
Fig. 2.1	Prototype Caltrans bridges (Ketchum et. al., 2004) .....	6
Fig. 2.2	Geometry and reinforcement of the Base Column specimen .....	10
Fig. 2.3	Geometry and reinforcement of the Shear-Short Column specimen.....	11
Fig. 2.4	Loading pattern matrix .....	12
Fig. 2.5	Displacement orbits at the top of the bridge column: (a) absolute displacements, (b) normalized displacements .....	13
Fig. 2.6	Loading pattern used for quasi-static lateral displacement tests .....	14
Fig. 2.7	Displacement history for test Base45 .....	15
Fig. 2.8	Lateral test setup .....	16
Fig. 2.9	Axial test setup .....	16
Fig. 2.10	Externally instrumented levels along the height of the specimens.....	17
Fig. 2.11	Details of the instrumented points of the specimen: (a) target points and piano wires, (b) locations of the instrumented points at one level.....	18
Fig. 2.12	Instrumentation frames .....	18
Fig. 2.13	Strain gage locations.....	19
Fig. 2.14	Axial force-displacement relationship and state of the specimen after the Base0 test.	21
Fig. 2.15	Lateral force-displacement response curves in the two major directions (X and Y) for the Base15 test.....	22
Fig. 2.16	State of the specimen at the maximum displacement level during the lateral sequence of the Base15 test .....	23
Fig. 2.17	State of the specimen at the end of the lateral sequence of the Base15 test.....	24
Fig. 2.18	Axial force-displacement relationship and state of the specimen after the axial sequence of the Base15 test.....	25
Fig. 2.19	Lateral force-displacement response curves in the two major directions (X and Y) for the Base30 test.....	26
Fig. 2.20	State of the specimen at the maximum displacement level during the lateral sequence of the Base30 test .....	27
Fig. 2.21	State of the specimen at the end of the lateral sequence of the Base30 test.....	28
Fig. 2.22	Axial force-displacement relationship and state of the specimen after the axial sequence of the Base30 test.....	29
Fig. 2.23	Lateral force-displacement response curves in the two major directions (X and Y) for the Base45 test.....	30
Fig. 2.24	State of the specimen at the maximum displacement level during the lateral sequence of the Base45 test .....	31
Fig. 2.25	State of the specimen at the end of the lateral sequence of the Base45 test.....	32
Fig. 2.26	Profiles of peak displacements, rotations and curvatures for test Base45.....	33
Fig. 2.27	Deviation of the column surface from a perfect cylinder with the diameter of 16 inches; after the lateral sequence of the Base45 test .....	34
Fig. 2.28	Axial force-displacement relationship and state of the specimen after the axial sequence of the Base45 test.....	34

Fig. 2.29	Comparison of the axial force-displacement relationships for tests Base0, Base15, Base30, and Base45.....	35
Fig. 2.30	Degradation of the axial strength of laterally damaged specimens.....	35
Fig. 2.31	Lateral force-displacement response curves in the two major directions (X and Y) for the ShearShort45 test.....	36
Fig. 2.32	State of the specimen after displacement ductility level of 3 during the ShearShort45 test .....	37
Fig. 2.33	State of the specimen at the end of the lateral sequence of the ShearShort45 test.....	38
Fig. 2.34	Axial force-displacement relationship and state of the specimen after the axial sequence of the ShearShort45 test.....	39
Fig. 2.35	Lateral force-displacement response curves in the two major directions (X and Y) for the ShearShort45 and Base45 tests.....	40
Fig. 2.36	Axial force-displacement relationships for the ShearShort45 and Base45 tests .....	40
Fig. 3.1	Key components of a hybrid simulation.....	43
Fig. 3.2	Physical and numerical portions of the hybrid model of the bridge.....	45
Fig. 3.3	Geometry and reinforcement of the hybrid simulation specimens.....	46
Fig. 3.4	Deck cross section (Ketchum et al., 2004) .....	47
Fig. 3.5	Analytical model of the numerical portion of the hybrid bridge model.....	48
Fig. 3.6	Column model geometry .....	49
Fig. 3.7	Unscaled Whittier Narrows ground motion acceleration record: <i>vwnuy</i> record from Van Nuys bin (see Appendix D).....	51
Fig. 3.8	P13 truck load (Caltrans, 2004).....	52
Fig. 3.9	Eccentric position of the truck with respect to the superstructure centerline.....	52
Fig. 3.10	Four positions of the P13 truck load on the bridge and corresponding loads .....	53
Fig. 3.11	Four DOFs controlled at the top of the experimental element during the hybrid simulations.....	54
Fig. 3.12	Schematic representation of the hybrid simulation setup lateral load application .....	55
Fig. 3.13	Hybrid simulation test setup .....	55
Fig. 3.14	Plan view of the hybrid simulation experimental setup .....	56
Fig. 3.15	Elevation (A-A) of the hybrid simulation experimental setup .....	57
Fig. 3.16	Coordinate transformation.....	58
Fig. 3.17	Schematic presentation of the rigid column extension (in red) and actuators (in dark blue) at the beginning of the hybrid simulation .....	59
Fig. 3.18	Schematic presentation of command displacement for actuator $i$ ( $i=1, 3$ ) .....	60
Fig. 3.19	Initial vs. deformed configuration of the axial test setup in x and y directions.....	62
Fig. 3.20	Externally instrumented levels along the height of the hybrid simulation specimens ..	63
Fig. 3.21	Lateral displacement histories at the control point (analytical simulation vs. hybrid simulation).....	65
Fig. 3.22	Sectional rotation histories at the control point (analytical simulation vs. hybrid simulation).....	66
Fig. 3.23	Lateral force histories at the control point (analytical simulation vs. hybrid simulation) .....	67
Fig. 3.24	Bending moment histories at the control point (analytical simulation vs. hybrid simulation).....	68
Fig. 3.25	State of the specimen at the maximum displacement during the hybrid simulation ....	69

Fig. 3.26	State of the specimen at the end of the hybrid simulation.....	70
Fig. 3.27	State of displacements, rotations and curvatures along the height of the specimen at a certain time during the earthquake (marked by the point on the control point displacement orbit).....	71
Fig. 3.28	Axial force-displacement relationship and state of the specimen after the axial sequence of the test.....	72
Fig. 3.29	Displacement histories at the control point (analytical simulation vs. hybrid simulation).....	74
Fig. 3.30	Sectional rotation histories at the control point (analytical simulation vs. hybrid simulation).....	75
Fig. 3.31	Lateral force histories at the control point (analytical simulation vs. hybrid simulation).....	76
Fig. 3.32	Bending moment histories at the control point (analytical simulation vs. hybrid simulation).....	77
Fig. 3.33	State of the specimen at the maximum displacement during the hybrid simulation ....	78
Fig. 3.34	State of the specimen at the end of the hybrid simulation.....	79
Fig. 3.35	State of displacements, rotations and curvatures along the height of the specimen at a certain time during the earthquake (marked point on the control point displacement orbit graph).....	80
Fig. 3.36	Axial force-displacement relationship and state of the specimen after the axial sequence of the test.....	81
Fig. 4.1	Uniaxial stress-strain relationship for Concrete01 material .....	83
Fig. 4.2	Uniaxial stress-strain relationship for Concrete02 material .....	84
Fig. 4.3	Nonlinear backbone curve of ReinforcingSteel material .....	84
Fig. 4.4	Fiber cross-section; arrangement of fibers for Column415.....	86
Fig. 4.5	Experimental vs. analytical force-displacement response for Column415 .....	87
Fig. 4.6	Lateral force-displacement response curves for three lateral quasi-static tests: Base15, Base30, and Base45 in two major directions, X and Y .....	88
Fig. 4.7	Force-displacement response envelopes for three lateral quasi-static tests: Base15, Base30, and Base45 in two major directions, X and Y .....	89
Fig. 4.8	Fiber cross-section; arrangement of fibers for Base Column specimen.....	90
Fig. 4.9	Experimental vs. analytical force-displacement response curves for the Base Column specimen with displacement ductility level of 1.5 .....	93
Fig. 4.10	Experimental vs. analytical force-displacement response curves for the Base Column specimen with displacement ductility level of 3.0 .....	94
Fig. 4.11	Experimental vs. analytical force-displacement response curves for the Base Column specimen with displacement ductility level of 4.5 .....	95
Fig. 4.12	Force-displacement response envelopes in two major directions, X and Y, for three lateral quasi-static tests: Base15, Base30, and Base45; Experiment vs. Analytical 1 .	96
Fig. 4.13	Force-displacement response envelopes in two major directions, X and Y, for three lateral quasi-static tests: Base15, Base30, and Base45; Experiment vs. Analytical 2 .	97
Fig. 4.14	Axial force-displacement relationships: experimental vs. analytical relationships for the “virgin” Base Column specimen .....	98
Fig. 4.15	Axial force-displacement relationships: experimental vs. analytical relationships for the Base Column specimen with displacement ductility level of 1.5.....	98

Fig. 4.16	Axial force-displacement relationships: experimental vs. analytical relationships for the Base Column specimen with displacement ductility level of 3.0.....	99
Fig. 4.17	Axial force-displacement relationships: experimental vs. analytical relationships for the Base Column specimen with displacement ductility level of 4.5.....	99
Fig. 4.18	Axial force-displacement relationships: experimental vs. analytical relationship for the bridge column exposed to medium seismic intensity.....	101
Fig. 4.19	Axial force-displacement relationships: experimental vs. analytical relationship for the bridge column exposed to high seismic intensity.....	101
Fig. 5.1	Analytical model of the bridge structure .....	104
Fig. 5.2	Standard HS20-44 truck (Caltrans, 2004) .....	107
Fig. 5.3	Two considered cases of the truck position relative to the superstructure centerline .....	108
Fig. 5.4	Critical positions of the truck on the bridge .....	109
Fig. 5.5	Relation between post-earthquake bridge truck load capacity and intensity measures, (a) Pseudo-spectral acceleration, (b) Arias intensity, and (c) RMS acceleration (Rx0 abutment, residual drift of 1.0%, truck is in the curb lane).....	111
Fig. 5.6	Relation between maximum earthquake drift and post-earthquake bridge truck load capacity (Rx0 abutment, residual drift of 1.0%, the truck is in the curb lane).....	112
Fig. 5.7	Relation between residual drift and post-earthquake bridge truck load capacity (Rx0 abutment, the truck is in the fast lane).....	112
Fig. 5.8	Relation between torsional stiffness of the superstructure and post-earthquake bridge truck load capacity (Rx1 abutment, residual drift of 1.0%, truck is in the curb lane, earthquake <i>v<sub>nuys</sub></i> from Van Nuys earthquake bin) .....	113
Fig. 5.9	Relation between ultimate strain of reinforcing bars and post-earthquake bridge truck load capacity (Rx1 abutment, residual drift of 2.5%, truck is in the curb lane, earthquake <i>v<sub>nuys</sub></i> from Van Nuys earthquake bin) .....	114
Fig. 5.10	Relation between eccentricity of the truck relative to the superstructure centerline and post-earthquake bridge truck load capacity (Rx0 abutment, residual drift of 1.0%, earthquake <i>v<sub>nuys</sub></i> from Van Nuys earthquake bin) .....	114
Fig. 5.11	Degradation of the post-earthquake bridge truck load capacity with increase in residual drift for the case of Rx1 abutments when the truck load is in the fast lane .....	117
Fig. 5.12	Degradation of the post-earthquake bridge truck load capacity with increase in residual drift for the case of Rx1 abutments when the truck load is in the curb lane .....	118
Fig. 5.13	Degradation of the post-earthquake bridge truck load capacity with increase in residual drift for the case of Rx0 abutments when the truck load is in the fast lane .....	118
Fig. 5.14	Degradation of the post-earthquake bridge truck load capacity with increase in residual drift for the case of Rx0 abutments when the truck load is in the curb lane .....	119
Fig. 5.15	Post-earthquake bridge truck load capacity vs. maximum earthquake drift for the residual drift of 0.5% and the following cases: (a) Rx0 abutment, the truck is in the fast lane; (b) Rx0 abutment, the truck is in the curb lane; (c) Rx1 abutment, the truck is in the fast lane; (d) Rx1 abutment, the truck is in the curb .....	121
Fig. 5.16	Post-earthquake bridge truck load capacity vs. maximum earthquake drift for the residual drift of 1.0% and the following cases: (a) Rx0 abutment, the truck is in the fast lane; (b) Rx0 abutment, the truck is in the curb lane; (c) Rx1 abutment, the truck is in the fast lane; (d) Rx1 abutment, the truck is in the curb .....	122
Fig. 5.17	Post-earthquake bridge truck load capacity vs. maximum earthquake drift for the residual drift of 1.5% and the following cases: (a) Rx0 abutment, the truck is in the	

	fast lane; (b) Rx0 abutment, the truck is in the curb lane; (c) Rx1 abutment, the truck is in the fast lane; (d) Rx1 abutment, the truck is in the curb .....	123
Fig. 5.18	Post-earthquake bridge truck load capacity vs. maximum earthquake drift for the residual drift of 2.0% and the following cases: (a) Rx0 abutment, the truck is in the fast lane; (b) Rx0 abutment, the truck is in the curb lane; (c) Rx1 abutment, the truck is in the fast lane; (d) Rx1 abutment, the truck is in the curb .....	124
Fig. 5.19	Post-earthquake bridge truck load capacity vs. maximum earthquake drift for the residual drift of 2.5% and the following cases: (a) Rx0 abutment, the truck is in the fast lane; (b) Rx0 abutment, the truck is in the curb lane; (c) Rx1 abutment, the truck is in the fast lane; (d) Rx1 abutment, the truck is in the curb .....	125
Fig. 5.20	Post-earthquake bridge truck load capacity vs. maximum earthquake drift for the residual drift of 3.0% and the following cases: (a) Rx0 abutment, the truck is in the fast lane; (b) Rx0 abutment, the truck is in the curb lane; (c) Rx1 abutment, the truck is in the fast lane; (d) Rx1 abutment, the truck is in the curb .....	126
Fig. 5.21	Pushover results for transverse bridge direction.....	127
Fig. 6.1	Methodology for evaluation of the remaining capacity of a bridge to carry traffic load after an earthquake event.....	129

## LIST OF TABLES

Table 2.1	Characteristics of the Bridge Type 1 columns (H=22')	7
Table 2.2	Characteristics of the Bridge Type 11 columns (H=50')	7
Table 2.3	Design parameters of the specimens	8
Table 2.4	Test matrix	9
Table 2.5	Basic dimensions and reinforcement of the models and the prototypes	11
Table 2.6	Material properties	12
Table 2.7	Displacement ductility levels of the primary cycles	15
Table 3.1	Test matrix	44
Table 3.2	Basic dimensions and reinforcement of the hybrid simulation specimens	46
Table 3.3	Material properties of the hybrid simulation specimens	47
Table 4.1	Basic parameters for Column415 and Base Column specimen	85
Table 4.2	Steel02 material model parameters	86
Table 4.3	Concrete02 material model parameters	86
Table 4.4	Analytical 1 - Steel02 material model parameters	90
Table 4.5	Analytical 1 - Concrete01 material model parameters	91
Table 4.6	Analytical 2 - Concrete02 material model parameters	91
Table 4.7	Analytical 2 - ReinforcingSteel material model parameters	91
Table 4.8	Residual axial strengths: experimental vs. analytical	100
Table 4.9	Residual axial strengths: experimental vs. analytical	102
Table 5.1	Matrix of analyzed cases for one ground motion	116

# Acknowledgments

First and foremost I would like to sincerely thank my research advisor and academic mentor, Prof. Božidar Stojadinović, for his guidance, kindness and support throughout my graduate studies. He has found the perfect balance in giving me the freedom to pursue research topic that I enjoy, while leading me in the overall right direction. It was a great pleasure to work alongside of him.

I also wish to thank Prof. Stephan Mahin and Prof. Douglas Dreger for serving as a member of my dissertation committee. I greatly appreciate their effort in reading and revising this dissertation.

I would like to thank my friend Andreas Schellenberg for his valuable and generous help while preparing hybrid simulation tests. Also I am very thankful to my friends Nicola Tondini, Kranthi Kiran Mandadapu and Ady Aviram for their immense help in the laboratory while preparing for my experiments and for making it fun time.

Special thanks are also due to the *nees@berkeley* and Earthquake Engineering Research Center (EERC) laboratory staff at the Richmond Field Station for helping make the experimental work a success. I am especially grateful to Dr. Shakhzod Takhirov for his extensive assistance and helpful advices. In addition, I would like to thank Wesley Neighbour, Don Clyde, Donald Patterson, Nathaniel Knight, Jose Robles and David McLam for their advice, assistance and help with various aspects of my experimental endeavors. Furthermore, I would like to thank the librarian Charles James for his help in acquiring papers and books for me.

I am so grateful to my former professors from the University of Belgrade in Serbia, Prof. Vanja Alendar and Prof. Dejan Bajić, and from the Institute of Earthquake Engineering and Engineering Seismology in Macedonia, Prof. Veronika Šendova and Prof. Zoran Milutinović, who provided me with the technical background, inspiration, and support to pursue my studies at the University of California at Berkeley.

To my friends, Ady Aviram, Aikaterini Konakli, Andreas Schellenberg, Athanasios Kiourtis, Dimitrios Konstantinidis, Filip Blagojević, Gaspard Duchene, Jose Luis Oviedo, Kranthi Kiran Mandadapu, Laura Sterponi, Nicola Tondini, Sonia Garcia Reyes, Sophie Veran, Svetlana Kostić, Tatjana Bolić, Tea Visnjić, Tony Yang, and Vlasta Vranješ, I am thankful for making Berkeley most wonderful place to live in.

Last and most of all I would like to thank my husband Uglješa and our daughter Tara. Your love, support and patience made this step in my life possible. Without you none of this would have any importance. I would also like to thank my parents, Dušanka and Živislav, for their love, support and understanding throughout my life. Especially, I would like to thank my mother for taking a great care of my daughter while I was writing the last chapter of this dissertation.

The work presented in this dissertation was supported in parts by an NSF EERC program grant EEC-9701568 as PEER Projects 209, 213 and 244, by the PEER Center Transportation

Systems Research Program and by Caltrans project EQ042-59A0506. The conclusion and opinions presented in this dissertation do not necessarily reflect those of the sponsors.



# 1 Introduction

## 1.1 MOTIVATION

Modern highway bridges in California, designed using the Caltrans Seismic Design Criteria (SDC) (Caltrans, 2006a), are expected to maintain at minimum a gravity load-carrying capacity during both frequent and extreme seismic events. As of now, there are no validated, quantitative guidelines for estimating the remaining load carrying capacity of the bridges after an earthquake event. Instead, the bridge inspectors and maintenance engineers provide an estimate of the bridge ability to function after the earthquake based on qualitative observations. Immediate decisions regarding bridge safety and serviceability after an earthquake are based on the opinions of individual engineers, with each judgment founded on personal experience. This can be overcome by developing an analytical model able to provide quantitative estimation of the post-earthquake bridge capacity to carry traffic loads. Availability of such analytical model would improve public safety and minimize economic impact caused by disruption of the road network due to possibly unnecessary bridge closures.

## 1.2 BACKGROUND

Numerous research projects have addressed modeling of bridge structures under seismic loading (e.g. Fenves and Ellery, 1998) and validation of analytical models against measured seismic response of instrumented bridges (e.g. Arici and Mosalam, 2003). However, only a few real bridges have been tested to evaluate their capacity in the field (Bollo et al., 1990; Gilani et al., 1995; Eberhard and Marsh, 1997a; Eberhard and Marsh, 1997b; Pantelides et al., 2002). The bridges involved in these research projects have not been designed according to current Caltrans SDC. Nevertheless, as long as there is some ductility in the response of bridge elements, the results of these research projects show that the capacity design principles Caltrans SDC is based on are valid. More important, however, is the fact that none of the bridge systems have been tested for the remaining traffic load capacity after some damage was induced under lateral loading. There was an attempt to evaluate the ability of a highway overpass bridge to carry traffic load after an earthquake using a finite element model of a typical California overpass bridge built using OpenSees (<http://opensees.berkeley.edu>) (Mackie and Stojadinovic, 2005). The major findings are listed herein:

1. Damage and permanent displacement induced by lateral loading reduce the gravity load capacity of a bridge.
2. The bridge column is the element of the bridge that provides the majority of the gravity load resistance after a seismic event. While other elements of the bridge do contribute to the ability to carry gravity load (for example: the bridge deck may help

to redistribute the load; the joints and shear keys have to carry wheel loads locally), the local damage to the column plastic hinge and the possible permanent displacement of the column are the most important factors contributing to the loss of the ability of the bridge to carry traffic load after an earthquake.

3. The finite element models of beam-column elements in use today are capable of representing the loss of gravity load capacity after some damage is induced in the models by lateral loads, but they have not been calibrated or validated using experimental data.
4. The design procedures built into reinforced concrete design codes (such as ACI 318) and bridge design procedures (such as Caltrans SDC) do not provide the means to evaluate the remaining axial load capacity of a damaged reinforced concrete column.

### **1.3 RESEARCH OBJECTIVES AND SCOPE**

The main goal of this project is to develop analytical model of a bridge which can be used for evaluation of its post-earthquake traffic load capacity. The analytical model of a bridge will be then used in estimating the post-earthquake truck load capacities of a typical overpass bridge in California for a suite of ground motions and set of parameters that have a great influence on the truck load capacity. To achieve this, analytical and experimental investigations are combined into an integrated research program. Chart in Fig. 1.1 shows the steps of the research program.

As the ability of a bridge to function after an earthquake depends directly on the remaining capacity of the bridge columns to carry load, this research program will start by testing the scaled bridge column specimens in two phases: (i) laterally and (ii) axially. In the lateral phase of testing the specimens will be displaced bi-laterally in the quasi-static manner up to a pre-determined incrementally increasing displacement ductility targets. In the axial phase of testing, the laterally damaged specimens will be compressed axially to get the axial strengths of the damaged columns. The relationship between earthquake-induced damage in reinforced concrete bridge columns and the capacity of the columns to carry axial load in a damaged condition will be developed. Based on the experimental results, a finite element model of a bridge column will be calibrated.

To validate the calibrated analytical model, two hybrid simulation tests will be performed on a typical overpass bridge in California for the same recorded ground motion scaled to represent two levels of seismic risk. Following the hybrid simulation tests, the physical portions of the hybrid models will be axially tested in the compression machine to get their remaining axial load capacities. In the hybrid simulation procedure, a specimen representing the bottom half of a bridge column will be treated as the physical portion of a hybrid model of the bridge, while the rest of the bridge will be treated as the numerical portion of the model. During the hybrid simulation test the bridge model will be subjected to three sequences of loading in the following order: (i) gravity load, (ii) recorded ground motion (with its three components: two horizontal and a vertical), and (iii) a truck load moving along the bridge. After the earthquake, loads corresponding to a heavy truck load in the most critical positions on the bridge will be applied on the hybrid model to, as directly as possible, demonstrate that a bridge damaged in an earthquake can withstand the heavy truck load.

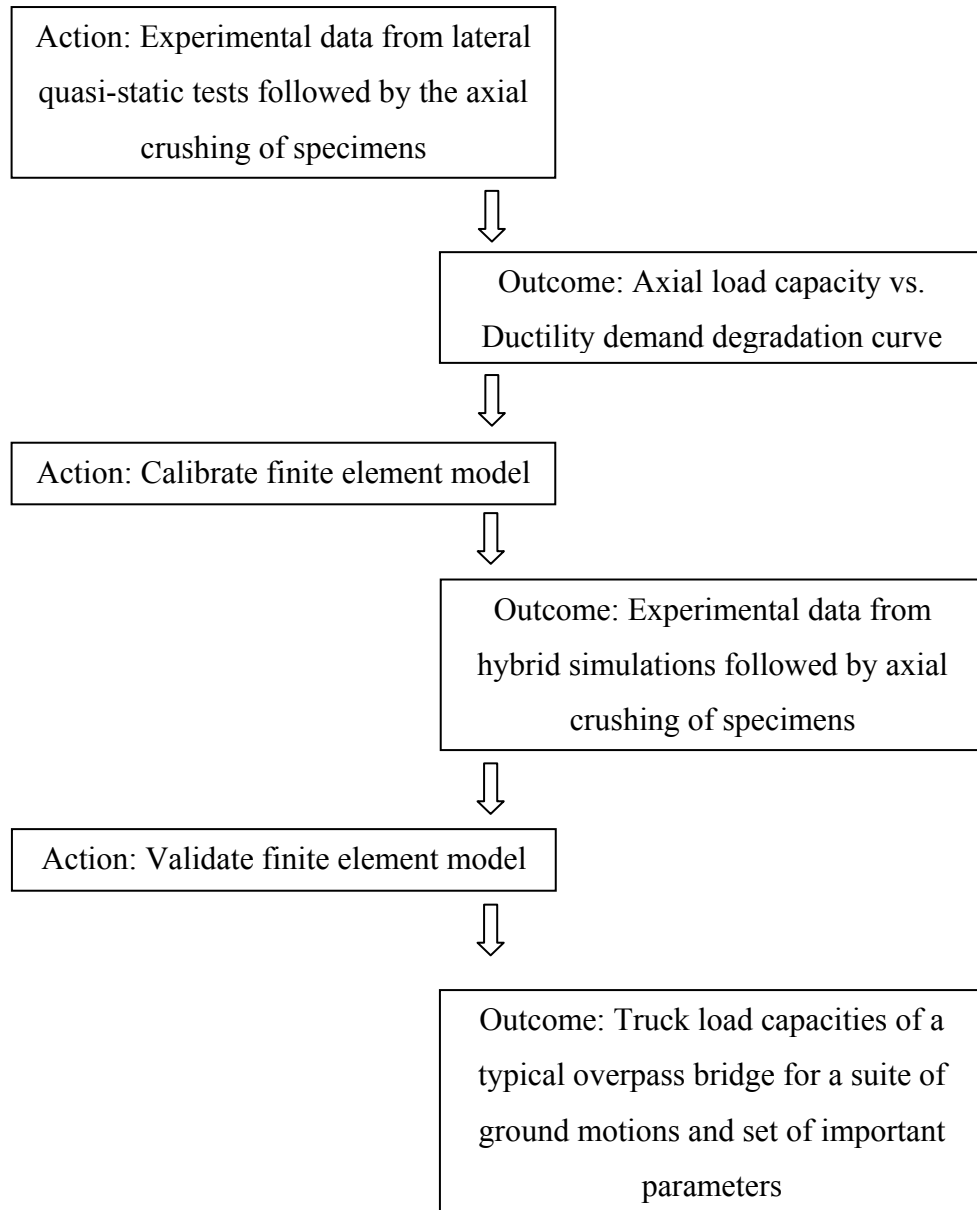


**Fig. 1.1 Methodology for evaluation of the remaining capacity of a bridge to carry traffic load after an earthquake event**

The developed analytical model of a bridge will be first used to identify parameters that have a great influence on the post-earthquake truck load capacity. The post-earthquake truck load capacities of a typical modern overpass bridge in California will be then estimated for a suite of ground motions and set of important parameters. The goal of this study is to provide first-of-its-kind analysis of the remaining load carrying capacity of the typical overpass bridge after an earthquake. Since the analysis is related to one specific bridge type, its main purpose is to show the trends of the post-earthquake truck load capacity of that bridge type with the change of significant parameters. Guidelines for bridge post-earthquake inspection, designed to support

the decision to close a bridge to all traffic, to allow only emergency traffic, or to keep the bridge open with or without restrictions, are proposed on the basis of the derived trends.

## **1.4 ORGANIZATION OF REPORT**

The report contains six chapters. Chapter 2 describes the manner of experimental evaluation of the residual axial capacity of the bridge column specimens with the earthquake-like damage. The chapter includes test program along with test results, observations and findings. The test program includes aspects of specimen modeling and details, loading protocol, test setup, and instrumentation details.

Chapter 3 describes the hybrid simulation tests performed on a typical California overpass bridge for an earthquake and a truck load and the axial tests performed on the physical portion of the hybrid model. The chapter briefly describes components and procedure of a hybrid simulation, gives the details of the test program and shows the test results. The test program includes details of the hybrid model, loading, integration algorithm used in hybrid simulations, test setup, geometric transformations necessary to provide proper communication between physical and numerical portion of the hybrid model, and instrumentation details.

Chapter 4 describes the analytical model of a bridge column that was first calibrated based on results of quasi-static and corresponding axial tests and then validated through hybrid simulations and corresponding axial tests. Comparison between experimental and analytical results is given for all tests.

Chapter 5 gives the results of analytically evaluated post-earthquake truck load capacities of the typical California overpass bridge for a suite of ground motions and set of important parameters. The chapter consists of two sections. The first section describes the bridge model and the loading regime that the bridge was exposed to in the process of evaluating the truck load capacity. The second section discusses the parameters that influence the post-earthquake truck load capacity of a bridge and shows the trends of the post-earthquake truck load capacity for the most influential parameters.

Finally, Chapter 6 presents a summary of the main findings and conclusions of this research and provides brief list of future research directions.

## **2 Experimental Investigations: Quasi-Static Tests**

### **2.1 INTRODUCTION**

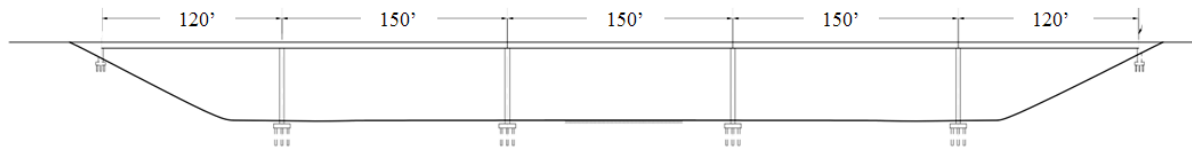
Evaluation of the post-earthquake capacity of a bridge to carry self-weight and traffic loads is essential for a safe and timely re-opening of the bridge after an earthquake. The ability of a bridge to function depends directly on the remaining capacity of the bridge columns to carry load. An experimental program was developed to investigate the relationship between earthquake-induced damage in reinforced concrete bridge columns and the capacity of the columns to carry axial load in a damaged condition. The results obtained from these tests will be used to calibrate a finite element model of the column. Four scaled models of typical circular bridge columns were tested in the two phases. The quasi-static bi-directional lateral test, as the first phase of the testing procedure, is designed to induce controlled amount of lateral damage into the specimen. In the quasi-static lateral tests, the cantilever circular specimens were displaced up to a pre-determined level of lateral displacement ductility. During the tests, the specimens were displaced in both horizontal directions such that the control point followed a circular orbit in the horizontal plane. An axial load equal to 10% of the column's nominal axial load capacity was maintained during lateral testing. At the end of the lateral tests the column specimens were re-centered by cycling them at low amplitudes of displacement. The axial test, as the second phase of the procedure, involved compressing the specimen by axial loading using a force controlled compression-tension machine. This was done to determine the axial load capacity of the column after a controlled amount of lateral load-induced damage. Additionally, a fifth undamaged column specimen was compressed axially to establish the original axial strength of the column used to evaluate the loss of column axial strength due to the damage induced by lateral loading.

### **2.2 EXPERIMENTAL SETUP AND TEST PROGRAM**

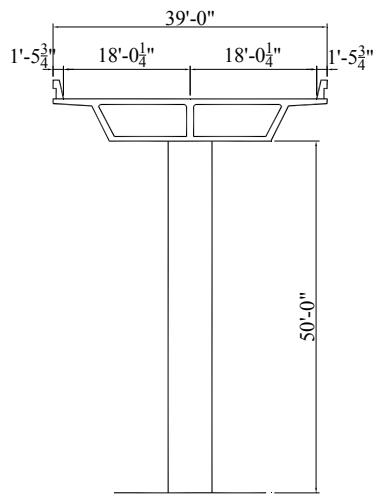
The following sections summarize the aspects of the experimental program including specimen modeling and details, loading, test setup and instrumentation.

## 2.2.1 Prototype and Model

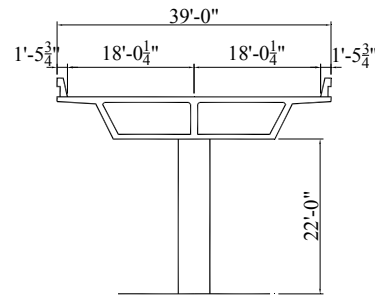
A prototype highway overpass bridges are chosen based on a study conducted by Dr. Mark Ketchum within a PEER project. This study, aimed at evaluating the relation between cost of new bridges and intensity of ground motion (Ketchum et. al., 2004), offers a number of typical Caltrans bridges. These bridges, although not completely detailed, are designed with sufficient detail to allow for an analytical evaluation of the remaining axial load capacity. Bridges Type 1 and Type 11 (Ketchum et al., 2004) shown in Fig. 2.1, typical for short and tall overpass bridges, respectively, were chosen as prototypes. The bridges are five-span single-column-bent overpasses with 120-foot (36.58 m) edge spans, 150-foot (45.72 m) inner spans, and a 39-foot (11.89 m) wide deck. The columns height of the bridge Type 1 is 22' (6.7 m) and of the bridge Type 11 it is 50' (15.24 m). Geometry and reinforcement characteristics of the bridge columns for the bridges Type 1 and Type 11 are given in Table 2.1 and Table 2.2, respectively, where  $D$  is the column diameter,  $H/D$  is column aspect ratio,  $\rho_l$  is ratio of longitudinal reinforcement and  $\rho_t$  is a ratio of transverse reinforcement. In this study, only the bridges with circular columns were considered.



(a) Bridge Elevation



(b) Column Type 11



(c) Column Type 1

**Fig. 2.1 Prototype Caltrans bridges (Ketchum et. al., 2004)**

**Table 2.1 Characteristics of the Bridge Type 1 columns (H=22')**

Column type	D <sub>1</sub> [ft]	D <sub>2</sub> [ft]	H/D	$\rho_t$ [%]	$\rho_l$ [%]
A oblong	4.00	4.00	5.5	2.00	1.59
B circular	4.00	4.00	5.5	3.00	2.10
C circular	5.00	5.00	4.4	1.00	1.24
D circular	4.00	6.00	3.7 - 5.5	1.00	0.81
E circular	4.00	6.00	3.7 - 5.5	2.00	1.24
F circular	4.00	6.00	3.7 - 5.5	3.00	1.71
G oblong	5.00	5.00	4.4	2.00	1.92
H oblong	6.00	6.00	3.7	1.00	1.35
I oblong	7.00	7.00	3.1	1.00	1.33
J oblong	5.50	8.25	2.7 - 4	1.00	0.98
K oblong	5.50	8.25	2.7 - 4	2.00	1.59
L oblong	7.00	10.50	2.1 - 3.1	1.00	1.23

**Table 2.2 Characteristics of the Bridge Type 11 columns (H=50')**

Column type	D <sub>1</sub> [ft]	D <sub>2</sub> [ft]	H/D	$\rho_t$ [%]	$\rho_l$ [%]
A oblong	4.00	6.00	8.3-12.5	3.00	1.11
B circular	6.00	6.00	8.33	2.00	1.10
C circular	6.00	6.00	8.33	3.00	1.57
D circular	7.00	7.00	7.14	1.00	0.73
E circular	7.00	7.00	7.14	2.00	1.45
F circular	8.00	8.00	6.25	1.00	0.73
G oblong	5.50	8.25	6 - 9	1.00	0.75
H oblong	5.50	8.25	6 - 9	2.00	0.87
I oblong	5.50	8.25	6 - 9	3.00	1.12
J oblong	7.00	10.50	4.8 - 7.2	1.00	0.71
K oblong	7.00	10.50	4.8 - 7.2	2.00	0.87
L oblong	7.00	10.50	4.8 - 7.2	3.00	1.23

The two principal parameters that affect the remaining axial load capacity of bridge columns (Mackie and Stojadinovic, 2005) are column aspect ratio (H/D) and column shear strength (or transverse reinforcement ratio  $\rho_t$ ). Different possible values of these two parameters,

bounded by the provisions of the Caltrans SDC (Caltrans, 2006a), were investigated. Based on the study, the two parameters for the columns of Type 1 bridge are chosen to be  $H/D=4.875$  and  $\rho_t=0.35\%$ . In the case of the columns of Type 11 bridge they are chosen to be  $H/D=8$  and  $\rho_t=0.75\%$ . An additional parameter that defines the element properties, the longitudinal reinforcement ratio  $\rho_l$ , is chosen to be the same for both column types and equal to 1.2%.

The Type 1 and Type 11 bridge columns are modeled with specimens referred to here as the Shear-Short and Base Column specimens, respectively. The column specimens are cantilever columns representing the bottom half of the prototype bridge columns. The specimens will be bi-laterally tested in a single curvature bending, assuming an inflection point at column mid-height. The specimen aspect ratio ( $L/D$ ) is 2.44 for the Shear-Short Column specimen and it is 4 for the Base Column specimen. The specimen diameters are chosen to be the same for all column specimens and equal to 16 inches (0.4 m). The choice of the specimen aspect ratios and diameter leads to the height of 39 inches (0.99 m) for the Shear-Short Column specimen and 64 inches (1.62 m) for the Base Column specimen. Thus, the models of Type 1 and Type 11 bridge column prototypes are scaled using a length scale factor of 3.385 and 4.6875, respectively. The corresponding prototype column diameters are 4.5 feet and 6.25 feet for Type 1 and Type 11 bridges, respectively. The basic design parameters for the two types of specimens are summarized in Table 2.3.

**Table 2.3 Design parameters of the specimens**

Specimen type	Scaling factor	D [in]	L [in]	L/D	$\rho_t$ [%]	$\rho_l$ [%]
Base	4.6875	16	64	4	0.75	1.2
Shear-Short	3.385	16	39	2.44	0.35	1.2

The Base Column specimen is expected to demonstrate pure bending behavior during the lateral test by forming a plastic hinge at the bottom of the column. Conversely, the Shear-Short Column specimen is designed such that after some inelastic bending action in the plastic hinge region of the specimen a transition to a shear failure mode occurs. Although not shear critical, the Shear-Short specimen can develop shear cracks that affect its axial load-carrying capacity. The aforementioned behavior of the specimen is achieved through the choice of aspect ratio of the specimen ( $L/D=2.44$ ) and ratio of transverse reinforcement ( $\rho_t=0.35\%$ ). The ratio of transverse reinforcement of the specimen is markedly smaller than that usually found in the modern bridge columns with the similar geometry (typically  $\rho_t>1\%$ ). As such, the design of the shear-short specimen is not in agreement with Caltrans SDC (Caltrans, 2006a). The main goal of testing the Shear-Short Column specimen is to provide the data for finite element calibration on columns that are not shear-critical, but can develop shear cracks that affect their axial load-carrying capacity.



### 2.2.2 Test Matrix

The experimental research study was developed to establish the effects of the earthquake induced damage in a bridge column on its residual axial load carrying capacity. In the first stage of the testing procedure, three Base and one Shear-Short Column specimens were tested by applying a bi-directional quasi-static incremental lateral displacement protocol with circular orbits of displacement up to the predetermined displacement ductility targets of 1.5, 3, 4.5, and 4.5 as shown in Table 2.4. In the second stage of the testing procedure, an undamaged Base Column specimen and the four damaged columns were subjected to a monotonically increasing axial force up to failure.

**Table 2.4 Test matrix**

Test designation	Specimen type	Ductility target	Test sequences
Base0	Base	0	Axial
Base15	Base	1.5	Lateral & Axial
Base30	Base	3.0	Lateral & Axial
Base45	Base	4.5	Lateral & Axial
ShearShort45	Shear-Short	4.5	Lateral & Axial

To differentiate among the tests they are named in Table 2.4. Each designation consists of the two parts. The letter part of designation relates to the type of the specimen the test is performed on. The numeral part specifies the target displacement ductility level the specimen will achieve during the lateral test (e.g., for test designation Base45, the letter part Base indicates that the type of the specimen is the Base Column specimen and the numeral 45 indicates that the target displacement ductility level of the specimen is 4.5). For test designation Base0, the numeral part indicates that displacement ductility target is zero which means that there was no lateral test. The test Base0 was purely axial.

### 2.2.3 Geometry and Reinforcement

The geometry and reinforcement of the Base Column specimen are detailed in Fig. 2.2. The specimen is a 16-inch (0.4 m) diameter circular column, 73.75 inches (1.875 m) in height with the square foundation block (84" x 84"; 2.13 x 2.13 m), 24 inches (0.61 m) high. The effective height of the column, from the base of the column to the level of lateral load application, is 64 inches (1.625 m). The extension of 9.75" (0.25 m) above the effective height of the column accommodates the installation of the 0.5-inch (1.3 cm) thick and 16 inches (0.4 m) high steel jacket. The steel jacket provides an attachment for the actuators at the top of the column.

The column has twelve longitudinal No.4 (Ø13) reinforcing bars placed around its perimeter. The transverse steel reinforcement is W3.5 continuous spiral with a center to center spacing of 1.25-inch (3.175 cm). The cover is 1/2" (1.3 cm) all around.

With the scaling factor of 4.6875 the specimen models half of a 6.25-foot (1.905 m) diameter, 50-foot (15.24 m) tall bridge column. The prototype column has 34 longitudinal No.11 (Ø36) reinforcing bars and No.8 (Ø25) spiral with a center to center spacing of 6 inches (0.15 m).

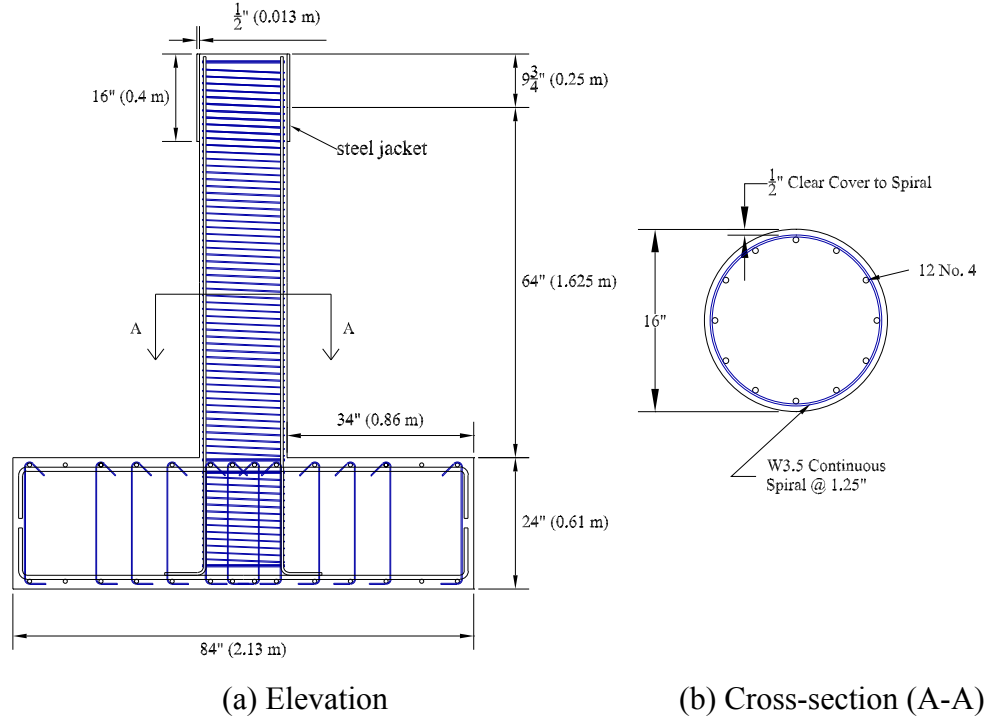


**Fig. 2.2 Geometry and reinforcement of the Base Column specimen**

In the case of the Shear-Short Column specimen, Fig. 2.3 shows geometry and reinforcement details. The only difference between the two types of specimens is the effective height and the vertical center to center spacing between spirals. The effective height of the shear-short specimen is 39 inches (0.99 m) and the vertical center to center spacing between spirals is 2.75 inches (7 cm).

With the scaling factor of 3.385 the specimen models half of a 4.5-foot (1.37 m) diameter, 22-foot (6.7 m) tall bridge column. The prototype column has 18 longitudinal No.11 (Ø36) reinforcing bars and No.8 (Ø25) spiral with a center to center spacing of 18.5 inches (0.47 m).

The basic dimensions and reinforcement for the two types of specimens along with the characteristics of their prototypes are summarized in Table 2.5.

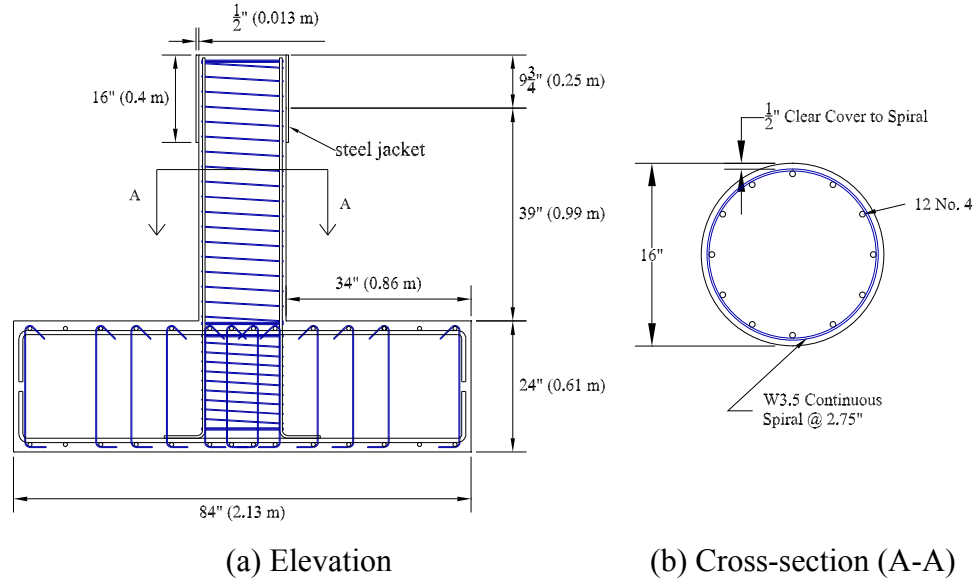


**Fig. 2.3 Geometry and reinforcement of the Shear-Short Column specimen**

**Table 2.5 Basic dimensions and reinforcement of the models and the prototypes**

Column Type	D	H	Longitudinal Bars	Transverse Reinforcement
Base Spec. (BS)	16"	64"	12 No.4	Wire3.5 @ 1.25" spa
Prototype for BS	6.25'	50'	34 No.11	Spiral No.8 @ 6" spa
Shear-short Spec. (SSS)	16"	39"	12 No.4	Wire3.5 @ 2.75" spa
Prototype for SSS	4.5'	22'	18 No.11	Spiral No.8 @ 18.5" spa

## 2.2.4 Material Properties

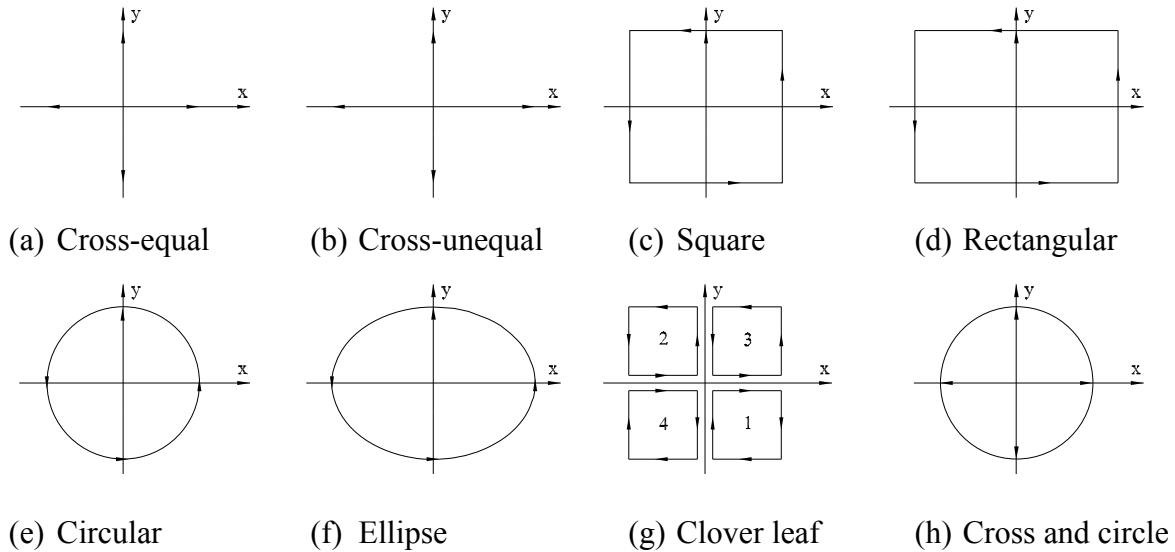
The material properties specification met the requirements in the Caltrans Standard Specifications (Caltrans, 2006b). According to the specification, column longitudinal reinforcement met the ASTM standard A 706, and spiral reinforcement met the ASTM standard A82. The concrete mix was designed to model a prototype mix. To match the parameters of the prototype without compromising its workability, the aggregate size was scaled from 1-inch maximum (prototype mix) to 3/8-inch maximum (scaled mix). The concrete mix was designed by Caltrans Engineers to reproduce the specified compressive strength, fracture energy, and modulus of elasticity. Table 2.6 shows the specified and actual strengths of the longitudinal steel, the spiral steel, and the concrete. The specified strength is the minimum permissible strength. The actual strength is the strength measured from the actual materials used in the test specimens. The yield strength for the high-strength A 82 wire used for the spiral was defined according to ASTM specification as the strength corresponding to a strain of 0.005. Details of the testing procedures and the measured stress-strain response for each material are described in Appendix A.

**Table 2.6 Material properties**

Material	Specified [ksi]		Actual [ksi]	
	Yield	Ultimate	Yield	Ultimate
Steel				
Longitudinal	60	80	70.7	120
Spiral	80		95	106
Concrete	5.0		4.96 to 6.34	

### 2.2.5 Loading Pattern: Quasi-Static Tests

A literature review preceded the selection of an appropriate loading pattern for bilateral quasi-static tests (Stojadinovic, 1995; Kawashima et al., 2006; Schoettler et al., 2006; Chung et al., 2006). The first step was to identify bidirectional patterns of loading commonly used in quasi-static tests. It was observed that the most common patterns of loading are: cross-equal, cross-unequal, square, rectangular, circular, ellipse, clover leaf, and cross and circle (Fig. 2.4).

**Fig. 2.4 Loading pattern matrix**

In order to define the most suitable pattern of loading for the quasi-static tests, nonlinear time history analyses were performed on the two existing bridges. Two suites of ground motions (20 records per suite) representing the two types of earthquakes with respect to different rupture mechanisms were considered. The ground motions originated from strike-slip near field and thrust fault far field earthquakes. Bridge configurations, ground motions and bridge responses are given in Appendix B of this document.

The specimens to be tested in quasi-static manner are cantilever circular columns (representing half of a bridge column) with the same boundary conditions, fixed-free, in any

direction. Thus, the lateral stiffness of the specimen is the same in any direction. On the other hand, single-column-bent bridges have columns with approximately fixed-fixed boundary conditions along the longitudinal axis of the bridge and approximately fixed-free boundary conditions along the transverse axis of the bridge. Consequently, lateral stiffness of the bridge column is different in different directions. Therefore, an appropriately scaled displacement history of the prototype (longitudinal and transverse components) applied on the model will not reproduce the deformation state of the prototype. However, a close correspondence of deformation states between the model and the prototype can be achieved by normalizing the displacement history of the prototype by yield displacements, different in different directions, and inducing the same displacement ductilities in the model. Fig. 2.5 shows how the top-of-the-column orbit plot changes when expressed in terms of displacement ductility.

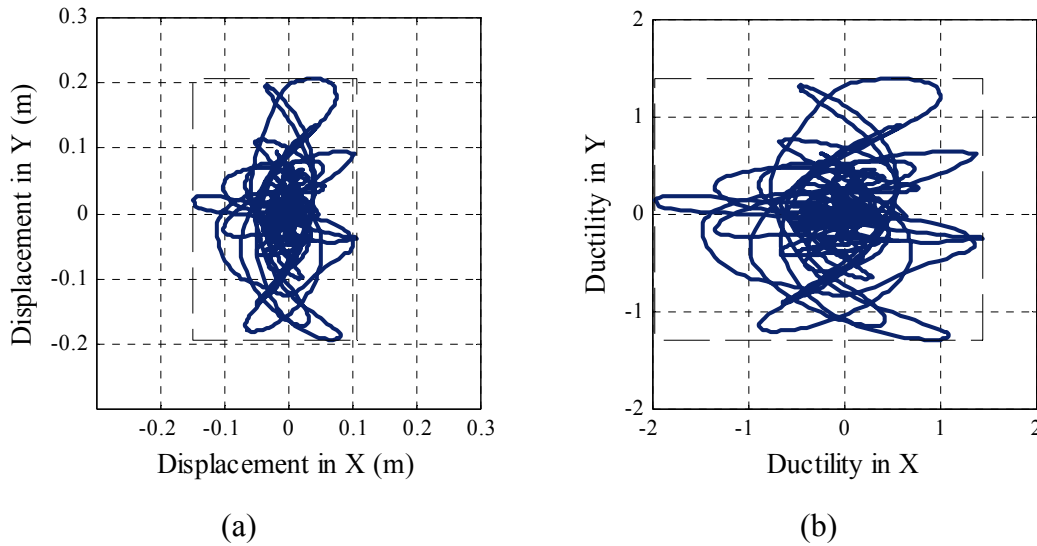


**Fig. 2.5 Displacement orbits at the top of the bridge column: (a) absolute displacements, (b) normalized displacements**

The displacement ductilities at the top of the columns were traced during nonlinear time history analyses on the two bridges and a circular loading pattern was chosen based on it (details are given in Appendix B). The circular loading pattern is defined by two cycles at each displacement level. In the first cycle, starting from the initial position O the specimen is displaced toward the position A, after which the circular pattern of displacement in clockwise direction follows until the end of the circle, point B. The specimen is then moved back to the initial position O (red line in Fig. 2.6). In the second cycle the path O-C-D-O is followed with the circular path C-D in the counterclockwise direction (blue line in Fig. 2.6).

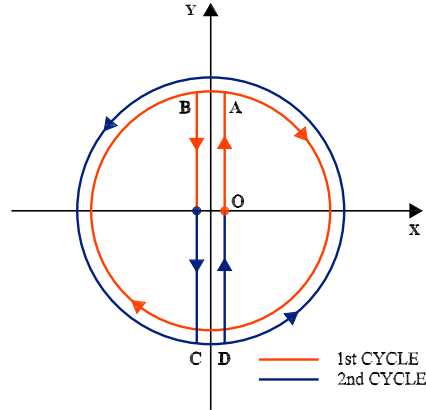


**Fig. 2.6 Loading pattern used for quasi-static lateral displacement tests**

In defining the displacement increments in the loading history for the quasi static tests, recommendations from ACI 374.1-05 and SAC/BD-00/10 reports were followed. Based on the recommendations for the major event of a far field type, the load history was developed for the two tests with ductility target of 4.5: Base45 and ShearShort45. The displacement histories for the lateral tests Base15 and Base30 were obtained by scaling the displacement history of the lateral test Base45 by 0.3 and 0.6, respectively. This way the number of primary cycles in the loading history was the same for all the tests.

For the tests Base45 and ShearShort45, the increments in the magnitude of the displacement ductility were planned to be: 0.08, 0.2, 0.4, 1.0, 1.5, 2.0, 3.0, and 4.5. The pre-yield displacement levels include: a displacement level prior to cracking, two levels between cracking and yielding, and a level approximately corresponding to the first yield of the longitudinal reinforcement. For the post-yield displacement levels, the magnitude of the subsequent primary displacement level is determined by multiplying the current level by a factor ranging from 1.25 to 1.5. The primary displacement levels are increased monotonically to provide an indication of the damage accumulation. The imposed displacement pattern with the two cycles at each displacement level provides an indication of the degradation characteristics of the specimen response. In the post-yield displacement history, each primary displacement level is followed by a small displacement level equal to one-third of the primary displacement level to evaluate intermittent stiffness degradation. The last primary displacement level is followed by the series of small cycles. The magnitude of the small cycles decreased gradually to reach zero. As a result, there were no residual lateral forces and displacements in the column at the end of the test. Consequently, the column did not move after the actuators were disconnected from the column. This way, the specimens were re-centered at the end of the test.

Fig. 2.7 shows the displacement history of the test Base45. The yield displacement of the Base Column specimens predicted in pre-test analyses (0.55 in. – 14 mm) matched the yield displacement observed in the tests. Consequently, the actual displacement history of tests Base15, Base30, and Base45 matched the planned one. In the case of Shear-Short Column specimen the predicted yield displacement (0.24 in. – 6 mm) was smaller than the yield displacement observed in the test (0.35 in. – 9 mm), so the actual displacement history differs from the planned one. The actual displacement histories of the primary cycles are shown in Table 2.7.

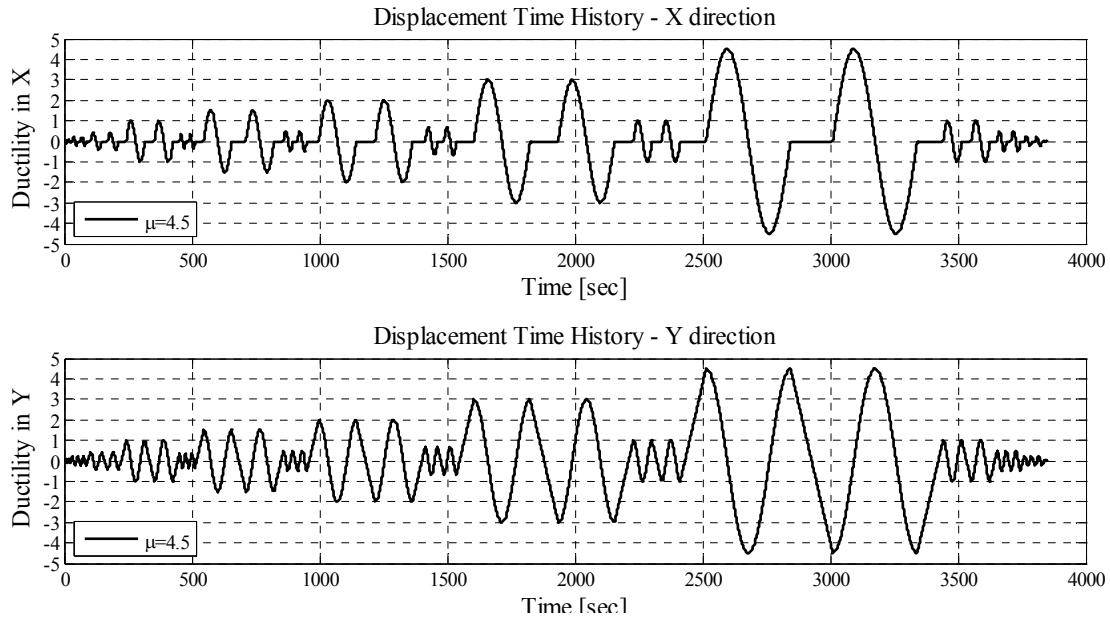


**Fig. 2.7 Displacement history for test Base45**

**Table 2.7 Displacement ductility levels of the primary cycles**

Cycles	Base15	Base30	Base45	ShearShort45
Cycle 1	0.02	0.05	0.08	0.05
Cycle 2	0.06	0.10	0.20	0.13
Cycle 3	0.12	0.25	0.40	0.27
Cycle 4	0.30	0.60	1.00	0.67
Cycle 5	0.45	1.00	1.50	1.00
Cycle 6	0.60	1.25	2.00	1.33
Cycle 7	1.00	1.80	3.00	2.00
Cycle 8	1.50	3.00	4.50	3.00
Cycle 9				4.50

### 2.2.6 Test Setup

In the first phase of the test, lateral and axial loads were applied at the top of the column. The lateral cyclic load with circular orbits of displacement was applied using the two servo-controlled hydraulic actuators (Fig. 2.8). An axial load approximately equal to 10% of the column's nominal axial load capacity was maintained during the lateral test. This load represents the typical dead and live load carried by columns of California overpass bridges. The axial load was applied through a spreader beam using pressure jacks and post-tensioning rods placed on

either side of the column (Fig. 2.8). Spherical hinges were provided at both ends of the rods in order to avoid bending of the rods during bi-directional displacements of the column. Moreover, a hinge connection was needed between the spreader beam and the column for the beam to remain horizontal in the plane of the rods during the lateral displacements of the column. In this way, buckling of the rods was also avoided. The test setup for the quasi-static tests is further detailed in Appendix C.

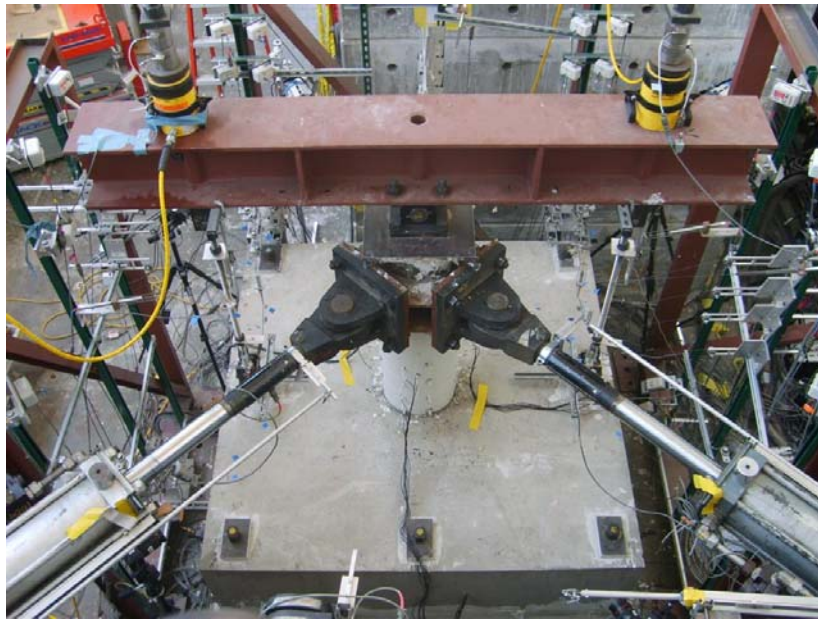


**Fig. 2.8 Lateral test setup**

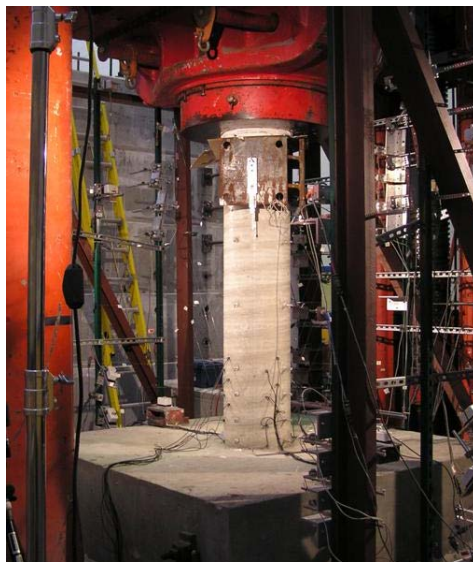


**Fig. 2.9 Axial test setup**



In the second phase of the test, the four laterally damaged column specimens and one undamaged column specimen were compressed axially to induce axial failure in the columns. To accomplish this, a compression-tension machine with a capacity of 4 million lbs and a constant rate of loading was used (Fig. 2.9).

### 2.2.7 Instrumentation

Each specimen was instrumented externally using displacement potentiometers and internally using strain gages. Externally, the column specimen was instrumented at six levels along the height in the case of the Shear-Short Column specimen (Fig. 2.10a) and at seven levels along the height in the case of the Base Column specimen (Fig. 2.10b), starting from the column base. Three points at each level (referred as target points, Fig. 2.11b) were instrumented with three displacement potentiometers per point. The instruments were connected to the target points of the column by piano wires (Fig. 2.11). All instruments were attached to the three instrumentation frames positioned on three sides of the column (Fig. 2.12). The displacements of any target point at any level of the column were measured in three arbitrary spatial directions and mathematically transformed to displacements of that point in the global coordinate system, referred to as the XYZ system. The axes of the global coordinate system are chosen to follow the right-hand rule with X axis aligned with the spreader beam and Z axis aligned with the column pointing upward. The measured displacements of the three target points at one level were then used to derive the 6 degrees of freedom (3 displacements and 3 rotations) for the section at that level (Appendix C). To insure that there were no lateral displacements of the anchor block during the lateral test, the anchor block was instrumented at three points by displacement potentiometers. The displacement potentiometers were connected to the small solid aluminum cubes that were glued to the laboratory floor.

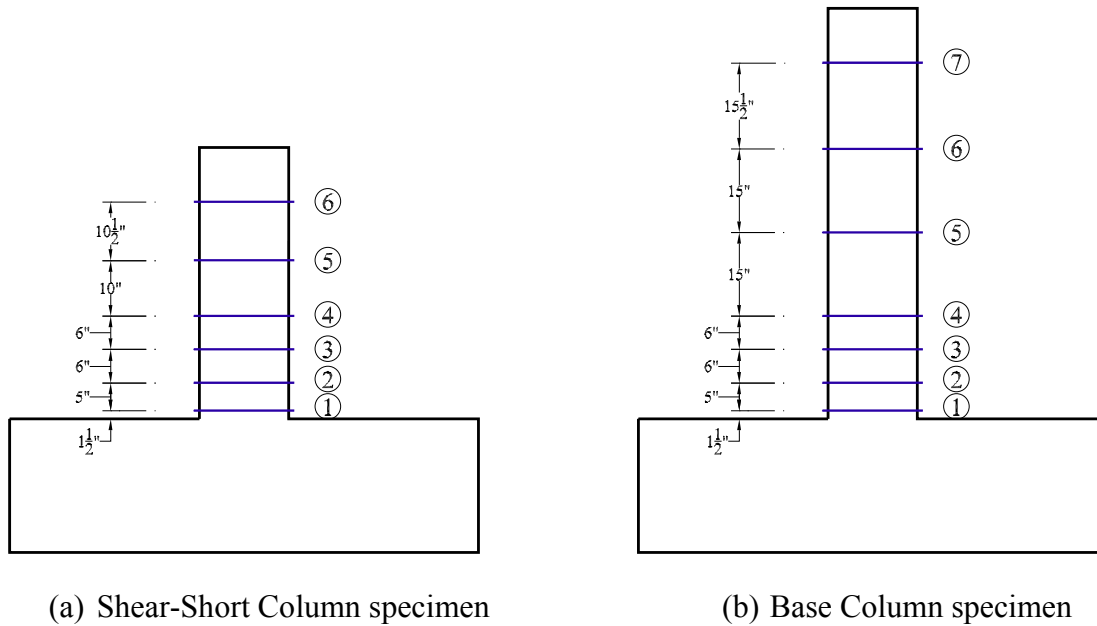
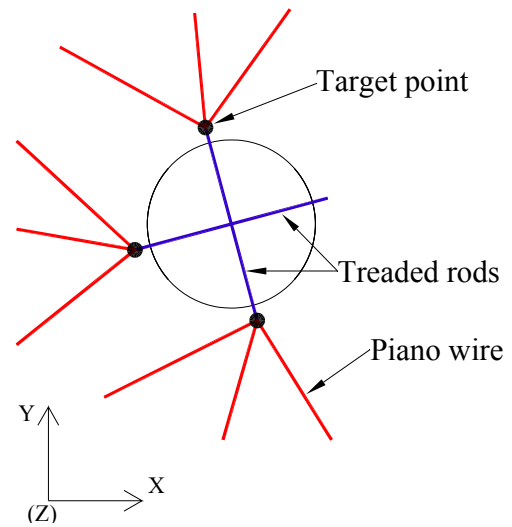


**Fig. 2.10 Externally instrumented levels along the height of the specimens**



(a)



(b)

**Fig. 2.11 Details of the instrumented points of the specimen: (a) target points and piano wires, (b) locations of the instrumented points at one level**



**Fig. 2.12 Instrumentation frames**

Internally, the columns were instrumented at five levels along the height of the column (Fig. 2.13). At each level strain gages were attached to four out of twelve longitudinal reinforcing bars. The first level of strain gages was in the foundation zone (Plane 1) and the other four levels were in the plastic hinge region. The bars with the strain gages attached to it coincided with the axes of application of the load. The spiral reinforcement was also instrumented by strain gages. The positions of strain gages attached to the spiral reinforcement coincided with the positions of the strain gages attached to the bars at levels 1a in Fig. 2.13.

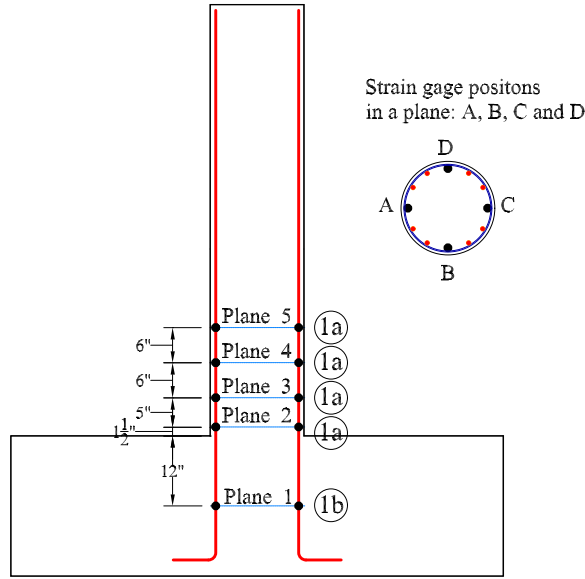


**Fig. 2.13 Strain gage locations**

The axial load setup used for the lateral displacement part of the tests was instrumented with displacement potentiometers and load cells. The spreader beam was instrumented with the four displacement potentiometers (wire pots) in X-Y plane (two on each end of the beam) to measure the lateral displacements of the beam. Additionally, the beam was instrumented with four displacement potentiometers (DCDTs) to measure the rotation of the beam around X axis. At each end of the beam two instruments were installed in parallel in the Y-Z plane having instruments aligned with the Z axis. The post-tensioned rods were instrumented with displacement potentiometers (one at each rod) to measure relative displacements ( $\Delta u$ ) of the rods. From the relative displacement between the two points on the rod with the distance  $\Delta l$ , the axial force in the rod can be calculated as:

$$P = \frac{\Delta u}{\Delta l} \cdot E \cdot A \quad (2.1)$$

where E is the modulus of elasticity of the rod and A is the cross-sectional area of the rod. The load cells were installed at the top of the pressure jacks to measure the forces applied on the spreader beam at locations of the pressure jacks.

During the axial load capacity tests, the same internal and external instrumentation layouts were used as for the quasi-static lateral displacement tests. The compression-tension machine, in addition to its own displacement potentiometer and a load cell, was externally

instrumented with two displacement potentiometer (on the either side of the machine head) to measure the vertical displacements of the machine during the test.

## **2.3 TEST RESULTS**

The test results for the four Base Column specimens and the Shear Short Column specimen are presented in this section. The global lateral and axial force-displacement relationships are given for lateral and axial test sequences, respectively. The lateral load-displacement relationships for the two major directions (X and Y) indicate the extent of nonlinearity in the specimen and show the degradation characteristics of the specimen during lateral loading. The axial force-displacement relationships provide the axial strength of the specimens with the certain amount of laterally induced damage. The force-displacement relationships are accompanied with figures that show intermediate and final states of the tested columns.

To summarize the experimental results, the axial strengths of damaged Base Column specimens are normalized with respect to their original axial strengths and shown with respect to the target displacement ductility levels of the specimens. Additionally, the influence of different geometry (aspect ratio) and transverse reinforcement ratio in the base and Shear-Short Column specimens on their residual axial strengths is shown in terms of the axial load-displacement relationships.

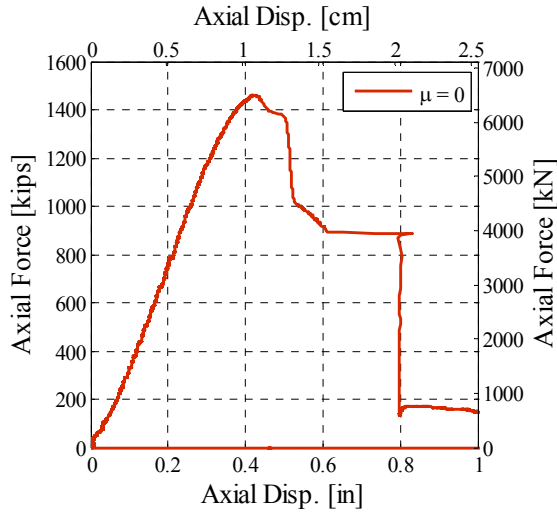
### **2.3.1 Test Results for the Base Column Specimens**

The test results for the Base Column specimens are shown in the following order: (i) Base0, (ii) Base15, (iii) Base30, and (iv) Base45. The results from the lateral load sequence of a test are followed by the results of the axial load sequence. The exception is the test Base0 that had only the axial load sequence.

#### ***2.3.1.1 Test Base0***

The test Base0 was performed to establish the axial strength of a laterally undamaged column specimen. The axial strength obtained from the test was used to normalize the axial strength of the laterally damaged columns. As a result, the reduction in the axial load carrying capacities of the columns due to the laterally induced damage was evaluated. Additionally, the test results are used to calibrate the analytical model.

Fig. 2.14(a) shows the axial force-deformation relationship of the Base Column specimen that was monotonically compressed to induce the axial failure of the column. To accomplish this, a force controlled compression-tension machine with a capacity of 4 million lbs in compression was used. The damaged state of the column is shown in Fig. 2.14(b). The axial failure resulted from the formation of the shear failure plane at the bottom of the column. The axial strength of the tested specimen, designated as  $P_0$ , was 1459 kips (6490 kN).



(a) Axial force-displacement relationship



(b) Axial failure of the column

**Fig. 2.14 Axial force-displacement relationship and state of the specimen after the Base0 test**

### 2.3.1.2 Test Base15

In the test Base15, the specimen was laterally loaded up to the displacement ductility level of 1.5 inducing yielding in the specimen. After reaching the target ductility displacement the column was re-centered by cycling it with very low amplitudes of displacement. The lateral test was followed by the axial compression test to get the axial strength of the laterally damaged column.

The lateral force-displacement response curves for the two major directions of loading (X and Y) are shown in Fig. 2.15. It can be observed that the column just entered its nonlinear response range. The state of the column (the bottom 22 inches) at the target displacement ductility level,  $\mu = 1.5$ , and at the end of the test are shown in Fig. 2.16 and Fig. 2.17, respectively. At the maximum (target) level of displacement the widths of the horizontal cracks, uniformly distributed along the height of the column, were less than 1/32 of an inch (Fig. 2.16). The distance between the cracks along the height of the column was approximately 6 inches. The width of the cracks gradually increased from the top to the bottom of the column. There were no visible cracks at the end of the test (Fig. 2.17).

Fig. 2.18(a) shows the axial force-deformation relationship of the specimen after the axial sequence of loading. The damaged state of the column is shown in Fig. 2.18(b). The axial failure resulted from the formation of the shear failure plane in the middle of the column. The axial strength of the tested specimen, designated as  $P_1$ , was 1137 kips (5057 kN). The ratio of the residual to original axial strength of the column,  $P_1/P_0$ , is 0.78. Thus, the reduction of the axial strength is 22%.

The measurements from the strain gages installed on the longitudinal bars indicated the inclination of the specimen (1% drift) during the axial sequence of the test. Although the specimen was re-centered after the lateral test, it was not properly leveled during its preparation for the axial test. Thus, the observed reduction of the axial strength was caused by: (i) the

material damage laterally induced in the specimen and (ii) the geometric imperfection of the specimen during the axial test. The position of the shear failure plane formed in the axial compression test indicates the predominant influence of geometric imperfection on the reduction of the specimen axial strength.

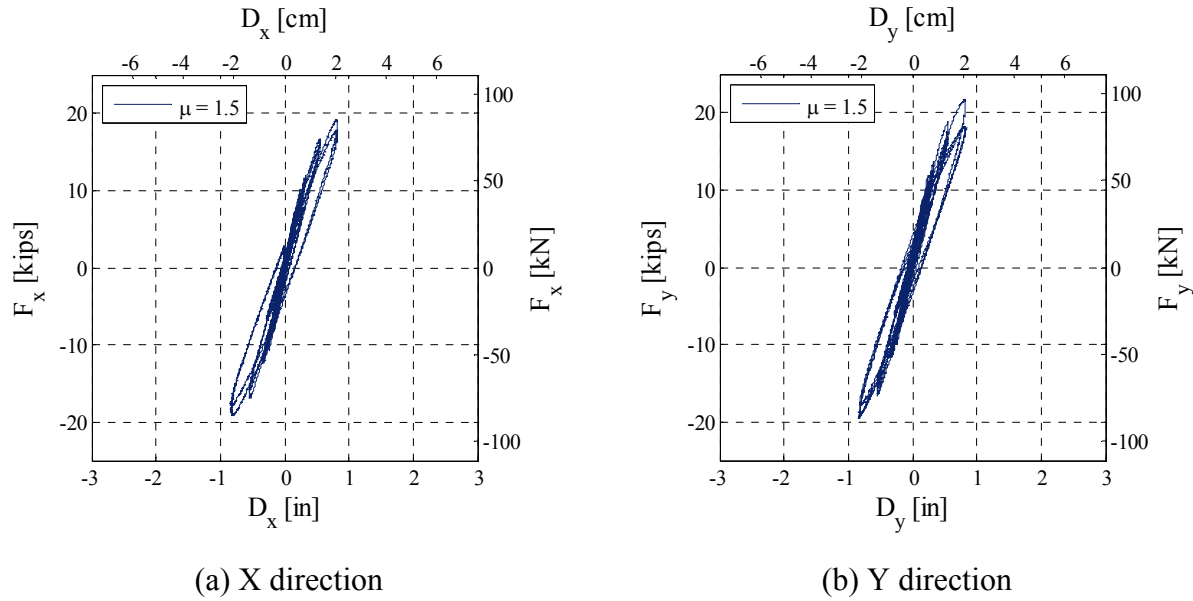


**Fig. 2.15 Lateral force-displacement response curves in the two major directions (X and Y) for the Base15 test**

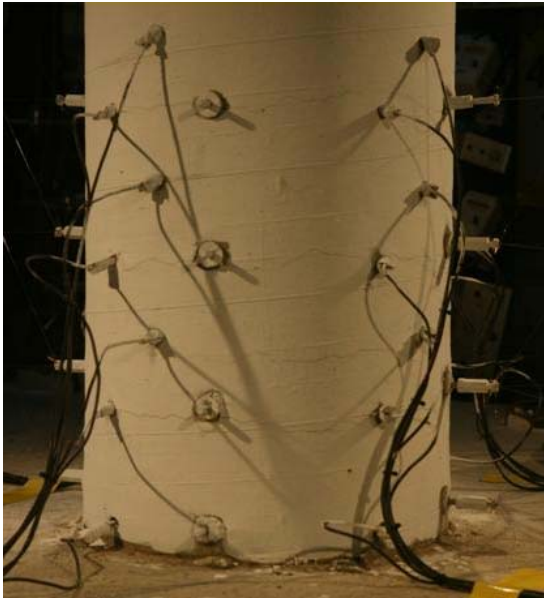




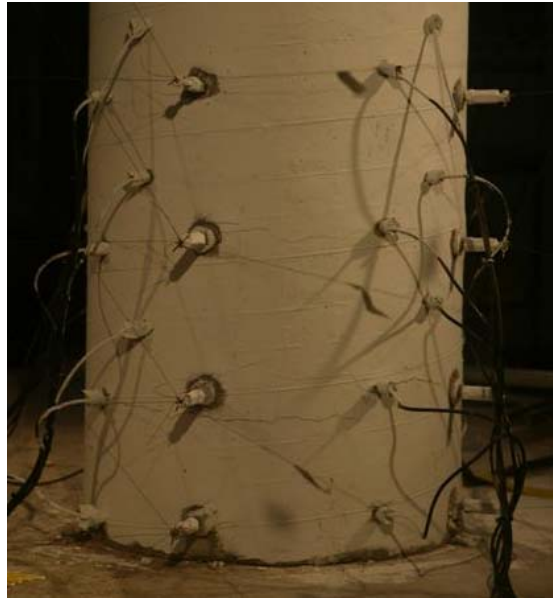
(a) North-East



(b) North-West



(c) South-West



(d) South-East

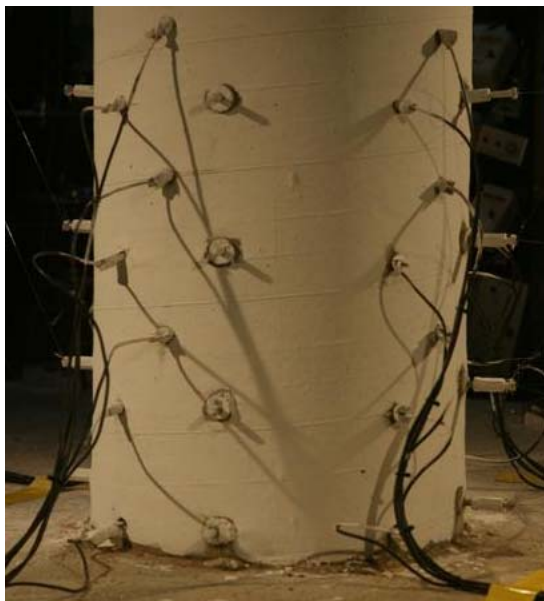
**Fig. 2.16 State of the specimen at the maximum displacement level during the lateral sequence of the Base15 test**



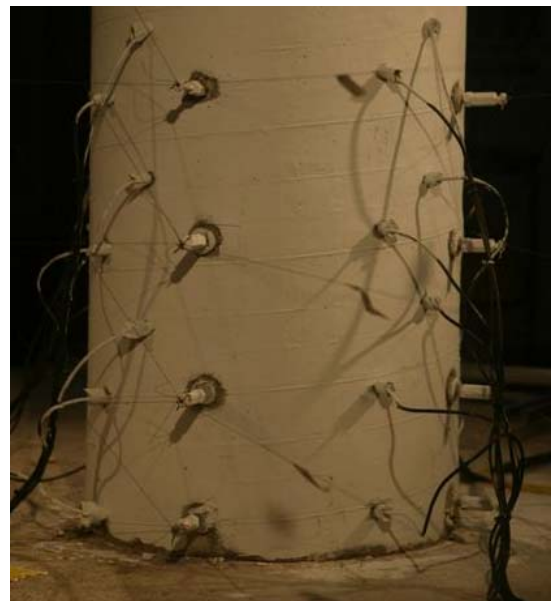
(a) North-East



(b) North-West



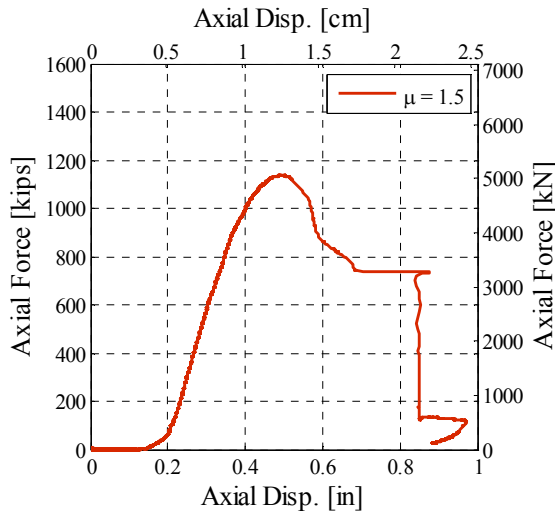
(c) South-West



(d) South-East

**Fig. 2.17 State of the specimen at the end of the lateral sequence of the Base15 test**





(a) Axial force-displacement relationship



(b) Axial failure of the column

**Fig. 2.18 Axial force-displacement relationship and state of the specimen after the axial sequence of the Base15 test**

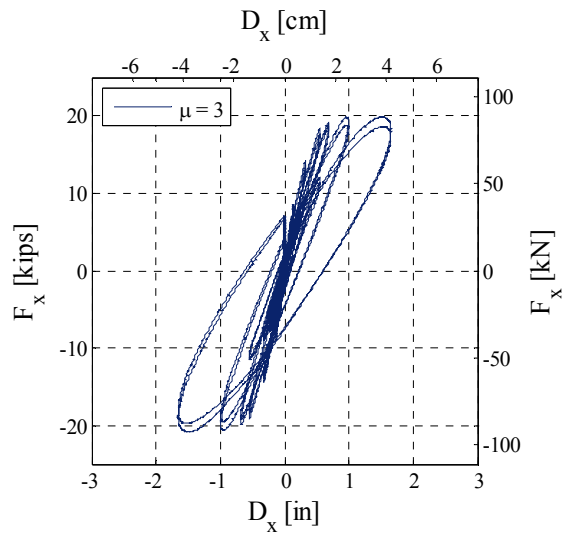
### 2.3.1.3 Test Base30

In the test Base30, the specimen was laterally loaded up to the displacement ductility level of 3.0, with the intention to induce significant yielding and strain hardening of the steel and initiating the spalling of concrete. After reaching the target ductility displacement, the column was re-centered. The lateral test was followed by the axial compression test to get the axial strength of the laterally damaged column.

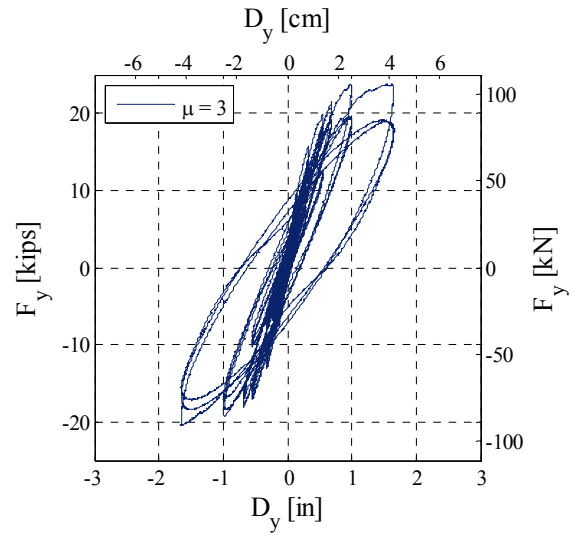
The lateral force-displacement response curves for the two major directions of loading (X and Y) are given in Fig. 2.19. From the hysteresis curves it can be observed that the extent of nonlinearity is significant. After yielding, specimen stiffness degraded with each cycle of loading. The lateral strength of the column slightly increased with increase in the displacement level due to strain hardening of the steel.

The state of the column (the bottom 22 inches) at the target displacement ductility level,  $\mu = 3.0$ , is shown in Fig. 2.20 and at the end of the test is shown in Fig. 2.21. In the plastic hinge region of the column (the bottom 12 inches) the distance between the cracks was 3 inches on average and the maximum width of the cracks during the test was approximately 1/16 of an inch. Outside the plastic hinge region the distance between the cracks was 6 inches on average with the widths of the cracks less than 1/32 of an inch. Fig. 2.21 shows horizontal cracks, vertical cracks, and some spalling of concrete at the bottom 8 inches of the column at the end of the test.

Fig. 2.22(a) shows the axial force-deformation relationship of the specimen after the axial sequence of loading. The damaged state of the column is shown in Fig. 2.22(b). The axial failure resulted from the formation of the shear failure plane at the bottom of the column. The axial strength of the tested specimen, designated as  $P_2$ , was 1355 kips (6027 kN). The ratio of the residual to original axial strength of the column,  $P_2/P_0$ , is 0.93. Thus, the reduction of the axial strength is 7%.

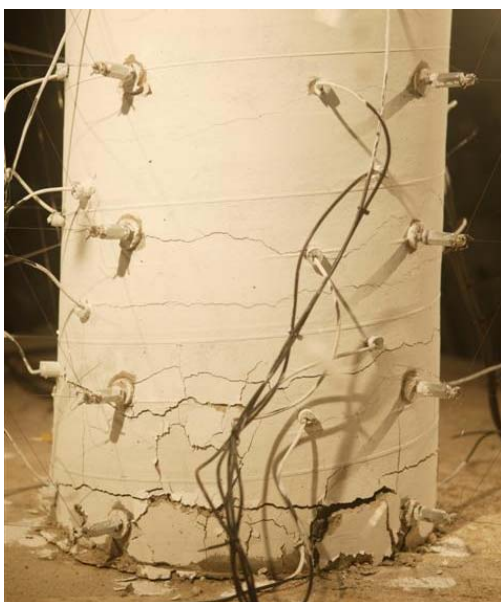


(a) X direction

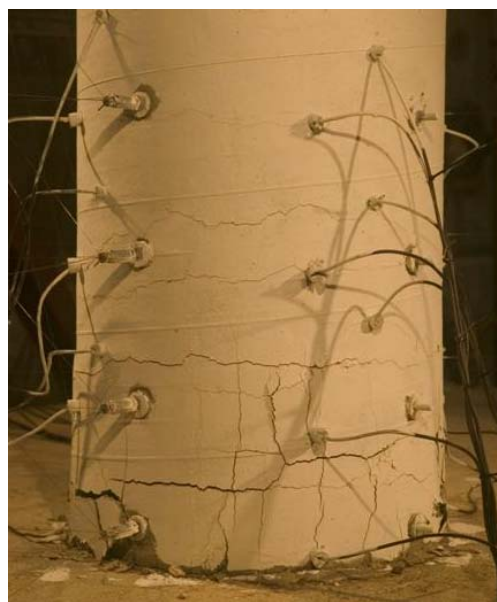


(b) Y direction

**Fig. 2.19 Lateral force-displacement response curves in the two major directions (X and Y) for the Base30 test**



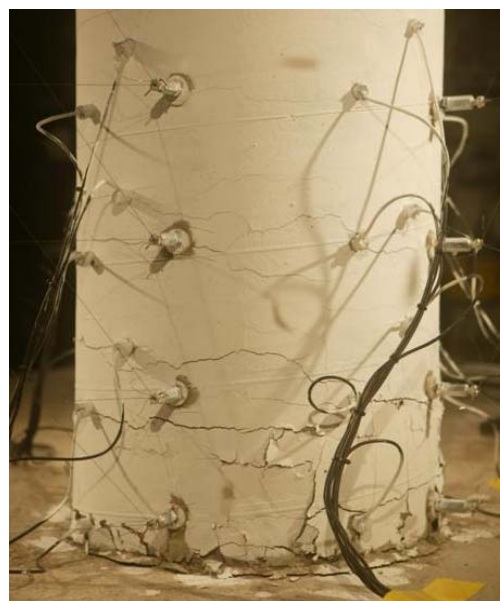
(a) North-East



(b) North-West

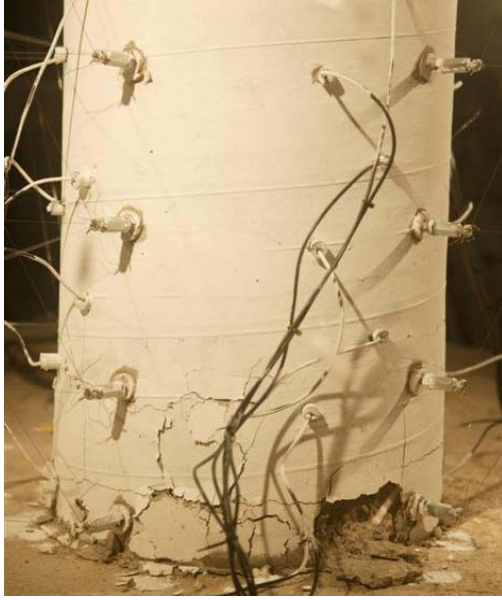


(c) South-West

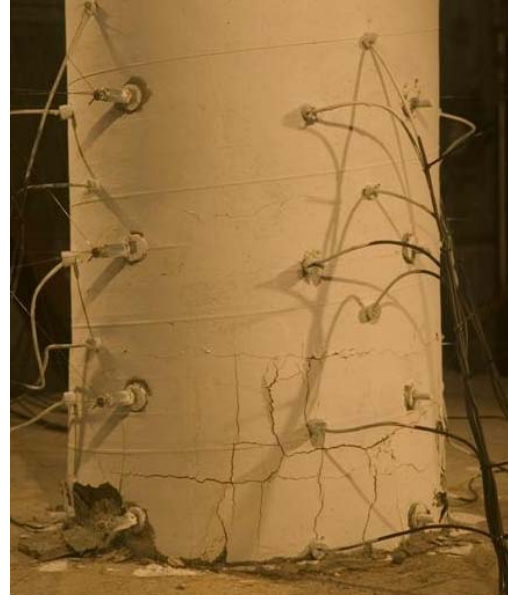


(d) South-East

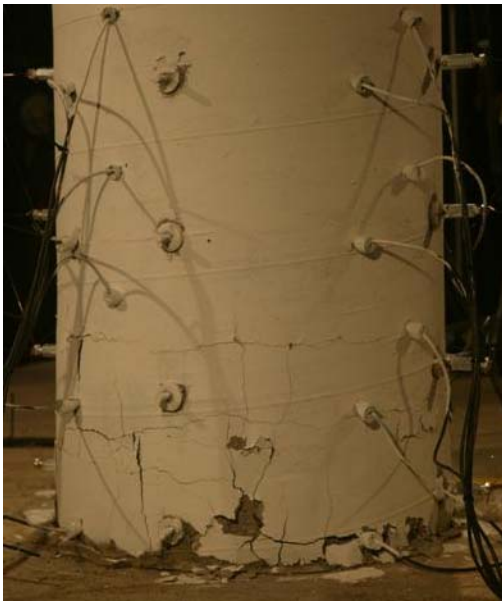
**Fig. 2.20 State of the specimen at the maximum displacement level during the lateral sequence of the Base30 test**



(a) North-East



(b) North-West

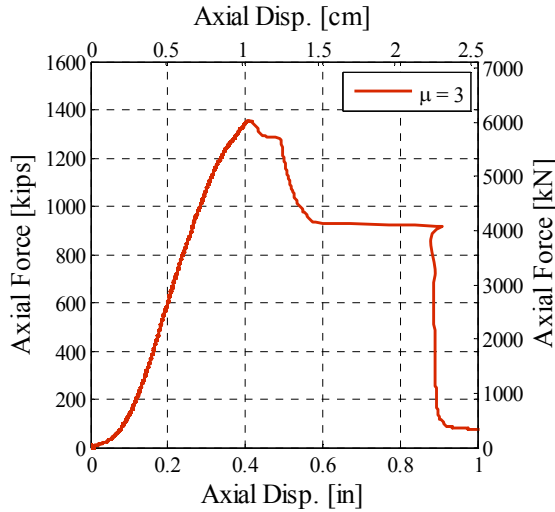


(c) South-West



(d) South-East

**Fig. 2.21 State of the specimen at the end of the lateral sequence of the Base30 test**



(a) Axial force-displacement relationship



(b) Axial failure of the column

**Fig. 2.22 Axial force-displacement relationship and state of the specimen after the axial sequence of the Base30 test**

#### **2.3.1.4 Test Base45**

In the test Base45, the specimen was laterally loaded up to the displacement ductility level of 4.5, inducing extensive yielding of the steel and spalling of concrete as well as a reduction in volume of the concrete core in the plastic hinge region. After reaching the target ductility displacement, the column was re-centered. The lateral test was followed by the axial compression test to get the axial strength of the laterally damaged column.

The lateral force-displacement response curves for the two major directions of loading (X and Y) are given in Fig. 2.23. From the hysteresis curves it can be observed that the nonlinear range of behavior is extensive. After passing the yield point, the stiffness degraded gradually with each cycle of loading. The lateral strength of the column slightly increased with increase in the displacement level due to the strain hardening of the steel. In the last cycle of loading at the target displacement ductility level a small amount of hysteresis loop pinching was observed.

The state of the column (the bottom 22 inches) at the target displacement ductility level,  $\mu = 4.5$ , is shown in Fig. 2.24 and at the end of the test is shown in Fig. 2.25. The specimen was scanned using a laser scanner after the test and deviation of the column surface (for the bottom 50 inches of the column) from the perfect cylinder with the diameter of 16 inches is shown in Fig. 2.27. Maximum deviation of the column surface from the perfect cylinder was between 0.68 in. and 0.86 in. It is bigger than the concrete cover (0.5 in.), thus the concrete core was damaged as well. No bar buckling or spiral fractures were observed.

Based on the crack distribution along the height of the column during the test, the column can be divided into three regions: (i) the plastic hinge region (the bottom 12 inches of column), (ii) the intermediate region (12 inches of the column next to the plastic hinge region), and (iii) the elastic region (the top 40 inches of the column). In the plastic hinge region the distance between the cracks was 3 inches on average and the maximum width of the cracks during the test



was approximately 1/8 of an inch (Fig. 2.24). Very extensive spalling of concrete and reduction in volume of the concrete core were observed (Fig. 2.25). In the intermediate region the distance between the cracks was 4 inches on average with the widths of the cracks less than 1/16 of an inch. In the elastic region the distance between the cracks was 6 inches on average with the widths of the cracks less than 1/32 of an inch.

Fig. 2.26 shows profiles of displacements, rotations, and average curvatures for the primary displacement ductility levels: 1.0, 1.5, 2.0, 3.0, and 4.5. There is a significant increase of rotation and curvature at the bottom of the column with the increase of the displacement ductility level. The results indicate the location and extent of plastic deformations in the specimen.

Fig. 2.28(a) shows the axial force-deformation relationship of the specimen after the axial sequence of loading. The damaged state of the column is shown in Fig. 2.28(b). The axial failure resulted from the formation of the shear failure plane along the total height of the column. The axial strength of the tested specimen, designated as  $P_3$ , was 1170 kips (5204 kN). The ratio of the residual to original axial strength of the column,  $P_3/P_0$ , is 0.80. Thus, the reduction of the axial strength is approximately 20%.

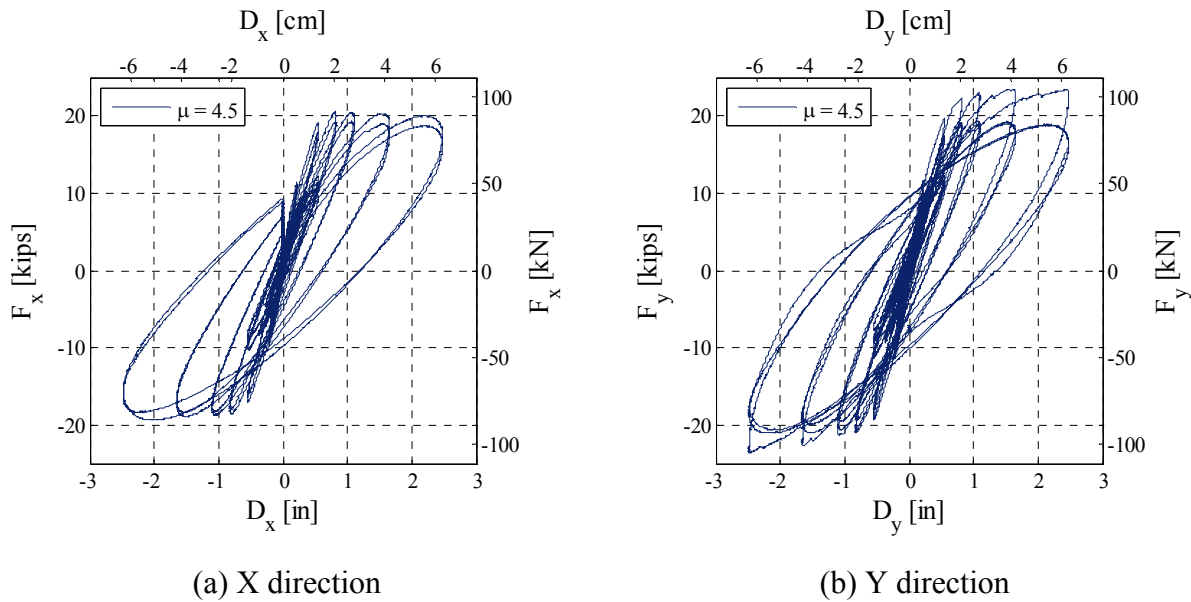


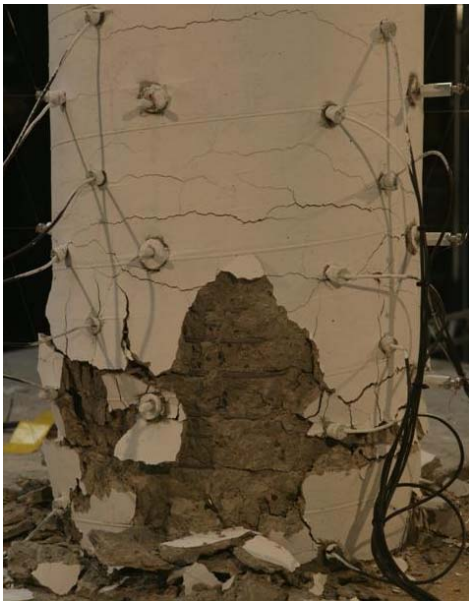
**Fig. 2.23 Lateral force-displacement response curves in the two major directions (X and Y) for the Base45 test**



(a) North-East



(b) North-West



(c) South-West



(d) South-East

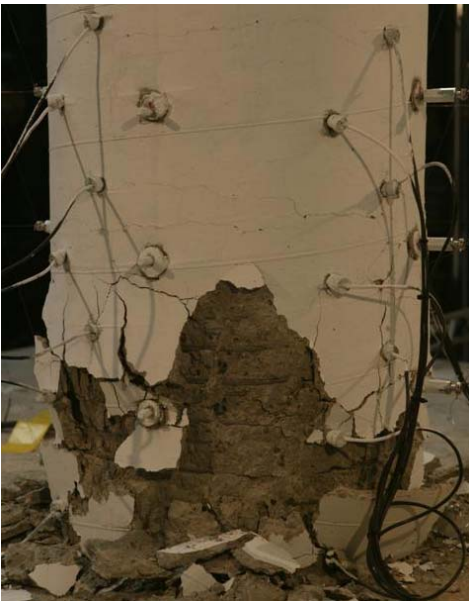
**Fig. 2.24 State of the specimen at the maximum displacement level during the lateral sequence of the Base45 test**



(a) North-East



(b) North-West



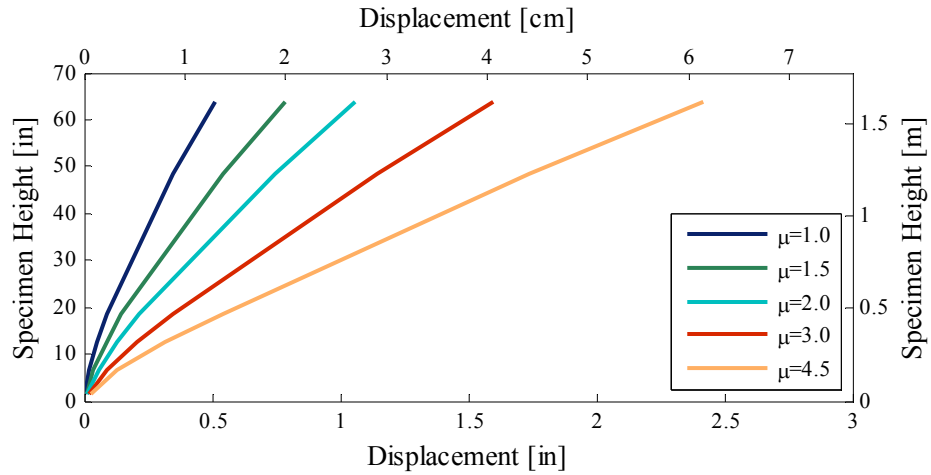
(c) South-West



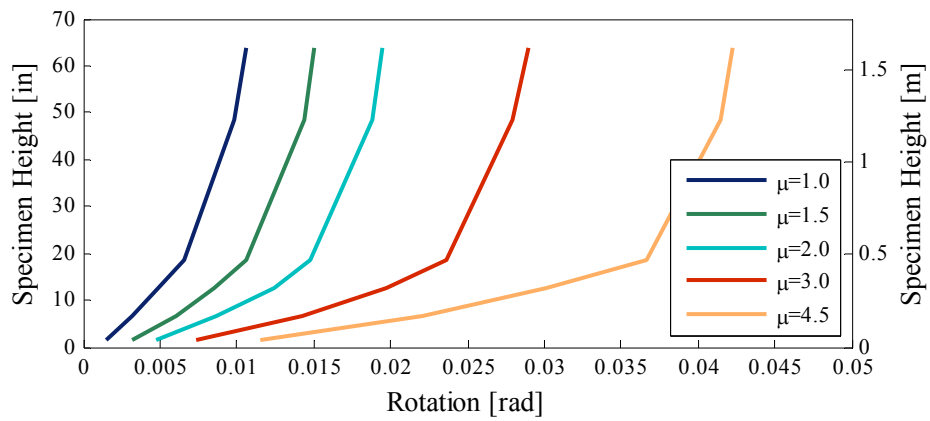
(d) South-East

**Fig. 2.25 State of the specimen at the end of the lateral sequence of the Base45 test**

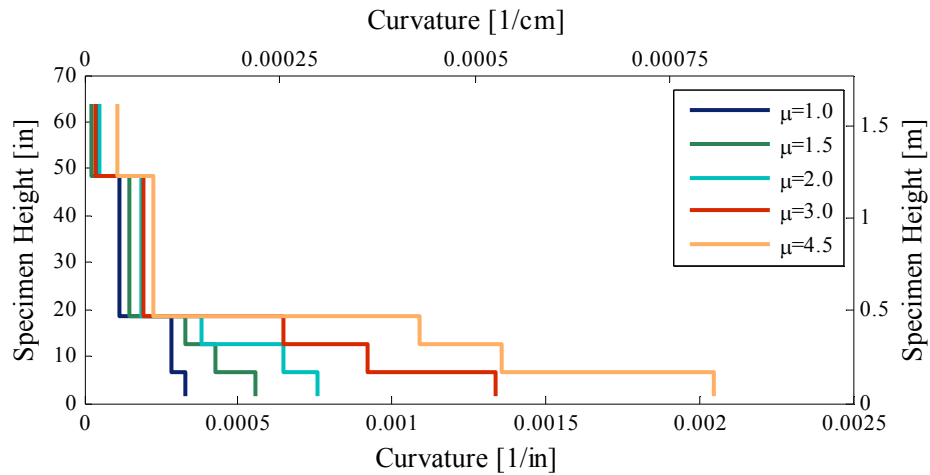




(a) Displacement profiles for primary displacement ductility levels



(b) Rotation profiles for primary displacement ductility levels



(c) Curvature profiles for primary displacement ductility levels

**Fig. 2.26 Profiles of peak displacements, rotations and curvatures for test Base45**

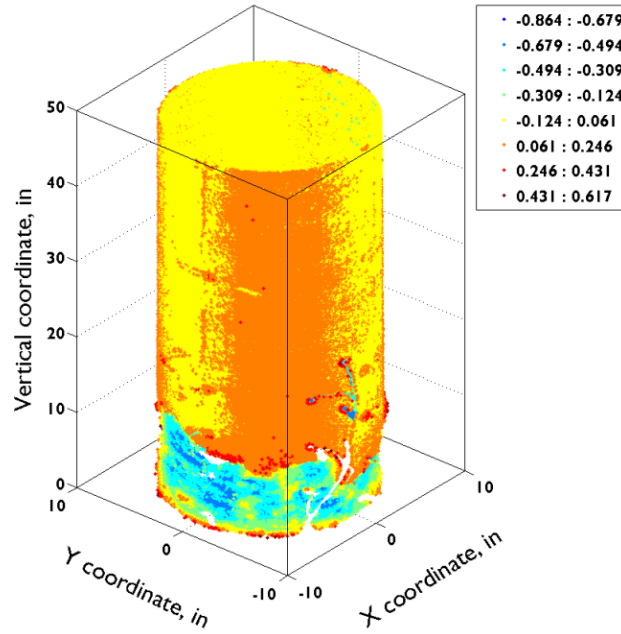
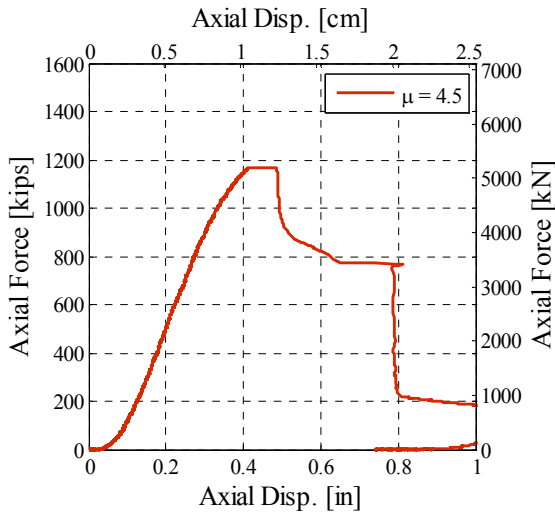


**Fig. 2.27** Deviation of the column surface from a perfect cylinder with the diameter of 16 inches; after the lateral sequence of the Base45 test



(a) Axial force-displacement relationship



(b) Axial failure of the column

**Fig. 2.28** Axial force-displacement relationship and state of the specimen after the axial sequence of the Base45 test

### ***2.3.1.5 Degradation of the Axial Strength with Accumulation of Laterally Induced Damage***

The axial force-displacement relationships from the axial sequences of loading on the Base Column specimens are given on the same graph (Fig. 2.29) to show how axial strength and

stiffness change for different target displacement ductility levels. Additionally, Fig. 2.30 shows how the remaining axial strength of the specimens changes with the increase of the target displacement ductility level. It is observed that both, the axial strength and stiffness degrade with the increase in the amount of the laterally induced damage or the target displacement ductility level.

During the axial sequence of loading, the specimen that was laterally tested up to the displacement ductility level of 1.5 had geometric imperfection in addition to slight material damage. As a consequence, a more pronounced degradation of the axial strength is observed. This result shows significance of the residual displacement of the bridge column on its post-earthquake axial strength.

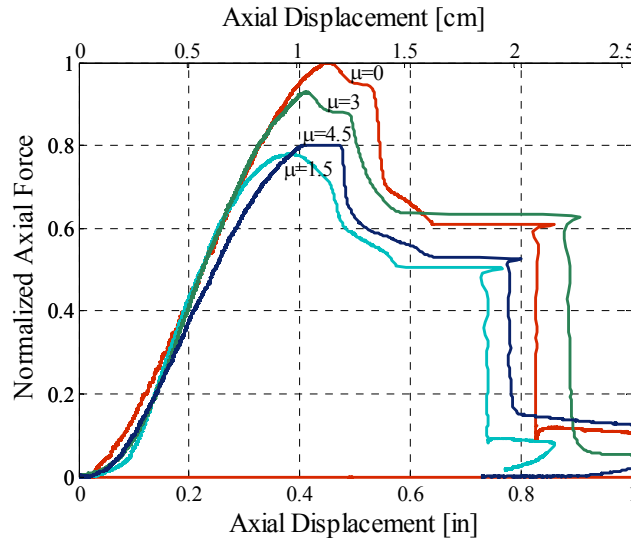


**Fig. 2.29 Comparison of the axial force-displacement relationships for tests Base0, Base15, Base30, and Base45**

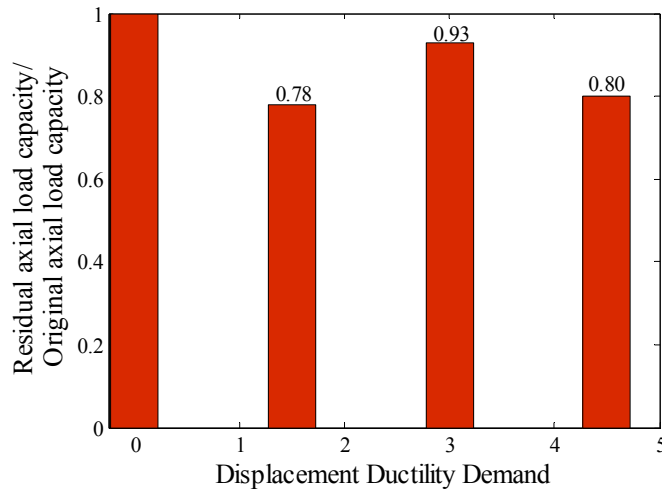


**Fig. 2.30 Degradation of the axial strength of laterally damaged specimens**

### 2.3.2 Test Results for the Shear-Short Column Specimen

In the test ShearShort45, the specimen was laterally loaded up to the displacement ductility level of 4.5 inducing fracture of spiral reinforcement, buckling of all the longitudinal bars and crushing of the concrete core in the plastic hinge region. The column was re-centered after reaching the target ductility displacement. The lateral test was followed by the axial compression test to get the axial strength of the laterally damaged column.

The lateral force-displacement response curves for the two major directions of loading (X and Y) are given in Fig. 2.31. The transition from predominant bending to shear behavior of the column occurred at the displacement ductility level of 2 and can be observed from the hysteresis curves (Fig. 2.31). The lateral strength degradation of the column after the displacement ductility level of 2 indicates the transition in the column behavior from bending into shear. The first cycle of loading at the displacement ductility level of 4.5 initiated the failure of the column. The failure progressed rapidly in the second cycle of loading.

The state of the column (the bottom 22 inches) at the displacement ductility level of 3 is shown in Fig. 2.32 and at the end of the test is shown in Fig. 2.33. Wide horizontal and diagonal cracks as well as extensive spalling of concrete are observed at the displacement ductility level of 3 (Fig. 2.32). The bending-shear failure of the column occurred at the target displacement ductility level,  $\mu = 4.5$ . The bending-shear failure of the column initiated by the fracture of spiral reinforcement in the plastic hinge region followed by a sequence buckling of reinforcing bars and crushing of concrete that occurred as the specimen was cycled along the test loading pattern.

Fig. 2.34(a) shows the axial force-deformation relationship of the specimen after the axial sequence of loading. The damaged state of the column is shown in Fig. 2.34(b). The axial failure resulted from the crushing of the concrete core in the plastic hinge region. The axial strength of the tested specimen was 289 kips (1285 kN). The ratio of the residual to original axial strength of the column is 0.20. Thus, the reduction of the axial strength is 80%. The original strength of the column is calculated analytically based on the model that was calibrated using the data of the test Base0.

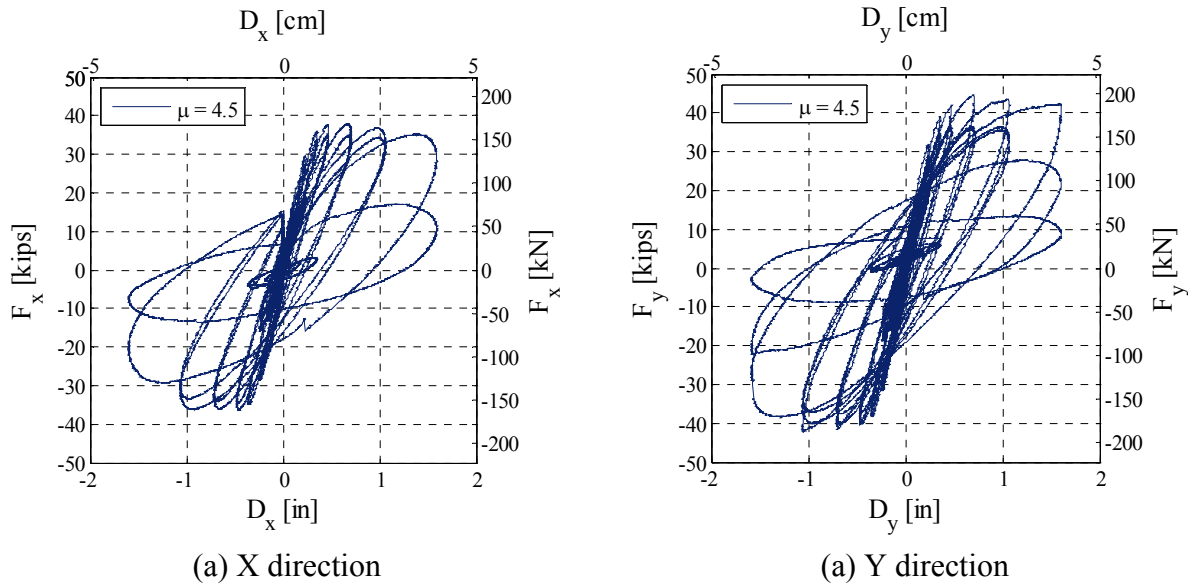


**Fig. 2.31 Lateral force-displacement response curves in the two major directions (X and Y) for the ShearShort45 test**



(a) North-East



(b) North-West



(c) South-West



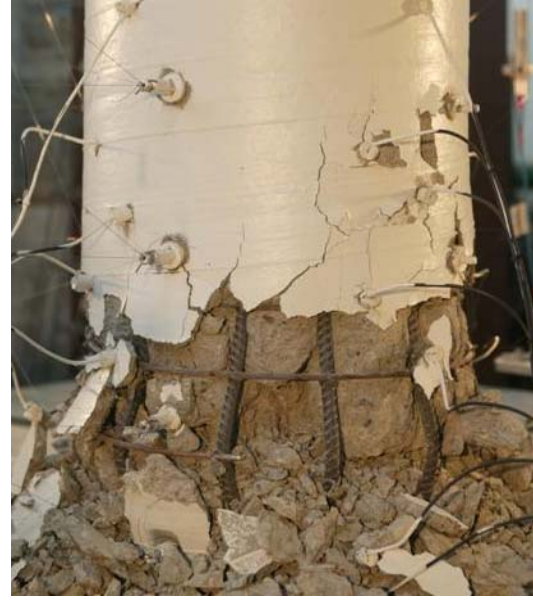
(d) South-East

**Fig. 2.32 State of the specimen after displacement ductility level of 3 during the ShearShort45 test**





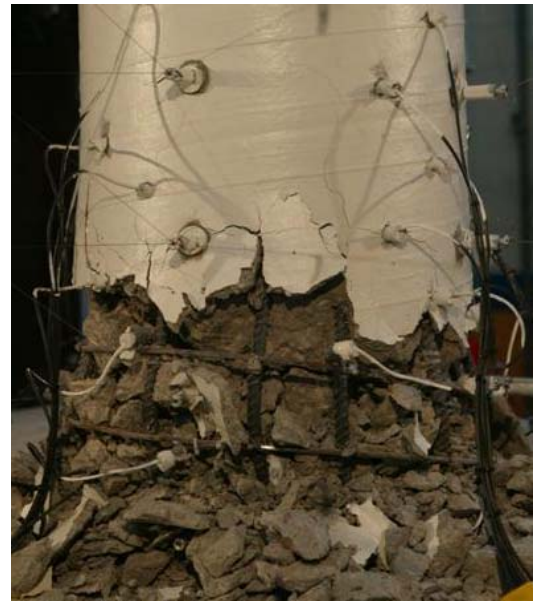
(a) North-East



(b) North-West

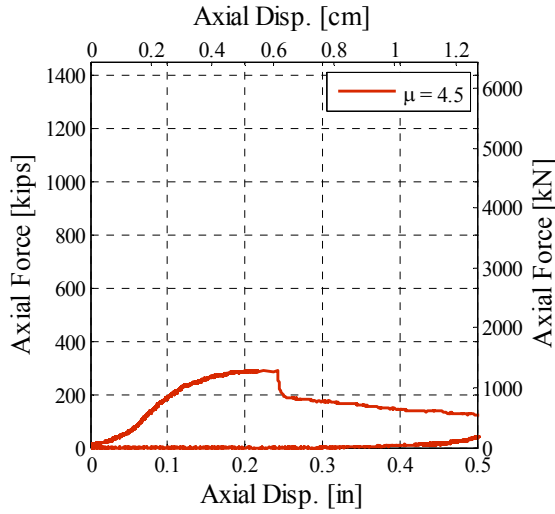


(c) South-West



(d) South-East

**Fig. 2.33 State of the specimen at the end of the lateral sequence of the ShearShort45 test**



(a) Axial force-displacement relationship



(b) Axial failure of the column

**Fig. 2.34 Axial force-displacement relationship and state of the specimen after the axial sequence of the ShearShort45 test**

### 2.3.3 Comparison of the Test Results from the Base45 and ShearShort45 Tests

The results from the two types of columns, the base and shear- short column specimens, loaded up to the same displacement ductility level of 4.5 are compared in this section. The hysterese curves from the lateral tests are given in Fig. 2.35 and the axial force-displacement relationships are given in Fig. 2.36. For the purpose of comparison, the axial forces of the laterally damaged columns are normalized by the axial strengths of the undamaged columns.

The hysterese curves from the lateral tests show significantly higher lateral strength and stiffness for the Shear-Short Column specimen compared to the Base Column specimen. These differences originate from the different aspect ratios of the two types of columns. On the other hand, the Base Column specimen reaches the target ductility level of 4.5 without major damage while the Shear-Short Column specimen fails at the same target ductility level. This difference in the response originates from the difference in the transverse reinforcement ratios and aspect ratios between the two types of columns. The ratios of the residual axial strengths to the original axial strengths for the base and Shear-Short Column specimens are 0.8 and 0.2, respectively (Fig. 2.36).

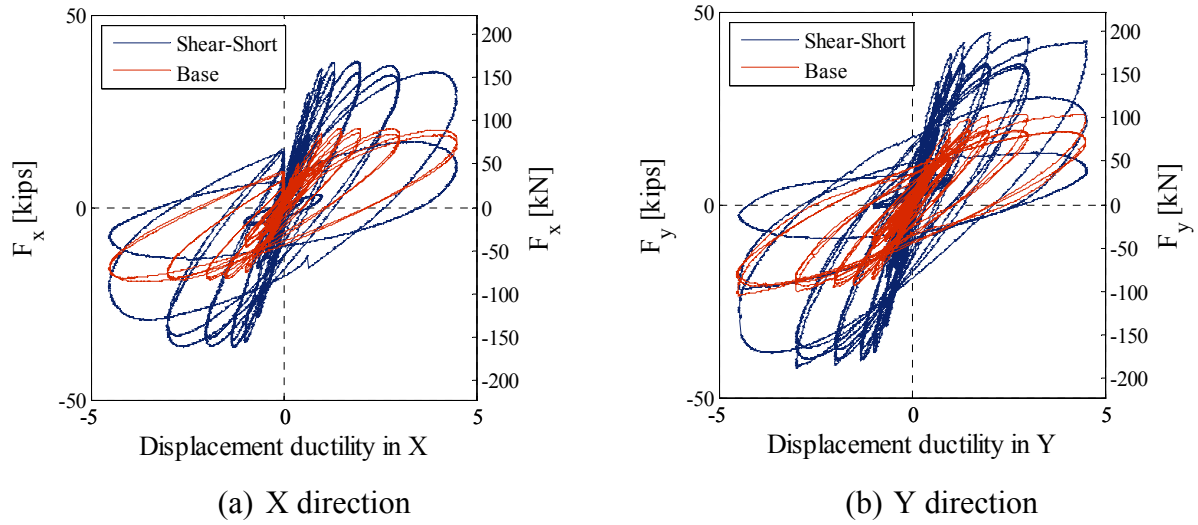


**Fig. 2.35 Lateral force-displacement response curves in the two major directions (X and Y) for the ShearShort45 and Base45 tests**

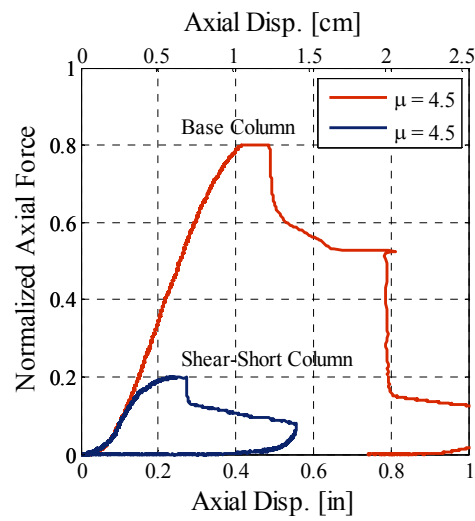


**Fig. 2.36 Axial force-displacement relationships for the ShearShort45 and Base45 tests**



## **3 Experimental Investigations: Hybrid Simulation Tests**

### **3.1 INTRODUCTION**

Hybrid simulation test method, formerly also called the pseudo-dynamic test method and the online computer-controlled test method, is an experimental testing technique conducted on a hybrid model that can be used for evaluating and analyzing performance of structures under dynamic loads. The hybrid model consists of consistently scaled physical and numerical components of a structural system integrated into a single model by enforcing displacement compatibility and force equilibrium at the shared nodes. The dynamic equation of equilibrium of the hybrid model is solved during a hybrid simulation in time domain using a step-by-step integration method. During the simulation the physical portions of the overall hybrid model are tested in the laboratory using computer-controlled actuators, while the numerical portions are simultaneously analyzed on one or more computers. As such, hybrid simulation may be viewed as an advanced form of actuator based testing, where the loading histories for the physical components of the model are determined during the course of an experiment. Alternatively, hybrid simulation can also be considered as a conventional finite element analysis, where physical models of some portions of the structure are embedded in the numerical model.

Hybrid simulation is a unique way to experimentally evaluate the post-earthquake traffic load capacity of a bridge. Using hybrid simulation, a reasonably large scale model of a bridge can be subjected to an earthquake excitation, damaged, and then loaded with traffic load that is increased until the model fails in order to establish its remaining capacity. While such tests could be conceived on a shaking table or in the field, obstacles to such tests are significant. If a shaking table is used, the scale of the bridge model may be too small to represent a prototype, and the risk of collapse and damage to the shaking table in a post-earthquake capacity test using a model traffic load may be unacceptable large. It is conceivable to conduct a field test on a bridge that is damaged after a real earthquake by loading it with ballast until collapse, but such opportunities are rare and costly. Thus, hybrid simulation emerges as the only way to conduct simulations to assess the ability of a structure to perform its function after an earthquake.

In this study, two hybrid simulation tests are performed to assess the ability of the PEER Testbed bridge (Type 11 bridge from Ketchum et al., 2004) to carry traffic loads after an earthquake. The principal difference between these two simulations is the level of seismic demand. Since the Type 11 bridge investigated in this study does not have a specific location (site), selection of ground motion intensity such that it has a certain probability of being exceeded in a given time period is not possible. Therefore, ground motion intensity for the hybrid simulations was selected such that two different damage states are induced in the physical model of the column: i) a moderate damage state corresponding to maximum column

displacement ductility demand of approximately 4; and ii) a significant damage state corresponding to maximum column displacement ductility demand of approximately 6. Following the earthquake loading, the hybrid model of the PEER testbed bridge was loaded with a model traffic load represented by an P13 truck (Caltrans, 2004). The critical positions of the truck were pre-determined using influence lines for the undamaged bridge. The truck load was increased to 150% of its nominal weight and returned to zero. Since the column specimens, which are the physical portions of the hybrid models, did not collapse, they were subsequently tested to collapse in a compression test to evaluate the remaining axial load capacity of columns with damage caused by actual earthquake ground motion instead of a quasi-static cyclic loading pattern.

### 3.2 COMPONENTS AND PROCEDURE OF A HYBRID SIMULATION

To perform a hybrid simulation, four key components including software and hardware are necessary. These interacting components are shown in Fig. 3.1 and described next.

The first component is a discrete model of the structure to be analyzed on a computer, including the static and dynamic loading. The finite element method is used to discretize the problem spatially and a time-stepping integration algorithm is then used for the time discretization. The resulting dynamic equations of motion for the finite number of discrete degrees of freedom are a system of second-order time ordinary differential equations.

$$\begin{aligned} \mathbf{M}\ddot{\mathbf{U}}_{i+1} + \mathbf{C}\dot{\mathbf{U}}_{i+1} + \mathbf{P}_r(\mathbf{U}_{i+1}) &= \mathbf{P}_{i+1} - \mathbf{P}_{0,i+1} \\ \mathbf{U}_{i=0} &= \mathbf{U}_0 \\ \dot{\mathbf{U}}_{i=0} &= \dot{\mathbf{U}}_0 \end{aligned} \quad (3.1)$$

In the above equations  $\mathbf{M}$  is the mass matrix assembled from the nodal and element mass matrices,  $\ddot{\mathbf{U}}$  is the acceleration vector at the structural degrees of freedom,  $\mathbf{C}$  is the viscous damping matrix,  $\dot{\mathbf{U}}$  is the velocity vector at the structural degrees of freedom,  $\mathbf{P}_r$  are the assembled element resisting forces (which depend on the displacements),  $\mathbf{P}$  are the externally applied nodal loads and  $\mathbf{P}_0$  are the assembled element loads.

The second required component is a transfer system consisting of a controller and actuators, so that the incremental displacements determined by the time-stepping integration algorithm can be applied to the physical portions of the structure. Quasi-static testing equipment is used for this purpose.

The third major component is the physical specimen that is being tested in the laboratory and a support against which the actuators of the transfer system can react against.

The fourth and last component is a data acquisition system including displacement transducers and load cells. The data acquisition system is responsible for measuring the response of the test specimen and returning the resisting forces to the time-stepping integration algorithm to advance the solution to the next analysis step.

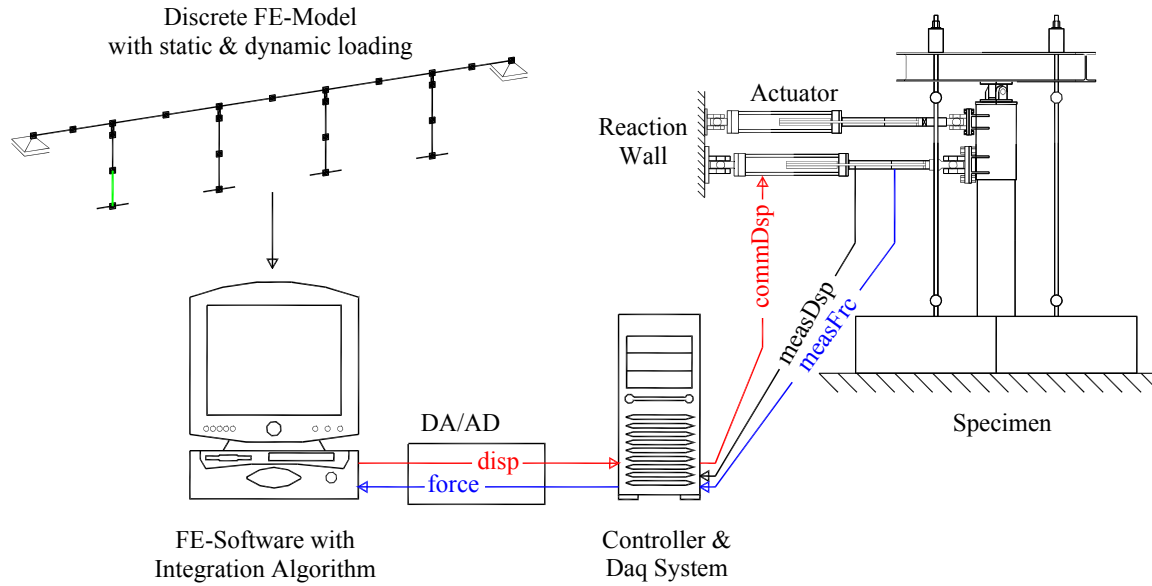


**Fig. 3.1 Key components of a hybrid simulation**

In the hybrid simulation procedure, a specimen representing the bottom half of a bridge column (shown green in Fig. 3.1) is treated as the physical portion of a hybrid model of the bridge, while the rest of the bridge is treated as the numerical portion of the model. During the hybrid simulation test the bridge model was subjected to three sequences of loading in the following order: (i) gravity load, (ii) recorded ground motion (with its three components: two horizontal and a vertical), and (iii) a truck load moving along the bridge. For each integration time step, the dynamics of the discrete model of the bridge structure is used to compute the displacements that are to be imposed at the top of the specimen. Using a controller and actuators these displacements are then applied on the physical model. The corresponding reactions (resisting forces) are measured using load-cells and passed to the data acquisition system (Daq system) that returns them to the time-stepping integration algorithm to advance the solution to the next analysis step.

To perform the hybrid simulation, the Open System for Earthquake Engineering Simulation, OpenSees (McKenna, 1997), is used as a finite element software to model and analyze the bridge structure. The Open-source Framework for Experimental Setup and Control, OpenFresco (Schellenberg, 2008), is used as a middleware to connect the finite element analysis software with a control and data acquisition software.

### 3.3 EXPERIMENTAL SETUP AND TEST PROGRAM

The experimental setup and test program of two hybrid simulation tests that are followed by the axial compression test to failure of the specimens are described in six subsections that follow. The test matrix of hybrid simulations and axial tests is given in the first subsection. The details of a hybrid model of a bridge and a loading that the bridge undergoes during hybrid simulations are given in the second subsection. The third subsection presents the integration algorithm used to solve the dynamics of the hybrid model. The fourth subsection describes the test setup for the

hybrid simulations and the axial compression tests. Geometric transformations from the numerical to the physical portion of the hybrid model, and vice versa, are described in the fifth subsection. The final subsection, the sixth, summarizes the instrumentation used during hybrid simulations and axial tests.

### 3.3.1 Test Matrix

Two hybrid simulation tests are conducted at the nees@berkeley Network for Earthquake Engineering Simulation (NEES) Equipment Site. The hybrid simulation tests are performed on the same bridge for the same recorded ground motion (see Section 3.3.2.3) scaled to represent two levels of seismic intensity: moderate and high. Following the hybrid simulation tests, the physical portions of the hybrid models were tested in axial compression to evaluate their remaining gravity load carrying capacity.

The ground motion selected for both hybrid simulation tests was the Whittier Narrows motion (designated as *wnuy* in Appendix D). To generate a moderate seismic intensity excitation, the acceleration intensity of the recorded Whittier Narrows ground motion was increased 2.3 times without changing its time scale. Such intensity-scaled earthquake loading produced the maximum displacement ductilities of the bridge columns in the major lateral axes X and Y of 3 and 4, respectively. To generate a high seismic intensity excitation, the acceleration intensity of the recorded Whittier Narrows ground motion was increased 3.3 times. Such scaled earthquake loading produced the maximum displacement ductilities of the bridge columns in the major lateral axes X and Y of 4.7 and 6.7, respectively.

The moderate-intensity hybrid simulation test had two sequences of loading: the gravity and the earthquake load. It was performed to validate the analytical modeling of the numerical components of the hybrid model and to access the remaining axial strength of the bridge columns after a moderately strong earthquake. The high-intensity hybrid simulation test used the validated finite element model of the bridge. It had three sequences of loading: the gravity, the earthquake, and the truck load moving along the bridge after the earthquake. This test allowed observation of the bridge ability to carry truck load immediately after a very strong earthquake.

The designations of the hybrid simulations and load sequences are provided in Table 3.1. Each designation consists of three letters. The first two letters of designation relate to the type of the test: HS indicates the hybrid simulation test. The third letter specifies the seismic intensity: M stands for the moderate and H stands for the high.

**Table 3.1 Test matrix**

Test designation	Ductility demand in X	Ductility demand in Y	Truck load	Test sequences
HSM	3.0	4.0	-	Hybrid Sim. & Axial
HSB	4.7	6.7	P13 (Caltrans, 2004)	Hybrid Sim. & Axial

### 3.3.2 Hybrid Model and Loading

Configuration of the bridge used in hybrid simulations corresponds to bridge Type 11 in Ketchum et al. (2004). It is a straight, cast-in-place box girder bridge with five spans and single-column-bents, and no skew of the deck at bridge abutments.

In the hybrid simulation procedure, a specimen representing the bottom half of an end bridge column is treated as the physical portion of a hybrid model of the bridge, while the rest of the bridge, comprising its deck, the abutments, both interior bridge columns and the remaining end column, is treated as the numerical portion of the model (Fig. 3.2). Two important decisions were made in the process of establishing the hybrid model of the bridge. The first decision relates to the choice of the portion of the bridge to be physically modeled. As one of the goals of the hybrid simulation is to validate the analytical model, the portion of the bridge that undergoes the most extensive damage under the specified load is chosen to be physically modeled. For the bridge under consideration, an end column is chosen over an inner column because it attracts larger seismic forces (has a higher energy dissipation demand) than an interior column for the same displacement demand. The end columns attract larger seismic forces than the inner columns due to the higher tributary mass. The second decision relates to the scaling factors for both the physical and the numerical portions of the bridge. The scaling factor is determined based on laboratory constraints and economic feasibility while taking care that the size effects are not pronounced. The numerical portion of the model represents the portion of the bridge in its full scale. The physical portion of the bridge is scaled down 4.6875 times.

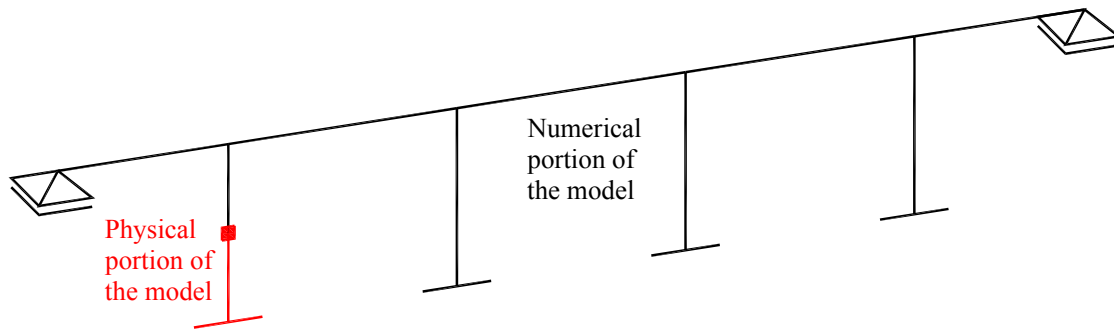


**Fig. 3.2 Physical and numerical portions of the hybrid model of the bridge**

#### ***3.3.2.1 Physical Portion of the Hybrid Model: Geometry, Reinforcement and Materials***

The geometry and dimensions as well as the reinforcement of the physical portion of the hybrid model, referred also as experimental element or specimen, are detailed in Fig. 3.3. The two hybrid simulation specimens are essentially identically to the quasi-statically tested specimens discussed in Chapter 2, but for the top portion of the specimens that was made taller to accommodate attachment of actuators. Each specimen is a 16-inch (0.4 m) diameter circular reinforced concrete column, 89.5 inches (2.27 m) in height with the square foundation block (84" x 84"; 2.13 x 2.13 m) 24 inches (0.61 m) high. The effective height of the column, from the base of the column to the level of lateral load application, is 64 inches (1.625 m). The extension of 25.5 inches (0.65 m) above the effective height of the column accommodates the installation of

the 1 inch (2.54 cm) thick and 31.75 inches (0.8 m) high steel jacket. The steel jacket provides an attachment for the actuators at the top of the column.

The column has twelve longitudinal No.4 (Ø13) reinforcing bars placed around its perimeter. The transverse steel reinforcement is W3.5 continuous spiral with a center to center spacing of 1.25-inch (3.175 cm). The cover is 1/2" (1.3 cm) all around. The basic dimensions and reinforcement of the specimen are summarized in Table 3.2.

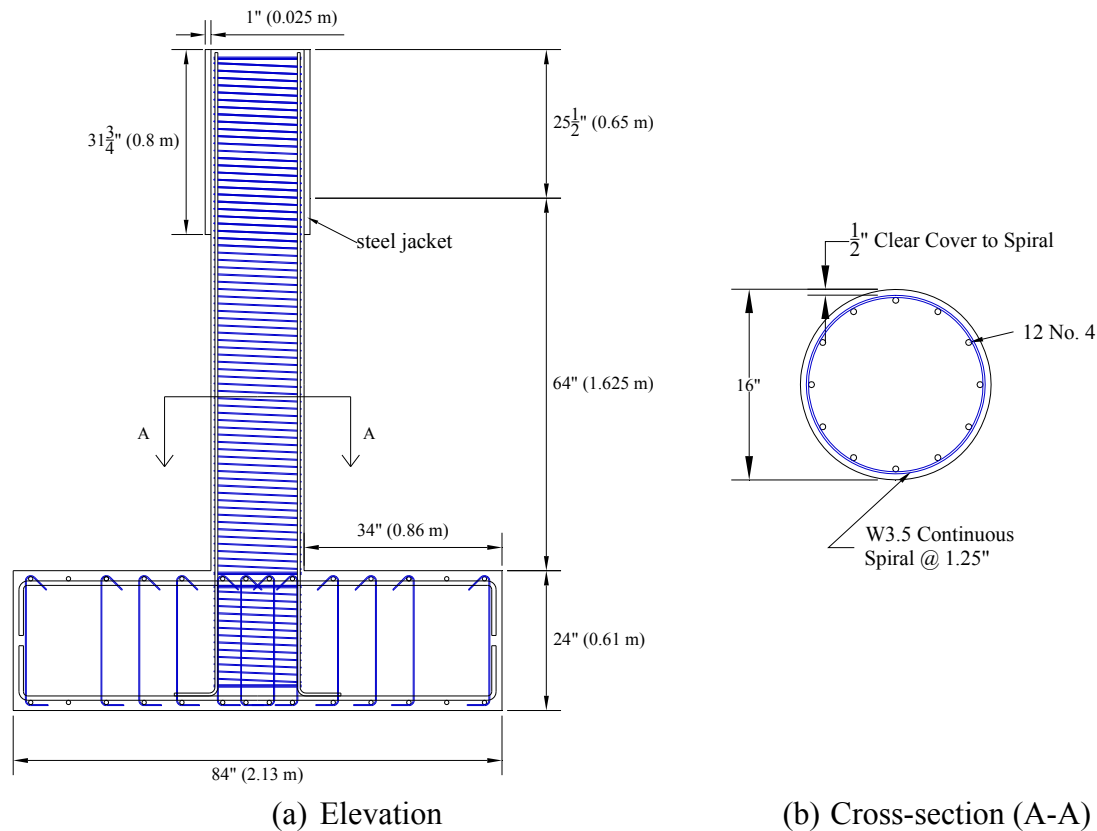


**Fig. 3.3 Geometry and reinforcement of the hybrid simulation specimens**

**Table 3.2 Basic dimensions and reinforcement of the hybrid simulation specimens**

Diameter	Height	Longitudinal Bars	Transverse Reinforcement
16" (0.4 m)	64" (1.625 m)	12 No.4 (Ø13)	Wire3.5 @ 1.25" spa

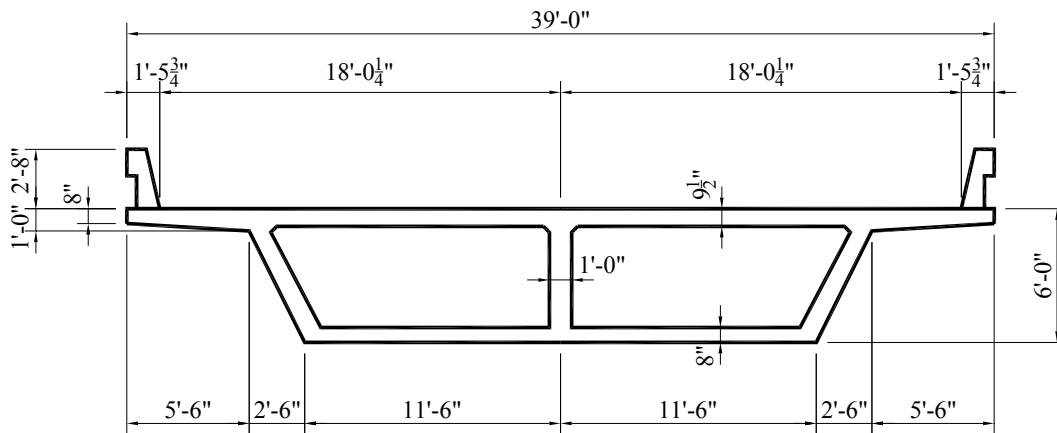
The materials used for hybrid simulation specimens are the same as for the specimens tested in quasi-static manner (see Section 2.3.3). In summary, the specified and actual strengths of the longitudinal steel, the spiral steel and the concrete are given in Table 3.3.

**Table 3.3 Material properties of the hybrid simulation specimens**

Material	Specified [ksi]		Actual [ksi]	
	Yield	Ultimate	Yield	Ultimate
Steel				
Longitudinal	60	80	70.7	120
Spiral	80		95	106
Concrete	5.0		6.21 to 6.39	

### 3.3.2.2 Numerical Portion of the Hybrid Model: Geometry, Reinforcement and Analytical Modeling

Since the numerical portion of the bridge is modeled in a full scale, its configuration corresponds to bridge Type 11 in Ketchum et al. (2004). In summary, it is a straight, cast-in-place box girder bridge with five spans and single-column-bents. The bridge has three internal spans of 150' (45.72 m), two external spans of 120' (36.58 m), a 39' (11.9 m) wide deck, and 50' (15.24 m) tall circular columns 6'- 3" (1.9 m) in diameter. The superstructure is a pre-stressed (CIP/PS) 2-cell box girder supported on neoprene bearing pads under each of the three box webs. Bridge elevation and column cross section are given in Fig. 2.1 (Chapter 2). Deck cross section dimensions are shown in Fig. 3.4.

**Fig. 3.4 Deck cross section (Ketchum et al., 2004)**

Reinforcement of a column consists of longitudinal bars placed around its perimeter and a continuous spiral encasing the longitudinal bars. Each column has 34 longitudinal No.11 (Ø36) reinforcing bars and No.8 (Ø25) spiral with a center to center spacing of 6 inches (0.15 m). Such reinforcement layout gives the longitudinal reinforcement ratio of 1.2% and transverse reinforcement ratio of 0.75%. The cover is 2" (5.1 cm) all around.

The superstructure reinforcement is detailed in Ketchum et al. (2004). In summary, the two-cell box girder contains two layers of longitudinal reinforcing bars in the deck, soffit, and girders, additional mild steel in the deck and soffit over the bents, and post-tensioned steel to provide a 7,000 kips (31,000 kN) pre-stressing force. A cover depth of 1.5 in. (3.8 cm) is used.

To model the numerical portion of the bridge, a three-dimensional nonlinear finite element model was developed. It is a spine model of the numerical portion of the bridge structure with line elements located at the centroid of the cross section following the alignment of the bridge (Fig. 3.5). Three-dimensional beam-column elements with corresponding cross-sectional properties were used to model the superstructure and columns. All six degrees of freedom were restrained at the base of the columns. Single point constraints against displacement in vertical direction (vertical support) and rotation about the superstructure longitudinal axis (full torsional restraint) were defined at the superstructure ends to model the bridge abutments. The PEER Center finite element platform OpenSees (<http://opensees.berkeley.edu>) was utilized.

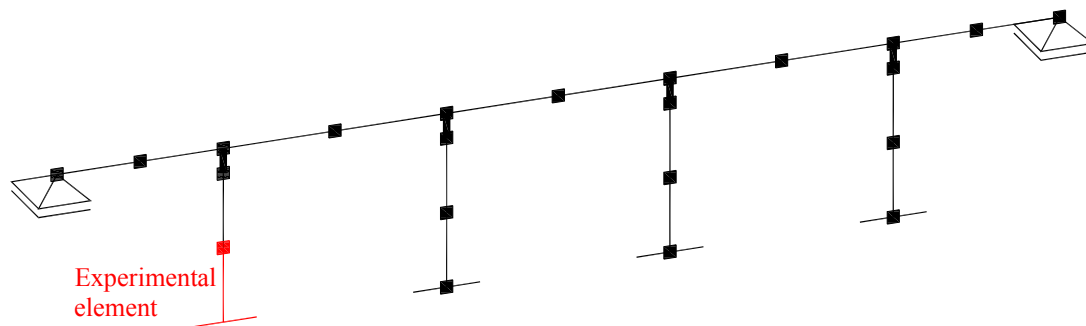


**Fig. 3.5 Analytical model of the numerical portion of the hybrid bridge model**

The superstructure and columns were modeled with nonlinear beam-column elements that are based on force formulation and consider the spread of plasticity along the element. The element is a line element with integration points at the element ends and along the element length. A fiber cross section, assigned to each integration point, was generated to explicitly account for longitudinal reinforcing bar placement and unconfined and confined concrete effects. Each material in the cross-section had a uniaxial stress-strain relationship assigned to it.

The columns were modeled with two types of elements. The top of the column with the length  $H_{RL}$  (Fig. 3.6) representing the portion of the column embedded in the superstructure is modeled as a rigid link. The remainder of the column with the length  $H_{col}$  (Fig. 3.6) is modeled with nonlinear beam-column elements. Two elements of equal lengths, each having five integration points, were defined for each column. Integration points along an element were distributed following Gauss-Lobatto integration rule. The fiber section was divided into three parts: reinforcing steel, concrete cover and concrete core, each having a uniaxial stress-strain relationship assigned to it. The reinforcing steel was modeled by a Giuffre-Menegotto-Pinto uniaxial strain-hardening material model (Menegotto and Pinto, 1973) designated in OpenSees as Steel02. The concrete constitutive models were based on the Kent-Scott-Park model (Kent and Park, 1971) designated in OpenSees as Concrete01. To define concrete material models the compressive strength of the unconfined concrete was adopted from the concrete cylinder tests performed on the day of the hybrid simulation test (Appendix A). Reinforcing steel and concrete material models are calibrated based on results of lateral quasi-static tests and corresponding axial tests performed on models of bridge columns. Parameters that define the material models



are given and described in Chapter 4 of this document. Although the effect of shear is not significant in tall columns reinforced following SDC, it is accounted for through aggregation of an elastic-plastic shear force-deformation relationship with the fiber column section at each integration point of the beam-column elements. The shear strength and stiffness are calculated following equations from Section 3.6 in Caltrans SDC (Caltrans, 2006a).

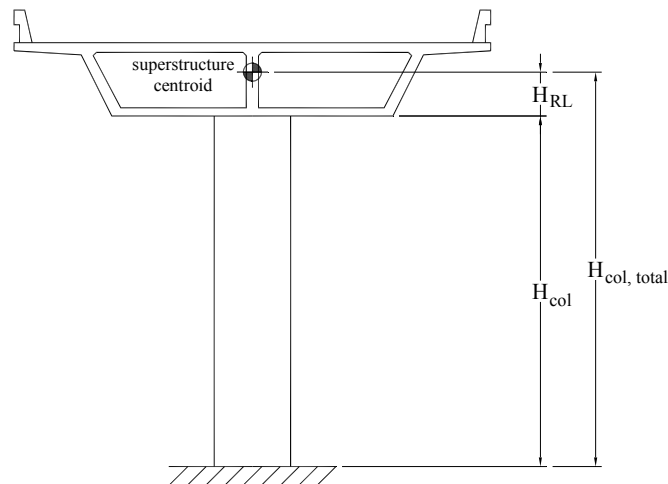


**Fig. 3.6 Column model geometry**

Each span of the superstructure was defined with two nonlinear beam-column elements of equal lengths, each having three integration points. Integration points were assigned at element ends and in the middle of the element. Integration weights were 1/6 for end points and 4/6 for the middle point. The constitutive models used for the deck elements are the same as the models used for the column elements. However, there is a difference in the strain hardening ratio for the reinforcing steel. It is 0.015 for the deck elements. Although this bridge is classified by Caltrans SDC (Caltrans, 2006a) as “ordinary standard bridge” whose reduction of the torsional moment of inertia ( $J$ ) is not required, the torsional moment of inertia is reduced 50% to accommodate for the full torsional restraint at the superstructure ends that is underconservative. Thus, the deck torsional response about its longitudinal axis was assumed to be elasto-plastic with an initial elastic stiffness of 0.5GJ/L. Torsional stress-strain relationship was aggregated with the deck sections at all integration points along the superstructure beam-column elements.

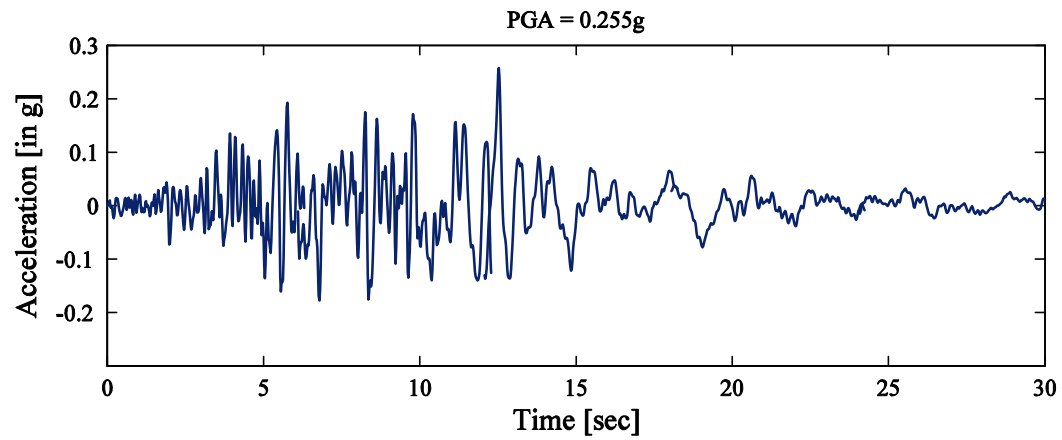
To perform a hybrid simulation of the bridge for an earthquake, all bridge elements had a distributed mass assigned along their lengths. Based on this distributed mass OpenSees automatically calculates the translational mass of all longitudinal elements in the three global directions of the bridge (longitudinal, transverse, and vertical) and assigns them as lumped masses at each node based on tributary lengths. The rotational mass (mass moment of inertia) for the superstructure is not generated automatically so it was assigned manually at each node. The assignment of superstructure rotational mass helps represent the dynamic response and modes of the bridge associated with the transverse direction of the bridge with the greater accuracy. The damping is modeled using Rayleigh damping coefficients that are mass and stiffness proportional. The first two modal periods of the bridge system, assuming the same damping ratio of 3% for both modes, are used to calculate Rayleigh damping coefficients.

The effects of column axial loads acting through large lateral displacements, known as P- $\Delta$  or second-order effects, are included while analyzing the bridge system. The consideration of P- $\Delta$  effects helps identify the structural instability hazard of the bridge by capturing the degradation of strength and amplification of the demand on the column bents, caused by the relative displacement between the column top and bottom.

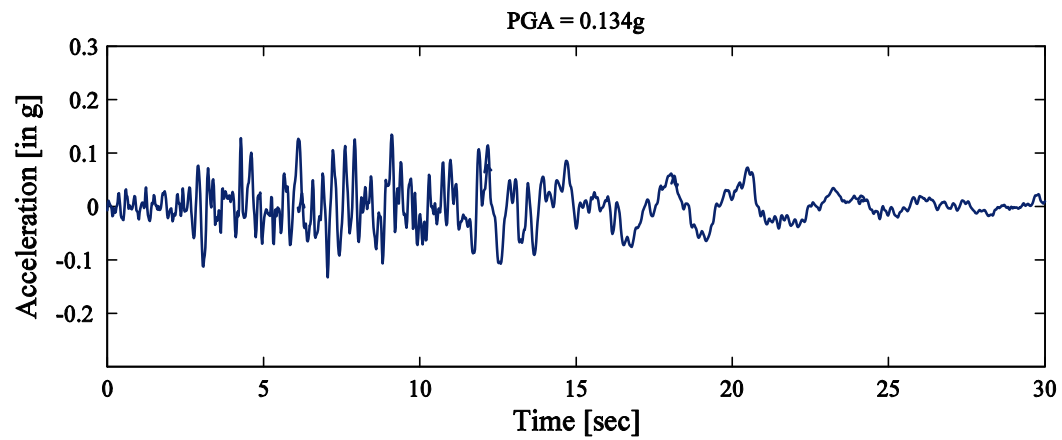
### ***3.3.2.3 Loading***

During the hybrid simulation test HSM the bridge was exposed to two sequences of loading: (i) gravity load and (ii) earthquake load, while during the hybrid simulation test HSH there were three sequences of loading in the following order: (i) gravity load, (ii) earthquake load, and (iii) truck load. The ground motion record with its three components of acceleration (two orthogonal horizontal components and one vertical) is shown in Fig. 3.7. The ground motion record was scaled by 2.3 and 3.3 during the hybrid simulations HSM and HSH, respectively. To simulate the truck load on the bridge P13 truck (Caltrans, 2004) was used. It is a six-axle truck (Fig. 3.8) with a fixed spacing of 18 feet (5.5 m) between the axles.

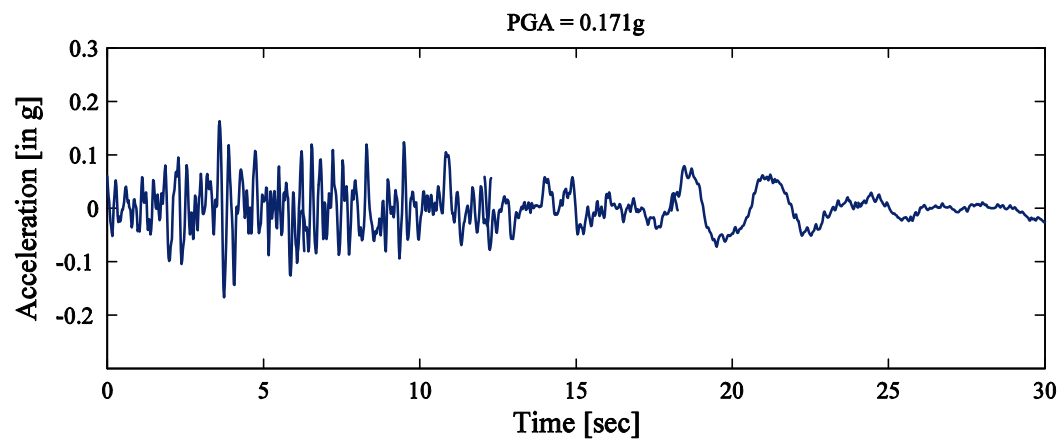
The truck load on the bridge is simulated by two sets of forces applied at superstructure elements in order to capture the location of the truck in the outermost lane of the bridge roadway. A vertical set of forces corresponds to the truck weight at its axle locations: six concentric forces with magnitudes that follow the ratio 0.54:1:1:1:1:1. Torsional set of forces corresponds to concentric torsional loads at axle locations of the truck generated by eccentric position of the truck relative to the superstructure centerline (Fig. 3.9). During hybrid simulation of the truck load on the bridge, the truck was occupying the outermost (curb) lane on the bridge and the load was monotonically increasing from zero to full P13 truck weight scaled by 1.5. The truck load was applied in four sequences that correspond to four truck positions on the bridge (Fig. 3.10). The truck was moved through four positions along the bridge to induce either maximum axial force or bending moment in the end bridge column that consist of an experimental and an analytical element.



(a) Horizontal component of ground motion: transverse bridge direction



(b) Horizontal component of ground motion: longitudinal bridge direction



(c) Vertical component of ground motion

**Fig. 3.7 Unscaled Whittier Narrows ground motion acceleration record: *vnvny* record from Van Nuys bin (see Appendix D)**

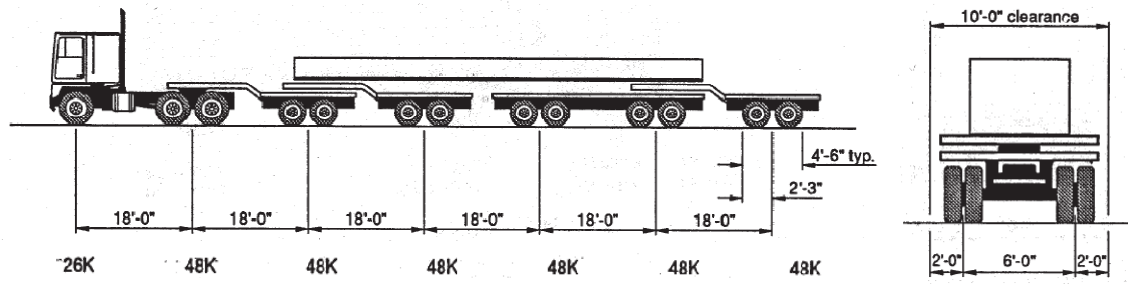


**Fig. 3.8 P13 truck load (Caltrans, 2004)**

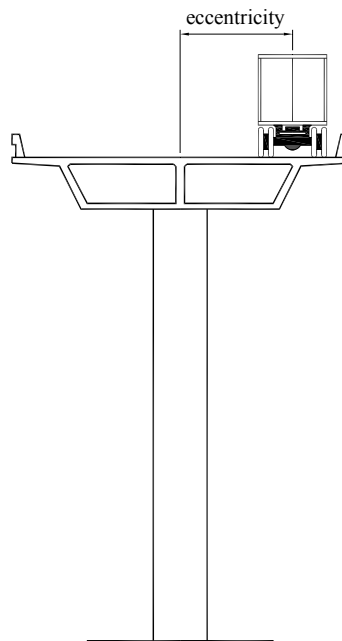
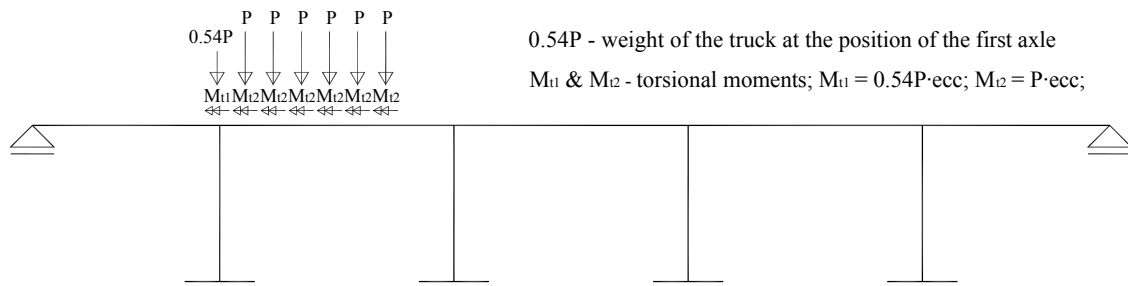
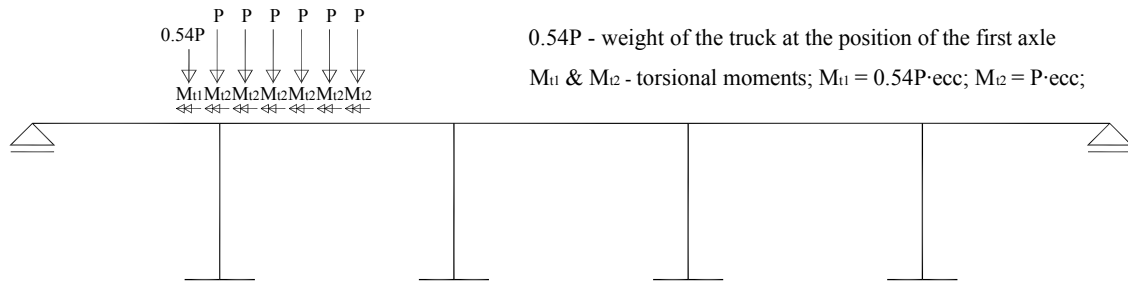


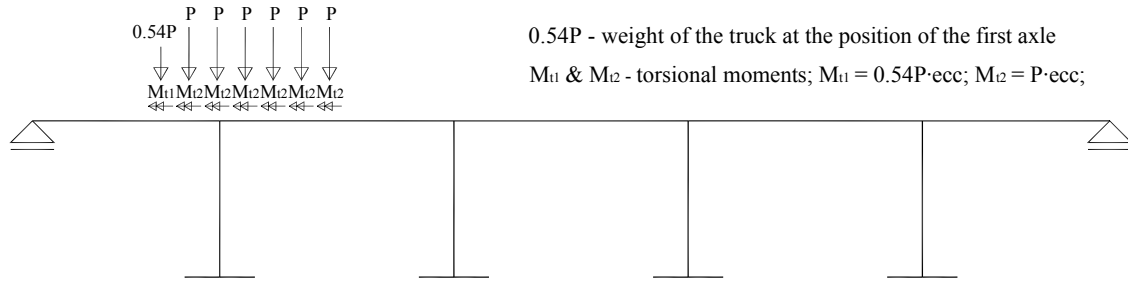
**Fig. 3.9 Eccentric position of the truck with respect to the superstructure centerline**



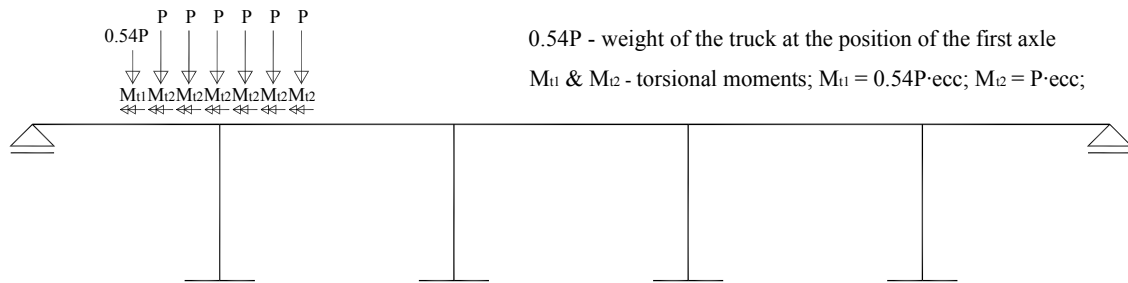
(a) First truck position on the bridge



(b) Second truck position on the bridge



(c) Third truck position on the bridge



(d) Fourth truck position on the bridge

**Fig. 3.10 Four positions of the P13 truck load on the bridge and corresponding loads**

### 3.3.3 Integration Algorithm

Time-stepping integration methods that act as the computational driver during a hybrid simulation are provided by or need to be implemented in the finite element analysis software. Operator-Splitting (OS) methods, which are unconditionally stable, relatively easy to implement, and computationally nearly as efficient as explicit methods, are excellent techniques for solving the equations of motion during hybrid simulations (Schellenberg, 2008). These integration methods are capable of providing unconditional stability without the need for iterative equilibrium solution processes. For the purpose of this study, Alpha-OS integration method (originally developed by Nakashima et al., 1988 and supported by OpenSees) with  $\alpha=0.9$  is adopted for use.

### 3.3.4 Test Setup

During hybrid simulation tests 6 degrees of freedom (DOFs), three displacements and three rotations, could be controlled at the point (designated as control point) where the physical and analytical portions of the bridge link together. To reduce the experimental costs, but keeping the effectiveness and accuracy of the testing method, it was decided to reduce the number of DOFs controlled in the hybrid simulation tests. The vertical displacement and torsional rotation of the column at the control point have negligible influence on the column behavior for an earthquake load. Thus, they were not controlled during hybrid simulation tests. The remaining 4 DOFs, 2 lateral displacement and 2 rotations about sectional axes (Fig. 3.11), are controlled during hybrid simulation tests as they govern column behavior during an earthquake excitation. Control of the rotation DOFs enables accurate modeling of the moment distribution (location of the inflection point) in the hybrid end column of the bridge. In addition, an axial load equal to the average axial load in the column during the earthquake ( $\sim 7\%$  of the column's nominal axial load capacity) was applied at the beginning of the hybrid simulation tests.

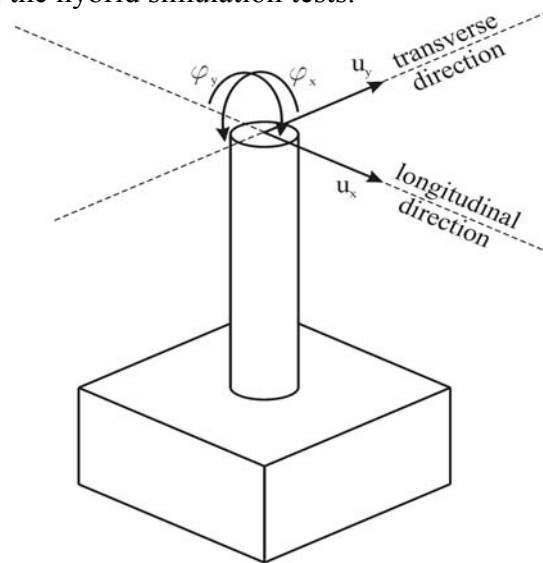


**Fig. 3.11 Four DOFs controlled at the top of the experimental element during the hybrid simulations**

The displacements and rotations that the control point of the bridge experiences during the earthquake (2 lateral displacement and 2 rotations about sectional axes) were applied to the control point of the specimen using four servo-controlled hydraulic actuators acting on the rigid extension of the column (Fig. 3.12 and Fig. 3.13). The column extension is made rigid by encasing the top portion of the column with an inch thick steel jacket. The actuators were placed in the two horizontal planes, 18 inches apart. Each plane contained two actuators. The actuators from one plane formed an angle of  $90^\circ$ . Lower pair of actuators (Act 1 & Act 2 from Fig. 3.12) acted on the control point (CP) applying two horizontal displacements. Upper pair of actuators (Act 3 & Act 4 from Fig. 3.12) acted on the rigid portion of the column applying two horizontal displacements at the point of the actuators attachment and thus two sectional rotations at the control point.

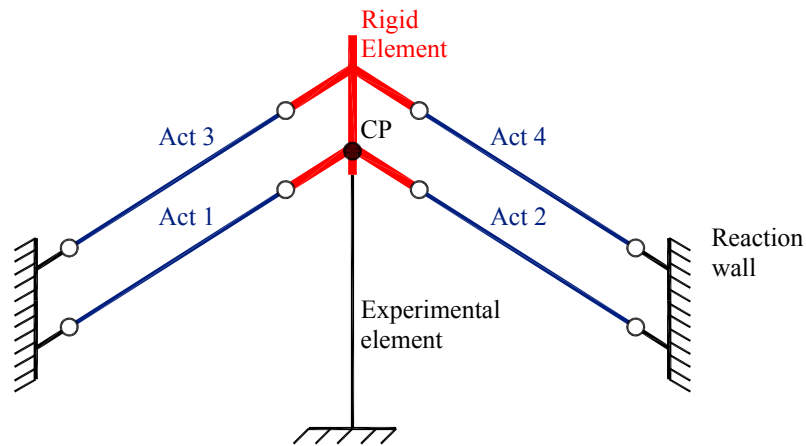


**Fig. 3. 12 Schematic representation of the hybrid simulation setup lateral load application**

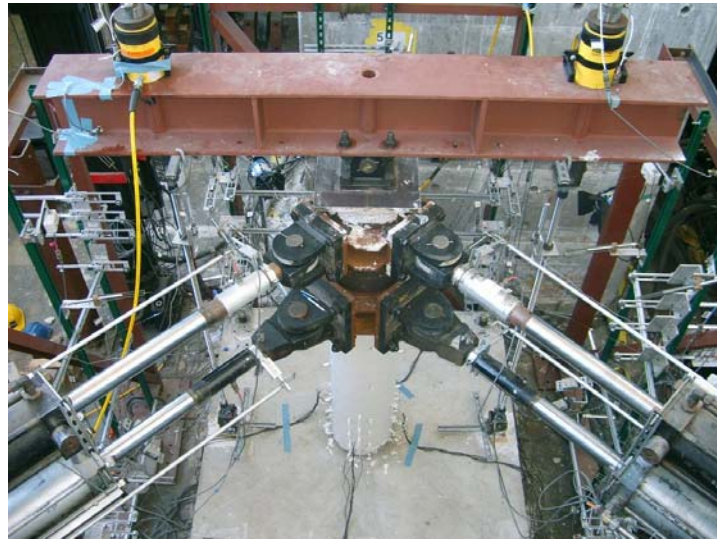


**Fig. 3.13 Hybrid simulation test setup**

The axial load setup is the same as for the quasi-static tests (Appendix C). In summary, the axial load was applied through a spreader beam using pressure jacks and post-tensioning rods

placed on either side of the column (Fig. 3.13, Fig. 3.14, and Fig. 3.15). Spherical hinges (3D swivels) were provided at both ends of the rods in order to avoid bending of the rods during bi-directional displacements of the specimen. A hinge connection (2D hinge) was also provided between the spreader beam and the specimen for the beam to remain horizontal in the plane of the rods during the lateral displacements of the specimen. In this way, buckling of the rods was avoided.

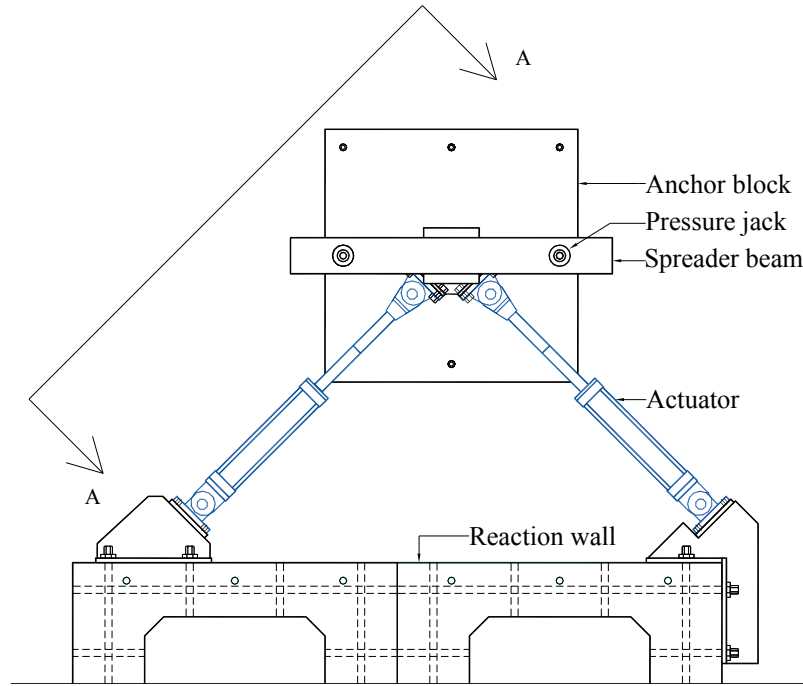


**Fig. 3.14 Plan view of the hybrid simulation experimental setup**



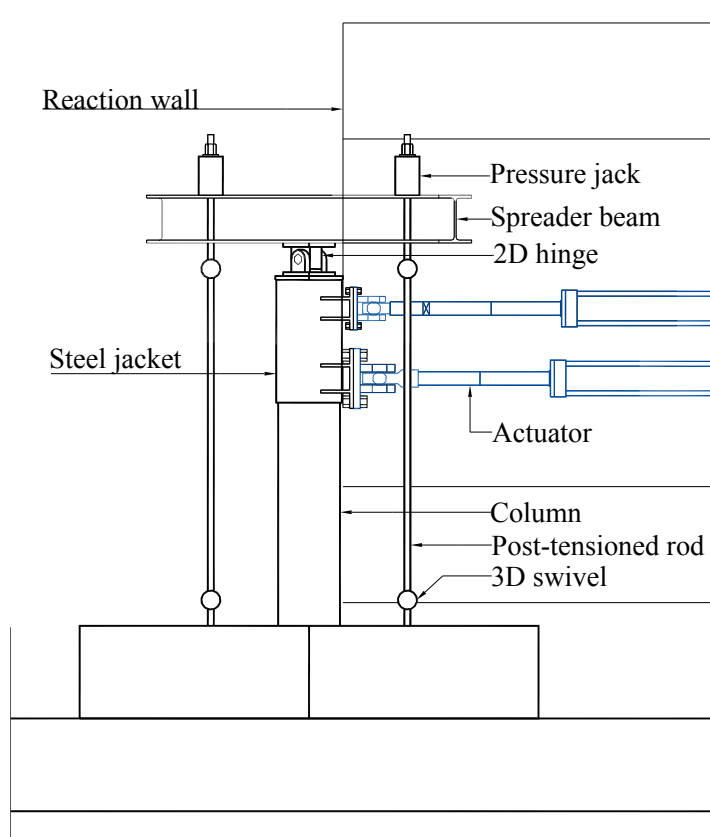


**Fig. 3.15 Elevation (A-A) of the hybrid simulation experimental setup**

After the columns were damaged in the hybrid simulation tests they were compressed axially to induce axial failure in the columns. To accomplish this, a compression-tension machine with a capacity of 4 million lbs in compression and a constant rate of loading was used.

### 3.3.5 Geometric Transformations

In the hybrid simulation procedure, a specimen representing the bottom half of a bridge column (shown red in Fig. 3.5) was treated as the physical portion of a hybrid model of the bridge, while the rest of the bridge was treated as the numerical portion of the model. The numerical portion of the model represents the portion of the bridge in its full scale while the physical portion of the bridge was scaled down 4.6875 times ( $S_L=4.6875$ ). For each integration time step, the dynamics of the discrete model of the bridge structure was used to compute the displacements that are to be imposed at the control point of the specimen. Using a controller and actuators these displacements were then applied on the physical model. To obtain the command displacements for actuators, the scaled values of calculated displacements underwent a set of geometric transformations. After applying these displacements on the specimen the corresponding reactions (resisting forces) were measured using load-cells and passed to the data acquisition system. The measured forces underwent the set of geometric transformations and then scaled before they were passed to the time-stepping integration algorithm to advance the solution to the next analysis step.

To obtain the command displacements for actuators, the scaled values of calculated displacements ( $U_x$ ,  $U_y$ ,  $\phi_x$ ,  $\phi_y$ ) first underwent coordinate transformation from coordinate system  $x$ - $y$  to coordinate system  $1$ - $2$  (Fig. 3.16). The scaling factor for lateral displacements was  $1/S_L = 1/4.6875 = 0.213$ , while the scale factor for sectional rotations was 1. The axes of the coordinate system  $1$ - $2$  are aligned with actuators 1 and 2. The angle,  $\phi$ , from the axis  $x$  to the axis 1 is  $45^\circ$ . The transformation matrix,  $\mathbf{T}$ , is given below:

$$\mathbf{T} = \begin{bmatrix} \cos \phi & \sin \phi \\ -\sin \phi & \cos \phi \end{bmatrix} = \begin{bmatrix} \sqrt{2}/2 & \sqrt{2}/2 \\ -\sqrt{2}/2 & \sqrt{2}/2 \end{bmatrix} \quad (3.2)$$

The horizontal displacements  $U_x$  and  $U_y$  and sectional rotations  $\phi_x$  and  $\phi_y$  are transformed to displacements  $U_1$  and  $U_2$  and sectional rotations  $\phi_1$  and  $\phi_2$  following Equations 3.3 and 3.4.

$$\mathbf{U}_{12} = \begin{bmatrix} U_1 \\ U_2 \end{bmatrix} = \mathbf{T} \cdot \mathbf{U}_{xy} = \mathbf{T} \cdot \begin{bmatrix} U_x \\ U_y \end{bmatrix} \quad (3.3)$$

$$\Phi_{12} = \begin{bmatrix} \phi_1 \\ \phi_2 \end{bmatrix} = \mathbf{T} \cdot \Phi_{xy} = \mathbf{T} \cdot \begin{bmatrix} \phi_x \\ \phi_y \end{bmatrix} \quad (3.4)$$

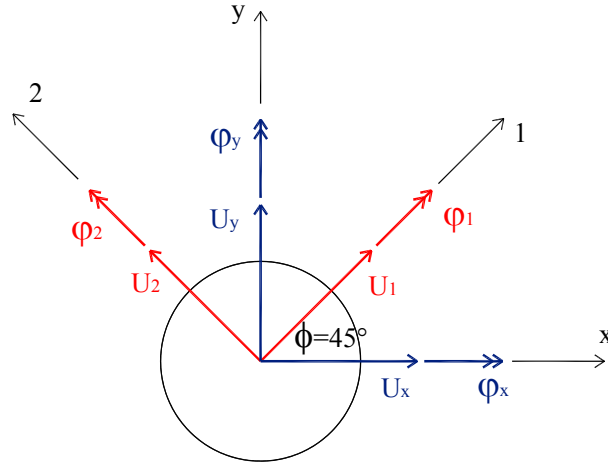


**Fig. 3.16 Coordinate transformation**

The horizontal displacements  $U_1$  and  $U_2$  and rotations  $\phi_1$  and  $\phi_2$  are applied at the control point (CP) of the specimen using four actuators acting on the rigid extension of the specimen at the points  $A_1$ ,  $A_2$ ,  $A_3$ , and  $A_4$  (Fig. 3.17). To get the command displacements for the actuators the displacements of the points  $A_1$ ,  $A_2$ ,  $A_3$ , and  $A_4$  had to be calculated first. The total displacements of points  $A_i$  ( $i=1$  to 4) are calculated as the sum of displacements due to translations ( $U_1$  and  $U_2$ ) and rotations ( $\phi_1$  and  $\phi_2$ ) of the rigid body. The displacements of a point due to rotation of the rigid body are determined using rotation matrix,  $\mathbf{R}$  (Equation 3.4), generated using Euler angles  $\alpha$ ,  $\beta$ , and  $\gamma$  (Equations 3.5, 3.6, and 3.7).

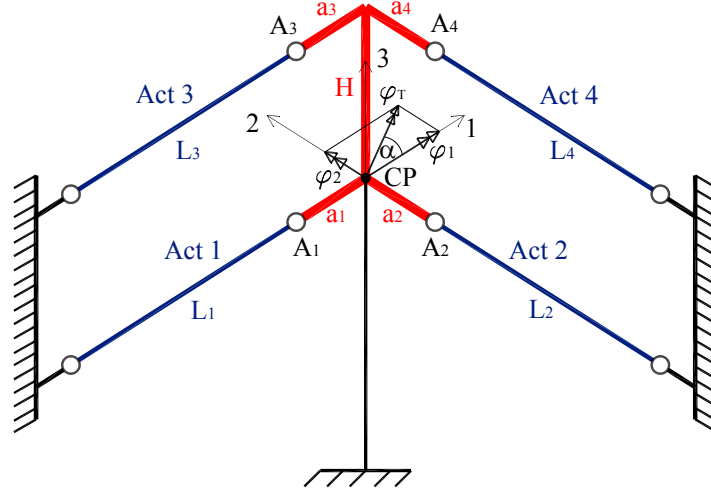


**Fig. 3.17 Schematic presentation of the rigid column extension (in red) and actuators (in dark blue) at the beginning of the hybrid simulation**

$$\mathbf{R} = \begin{bmatrix} \cos \gamma & \sin \gamma & 0 \\ -\sin \gamma & \cos \gamma & 0 \\ 0 & 0 & 1 \end{bmatrix} \cdot \begin{bmatrix} 1 & 0 & 0 \\ 0 & \cos \beta & \sin \beta \\ 0 & -\sin \beta & \cos \beta \end{bmatrix} \cdot \begin{bmatrix} \cos \alpha & \sin \alpha & 0 \\ -\sin \alpha & \cos \alpha & 0 \\ 0 & 0 & 1 \end{bmatrix} \quad (3.4)$$

$$\alpha = \arctan \frac{\varphi_2}{\varphi_1}, \text{ if } \varphi_1 \neq 0 \quad (3.5)$$

$$\alpha = \text{sgn}(\varphi_2) \cdot \frac{\pi}{2}, \text{ if } \varphi_1 = 0$$

$$\beta = \varphi_T = -\text{sgn}(\varphi_1) \cdot \sqrt{\varphi_1^2 + \varphi_2^2} \quad (3.6)$$

$$\gamma = -\alpha \quad (3.7)$$

The coordinates (relative to the coordinate system 123 (Fig. 3.17 )) of the points A<sub>1</sub>, A<sub>2</sub>, A<sub>3</sub>, and A<sub>4</sub> after rotation of the rigid body are given by Equation 3.8:

$$\mathbf{V}_R = \mathbf{R} \cdot \mathbf{V}, \quad \mathbf{V} = \begin{bmatrix} -a_1 & 0 & -a_3 & 0 \\ 0 & -a_2 & 0 & -a_4 \\ 0 & 0 & h & h \end{bmatrix} \quad (3.8)$$

where  $\mathbf{V}$  is the matrix whose columns are the coordinates of the points A<sub>1</sub>, A<sub>2</sub>, A<sub>3</sub>, and A<sub>4</sub> before the rotation and  $\mathbf{V}_R$  is the matrix of the coordinates of the same points after the rotation. Designate with  $\mathbf{V}(A_i)$  and  $\mathbf{V}_R(A_i)$  the vectors of coordinates of a point A<sub>i</sub> (i=1 to 4) before and after the rotation of the rigid body, respectively. The displacements of a point A<sub>i</sub> (i=1 to 4) due to the rotation of a rigid body,  $\mathbf{D}_R(A_i)$ , is then given by Equation 3.9. For the given translation vector,  $\mathbf{D}_T$  (Equation 3.10), the total displacement of a point A<sub>i</sub> (i=1 to 4) is given by vector  $\mathbf{D}(A_i)$  (Equation 3.11). The command displacements for the actuators,  $U_{Act,i}$  (i=1 to 4), are given by Equations 3.12a and 3.12b and shown in Fig. 3.18 , where  $L_i$  (i=1 to 4) is the length of actuator i (i=1 to 4).

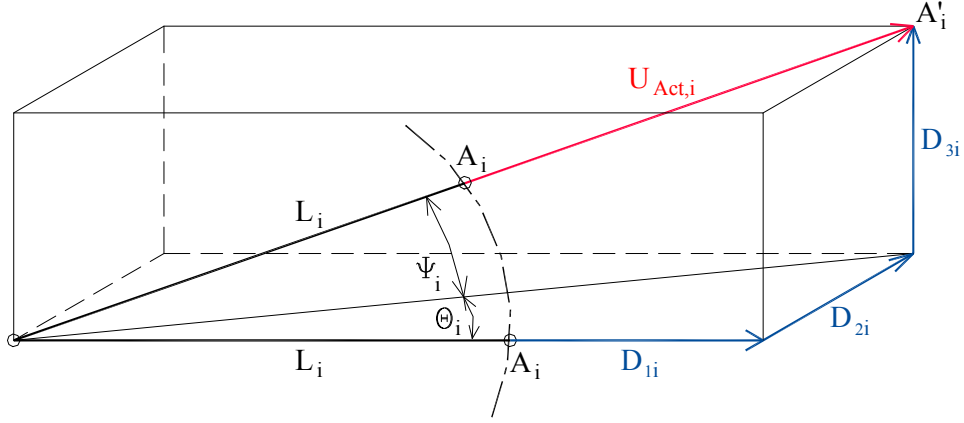


**Fig. 3.18 Schematic presentation of command displacement for actuator  $i$  ( $i=1, 3$ )**

$$\mathbf{D}_R(A_i) = \mathbf{V}_R(A_i) - \mathbf{V}(A_i), \quad i = 1, 2, 3, 4 \quad (3.9)$$

$$\mathbf{D}_T = \begin{bmatrix} U_1 \\ U_2 \\ 0 \end{bmatrix} \quad (3.10)$$

$$\mathbf{D}(A_i) = \mathbf{D}_R(A_i) + \mathbf{D}_T = \begin{bmatrix} D_{1i} \\ D_{2i} \\ D_{3i} \end{bmatrix}, \quad i = 1, 2, 3, 4 \quad (3.11)$$

$$U_{Act,i} = \sqrt{(L_i + D_{1i})^2 + D_{2i}^2 + D_{3i}^2} - L_i, \quad i = 1, 3 \quad (3.12a)$$

$$U_{Act,i} = \sqrt{D_{1i}^2 + (L_i + D_{2i})^2 + D_{3i}^2} - L_i, \quad i = 2, 4 \quad (3.12b)$$

After applying the displacements on the specimen the corresponding reactions (resisting forces) were measured using load-cells and passed to the data acquisition system. Total of six forces were measured: four resisting forces from the actuators and two forces from the pressure jacks that applied the axial force on the specimen. The measured forces underwent geometric transformation before they were passed to the time-stepping integration algorithm.

The forces measured by the actuators,  $F_i$  ( $i=1$  to 4), are transformed to forces  $F_{x,i}$  and  $F_{y,i}$  ( $i=1$  to 4) using Equations 3.13 and 3.14,

$$F_{x,i} = F_i \cdot \cos \theta_i \cdot \cos \psi_i, \quad i = 1, 3 \quad (3.13a)$$

$$F_{x,i} = -F_i \cdot \cos \theta_i \cdot \cos \psi_i, \quad i = 2, 4 \quad (3.13b)$$

$$F_{y,i} = F_i \cdot \sin \theta_i \cdot \cos \psi_i, \quad i = 1, 2, 3, 4 \quad (3.14)$$

where  $\theta_i$  and  $\psi_i$  are angles calculated using Equations 3.15 and 3.16 (Fig. 3.19).

$$\theta_i = \phi + \arctan\left(\frac{D_{2i}}{L_i + D_{1i}}\right), \quad i = 1, 3 \quad (3.15a)$$

$$\theta_i = \left(\frac{\pi}{2} - \phi\right) + \arctan\left(\frac{D_{1i}}{L_i + D_{2i}}\right), \quad i = 2, 4 \quad (3.15b)$$

$$\psi_i = \arctan\left(\frac{D_{3i}}{\sqrt{D_{1i}^2 + D_{2i}^2}}\right), \quad i = 1, 2, 3, 4 \quad (3.16)$$

The forces and moments (at the control point of the specimen) originating from the actuators ( $F_{x,Act}$ ,  $F_{y,Act}$ ,  $M_{x,Act}$ ,  $M_{y,Act}$ ) are given by Equations 3.17 to 3.20,

$$F_{x,Act} = \sum_{i=1}^4 F_{x,i} \quad (3.17)$$

$$F_{y,Act} = \sum_{i=1}^4 F_{y,i} \quad (3.18)$$

$$M_{x,Act} = -(F_{y,3} + F_{y,4}) \cdot H \quad (3.19)$$

$$M_{y,Act} = (F_{x,3} + F_{x,4}) \cdot H \quad (3.20)$$

where  $H$  is the centerline distance between the upper and the lower actuator.

The forces measured by the pressure jacks,  $P_i$  ( $i=1, 2$ ), are transformed to forces in the global coordinate system,  $F_{x,Rods}$ ,  $F_{y,Rods}$ , and  $F_{z,Rods}$  using Equations 3.21 to 3.23,

$$F_{x,Rods} = (P_1 + P_2) \cdot \cos(-\varphi_x) \cdot \frac{U_{x,beam}}{L_{rod}} \quad (3.21)$$

$$F_{y,Rods} = (P_1 + P_2) \cdot \sin(-\varphi_x) \quad (3.22)$$

$$F_{z,Rods} = (P_1 + P_2) \cdot \cos(-\varphi_x) \quad (3.23)$$

where  $\varphi_x$  is a rotation of the spreader beam around  $x$  axis (its only axis of rotation),  $U_{x,beam}$  is a displacement of the spreader beam in  $x$  direction and  $L_{rod}$  is the length of the post-tensioned rod (pin-to-pin distance) (Fig. 3.19). The moments (at the control point of the specimen) originating from the axial load setup,  $M_{x,Rods}$  and  $M_{y,Rods}$ , are given by Equations 3.24 and 3.25,

$$M_{x,Rods} = F_{z,Rods} \cdot (U_{y,beam} - U_y) - F_{y,Rods} \cdot H_2 \quad (3.24)$$

$$M_{y,Rods} = -F_{z,Rods} \cdot (U_{x,beam} - U_x) + F_{x,Rods} \cdot H_1 \quad (3.25)$$

where  $U_{y,beam}$  is a displacement of the spreader beam in  $y$  direction,  $U_x$  and  $U_y$  are horizontal displacements of the specimen at the control point,  $H_1$  is the distance between the control point and 2D hinge, and  $H_2$  is the distance between the control point and the spreader beam centerline (Fig. 3.19).

Finally, the total forces and moments,  $F_x$ ,  $F_y$ ,  $M_x$ ,  $M_y$ , to be scaled and passed to the time-integration algorithm are expressed by Equations 3.26 to 3.29.

$$F_x = F_{x,Act} + F_{x,Rods} \quad (3.26)$$

$$F_y = F_{y,Act} + F_{y,Rods} \quad (3.27)$$

$$M_x = M_{x,Act} + M_{x,Rods} \quad (3.28)$$

$$M_y = M_{y,Act} + M_{y,Rods} \quad (3.29)$$

The scaling factor for lateral forces is  $S_L^2 = 4.6875^2 = 21.97$  and for bending moments it is  $S_L^3 = 4.6875^3 = 103$ .

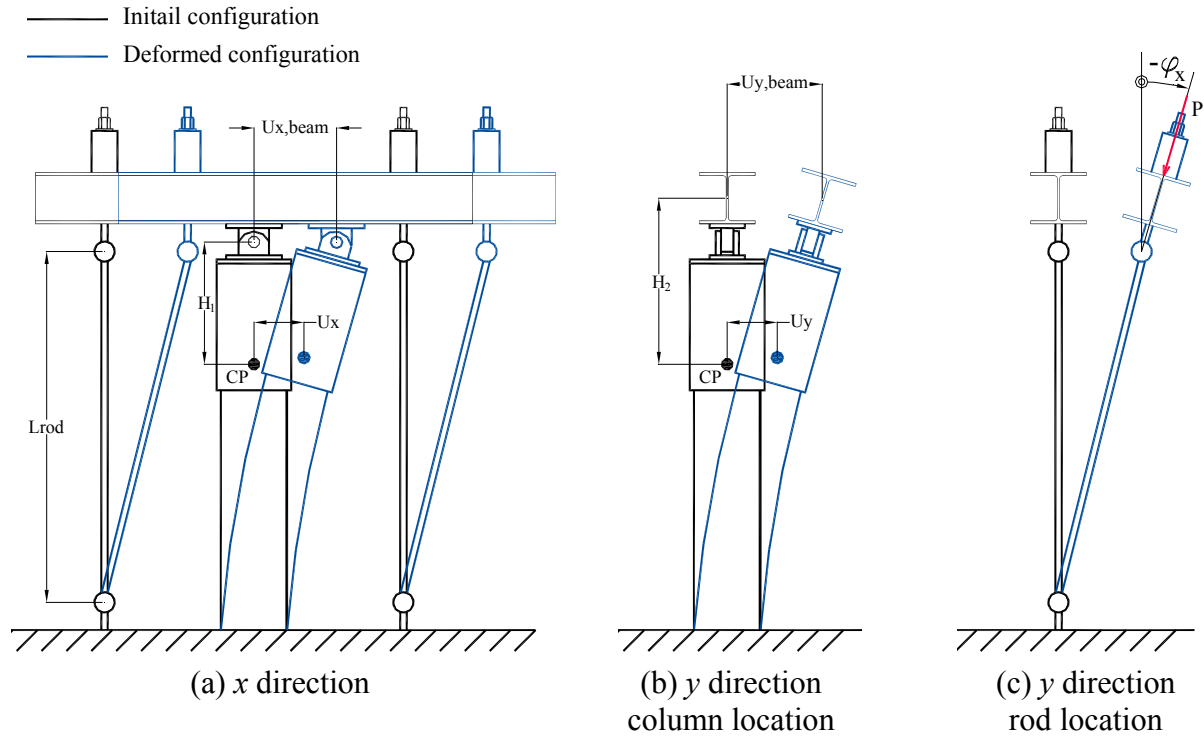


**Fig. 3.19 Initial vs. deformed configuration of the axial test setup in x and y directions**

### 3.3.6 Instrumentation

Instrumentation of specimens tested in the hybrid simulation manner is the same as for specimens tested in the quasi-static manner (for details see Chapter 2). The only difference is additional instrumentation of the rigid column extension. To instrument the rigid column extension two levels of external instrumentation were added. Thus, the column was instrumented at nine levels along its height (Fig. 3.20). At each level, three points were instrumented with three displacement potentiometers per point.

For the axial test of the specimen, the same instrumentation layout was used as for the hybrid simulation test. Thus, the specimen was instrumented externally using displacement potentiometers and internally using strain gages. The compression-tension machine, in addition to its own displacement potentiometer and a load cell, was externally instrumented with two displacement potentiometer (on the either side of the machine head) to measure the vertical displacements of the machine during the test.

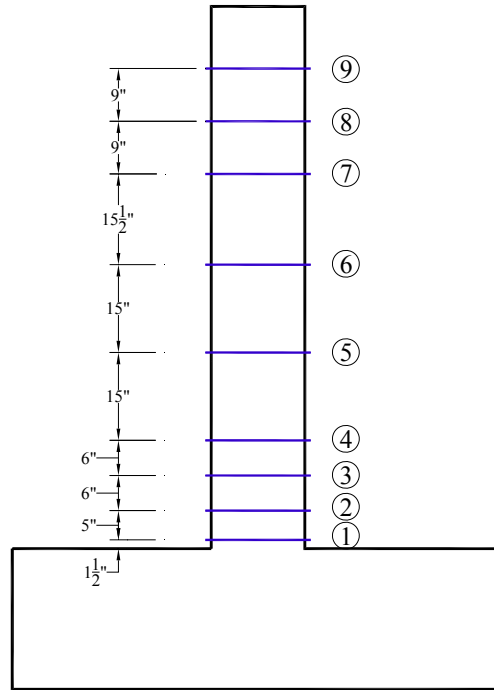


**Fig. 3.20 Externally instrumented levels along the height of the hybrid simulation specimens**

### 3.4 OVERVIEW OF EXPERIMENTAL OBSERVATIONS

The important results from the two hybrid simulation tests followed by the axial crushing of the specimens are given in the two subsections that follow. The results from the test HSM are given in the first subsection and the results from the test HSH are given in the second subsection.

#### 3.4.1 Results of the HSM test

During the HSM test the specimen was exposed to the earthquake loading of a medium intensity inducing significant yielding and strain hardening of the steel and initiating the spalling of concrete. The maximum displacement ductilities of the bridge columns in the longitudinal (X) and transverse (Y) bridge directions were 3 and 4, respectively. The hybrid simulation was followed by the axial compression test to get the axial strength of the column with the earthquake induced damage.

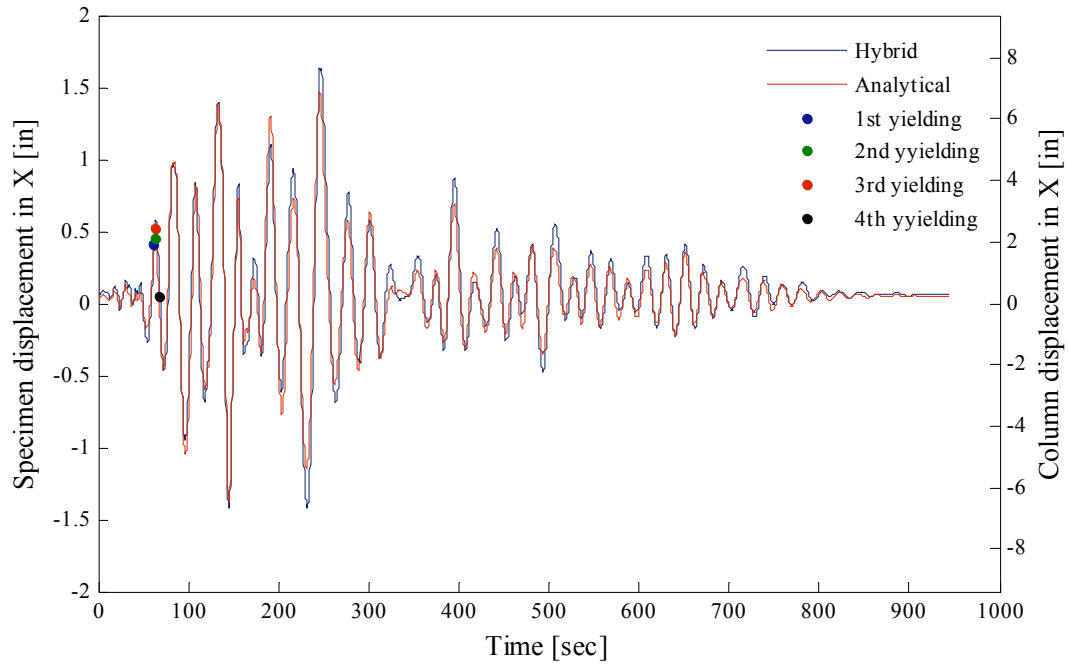
Histories of lateral displacements, sectional rotations, lateral forces and bending moments at the control point of the hybrid model are given in Fig. 3.21 to Fig. 3.24. To validate the calibrated analytical model of the column, each response quantity is given for the hybrid and analytical simulation on the same plot. There is a very close correspondence of the response quantities from the two simulations. Thus, the analytical model of the bridge column calibrated based on the results of quasi-static tests (see Chapter 4) can be used for an earthquake load with a great reliability.

The state of the column (the bottom 22 inches) for the maximum displacement during the hybrid simulation and at the end of the hybrid simulation is shown in Fig. 3.25 and Fig. 3.26 , respectively. In the plastic hinge region of the column (the bottom 12 inches) the distance between the cracks was 3 inches on average and the maximum width of the cracks during the test was approximately  $1/8$  of an inch. Outside the plastic hinge region the distance between the cracks was 6 inches on average with the widths of the cracks less than  $1/16$  of an inch. Fig. 3.26 shows spalling of concrete at the bottom of the column at the end of the test.

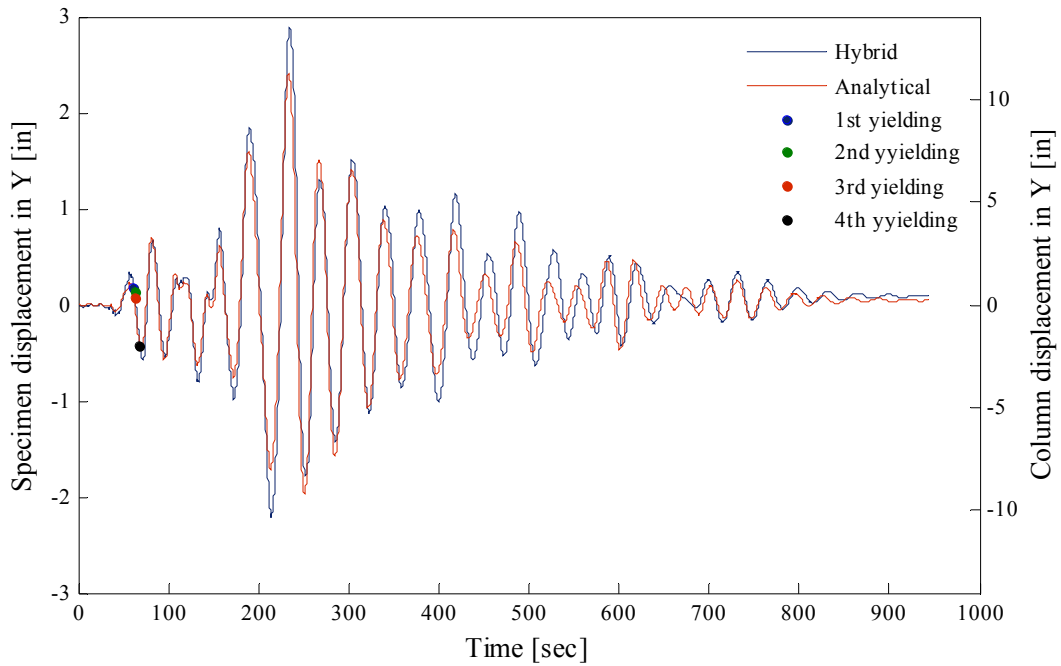
Fig. 3.27 shows profiles of displacements, rotations, and average curvatures for the two major directions, X and Y, at a certain time during the hybrid simulation (marked point on the graph with the orbits of displacement). There is a significant increase of rotations at the bottom of the column. The curvature is very pronounced at the bottom of the column compared to the rest of the column. The presented graphs indicate the location and extent of plastic deformations in the specimen.

Fig. 2.28(a) shows the axial force-deformation relationship of the specimen after the axial sequence of loading. The damaged state of the column is shown in Fig. 2.28(b). The axial failure resulted from the formation of the shear failure plane at the bottom half of the column. The axial strength of the tested specimen was 1417 kips (6303 kN). The ratio of the residual to original axial strength of the column is 0.87. The original axial strength of the column is analytically calculated using the calibrated analytical model (Chapter 4). Thus, the reduction of the axial strength is 13%.



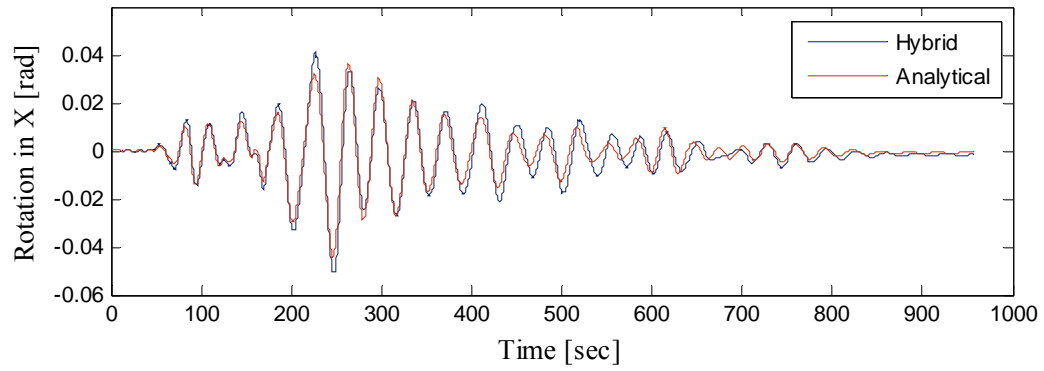


(a) Displacement history in longitudinal (X) bridge direction

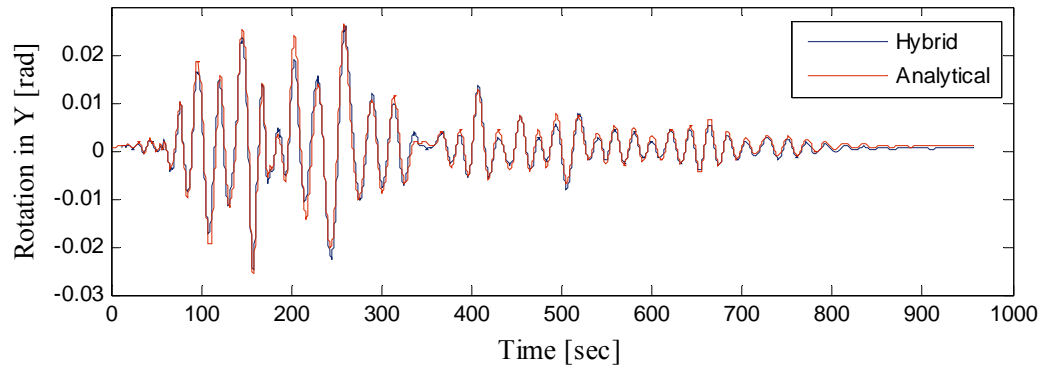


(b) Displacement history in transverse (Y) bridge direction

**Fig. 3.21 Lateral displacement histories at the control point (analytical simulation vs. hybrid simulation)**

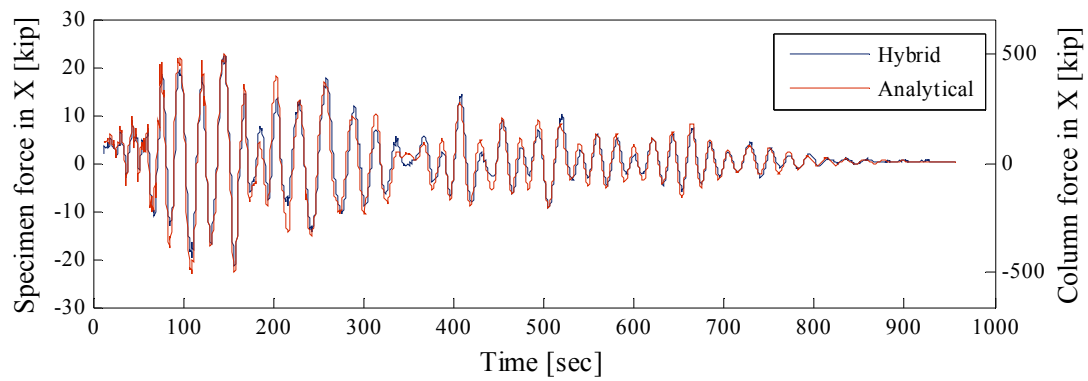


(a) Rotation history around X axis (longitudinal bridge direction)

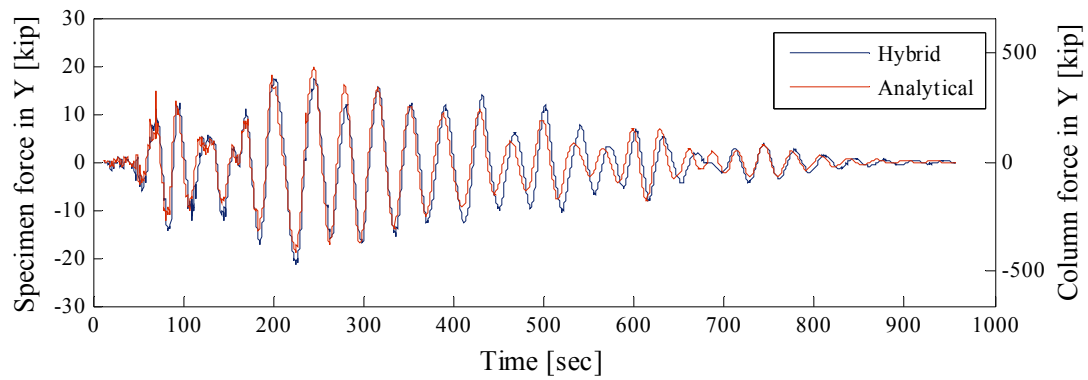


(b) Rotation history around Y axis (transverse bridge direction)

**Fig. 3.22 Sectional rotation histories at the control point (analytical simulation vs. hybrid simulation)**

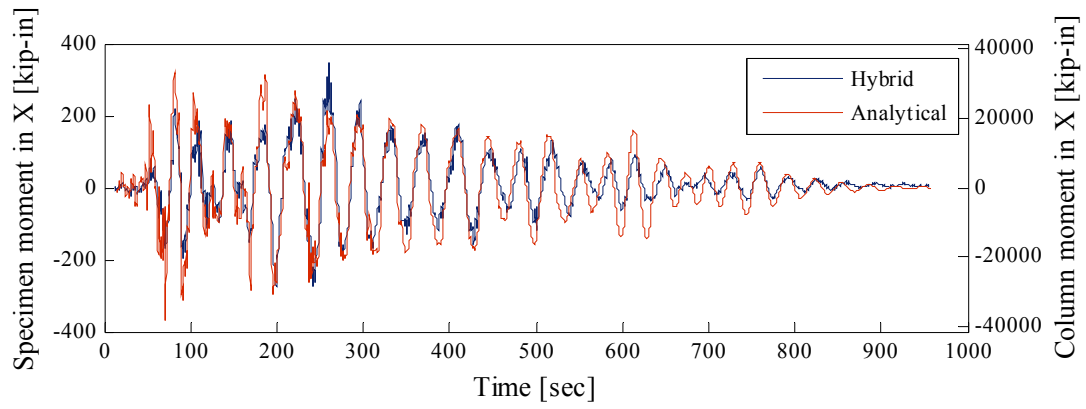


(a) Force history in longitudinal bridge direction

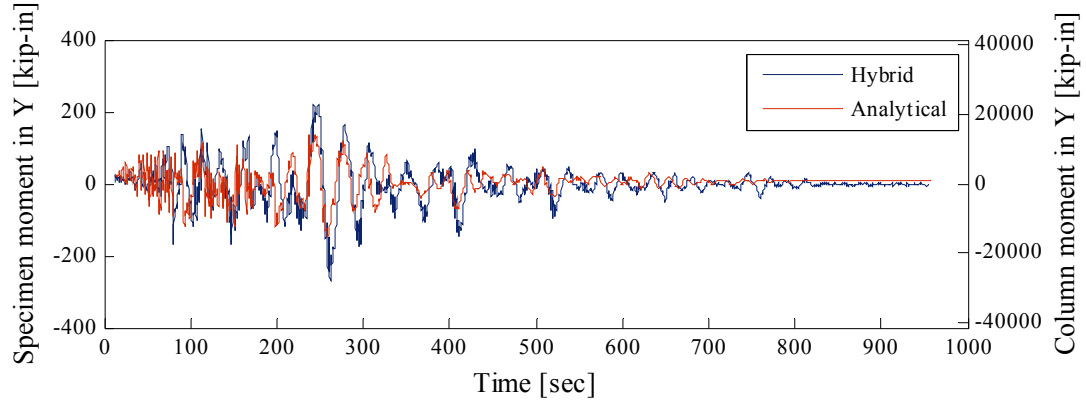


(b) Force history in transverse bridge direction

**Fig. 3.23 Lateral force histories at the control point (analytical simulation vs. hybrid simulation)**



(a) Bending moment history around X axis (longitudinal bridge direction)

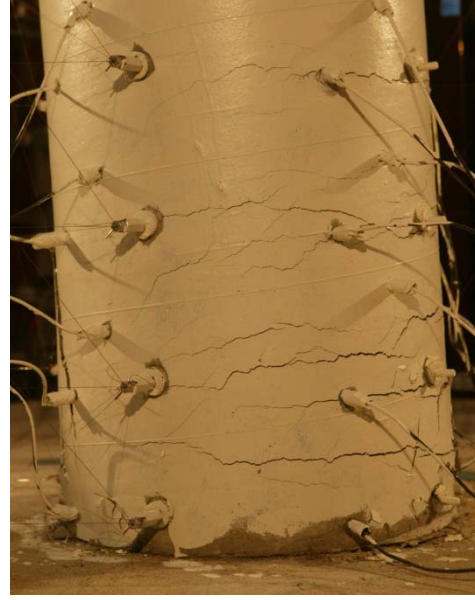


(b) Bending moment history around Y axis (transverse bridge direction)

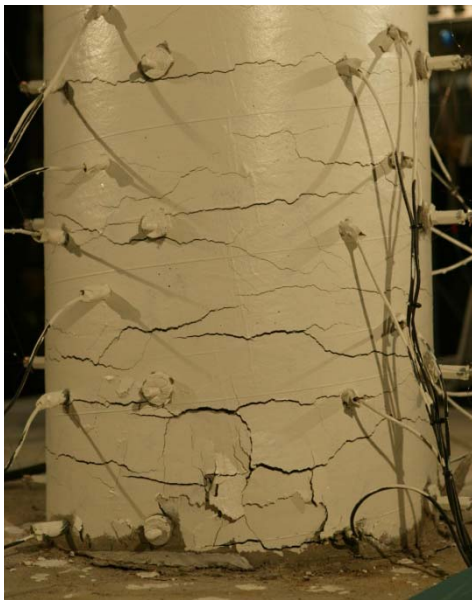
**Fig. 3.24 Bending moment histories at the control point (analytical simulation vs. hybrid simulation)**



(a) North-East



(b) North-West



(c) South-West

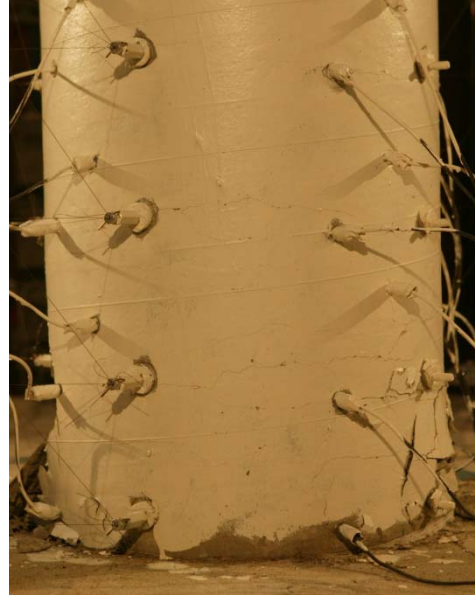


(d) South-East

**Fig. 3.25 State of the specimen at the maximum displacement during the hybrid simulation**



(a) North-East



(b) North-West



(c) South-West



(d) South-East

**Fig. 3.26 State of the specimen at the end of the hybrid simulation**

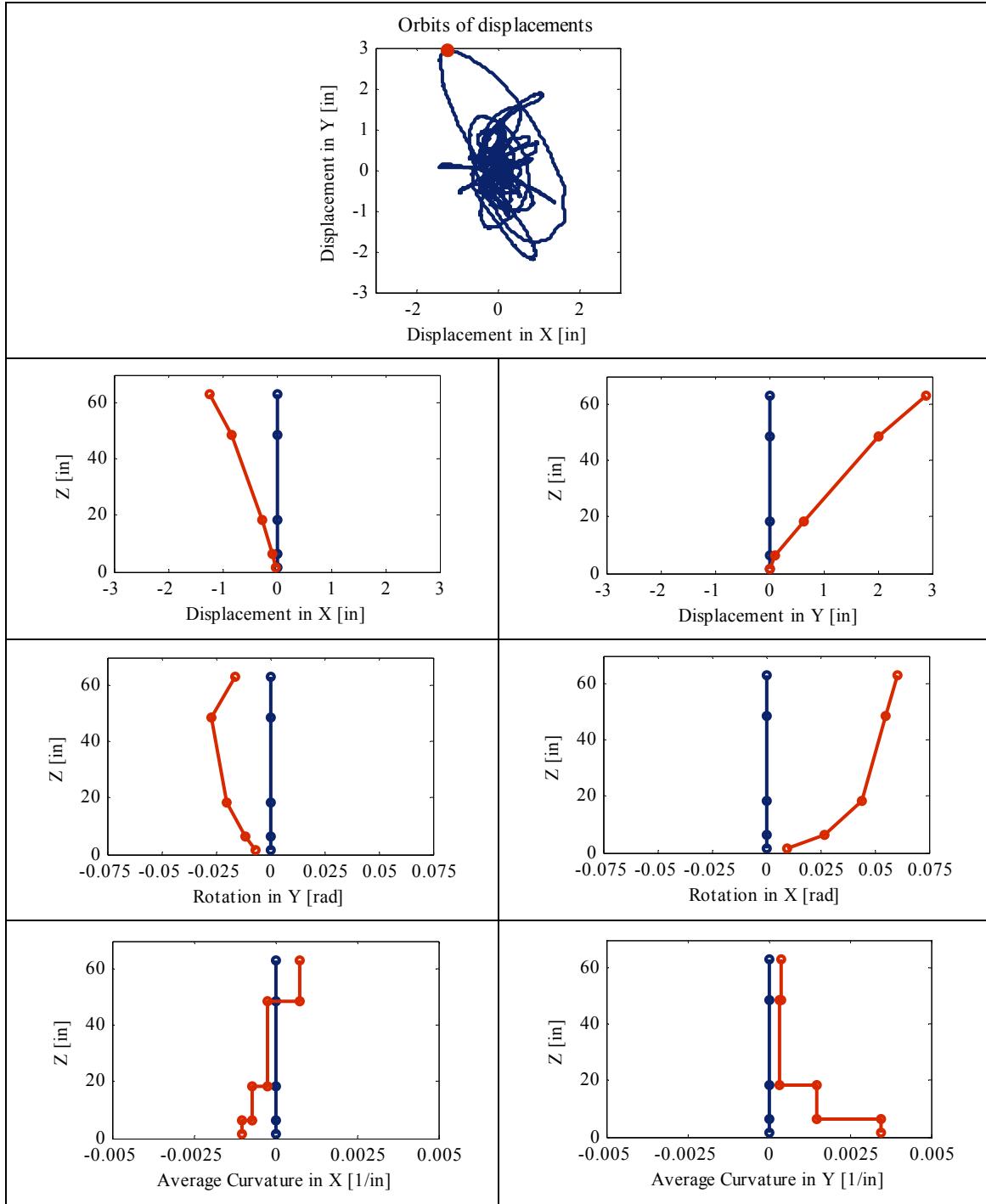
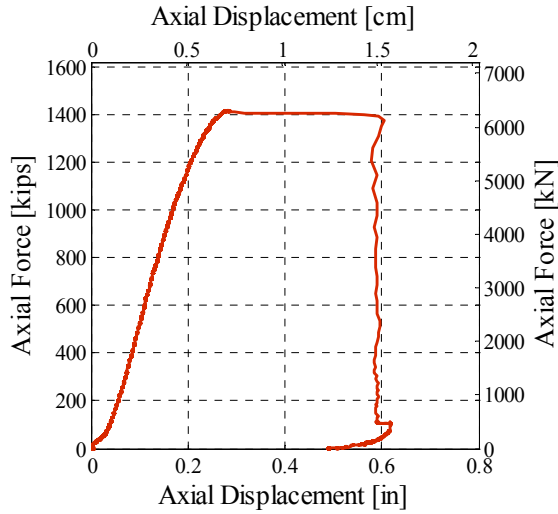


**Fig. 3.27 State of displacements, rotations and curvatures along the height of the specimen at a certain time during the earthquake (marked by the point on the control point displacement orbit)**





(a) Axial force-displacement relationship



(b) Axial failure of the column

**Fig. 3.28 Axial force-displacement relationship and state of the specimen after the axial sequence of the test**

### 3.4.2 Results of the HSH test

During the HSH test, the specimen was exposed to three sequences of loading: gravity load, earthquake load of a high intensity, and truck load moving along the bridge. The maximum displacement ductilities of the bridge columns during the hybrid simulation were 4.7 in the longitudinal (X) and 6.7 in the transverse (Y) bridge direction. The earthquake loading induced extensive yielding of the steel, spalling of concrete, and a reduction in volume of the concrete core in the plastic hinge region. Residual displacements at the top of the bridge column were negligible after the earthquake. Thus, the truck load moving along the bridge after the earthquake did not induce visible damage in the column specimen. The hybrid simulation was followed by the axial compression test to get the axial strength of the column.

Histories of lateral displacements, sectional rotations, lateral forces and bending moments at the control point of the hybrid model are given in Fig. 3.29 to Fig. 3.32. In the given figures, response of the bridge column to the earthquake loading is given in the first 943 seconds. Response to the truck load starts at 943 seconds. To validate the calibrated analytical model of the column, each response quantity is given for the hybrid and analytical simulation on the same plot. There is a very close correspondence of the response quantities from the two simulations. Thus, the analytical model of the bridge column calibrated based on the results of quasi-static tests (see Chapter 4) can be used for an earthquake load with a great reliability.

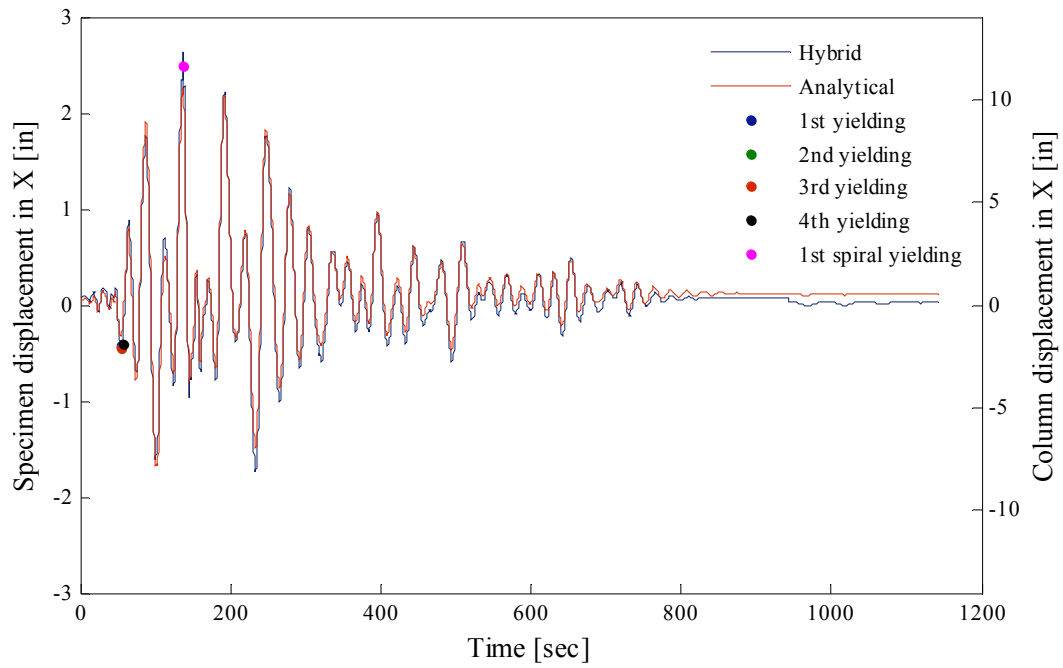
The state of the column (the bottom 22 inches) for the maximum displacement during the hybrid simulation and at the end of the hybrid simulation is shown in Fig. 3.33 and Fig. 3.34, respectively. Based on the crack distribution along the height of the column during the test, the column can be divided into three regions: (i) plastic hinge region (the bottom 12 inches of column), (ii) intermediate region (12 inches of the column next to the plastic hinge region), and (iii) elastic region (the top 40 inches of the column). In the plastic hinge region the distance between the cracks was 3 inches on average and the maximum width of the cracks during the test



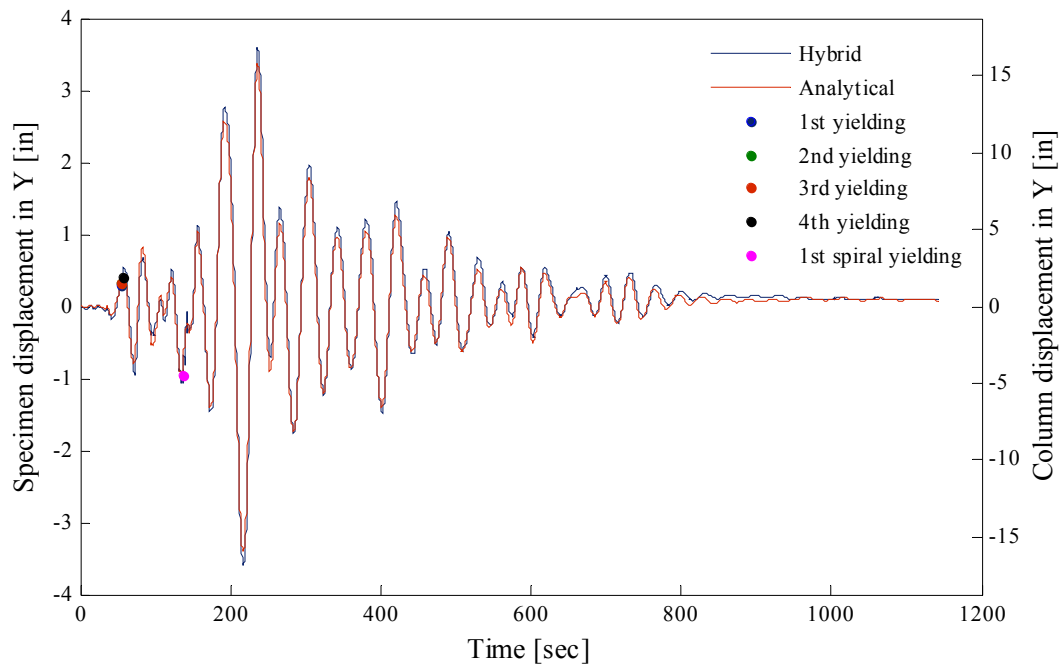
was approximately 3/16 of an inch. Very extensive spalling of concrete and reduction in volume of the concrete core in the plastic hinge region were observed at the end of the test. In the intermediate region the distance between the cracks was 4 inches on average with the widths of the cracks less than 1/8 of an inch. In the elastic region the distance between the cracks was 6 inches on average with the widths of the cracks less than 1/32 of an inch.

Fig. 3.35 shows profiles of displacements, rotations, and average curvatures for the two major directions, X and Y, at a certain time during the hybrid simulation (marked point on the graph with the orbits of displacement). There is a significant increase of rotations at the bottom of the column. The curvature is very pronounced at the bottom of the column compared to the rest of the column. The presented graphs indicate the location and extent of plastic deformations in the specimen.

Fig. 3.36 (a) shows the axial force-deformation relationship of the specimen after the axial sequence of loading. The damaged state of the column is shown in Fig. 3.36 (b). The axial failure resulted from the formation of the shear failure plane at the bottom half of the column. The axial strength of the tested specimen was 1396 kips (6209 kN). The ratio of the residual to original axial strength of the column is 0.86. The original axial strength of the column is analytically calculated using the calibrated analytical model (Chapter 4). Thus, the reduction of the axial strength is 14%.

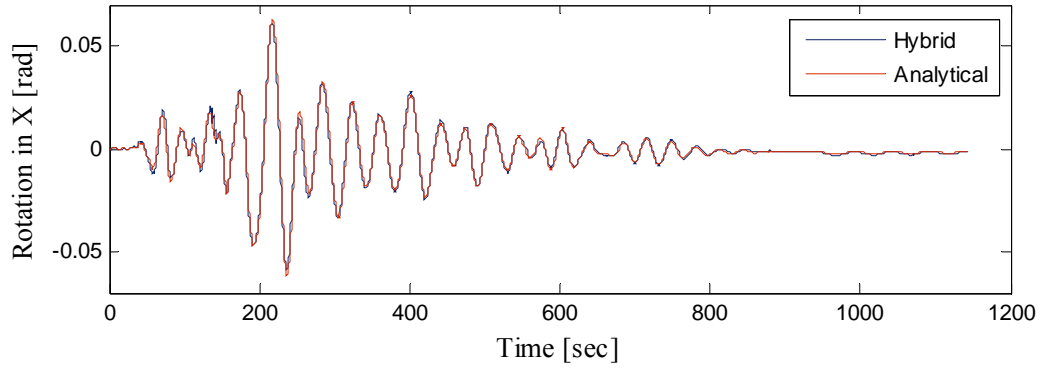


(a) Displacement history in longitudinal bridge direction

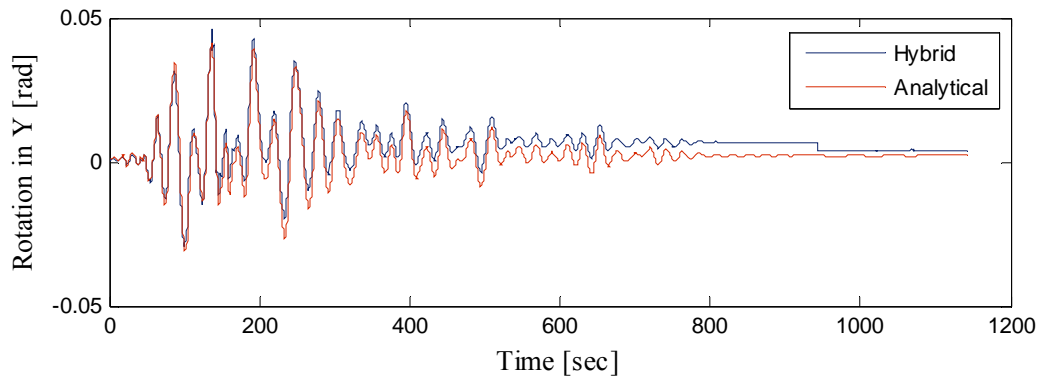


(b) Displacement history in transverse bridge direction

**Fig. 3.29 Displacement histories at the control point (analytical simulation vs. hybrid simulation)**

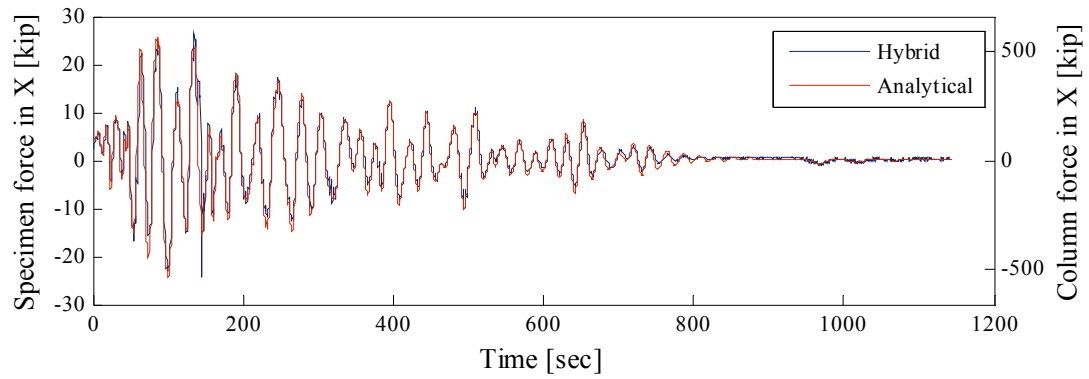


(a) Rotation history around X axis (longitudinal bridge direction)

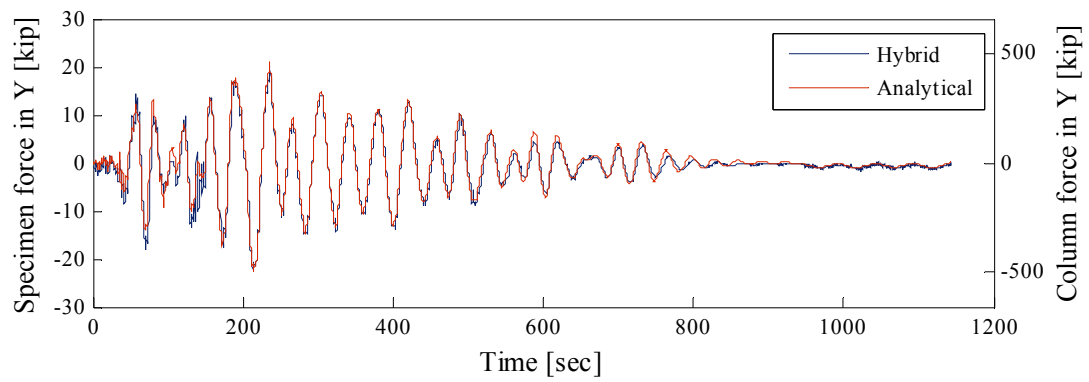


(b) Rotation history around Y axis (transverse bridge direction)

**Fig. 3.30 Sectional rotation histories at the control point (analytical simulation vs. hybrid simulation)**

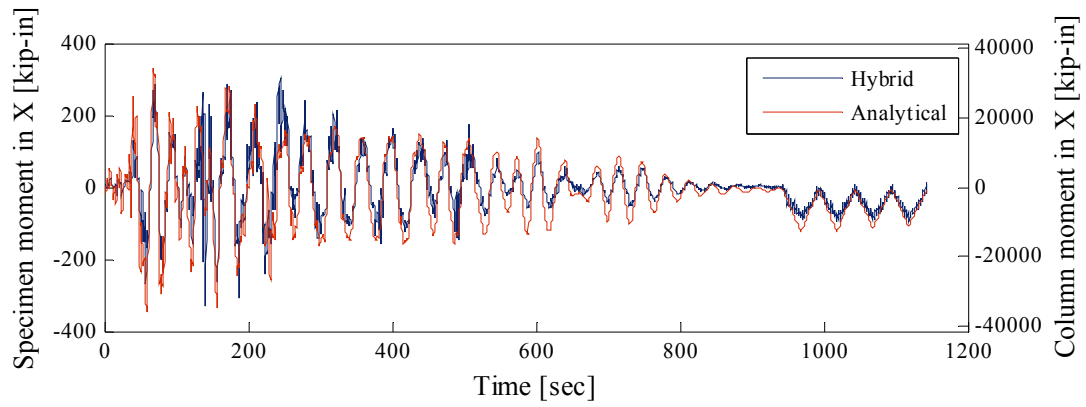


(a) Force history in longitudinal bridge direction

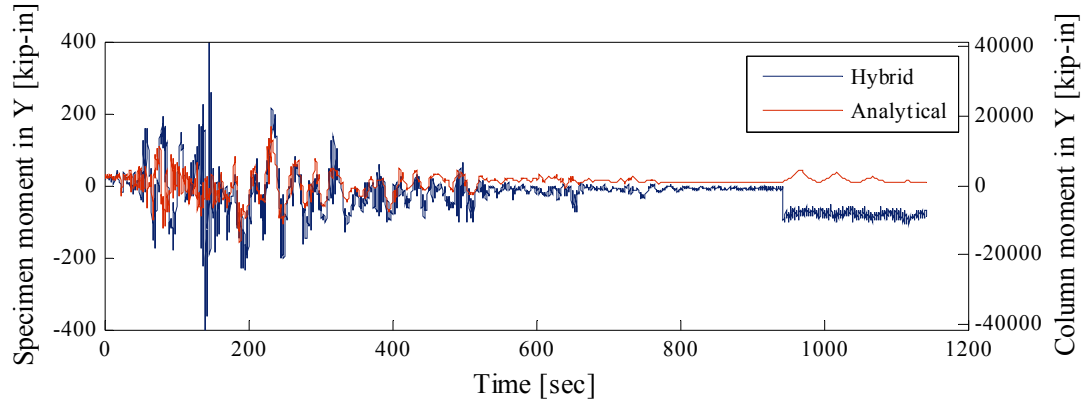


(b) Force history in transverse bridge direction

**Fig. 3.31 Lateral force histories at the control point (analytical simulation vs. hybrid simulation)**



(a) Bending moment history around X axis (longitudinal bridge direction)



(b) Bending moment history around Y axis (transverse bridge direction)

**Fig. 3.32 Bending moment histories at the control point (analytical simulation vs. hybrid simulation)**



(a) North-East



(b) North-West



(c) South-West



(d) South-East

**Fig. 3.33 State of the specimen at the maximum displacement during the hybrid simulation**



(a) North-East



(b) North-West



(c) South-West



(d) South-East

**Fig. 3.34 State of the specimen at the end of the hybrid simulation**

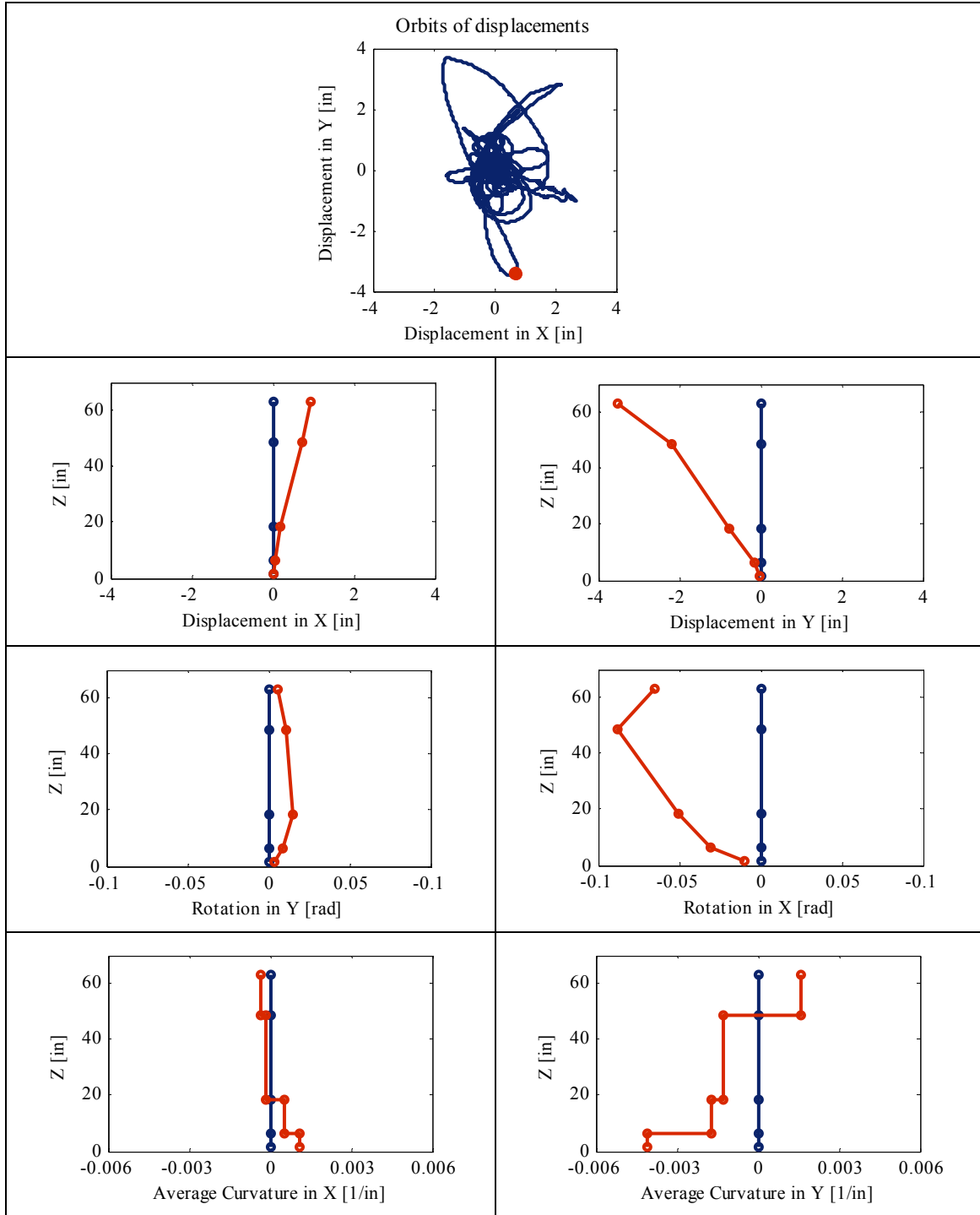
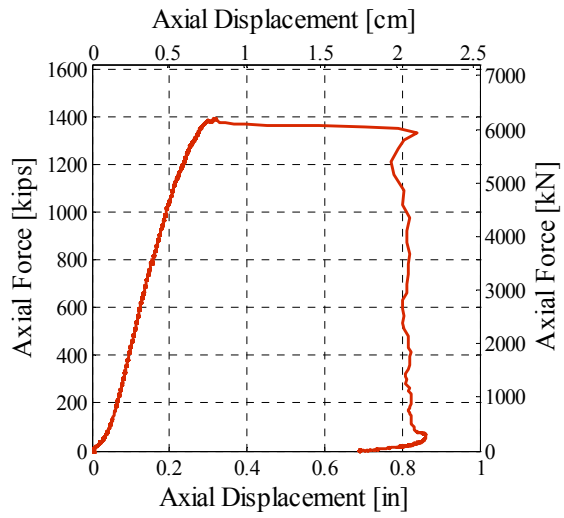


**Fig. 3.35 State of displacements, rotations and curvatures along the height of the specimen at a certain time during the earthquake (marked point on the control point displacement orbit graph)**





(a) Axial force-displacement relationship



(b) Axial failure of the column

**Fig. 3.36 Axial force-displacement relationship and state of the specimen after the axial sequence of the test**

## 4 Analytical Modeling

The main objective of this project is to determine the maximum weight of the truck on the bridge immediately after an earthquake. To accomplish the objective, the set of analytical simulations was performed on a typical California overpass bridge. To develop an analytical model able to determine the maximum weight of a truck the bridge is capable of carrying immediately after an earthquake, quasi-static tests and hybrid simulations were conducted to provide the data needed to test and calibrate the model. Bi-lateral quasi-static tests on a model of a bridge column were performed first to induce earthquake like damage in the column. The damaged columns were then axially crushed to get their remaining axial capacities. The test results were used to calibrate analytical model of a bridge column. For an earthquake and a truck load on the bridge, the analytical model was validated through hybrid simulation tests on a typical California overpass bridge. The physical portion of the hybrid model, the bottom half of a bridge column, was axially tested in compression after the hybrid simulation test to get its remaining axial capacity. The axial crushing of an earthquake damaged bridge column was analytically simulated and the analytical model of a bridge column was verified.

The sequential development of the analytical model is presented in this chapter. The force based element, used to model the bridge column, is described in the first section of this chapter. Next section gives the details of the pre-test calibration of the analytical model of a bridge column. This analytical model is used to design the specimens and the test setup for both, the quasi-static and the hybrid simulation tests. The subsequent sections give the details of calibration of analytical model based on results of quasi-static followed by the axial tests and its validation through hybrid simulations followed by the axial tests.

### 4.1 MODEL OF A BRIDGE COLUMN

The reinforced concrete bridge column is modeled in Open System for Earthquake Engineering Simulation (OpenSees) utilizing a fiber cross-section and force based beam-column element with distributed plasticity (Neuenhofer and Filippou, 1997). The cross-sections of the element are represented by assemblages of longitudinally oriented, unidirectional steel and concrete fibers. Each material in the cross-section has a uniaxial stress-strain relation assigned to it. The element is a line element discretized using Gauss-Lobatto integration scheme with integration points at the ends of the element and along the element length. The fiber cross-sections are assigned to the integration points.

A flexibility-based formulation of the element imposes a moment and axial force distribution along the length of the element in equilibrium with the loads imposed at the end nodes of the member. The curvatures and axial deformations at each integration point are subsequently estimated by iterations given the moment and axial load at the section. The column

response is then obtained through weighted integration of the section deformations along the length of the member.

To model reinforced concrete section, the fiber section that accounts for axial-bending interaction is divided into three parts: concrete cover, concrete core and reinforcing steel. To model the concrete cover (unconfined concrete) and concrete core (confined concrete) two uniaxial material models of concrete, designated in OpenSees as Concrete01 and Concrete02, were considered. To model reinforcing steel (longitudinal bars) two uniaxial material models of reinforcing steel, designated in OpenSees as Steel02 and ReinforcingSteel, were considered.

The Concrete01 material model uses the Kent-Scott-Park model (Kent and Park, 1971) to represent the stress-strain relationship of concrete in compression (Fig. 4.1). The material model has degraded linear unloading-reloading stiffness (Karsan and Jirsa, 1969) and no tensile strength. The parameters that define the concrete model are: concrete compressive strength ( $f_c$ ), concrete strain at maximum strength ( $\epsilon_0$ ), concrete crushing strength ( $f_{cu}$ ), and concrete strain at crushing strength ( $\epsilon_{cu}$ ). The initial slope of the model is:  $E_c = 2 f_c / \epsilon_0$ .

The Concrete02 material model is an extension of Concrete01 material model. It uses the Kent-Scott-Park model to represent the stress-strain relationship of concrete in compression and bi-linear relationship to represent the stress-strain relationship in tension (Fig. 4.2). The parameters that define the concrete model are: concrete compressive strength ( $f_c$ ), concrete strain at maximum strength ( $\epsilon_0$ ), concrete crushing strength ( $f_{cu}$ ), concrete strain at crushing strength ( $\epsilon_{cu}$ ), ratio between unloading slope at  $\epsilon_{cu}$  and initial slope ( $\lambda$ ), tensile strength ( $f_t$ ), and tension softening stiffness ( $E_{ts}$ ). The initial slope of the model is:  $E_c = 2 f_c / \epsilon_0$ .

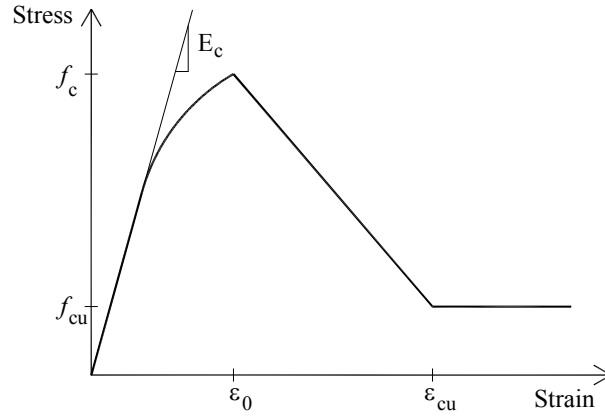


**Fig. 4.1 Uniaxial stress-strain relationship for Concrete01 material**

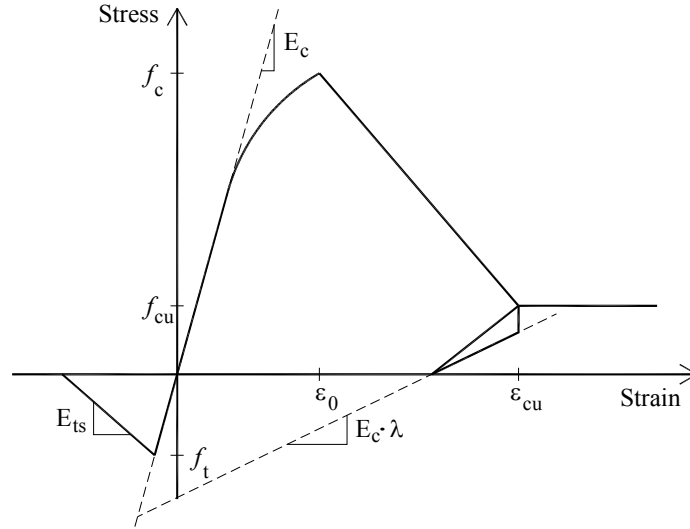


**Fig. 4.2 Uniaxial stress-strain relationship for Concrete02 material**

The Steel02 material model is defined using the Giuffre-Manegotto-Pinto uniaxial strain-hardening material model (Taucer et al., 1991). The model has a bi-linear backbone curve with a post-yield stiffness expressed as a fraction of the initial stiffness. The model accounts for Bauschinger effect and is characterized by continuity in the tangent stiffness during loading and unloading. The parameters that define the reinforcing steel model are: yield strength of reinforcing bar ( $f_y$ ), modulus of elasticity of steel ( $E_s$ ), strain-hardening ratio ( $b$ ), and parameters that control transition from elastic to plastic branches ( $R_0$ ,  $c_{R1}$ , and  $c_{R2}$ ).

The ReinforcingSteel material model uses nonlinear backbone curve (Fig. 4.3). To account for change in area as the bar is stressed, the backbone curve is transformed from engineering stress space to natural stress space. This allows the single backbone curve to represent both tensile and compressive stress-strain relations. The parameters that define the reinforcing steel model are: yield stress in tension ( $f_y$ ), ultimate stress in tension ( $f_{su}$ ), modulus of elasticity of steel ( $E_s$ ), tangential stiffness at initiation of strain hardening ( $E_{sh}$ ), strain corresponding to initial strain hardening ( $\epsilon_{sh}$ ), and strain at peak stress ( $\epsilon_{su}$ ).

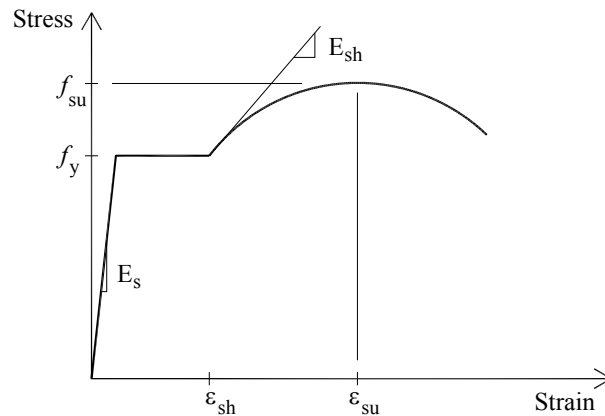


**Fig. 4.3 Nonlinear backbone curve of ReinforcingSteel material**

## 4.2 PRE-TEST CALIBRATION OF THE ANALYTICAL MODEL

To design the specimen and the test setup, the reinforced concrete column was modeled in OpenSees utilizing a fiber cross-section and force based beam-column element with distributed plasticity. To predict the response of the tested specimens the analytical model was calibrated using the results from Lehman's test (Lehman, 2000) on the column with the same aspect ratio and similar ratios of the longitudinal and transverse reinforcement as the Base Column specimen.

To calibrate the constitutive models for reinforcing steel, confined, and unconfined concrete, the results from Lehman's Column415 (Lehman, 2000) test were used. Column415 was a cantilever column tested by applying uni-directional quasi-static incremental lateral displacement protocol up to the failure of the column. An axial load equal to 7% of the column's nominal axial load capacity was maintained during lateral testing. The aspect ratio of the Column415 was 4, the ratio of transverse reinforcement was 0.7% and the ratio of the longitudinal reinforcement was 1.5%. The basic parameters of geometry, reinforcement, and load for the Column415 and the Base Column specimen are given in Table 4.1.

**Table 4.1 Basic parameters for Column415 and Base Column specimen**

Parameters	Column415 (Lehman, 2000)	Base Column specimen
Aspect ratio	$L/D = 4$	$L/D = 4$
Longitudinal reinforcement	$\rho_l = 1.5\%$	$\rho_l = 1.2\%$
Transverse Reinforcement	$\rho_t = 0.7\%$	$\rho_t = 0.75\%$
Axial load	$P/f_c' A_g = 0.07$	$P/f_c' A_g = 0.10$

Analytical model that provides satisfactory matching with the experimental results is defined by 5 integration points along the height of the column and a cross-section with 142 fibers (24 for unconfined cover, 96 for confined core and 22 for reinforcing steel) arranged as shown in Fig. 4.4. Geometric transformation was applied on the model to account for P-Δ effect. To model the reinforcing bars Steel02 material model was used. Concrete cover and core were modeled with Concrete02 material model. The parameters that defined the reinforcing bars are given in Table 4.2 and the parameters that defined concrete cover and concrete core are given in Table 4.3. Description of material models and their parameters is given in Section 4.1. To define confined concrete, maximum compressive strength ( $f_{cc}'$ ) and concrete crushing strength ( $f_{cu}$ ) are calculated according to Mander et al. (1988), modulus of elasticity of concrete is specified to be  $57000\sqrt{f_c'}$  (psi) (Caltrans, 2006a), and strain at crushing strength ( $\epsilon_{cu}$ ) is calculated according to Equation 4.1,

$$\epsilon_{cu} = 0.004 + 0.14 \cdot \rho_t \cdot \frac{f_{ys}}{f_c'} \quad (4.1)$$

where  $\rho_t$  is the ratio of transverse reinforcement,  $f_{ys}$  is yielding strength of spirals, and  $f_c'$  is the maximum compressive strength of plane concrete. Fig. 4.5 shows experimental and analytical force-displacement response curves for Column415. Satisfactory matching is achieved.

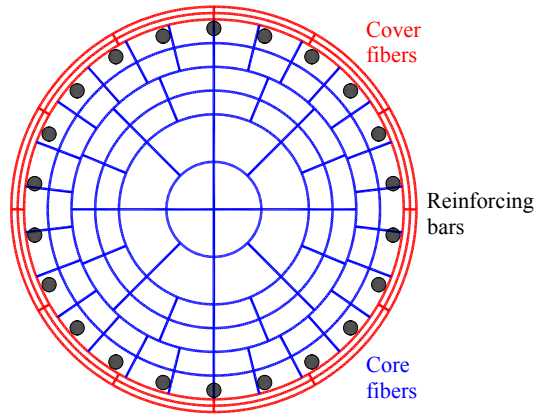


**Fig. 4.4 Fiber cross-section; arrangement of fibers for Column415**

**Table 4.2 Steel02 material model parameters**

Material	$f_y$	$E_s$ (ksi)	b	$R_0$	$c_{R1}$	$c_{R2}$
Reinforcing steel	$f_y^*$	29000	0.025	20	0.925	0.15

\* From coupon tests

**Table 4.3 Concrete02 material model parameters**

Material	$f_c$	$\epsilon_0$	$f_{cu}$	$\epsilon_{cu}$	$\lambda$	$f_t$	$E_{ts}$
Concrete cover	$f_c'^*$	$2f_c'/E_c$ ***	0	0.005	0.1	$0.04f_c'$	$f_t'/\epsilon_0$
Concrete core	$f_{cc}'^{**}$	$2f_{cc}'/E_c$ ***	$f_{cu}^{**}$	$\epsilon_{cu}^{****}$	0.1	$0.04f_{cc}'$	$f_t'/\epsilon_0$

\* From test results on concrete cylinders

\*\* Equation from Mander et al. (1988)

\*\*\*  $E_c = 57000\sqrt{f_c'}$  (psi) (Caltrans, 2006a)

\*\*\*\* Equation 4.1

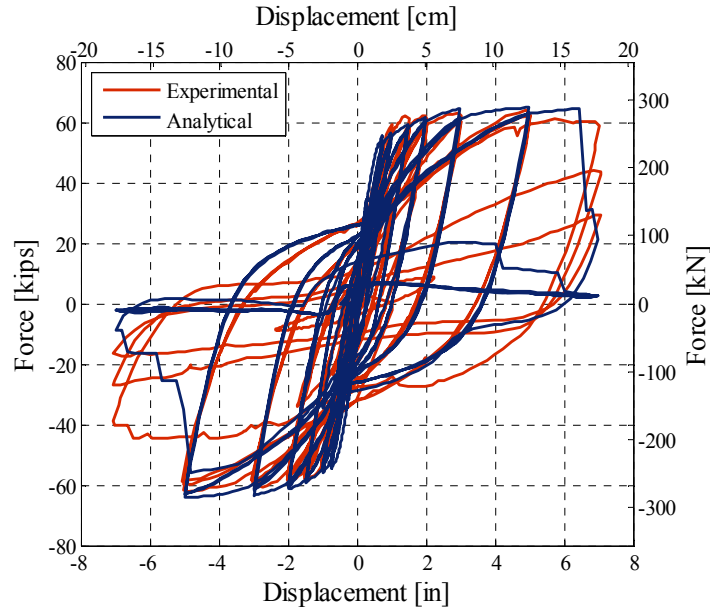
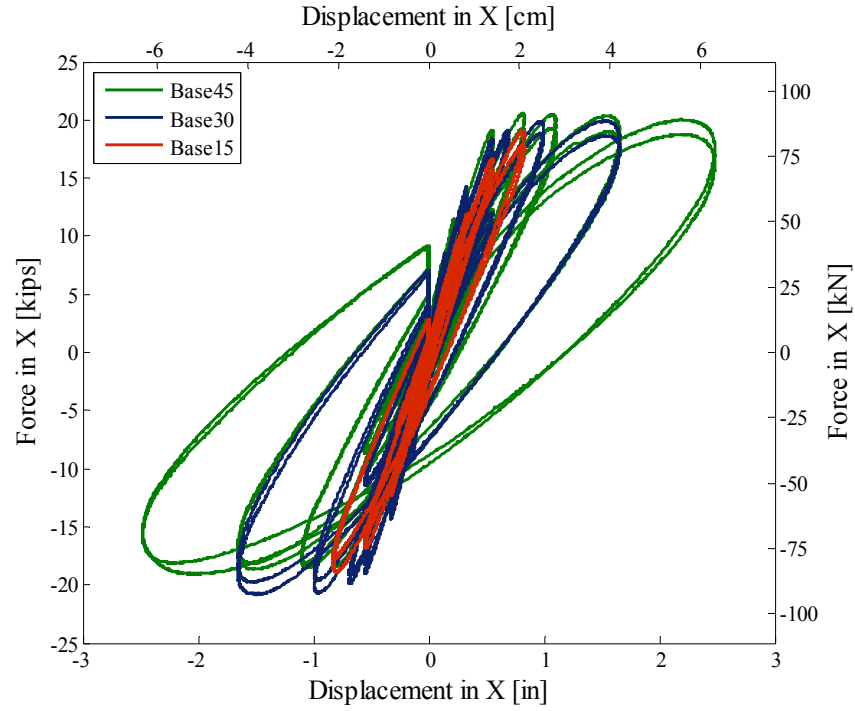


**Fig. 4.5 Experimental vs. analytical force-displacement response for Column415**

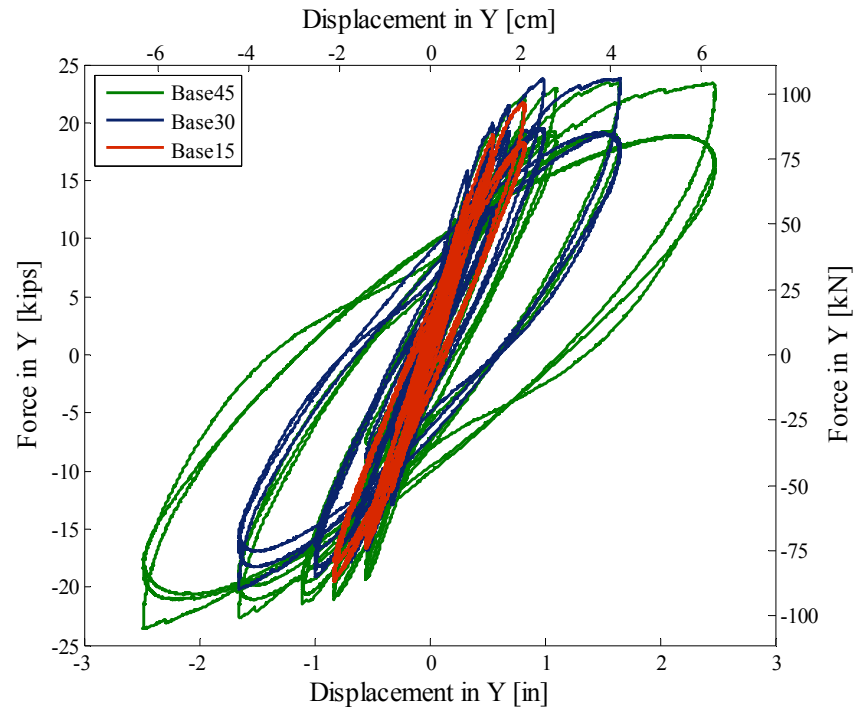
### **4.3 CALIBRATION OF ANALYTICAL MODEL BASED ON QUASI-STATIC AND AXIAL TESTS RESULTS**

Bi-lateral quasi-static tests on a model of a bridge column were performed first to induce earthquake like damage in the column. The damaged columns were then axially tested in compression to get their remaining axial capacities (Chapter 2). The test results were used to calibrate analytical model of a bridge column.

In developing analytical model of a bridge column, the first step was to compare the force-displacement response curves and their envelopes from the three quasi-static tests (Base15, Base30 and Base45) performed on nominally identical specimens (Fig. 4.6 and Fig. 4.7). Although the specimens were built using the steel and concrete from the same batch and were tested within 20 days, their stiffness and strength are different. However, when displaced to the same displacement level, unloading and reloading branches of the force-displacement response curves match well. Thus, a compromise between initial and post-cracking stiffness and strength was made while developing the analytical model of a bridge column.



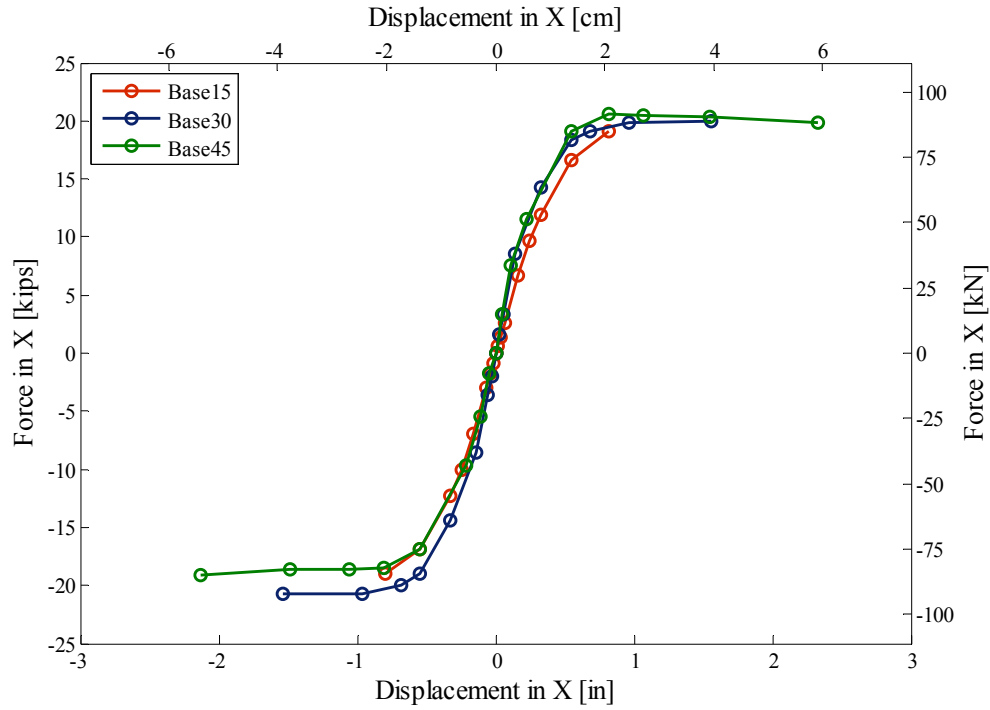
(a) Lateral force-displacement response in X direction



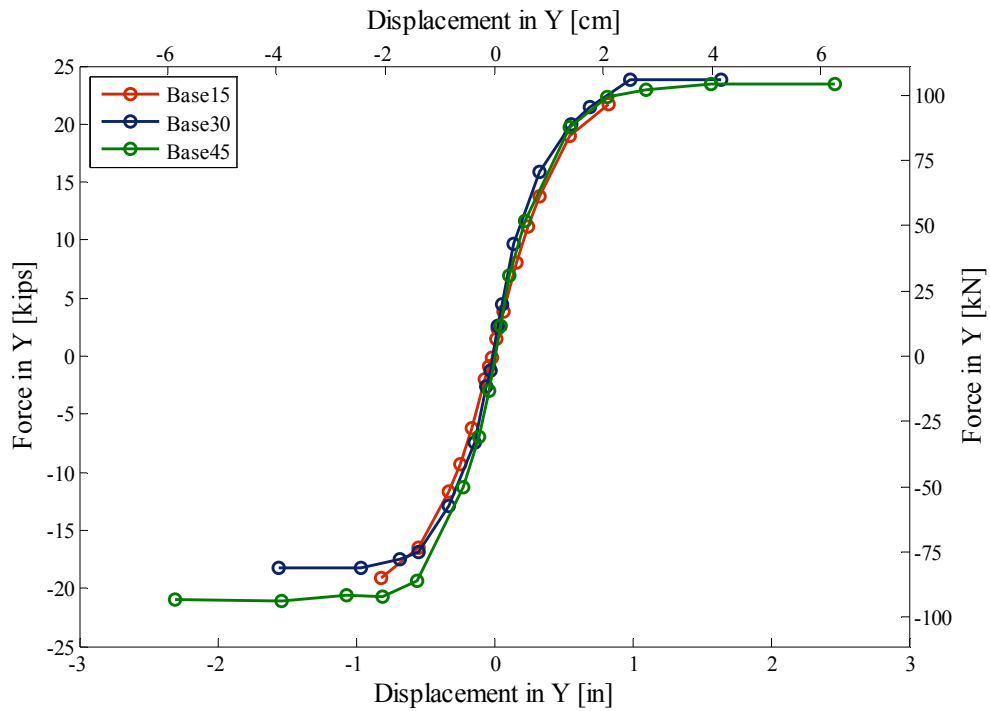
(b) Lateral force-displacement response in Y direction

**Fig. 4.6 Lateral force-displacement response curves for three lateral quasi-static tests: Base15, Base30, and Base45 in two major directions, X and Y**





(a) Force-displacement response envelopes in X direction



(b) Force-displacement response envelopes in Y direction

**Fig. 4.7 Force-displacement response envelopes for three lateral quasi-static tests: Base15, Base30, and Base45 in two major directions, X and Y**

Two analytical models, referred to here as Analytical 1 and Analytical 2, provided satisfactory matching with the experimental results. Both analytical models are defined by 5 integration points along the height of the column and a cross-section with 132 fibers (24 for unconfined cover, 96 for confined core and 12 for reinforcing steel) arranged as shown in Fig. 4.8. Geometric transformation was applied on the models to account for P- $\Delta$  effect. The two models differ in the uni-axial relationships for the reinforcing steel and concrete. The Analytical 1 model uses Steel02 material to model the reinforcing bars and Concrete01 material to model the concrete cover and core. The Analytical 2 model uses ReinforcingSteel material to model the reinforcing bars and Concrete02 material to model the concrete cover and core. The parameters that define the reinforcing bars are given in Table 4.4 for the Analytical 1 model and in Table 4.6 for the Analytical 2 model. The parameters that define concrete cover and concrete core are given in Table 4.5 for the Analytical 1 model and in Table 4.7 for the Analytical 2 model. Description of material models and their parameters is given in Section 4.1. To define confined concrete, maximum compressive strength ( $f_{cc}'$ ) and concrete crushing strength ( $f_{cu}$ ) are calculated according to Mander et al. (1988), modulus of elasticity of concrete is specified to be  $57000\sqrt{f_c'}$  (psi) (Caltrans, 2006a), and strain at crushing strength of concrete ( $\epsilon_{cu}$ ) is calculated according to Equation 4.1.

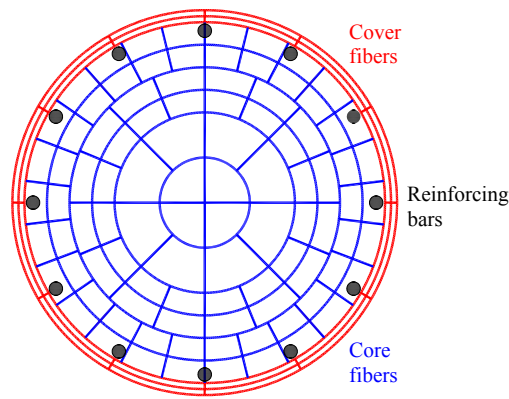


**Fig. 4.8 Fiber cross-section; arrangement of fibers for Base Column specimen**

**Table 4.4 Analytical 1 - Steel02 material model parameters**

Material	$f_y$	$E_s$ (ksi)	b	$R_0$	$c_{R1}$	$c_{R2}$
Reinforcing steel	70.7*	29000	0.025	15	0.925	0.15

\* From coupon tests

**Table 4.5 Analytical 1 - Concrete01 material model parameters**

Material	$f_c$	$\epsilon_0$	$f_{cu}$	$\epsilon_{cu}$
Concrete cover	$f_c^{**}$	$2f_c'/E_c^{***}$	0	0.005
Concrete core	$f_{cc}^{***}$	$2f_{cc}'/E_c^{***}$	$f_{cu}^{**}$	$\epsilon_{cu}^{****}$

\* From test results on concrete cylinders

\*\* Equation from Mander et al. (1988)

\*\*\*  $E_c = 57000\sqrt{f_c'}$  (psi)

\*\*\*\* Equation 4.1

**Table 4.6 Analytical 2 - Concrete02 material model parameters**

Material	$f_c$	$\epsilon_0$	$f_{cu}$	$\epsilon_{cu}$	$\lambda$	$f_t$	$E_{ts}$
Concrete cover	$f_c^{**}$	$2f_c'/E_c^{***}$	0	0.005	0.1	$0.04f_c'$	$f_t/\epsilon_0$
Concrete core	$f_{cc}^{***}$	$2f_{cc}'/E_c^{***}$	$f_{cu}^{**}$	$\epsilon_{cu}^{****}$	0.1	$0.04f_{cc}'$	$f_t/\epsilon_0$

\* From test results on concrete cylinders

\*\* Equation from Mander et al. (1988)

\*\*\*  $E_c = 57000\sqrt{f_c'}$  (psi)

\*\*\*\* Equation 4.1

**Table 4.7 Analytical 2 - ReinforcingSteel material model parameters**

Material	$f_y$	$f_{su}$	$E_s$ (ksi)	$E_{sh}$ (ksi)	$\epsilon_{sh}$	$\epsilon_{su}$
Reinforcing steel	70.7*	120*	29000	725*	0.01*	0.12*

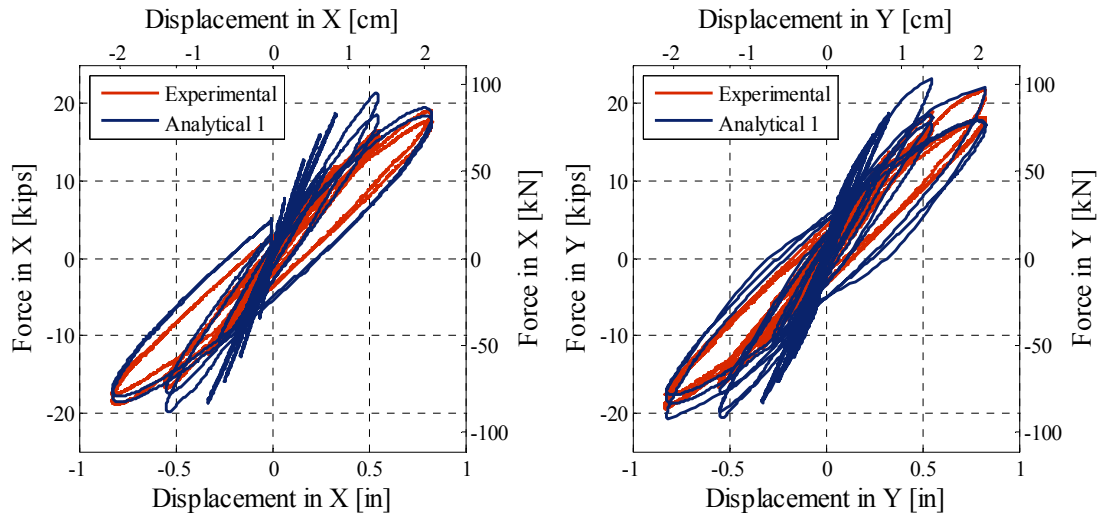
\* From coupon tests

Lateral force-displacement response curves of the tested specimens compared to their analytical models (Analytical 1 and Analytical 2) for the three quasi-static tests: Base15, Base30, and Base45 in the two major directions, X and Y, are given in Fig. 4.9 to Fig. 4.11. Comparisons of the response envelopes are given Fig. 4.12 and Fig. 4.13. Both analytical models, Analytical 1 and Analytical 2, show good correspondence with the experimental results.

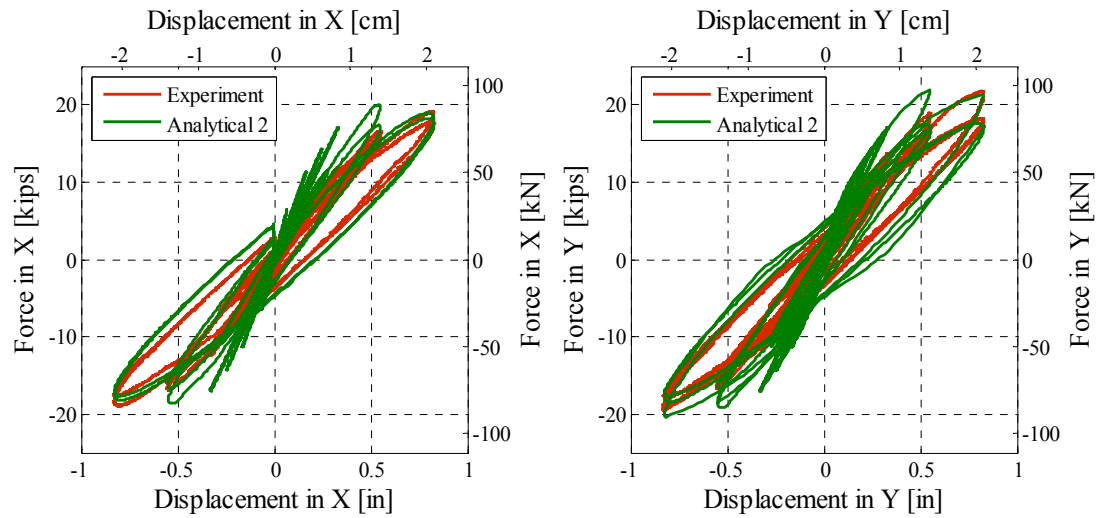
Axial force-displacement relationships for the axial sequence of loading of the tested specimens compared to their analytical models (Analytical 1 and Analytical 2) for the tests: Base0, Base15, Base30, and Base45 are shown in Fig. 4.14 to Fig. 4.17. To study traffic capacity of a bridge after an earthquake it is important to develop an analytical model able to estimate the residual axial strength of the bridge columns. Thus, the analytical models are calibrated to match the residual axial strengths of the tested specimens. For comparison purposes, the residual axial strengths of the tested specimens together with the analytically calculated strengths are given in

Table 4.8. Although both analytical models match the results from the lateral tests equally well, the Analytical 1 model provides better correspondence with the axial test results than the Analytical 2 model. Note, however, that the quality of the match of the axial load-displacement response after lateral load damage is not as high as the match of the lateral load force-displacement response.

Permanent lateral displacements of bridge columns after an earthquake have great influence on their residual axial strengths. The test Base15, had the lateral drift of  $\sim 1.0\%$  in the axial sequence of loading. This drift has the same influence on the residual axial strength of the specimen as the permanent lateral displacement of a bridge column after an earthquake. Thus, to study traffic load capacity of a bridge after an earthquake it is important to develop analytical model able to match the results from the axial sequence of the test Base15. The Analytical 1 model estimates the residual axial strength of specimen Base15 with an error of 0.26%. The Analytical 2 model overestimates it with an error of 9.81%. Consequently, the Analytical 1 model was chosen for analytical study of the traffic capacity of a bridge after an earthquake (Chapter 5).

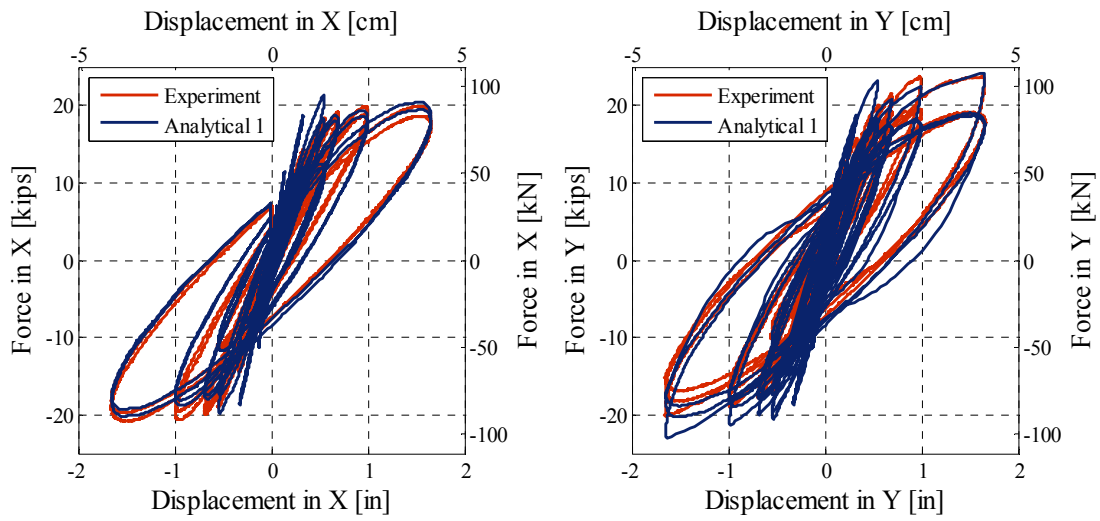


(a) Lateral force-displacement response curves in X and Y direction: Experimental vs. Analytical 1

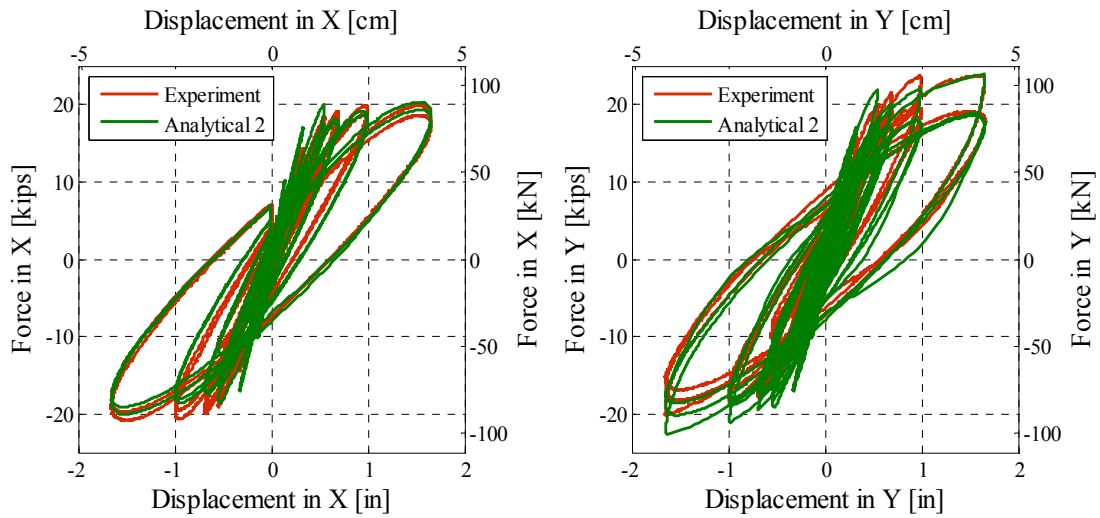


(b) Lateral force-displacement response curves in X and Y direction: Experimental vs. Analytical 2

**Fig. 4.9 Experimental vs. analytical force-displacement response curves for the Base Column specimen with displacement ductility level of 1.5**

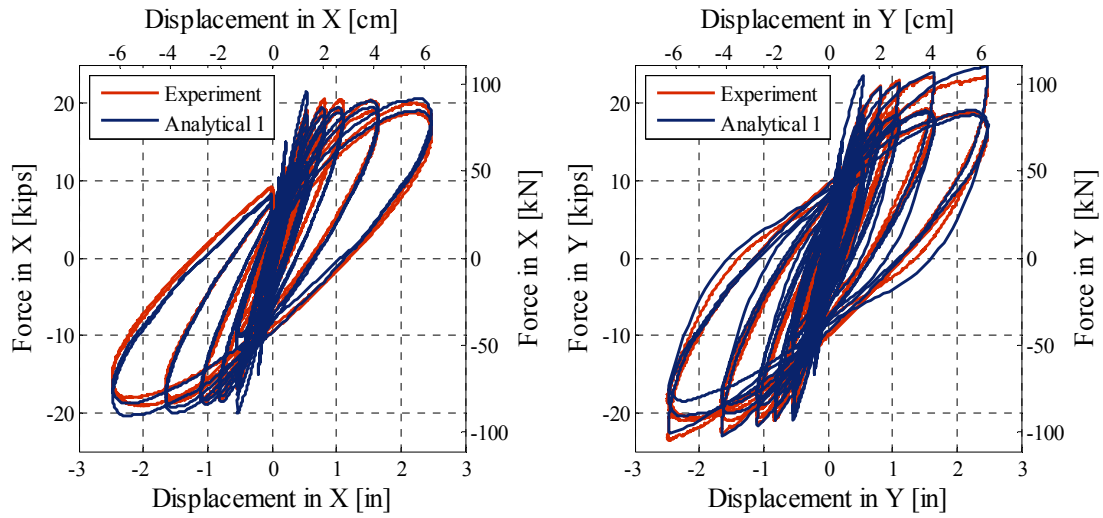


(a) Lateral force-displacement response curves in X and Y direction: Experimental vs. Analytical 1

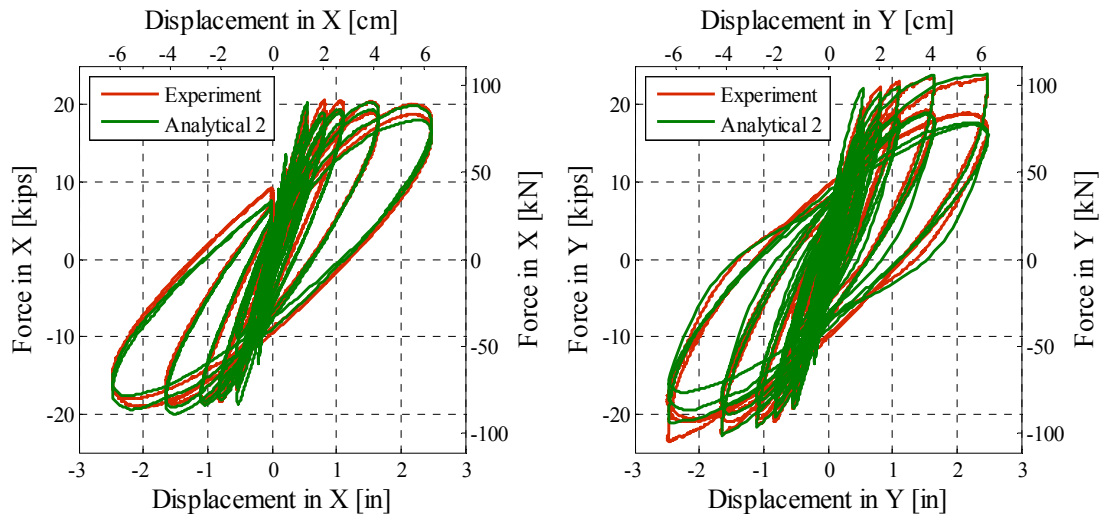


(b) Lateral force-displacement response curves in X and Y direction: Experimental vs. Analytical 2

**Fig. 4.10 Experimental vs. analytical force-displacement response curves for the Base Column specimen with displacement ductility level of 3.0**

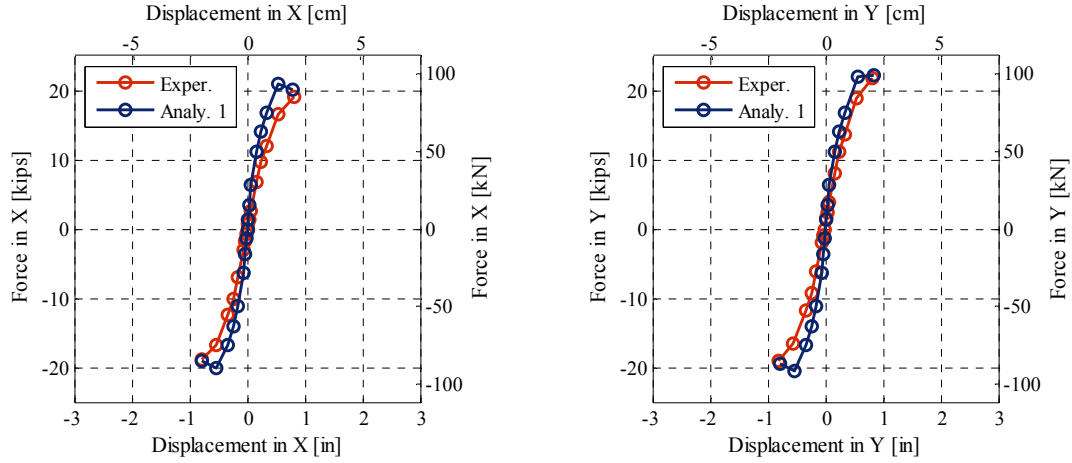


(a) Lateral force-displacement response curves in X and Y direction: Experimental vs. Analytical 1

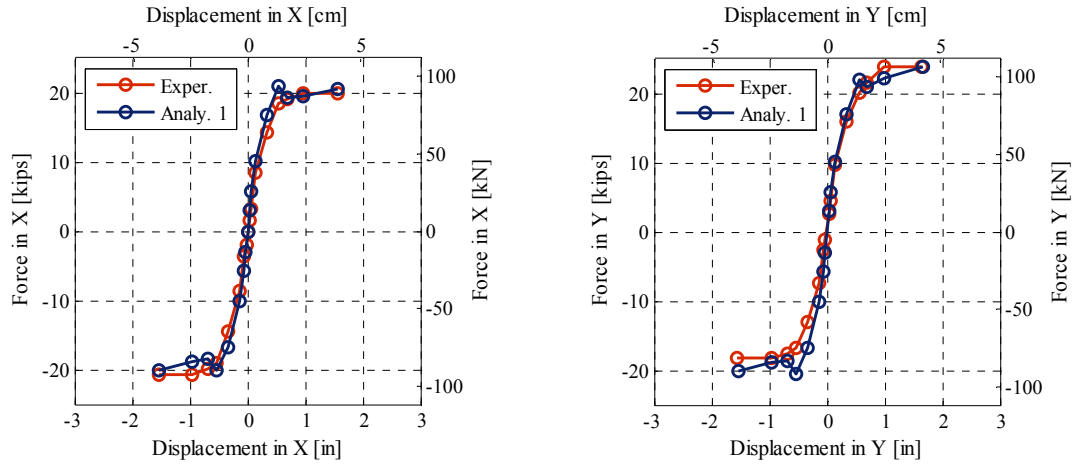


(b) Lateral force-displacement response curves in X and Y direction: Experimental vs. Analytical 2

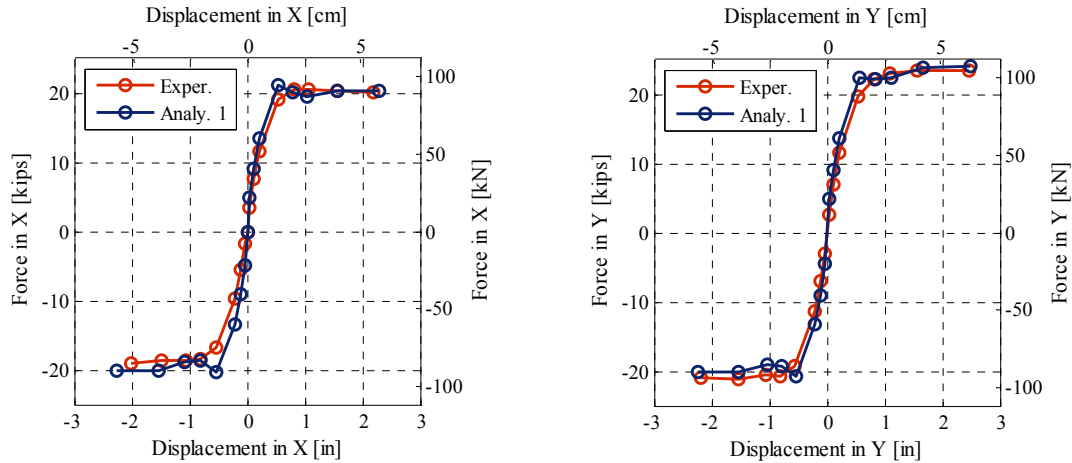
**Fig. 4.11 Experimental vs. analytical force-displacement response curves for the Base Column specimen with displacement ductility level of 4.5**



(a) Force-displacement response envelopes in X and Y direction for test Base15



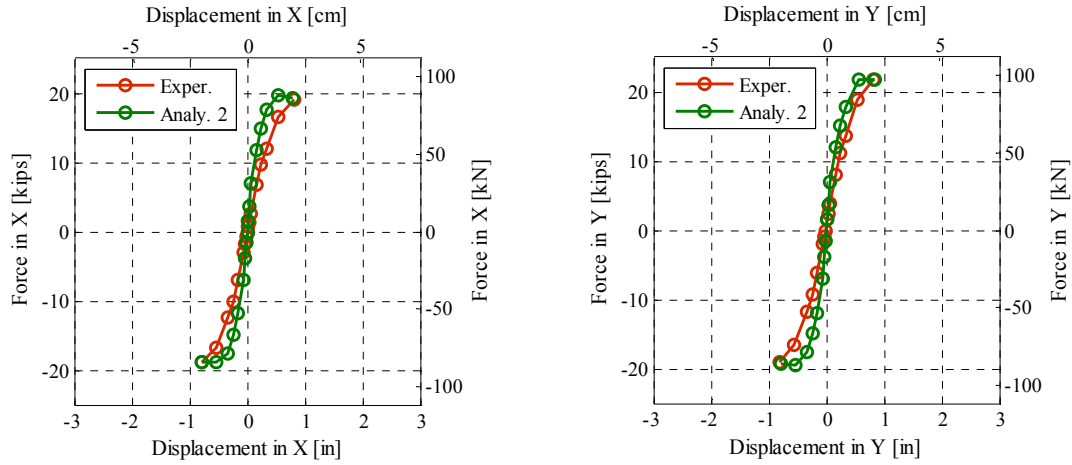
(b) Force-displacement response envelopes in X and Y direction for test Base30



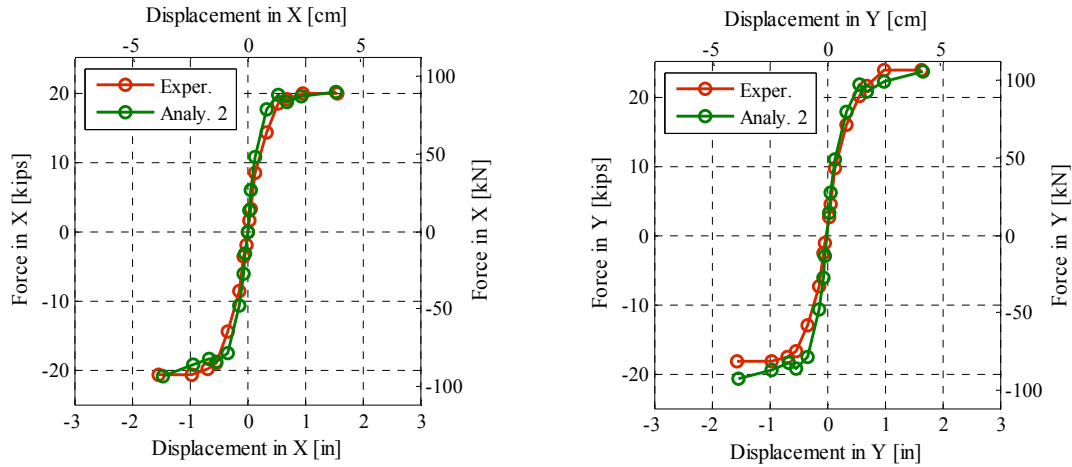
(c) Force-displacement response envelopes in X and Y direction for test Base45

**Fig. 4.12 Force-displacement response envelopes in two major directions, X and Y, for three lateral quasi-static tests: Base15, Base30, and Base45; Experiment vs. Analytical 1**

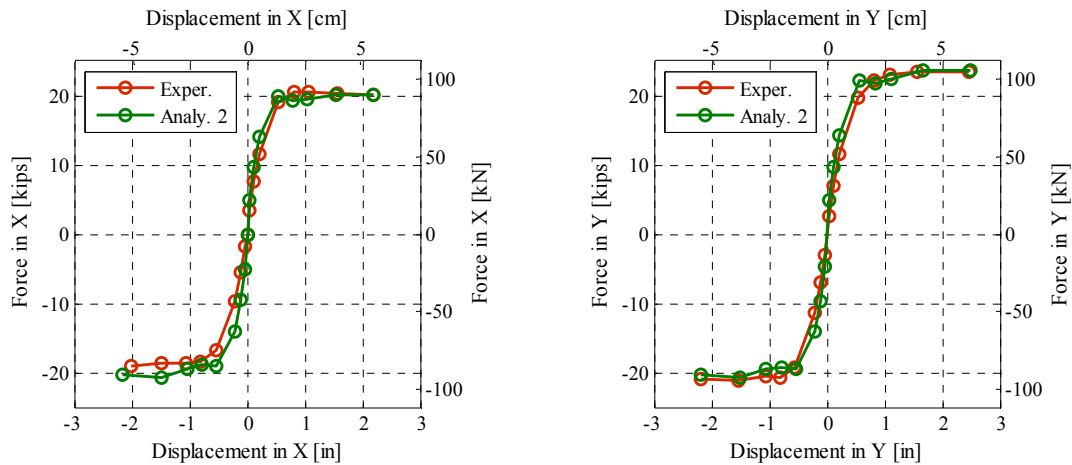




(a) Force-displacement response envelopes in X and Y direction for test Base15



(b) Force-displacement response envelopes in X and Y direction for test Base30



(c) Force-displacement response envelopes in X and Y direction for test Base45

**Fig. 4.13 Force-displacement response envelopes in two major directions, X and Y, for three lateral quasi-static tests: Base15, Base30, and Base45; Experiment vs. Analytical 2**

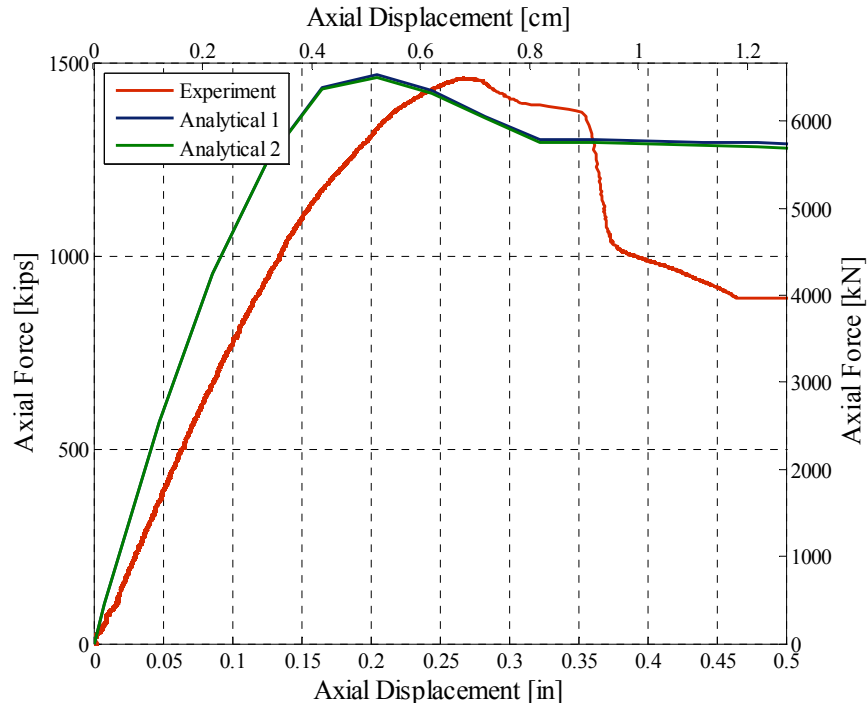


**Fig. 4.14 Axial force-displacement relationships: experimental vs. analytical relationships for the “virgin” Base Column specimen**

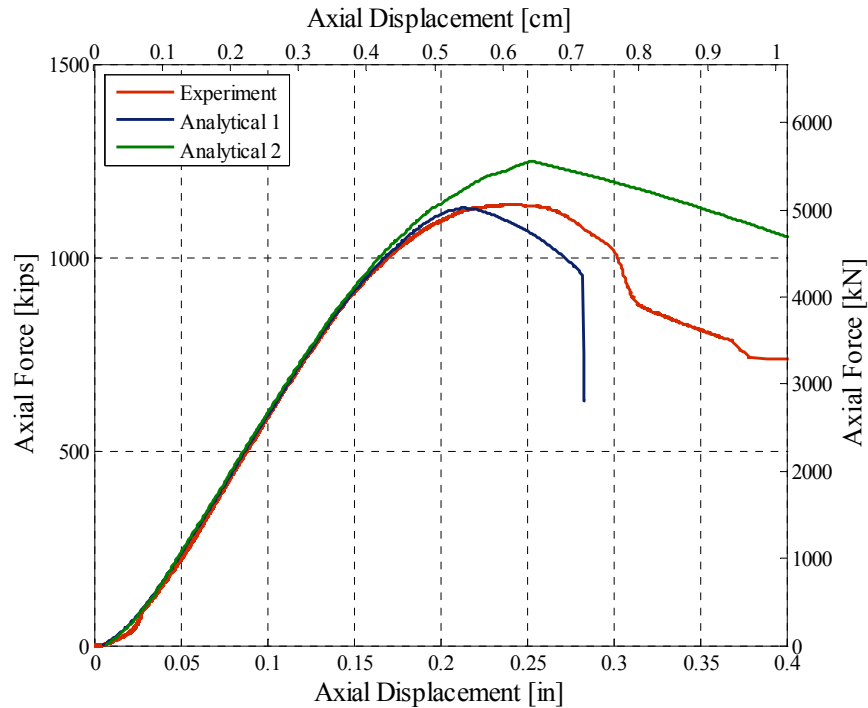


**Fig. 4.15 Axial force-displacement relationships: experimental vs. analytical relationships for the Base Column specimen with displacement ductility level of 1.5**

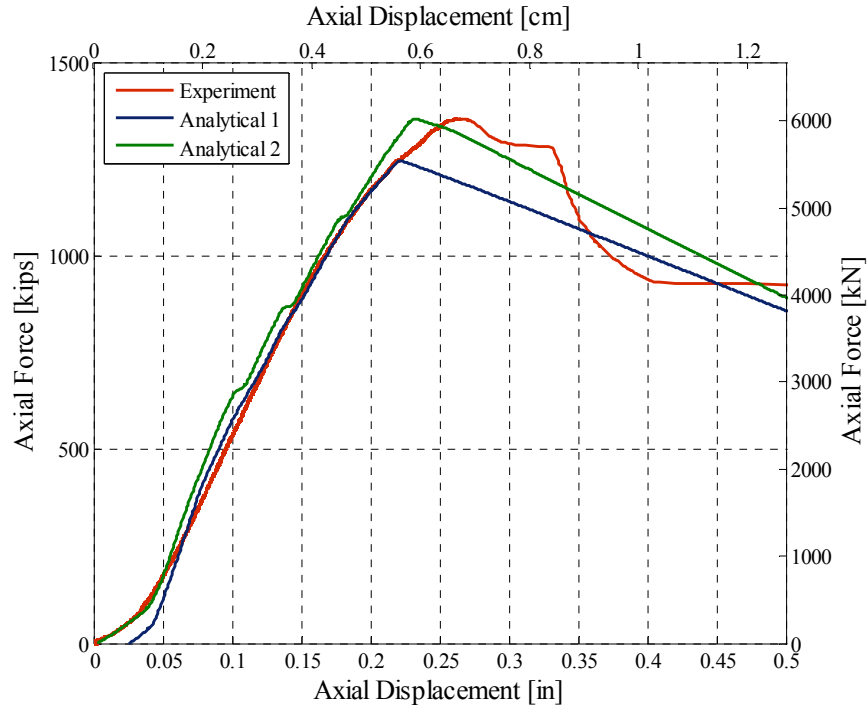


**Fig. 4.16 Axial force-displacement relationships: experimental vs. analytical relationships for the Base Column specimen with displacement ductility level of 3.0**

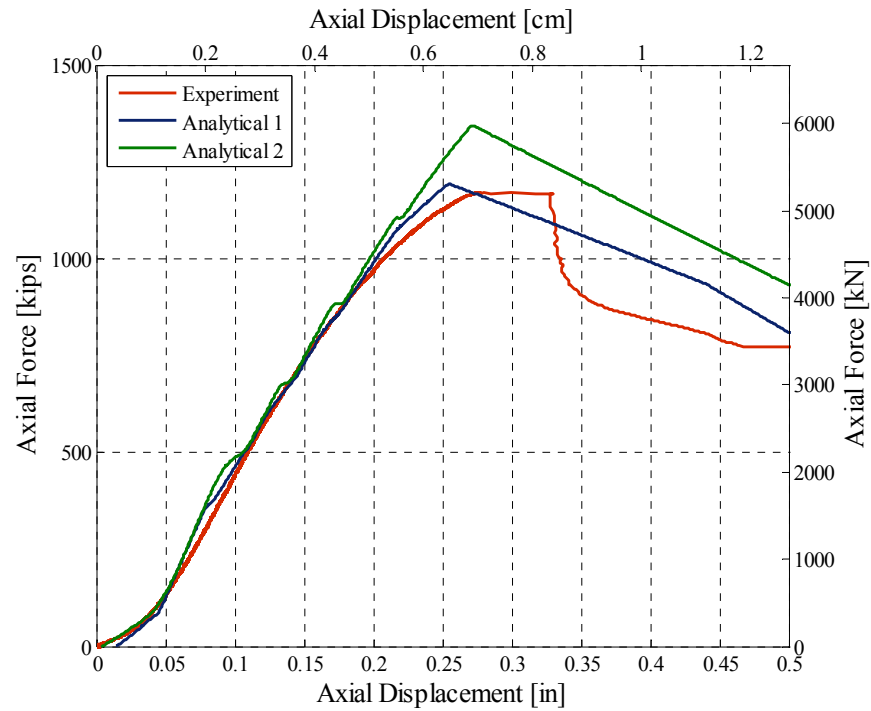


**Fig. 4.17 Axial force-displacement relationships: experimental vs. analytical relationships for the Base Column specimen with displacement ductility level of 4.5**

**Table 4.8 Residual axial strengths: experimental vs. analytical**

Test	Experiment	Analytical 1	Analytical 2	Error 1	Error 2
	[kips]	[kips]	[kips]	[%]	[%]
Base0	1459	1467	1462	0.55	0.20
Base15	1137	1133	1248	0.26	9.81
Base30	1355	1245	1354	8.12	0.07
Base45	1170	1192	1342	1.88	14.7

#### **4.4 VALIDATION OF ANALYTICAL MODEL BASED ON HYBRID SIMULATIONS AND AXIAL TESTS RESULTS**

For an earthquake and a truck load on the bridge, the analytical model developed based on lateral quasi-static tests (Analytical 1) was validated through hybrid simulation tests on a typical California overpass bridge (Chapter 3). The physical portion of the hybrid model, the bottom half of a bridge column, was axially crushed after the hybrid simulation test to get its remaining axial capacity. The axial crushing of an earthquake damaged bridge column was analytically simulated and the results are compared with the test results (Fig. 4.18 and Fig. 4.19). The residual axial strengths of the tested and analytically modeled specimens are given in Table 4.9. Since there is a good correspondence between experimental and analytical results, the analytical model of a bridge column is considered verified, and will be used to study traffic capacity of a bridge after an earthquake.

The axial compression test of the specimen that was part of the hybrid bridge model is analytically simulated in the following way. The specimen is modeled using Analytical 1 model. Displacement and rotation histories at the control node (node that connects physical and numerical portions of the hybrid model) during hybrid simulation are applied at the top of the analytically modeled specimen. Thus, the earthquake induced damage in the specimen is analytically simulated. Monotonically increasing axial load is applied next to induce the axial crushing of the analytically modeled specimen. The residual axial strength of a column with earthquake induced damage is thus analytically estimated.

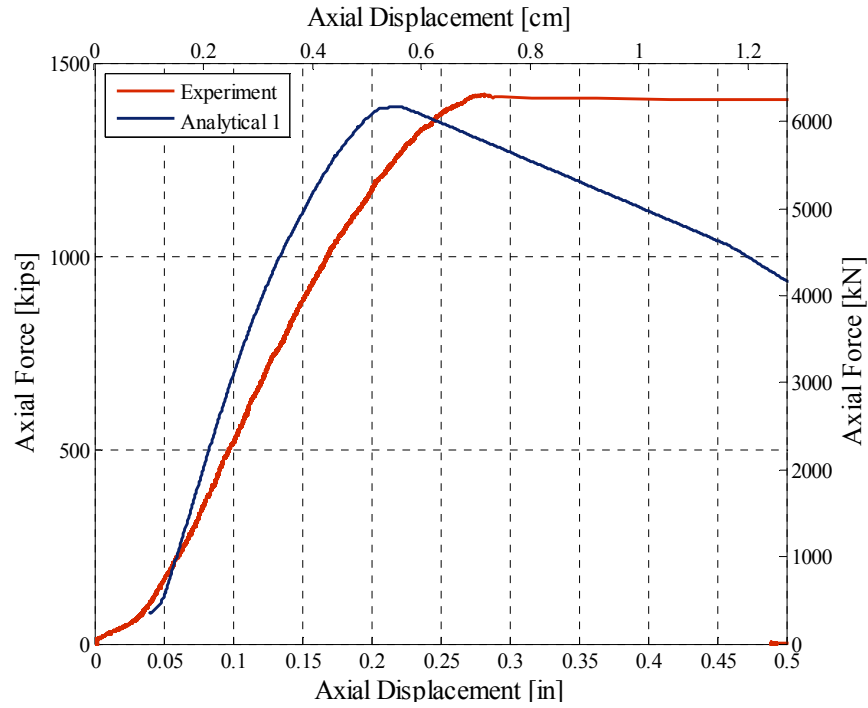


**Fig. 4.18 Axial force-displacement relationships: experimental vs. analytical relationship for the bridge column exposed to medium seismic intensity**

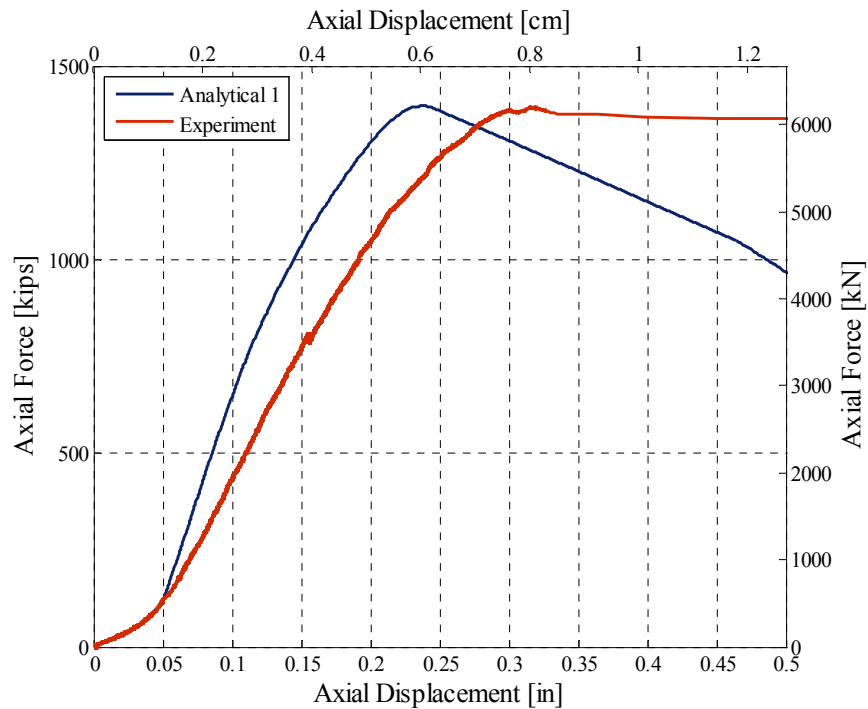


**Fig. 4.19 Axial force-displacement relationships: experimental vs. analytical relationship for the bridge column exposed to high seismic intensity**

**Table 4.9 Residual axial strengths: experimental vs. analytical**

Test	Experiment	Analytical 1	Error 1
	[kips]	[kips]	[%]
HSM	1419	1387	2.25
HSH	1395	1397	0.14

## **5 Post-earthquake Bridge Truck Load Capacity**

The post-earthquake traffic load capacity of a damaged bridge will be defined indirectly by computing the maximum weight of a single standard truck positioned at a critical location on the bridge. This simplification is done to avoid a large number of possible traffic load distribution combinations using an assumption that after an earthquake the traffic on damaged bridges will be strictly controlled and that a single truck may be the only traffic load on the bridge. The post-earthquake bridge truck load capacity will be evaluated using the calibrated analytical model of the typical California overpass bridge described in Chapter 3.

This chapter consists of two sections. The first section describes the bridge model and the loading regime that the bridge was exposed to in the process of evaluating the post-earthquake bridge truck load capacity. The second section discusses the parameters that influence the post-earthquake bridge truck load capacity and shows the trends of the post-earthquake bridge truck load capacity for the most influential parameters.

### **5.1 BRIDGE MODEL AND LOADING REGIME**

The bridge model and loading regime are described in three subsections. The first subsection gives the details related to bridge geometry and reinforcement. The second subsection describes analytical model of a bridge. The third subsection presents the loading sequences that the bridge was exposed to in the analytical simulations.

#### **5.1.1 Bridge Geometry and Reinforcement**

Configuration of the bridge used in analytical simulations corresponds to bridge Type 11 in Ketchum et al. (2004). It is a straight, cast-in-place box girder bridge with five spans and single-column-bents. Geometry and reinforcement of the bridge are given in Chapter 3 of this document.

#### **5.1.2 Analytical Modeling**

A three-dimensional nonlinear finite element bridge model was developed for the chosen bridge. It is a spine model of the bridge structure with line elements located at the centroid of the cross section following the alignment of the bridge (Fig. 5.1). Three-dimensional beam-column elements with corresponding cross-sectional properties were used to model the superstructure

and columns. The PEER Center finite element platform OpenSees (<http://opensees.berkeley.edu>) was utilized.

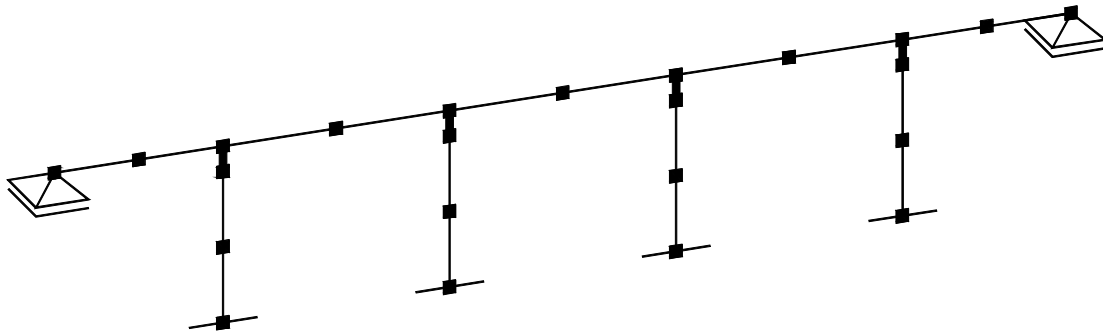


**Fig. 5.1 Analytical model of the bridge structure**

Modeling of the superstructure, columns, bridge mass, and bridge damping are described in Chapter 3 of this document with the following changes made for the purpose of this study: (i) the compressive strength of the unconfined concrete is 5 ksi (34,475 kPa) for all bridge elements, (ii) the yield strength of steel is 68 ksi (475,000 kPa) for all bridge elements (Caltrans, 2006a), (iii) it is specified that a column longitudinal bar fails at the tensile strain of 0.06 (conservative estimate for the column bar size based on Caltrans SDC Guidelines; Caltrans, 2006a), (iv) the torsional moment of inertia ( $J$ ) of the deck is not reduced (Caltrans, 2006a), (v) two roller abutment models are considered, one with and one without deck torsion restraint.

#### **5.1.2.1 Modeling of the Abutments**

Abutment modeling plays a significant role when determining the post-earthquake bridge truck load capacity. Two simple abutment models that generate upper and lower bound of the bridge response for the earthquake and truck load are considered in this study. The actual response of the bridge will lie between these two abutment models. The first abutment model, designated as  $R_x1$ , consists of a simple boundary condition module that applies single point constraints against displacement in vertical direction (vertical support) and rotation about the superstructure longitudinal axis (full deck torsion restraint). The second abutment model, designated as  $R_x0$ , applies single point constraint against displacement in vertical direction representing a roller boundary condition at the superstructure end. The designations “1” and “0” are drawn from the specifications of the boundary condition release codes in OpenSees.

In the case of  $R_x1$  abutment model, where the abutment is modeled to restrain torsion of the bridge deck, the post-earthquake bridge truck load capacity will be overestimated, especially if vehicle is occupying the outer (further from the bridge centerline) lanes of the bridge. Overestimation of the post-earthquake bridge truck load capacity happens as the deck torsion component of the truck load gets primarily taken by the torsionally stiff superstructure while the columns get small fractions of the load. This abutment model thus generates an upper bound estimate of the post-earthquake bridge truck load capacity.

In the case of abutment model  $R_x0$  superstructure does not provide significant rotational restraint at the top of the columns. Consequently, the bridge will resist the displacements in the



transverse direction of the bridge and rotation of the superstructure along its longitudinal axis only through cantilever action of its columns. This abutment model thus generates a lower bound estimate of the post-earthquake bridge truck load capacity.

### ***5.1.2.2 Integration Method***

Newmark's time-stepping integration method was used to solve numerically the system of differential equations governing the response of the bridge. The parameters of integration  $\beta$  and  $\gamma$  that define the variation of acceleration over a time step and determine stability and accuracy characteristics of the method are chosen to be  $\beta = 0.5$  and  $\gamma = 0.25$ . Such selection of parameters of integration ( $\beta$  and  $\gamma$ ) leads to a special case of Newmark's method known as average acceleration method. Average acceleration method assumes that the variation of acceleration over a time step is constant and equal to the average acceleration.

### **5.1.3 Loading**

During an analytical simulation with the purpose of estimating post-earthquake bridge truck load capacity, the bridge was exposed to four sequences of loading in the following order: (i) gravity load, (ii) earthquake load, (iii) simulation of residual displacements in the transverse direction of the bridge, and (iv) truck load. The analytical model of the bridge is not capable of capturing the residual displacements of the bridge. Hence, after an earthquake the residual displacements are simulated in the third loading sequence by applying lateral displacement to the bridge model. The truck load, located in the critical position on the bridge, is applied next by monotonic increase of the truck weight to induce the failure of the bridge. This way the post-earthquake bridge truck load capacity was established.

#### ***5.1.3.1 Earthquake Load***

In the process of analytical simulations the bridge was subjected to suites of recorded ground motions. A total of 8 bins, each containing 20 records, were utilized. All ground motions were obtained from the PEER Strong Motion Database (<http://peer.berkeley.edu/smcat>). Each ground motion record has two orthogonal horizontal components and a vertical acceleration component. A uniform scale factor of 2 was applied to all motions to guarantee the development of nonlinear action in the bridge columns. For the purpose of this study, the motions were applied uniformly at the base of the structure.

The bins of ground motions differ by the magnitude of the earthquake, the distance to the fault, the fault type, and presence of directivity effects. The characteristics of all ground motions, separately for each bin, are presented in Appendix D.

The first four bins, designated as LMSR (large magnitude, small distance), LMLR (large magnitude, large distance), SMSR (small magnitude, small distance), and SMLR (small magnitude, large distance) are identical to those used in previous bridge studies by Mackie and Stojadinovic (2005) and correspond to typical non-near-fault ( $R > 15$  km) California recordings. The delineation between small (SM) and large (LM) magnitude bins was at  $M_w = 6.5$ . Ground

motions with closest distance  $R$  ranging between 15 and 30 km were grouped into a small distance (SR) bin, while ground motions with  $R > 30$  km were in the large distance (LR) bin.

The fifth bin (VN) was obtained from the unscaled PEER Van Nuys Testbed motions (Krawinkler, 2005). The Van Nuys Testbed is located in the San Fernando Valley which has a variety of faults laying beneath it and the large San Andreas Fault passing some 50 kilometers to the northeast. Although the site is located near active faults none of the faults that dominate the seismic hazard at the site is oriented in such a way that the site will experience strong rupture directivity effects. Thus, all selected ground motions are from thrust earthquakes and free from strong directivity effects.

Three last bins of ground motions contain near-field ground motions with strong directivity effect. Two bins were created from the ground motions selected for the I-880 PEER Testbed study (Kunnath, 2006). This site is located near the Hayward fault: thus, the motions are anticipated to exhibit distinct directivity effects. The I-880p bin contains all the motions from the I-880 PEER Testbed project with the original fault parallel motions aligned with the bridge transverse direction. Similarly, the I-880n bin contains all the original fault normal motions aligned with the transverse bridge direction. The final, eighth, bin (Near) comprises ground motions from Luco's (Luco, 2001) nearby-field bin. These are high-magnitude earthquakes measured at a distance ( $R$ ) of less than 15 km.

#### ***5.1.3.2 Residual Post-Earthquake Displacements of the Bridge***

Although finite elements and materials calibrated based on results of the experiments conducted for the purpose of this study satisfactory match a broad range of bridge column response quantities (demonstrated in Chapter 4), the bridge model is unable to capture the residual (permanent) displacements of the bridge after an earthquake. The exact reason for such behavior of the bridge model was not established, however, it became clear that re-centering of the analytical model occurred during the ground motion record. Such behavior of the model may be due to the selected convergence test procedure, which attempts to minimize residual energy errors, or due to the elastic response of the undamaged elements of the bridge (such as the bridge deck or bridge deck supports) that tend to straighten the bridge, or due to the properties of the material models for concrete and reinforcement (Jeong et al., 2008).

The magnitude of the residual displacements, primarily due to the  $P-\Delta$  effects, can greatly affect the post-earthquake bridge truck load capacity. Thereafter, residual displacements of the bridge cannot be ignored while evaluating the post-earthquake bridge truck load capacity. Hence, they are manually applied on the bridge as a loading sequence immediately following the earthquake.

The residual displacements of the same magnitude and direction are applied at the top of all bridge columns. In general, the profile of residual displacements along the bridge can have different shapes depending on boundary conditions at the superstructure ends. In the case of the considered bridge, roller supports (free displacements in longitudinal and transverse direction of the bridge) are assumed at the superstructure ends. This implies synchronous motion of all columns during an earthquake and thus the same residual displacements of all columns after the earthquake.

For the purpose of this study, it is sufficient to apply residual displacements at the top of the columns in the transverse direction of the bridge. The first reason for this choice is the greater

horizontal stiffness of the bridge in the longitudinal then in transverse direction of the bridge. This creates potential for greater residual displacements in the transverse than in longitudinal direction of the bridge, especially in the case of near field earthquakes. The second reason for the choice of residual displacements is the nature of the traffic load. The traffic load is always eccentric with respect to the bridge deck centerline; thus, it induces torsion of the deck that, in turn, bends the bridge columns in the direction transverse to the bridge deck axis. The columns in the transverse direction act as cantilevers, thus, the traffic-load induced bending moment amplifies the displacements at the top of the columns in the transverse direction of the bridge. Increase in the transverse displacements leads to progression of the plastic hinges at the bottom of the columns and creates potential for bending failure of the columns. The third reason for the choice of residual displacements is the bridge frame configuration in its longitudinal direction that, under traffic loads, distributes the traffic load effects between the deck and the columns and significantly reduces the second-order effects of the traffic load, compared to the transverse direction. As the failure in the columns due to the traffic load happens much faster (smaller traffic capacity) if there are residual displacements in the transverse than in the longitudinal direction of the bridge it suffices to consider only the presence of residual displacements in the transverse direction of the bridge.

Following an earthquake, the top of the columns were displaced to produce the following drifts: 0.5%, 1%, 1.5%, 2%, 2.5% and 3%, one at a time in a separate analysis run. The bridge exposed to a far-field earthquake will most likely attain residual drift that is closer to the lower bound of the considered drift range, while the bridge exposed to a near-field earthquake with a strong directivity effect can reach residual drift that is closer to the upper bound of the considered drift range. Following the gravity load and an earthquake, the residual drift was applied to the bridge model up to the magnitude that does not exceed the maximum drift attained during the earthquake.

### 5.1.3.3 Truck Load

To simulate the truck load on the bridge standard HS20-44 truck (Section 3.7.6 of Caltrans Bridge Design Specifications: Caltrans, 2004) was used as a typical truck vehicle. It is a three-axle truck (Fig. 5.2) with a fixed spacing of 14 feet (4.3 m) between the first two axles and variable spacing of 14 to 30 feet (4.3 – 9.1 m) between the last two axles. The spacing between the two rear axles has to be chosen to produce the maximum stresses in the bridge.

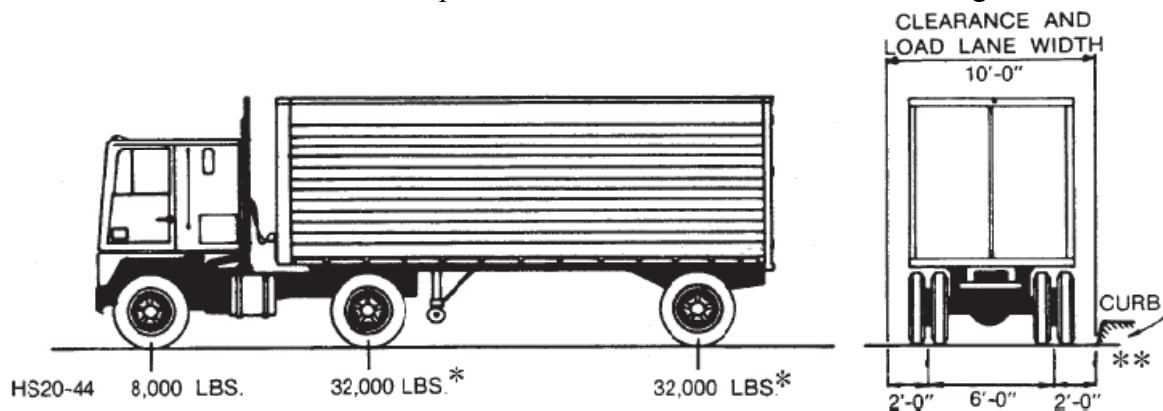


**Fig. 5.2 Standard HS20-44 truck (Caltrans, 2004)**

The truck load on the bridge is simulated by two sets of forces applied at superstructure elements: vertical and torsional. Vertical set of forces corresponds to the truck weight applied at its axle locations: three concentric forces with magnitudes that follow the ratio 1:4:4. Torsion moments correspond to axle loads placed eccentrically with respect to the bridge deck centerline occurring because of the truck positioned in conventional traffic lanes (Fig. 5.3).

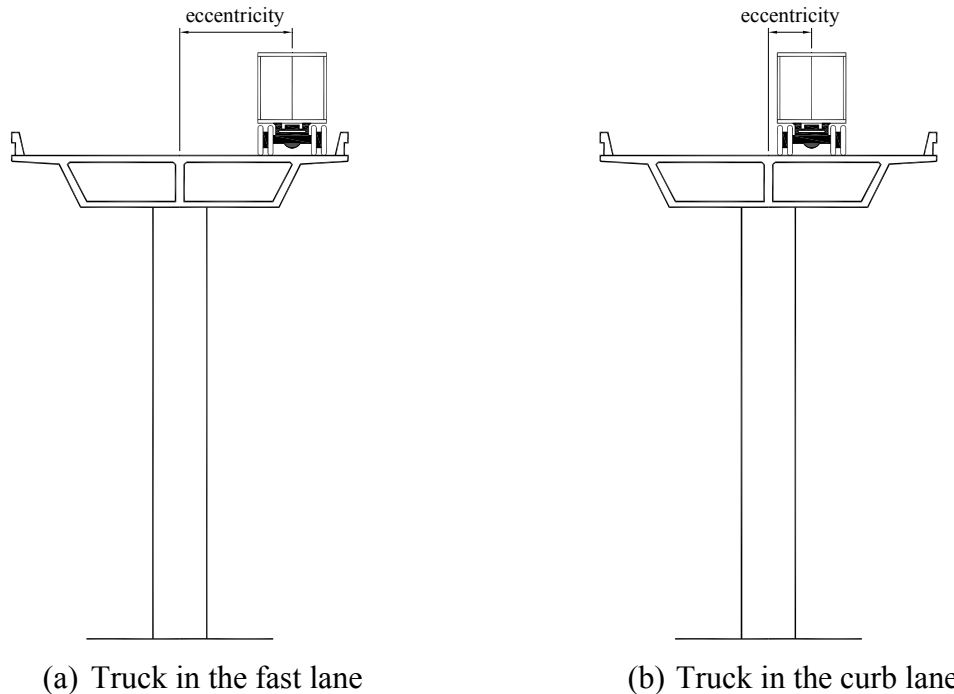
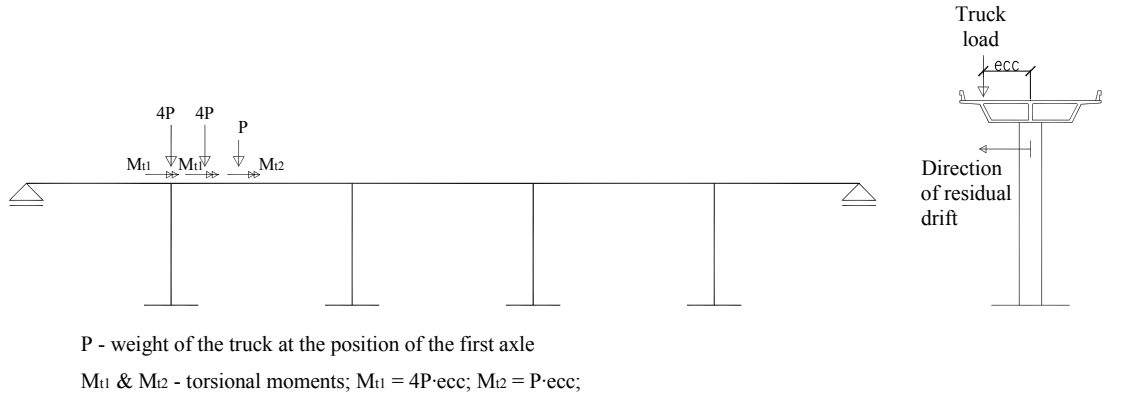


**Fig. 5.3 Two considered cases of the truck position relative to the superstructure centerline**

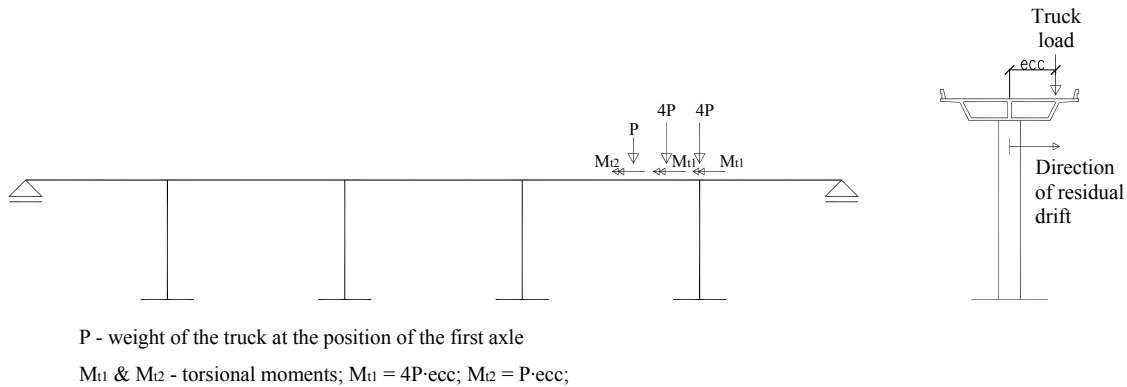
Modern bridges in California (designed following capacity design approach) damaged in an earthquake can experience either of the two possible failure modes when exposed to the traffic load: (i) the bending failure or (ii) the axial failure of the bridge columns. Influence lines for axial load and bending moments in the columns were examined to find the critical positions of the truck along the bridge superstructure. The damaged bridge was analyzed for the critical truck positions to find the position that will first induce the failure of a column. To cover the broad range of possible damage of the bridge after an earthquake the bridge was analyzed for each one of the selected strong ground motions, followed by application of two limiting values from the range of considered residual drifts (0.5% and 3.0%), one at the time, for two considered boundary conditions at the superstructure ends ( $R_x0$  and  $R_x1$ ). In the process of analyzing the bridge due to the truck load, the loads representing the truck load in the specific position on the bridge were increasing monotonically from zero until they induced the failure of a column. Two positions of the truck on the bridge relative to the superstructure centerline were considered. The first position was when the truck is using the fast lane, the lane closest to the superstructure centerline (Fig. 5.3(a)), and the second position was when the truck is using the curb lane, the lane furthest away from the superstructure centerline (Fig. 5.3(b)). So, each ground motion analysis was repeated eight times to cover range of truck load positions, abutment restraint

conditions and residual drift. Based on these analyses, the critical failure mode and the most critical truck position were identified.

The critical failure mode of the bridge is the bending failure of the end column when the truck is positioned to induce the biggest bending moment in the column. Depending on the sign of the residual drifts after an earthquake (positive or negative) two positions of the truck along the bridge (that correspond to the failure mode) are adopted for further analyses of the post-earthquake bridge truck load capacity. Position 1 (Fig. 5.4(a)) of the truck corresponds to the positive direction of the residual drift and Position 2 (Fig. 5.4(b)) corresponds to the negative direction of the residual drift.



(a) Truck Position 1 and corresponding truck forces



(b) Truck Position 2 and corresponding truck forces

**Fig. 5.4 Critical positions of the truck on the bridge**

## 5.2 PARAMETRIC STUDY

There are many parameters that have an influence on the post-earthquake bridge truck load capacity. Parametric study of the post-earthquake bridge truck load capacity is thus necessary and will be described in three subsections that follow. The first subsection identifies parameters that have a great influence on the post-earthquake bridge truck load capacity. The second subsection gives the matrix of all analyzed cases for one ground motion based on parameters

chosen to be studied. The third subsection presents and comments on results of the parametric study.

### 5.2.1 Choice of Parameters

To identify the parameters that have great influence on the post-earthquake bridge truck load capacity, the pool of potentially influential parameters was established. The parameters were divided into four groups: (i) ground motion intensity measures; (ii) engineering demand parameters; (iii) modeling parameters; and (iv) truck load related parameters.

Three parameters representing ground motion intensity measures were considered: (i) pseudo-spectral acceleration (component that corresponds to the transverse bridge direction), (ii) Arias intensity and (iii) RMS (root-mean-square) acceleration. Relation between the post-earthquake bridge truck load capacity and the three ground motion intensity measures are shown in Fig. 5.5 for a residual drift of 1.0%: truck load capacity data distributions at other residual drift levels are similar. In all cases, the post-earthquake bridge truck load capacity did not strongly depend on the intensity of the applied ground motions.

Two engineering demand parameters were considered: maximum earthquake drift in the transverse direction of the bridge and residual drift after an earthquake in the transverse direction of the bridge. The influence of the two parameters on the post-earthquake bridge truck load capacity was considered under condition that none of the columns fails during an earthquake. While the post-earthquake bridge truck load capacity is correlated to the maximum earthquake drift it is not very sensitive to this engineering demand parameter (Fig. 5.6). On the other hand, the post-earthquake bridge truck load capacity is strongly correlated and very sensitive to the residual drift engineering demand parameter (Fig. 5.7).

The reasons for low sensitivity of the post-earthquake bridge truck load capacity to the maximum earthquake drift will be indicated hereafter. It is important to note that the maximum drift attained during the great majority of the analyzed earthquakes is less than 4% (Fig. 5.6). Thus, maximum damage in the columns is extensive spalling of concrete in the plastic hinge regions. With the increase of maximum earthquake drift, the amount of spalled concrete in the plastic hinge regions increases. However, the cover concrete fibers do not contribute significantly to the bending strength of the column section: therefore, spalling will not have a noticeable influence on the post-earthquake bridge truck load capacity of the bridge (defined by bending failure of the columns). Since the longitudinal reinforcing bars contribute significantly to the bending strength of the column section, their influence on the post-earthquake bridge truck load capacity has to be explored as well. During an earthquake reinforcing bars can experience high strains depending on the maximum earthquake drift. However, after an earthquake they have residual strains and stresses that are small fractions of their ultimate values. Thus, the post-earthquake conditions of strains and stresses in the fibers representing reinforcing bars do not vary significantly with the change of earthquake and consequently do not depend strongly on the maximum earthquake drift.

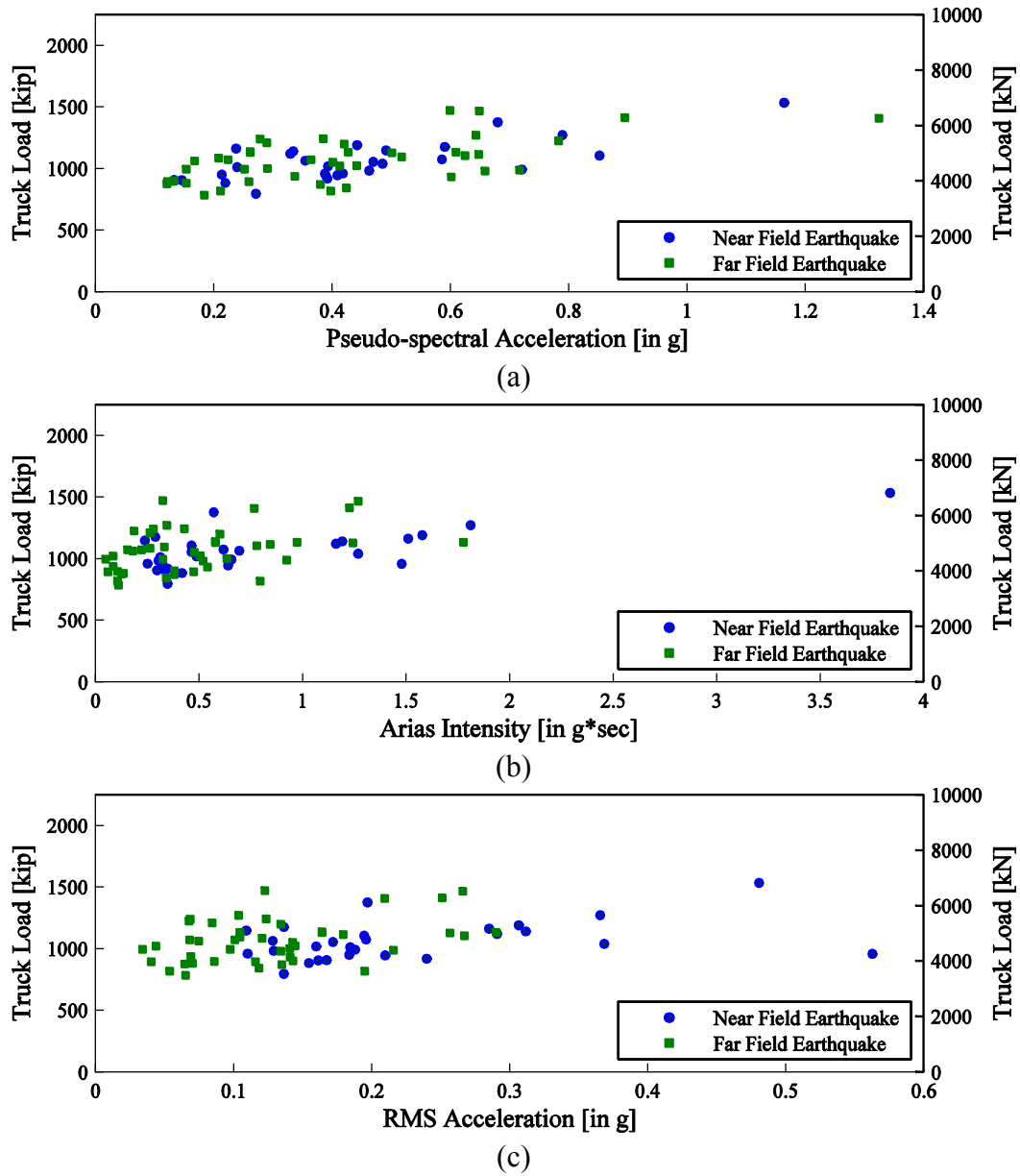


**Fig. 5.5 Relation between post-earthquake bridge truck load capacity and intensity measures, (a) Pseudo-spectral acceleration, (b) Arias intensity, and (c) RMS acceleration (Rx0 abutment, residual drift of 1.0%, truck is in the curb lane)**

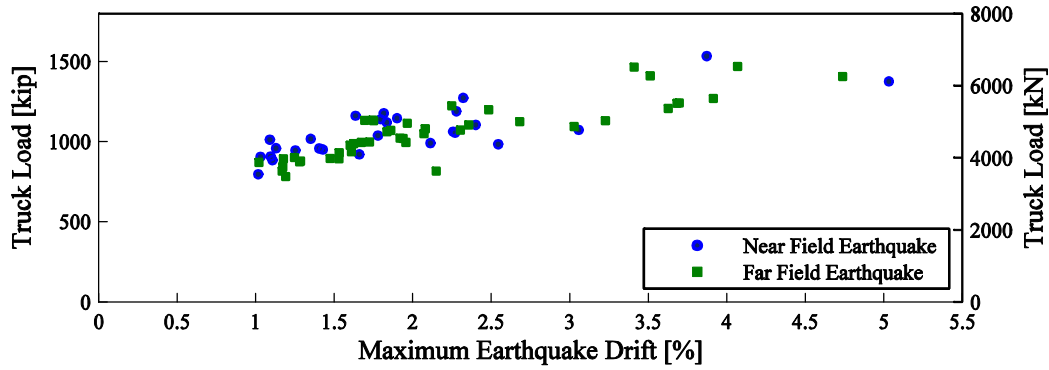


**Fig. 5.6 Relation between maximum earthquake drift and post-earthquake bridge truck load capacity (Rx0 abutment, residual drift of 1.0%, the truck is in the curb lane)**

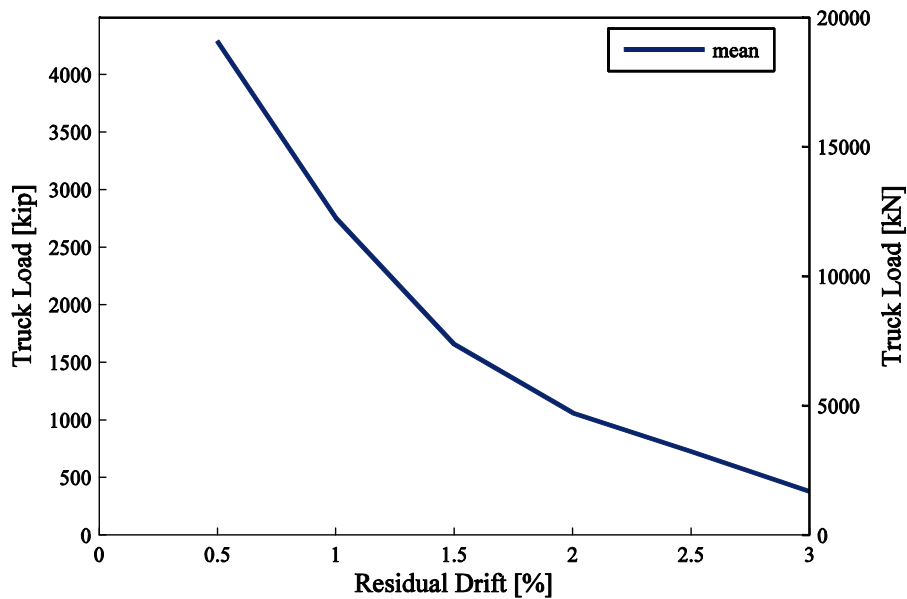


**Fig. 5.7 Relation between residual drift and post-earthquake bridge truck load capacity (Rx0 abutment, the truck is in the fast lane)**

Parameters that might influence the post-earthquake bridge truck load capacity and are related to the bridge modeling are: (i) modeling of the abutment, (ii) modeling of the superstructure torsional stiffness, and (iii) material modeling of steel and concrete fibers of the bridge columns. The effect of abutment model on the post-earthquake truck capacity of a bridge is described in Section 5.1.2.3. The effect of the superstructure torsional stiffness is explained hereafter. As there is a torsional component of the truck load acting on the superstructure (due to eccentric position of the vehicles on the bridge), careful modeling of the superstructure torsional stiffness is necessary as it can greatly affect the post-earthquake bridge truck load capacity. Reduction of torsional stiffness leads to reduction of the post-earthquake bridge truck load capacity (Fig. 5.8). In the case of bridge superstructures that meet the Ordinary Bridge requirements in section 1.1 of Caltrans SDC (Caltrans, 2006a) and do not have a high degree of in-plane curvature, Caltrans does not recommend any reduction of the bridge deck torsional



stiffness. Different bridge superstructures that can develop cracks during an earthquake experience reduction of torsional stiffness which has to be carefully accounted for.

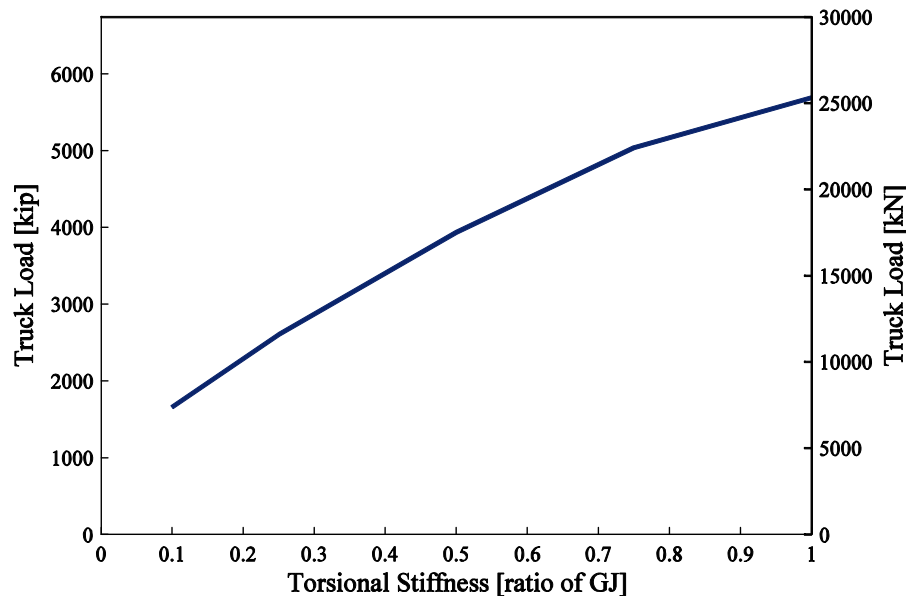


**Fig. 5.8 Relation between torsional stiffness of the superstructure and post-earthquake bridge truck load capacity (Rx1 abutment, residual drift of 1.0%, truck is in the curb lane, earthquake *vvnuy* from Van Nuys earthquake bin)**

The effect of the material modeling of steel and concrete fibers of the bridge columns is discussed next. As post-earthquake truck capacity on the bridge is limited by the bending failure of a bridge column, it is necessary to carefully define the ultimate strains of fibers that represent either reinforcing bars or concrete. Influence of ultimate strain of the reinforcing bars on the post-earthquake bridge truck load capacity is presented in Fig. 5.9. Decrease in ultimate strain of the reinforcing bars leads to significant reduction in post-earthquake bridge truck load capacity. For the purpose of this study, the ultimate strain of reinforcing bars is set at 6%, based on conservative recommendations from Caltrans SDC (Caltrans, 2006a) for the column bar size. Constitutive relationship of concrete along with definition of the ultimate strain is detailed in Chapter 4.

Position of the truck load relative to the superstructure centerline greatly influences the post-earthquake bridge truck load capacity. As eccentricity of the truck load relative to the superstructure centerline increases the post-earthquake bridge truck load capacity decreases (Fig. 5.10). For the purpose of this study, two limiting cases are considered: (i) the truck is in the fast lane (the smallest eccentricity) and (ii) the truck is in the curb lane (the biggest eccentricity).

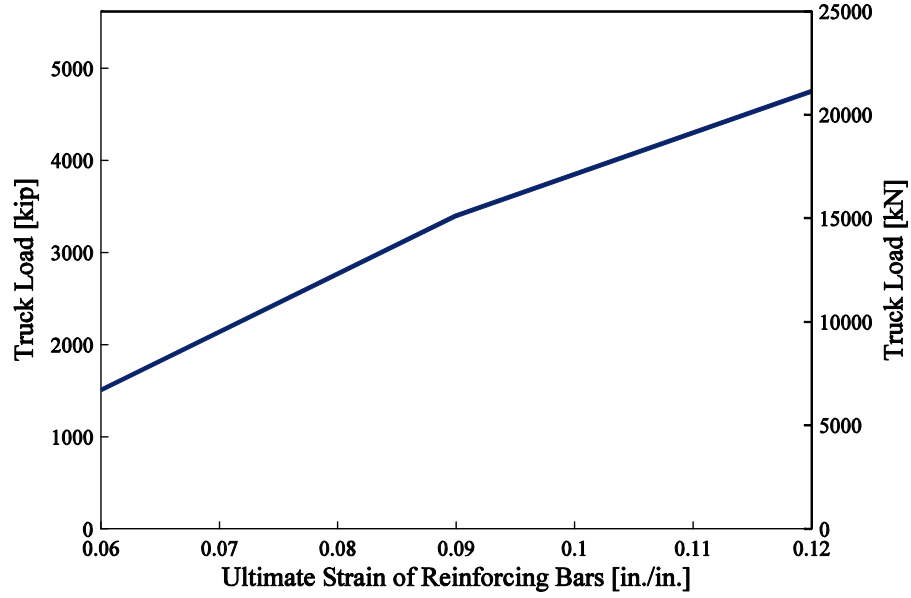


**Fig. 5.9** Relation between ultimate strain of reinforcing bars and post-earthquake bridge truck load capacity (Rx1 abutment, residual drift of 2.5%, truck is in the curb lane, earthquake *vvnuy* from Van Nuys earthquake bin)

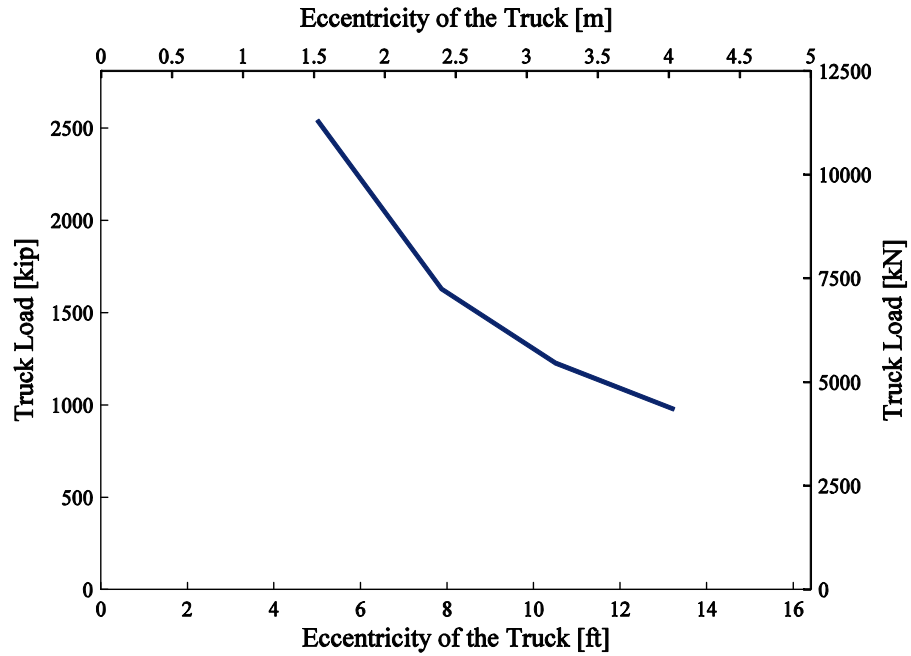


**Fig. 5.10** Relation between eccentricity of the truck relative to the superstructure centerline and post-earthquake bridge truck load capacity (Rx0 abutment, residual drift of 1.0%, earthquake *vvnuy* from Van Nuys earthquake bin)

### 5.2.2 Matrix of Analyzed Cases

The parametric analyses (Section 5.2.1) showed that parameters that have a significant influence on the post-earthquake truck load capacity of the considered bridge are: abutment type, residual drift of the bridge after an earthquake, position of the truck on the bridge relative to the superstructure centerline, and ultimate strain in column reinforcing bars. For the purpose of this study, the ultimate strain of reinforcing bars is set at 6%, based on conservative recommendations from Caltrans SDC (Caltrans, 2006a) for the prototype column bar size. To examine how post-earthquake truck capacity of the bridge depends on abutment type ( $R_x1$  and  $R_x0$ ), position of the truck relative to the superstructure centerline, and residual drift of the bridge after an earthquake, 24 analyses were performed for each ground motion (Table 5.1). The results of the analyses are presented and commented in Section 5.2.3.

**Table 5.1 Matrix of analyzed cases for one ground motion**

Abutment type	Truck position	Residual drift [%]
$R_{x0}$	Fast lane	0.5
		1.0
		1.5
		2.0
		2.5
		3.0
	Curb lane	0.5
		1.0
		1.5
		2.0
		2.5
		3.0
$R_{x1}$	Fast lane	0.5
		1.0
		1.5
		2.0
		2.5
		3.0
	Curb lane	0.5
		1.0
		1.5
		2.0
		2.5
		3.0

### 5.2.3 Post-earthquake Bridge Truck Load Capacity

Influence of the abutment type, the truck position on the bridge relative to the superstructure centerline, and residual drift on the post-earthquake bridge truck load capacity will be presented in this section. Since the results (that will be presented hereafter) relate to a specific bridge analyzed in this study, their main purpose is to show the trends and emphasize the parameters that have significant influence on the post-earthquake bridge truck load capacity. All results are

divided into two groups based on damage that an earthquake causes to the bridge. Analytical results of the post-earthquake bridge truck load capacity for earthquakes that did not cause the failure of bridge columns belong to the first group of results and are shown in Subsection 5.2.3.1. For earthquakes that cause the failure of any of the bridge columns the analytical results belong to the second group and are presented in Subsection 5.2.3.2. For the considered bridge columns (modeled as explained in Chapter 3) and the adopted 6% reinforcement strain limit, failure of the bridge columns is directly related to the failure of reinforcing bars; practically no concrete core failures were observed before reinforcement failures occurred in the model.

### 5.2.3.1 Case 1: No bridge columns failures during an earthquake

In the case of earthquakes that do not cause the failure of the bridge columns, post-earthquake bridge truck load capacity is not sensitive to the intensity of the ground motion (Fig. 5.5) or to the maximum earthquake drift (Fig. 5.6). Therefore, the post-earthquake bridge truck load capacity is presented as a function of the residual drift with respect to the abutment type ( $R_x1$  and  $R_x0$ ) and the position of the truck load relative to the superstructure centerline (Fig. 5.11 to Fig. 5.14). Mean values of the post-earthquake bridge truck load capacity, along with the one and three standard deviation bands, are plotted for different values of residual drifts. To generate this data the post-earthquake bridge truck load capacity was computed only for residual drifts that are smaller than the maximum drifts attained during a particular earthquake. Weight of the standard HS20-44 truck is additionally indicated on the plots for comparison purposes.

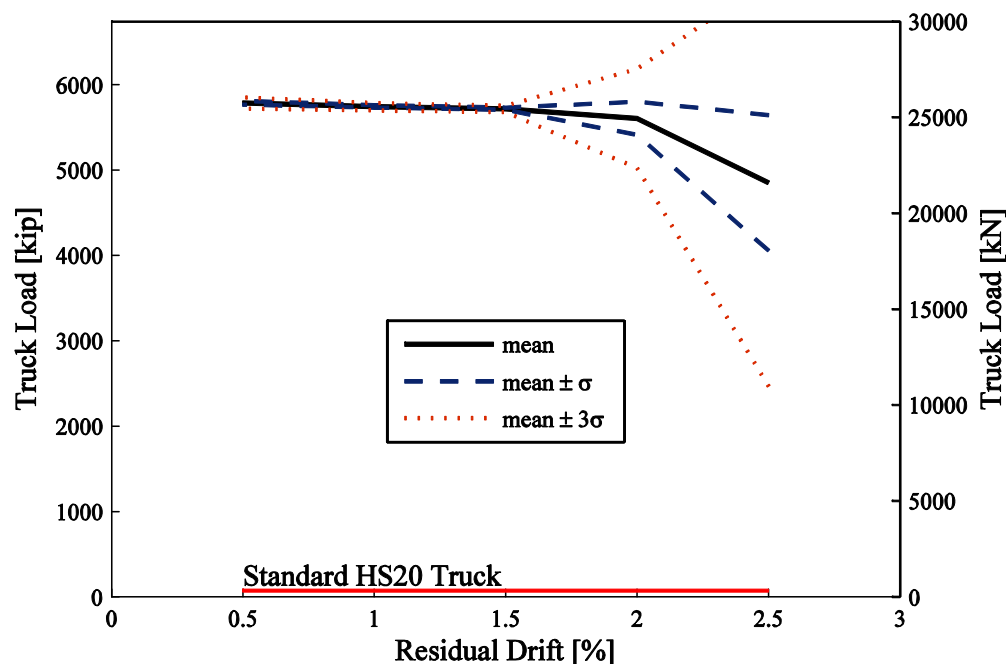


**Fig. 5.11 Degradation of the post-earthquake bridge truck load capacity with increase in residual drift for the case of  $R_x1$  abutments when the truck load is in the fast lane**

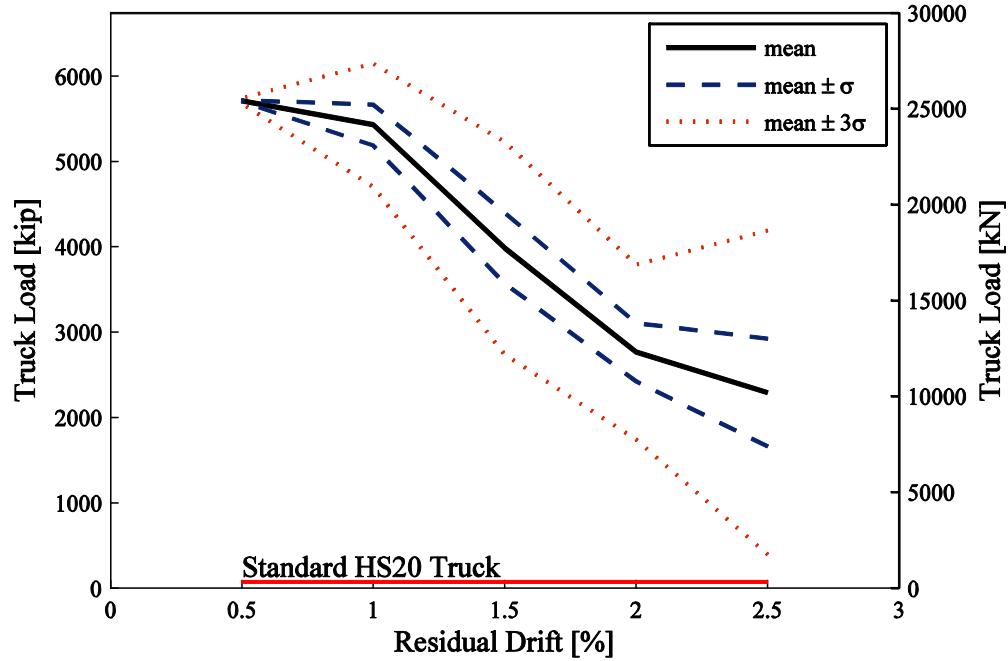


**Fig. 5.12** Degradation of the post-earthquake bridge truck load capacity with increase in residual drift for the case of Rx1 abutments when the truck load is in the curb lane

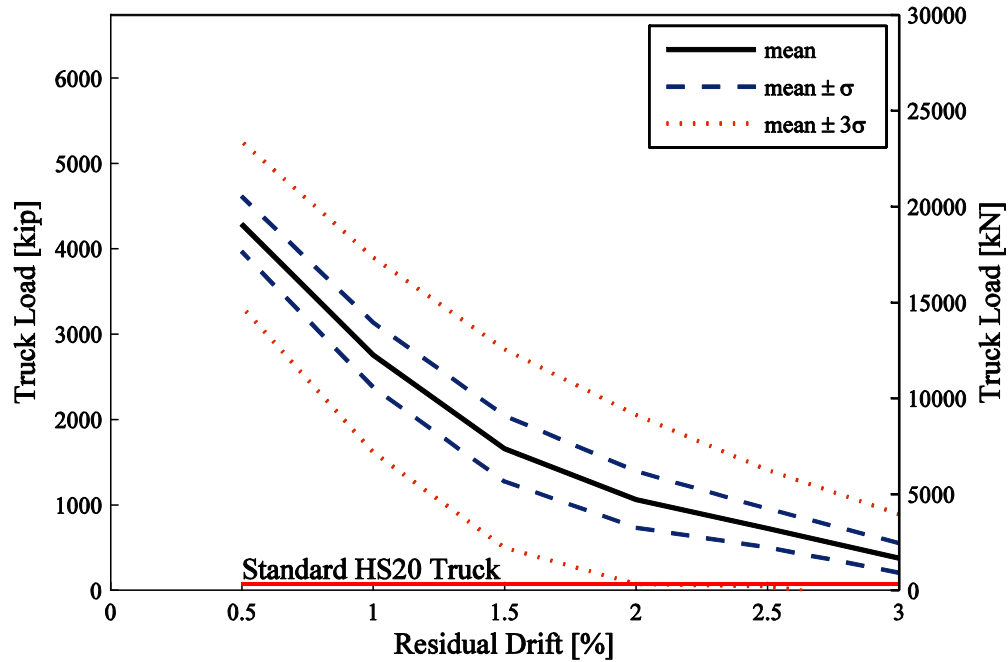


**Fig. 5.13** Degradation of the post-earthquake bridge truck load capacity with increase in residual drift for the case of Rx0 abutments when the truck load is in the fast lane

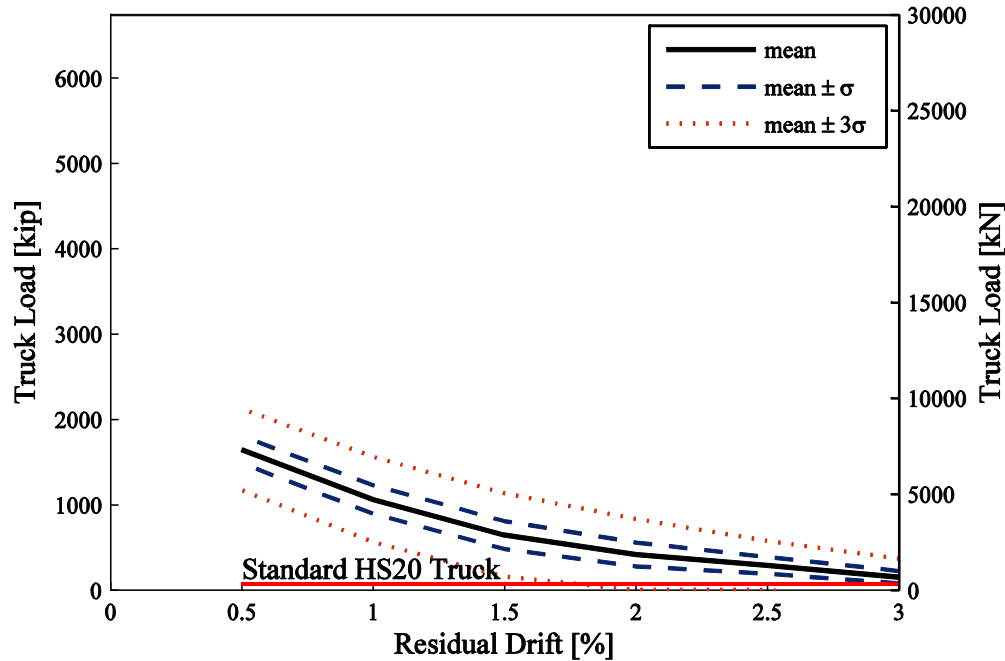


**Fig. 5.14 Degradation of the post-earthquake bridge truck load capacity with increase in residual drift for the case of Rx0 abutments when the truck load is in the curb lane**

Post-earthquake bridge truck load capacity as a function of residual drift degrades faster in the case of the bridge with no torsional restraints at the superstructure ends ( $R_x0$  abutments) than in the case of the bridge with torsional restraints at the superstructure ends ( $R_x1$  abutments). There is an additional reduction of the post-earthquake bridge truck load capacity if the truck is located in the curb lane (maximum eccentricity of the truck load) compared to the case when the truck is located in the fast lane (minimum eccentricity of the truck load).

In the case of the considered bridge that has torsional restraints at the superstructure ends ( $R_x1$  abutments) and damaged but not failed columns, a truck equivalent to the standard HS20 truck can safely use the bridge after an earthquake regardless of the truck position on the bridge. In the case of the bridge with no torsional restraints at the superstructure ends ( $R_x0$  abutments) special consideration is necessary if residual drifts are bigger than 1.5%. In this case, traffic speed and truck weight should be restricted such that the total vertical force exerted by the truck does not exceed the weight of the standard HS20 truck. However, none of the two considered abutment types is realistic: they generate lower and upper bounds for the post-earthquake bridge truck load capacity.

#### **5.2.3.1 Case 2: At least one column has failed during an earthquake**

For earthquakes that cause the failure of at least one bridge column, the truck load capacities versus maximum earthquake drifts are plotted separately for each combination of the three considered parameters (Fig. 5.15 to Fig. 5.20). Each plot group shown in these figures differs by the amount of applied residual drift. Post-earthquake bridge truck load capacity for an earthquake

that causes failure of a column and for a residual drift does not exceed the maximum earthquake drift is plotted as one point on the graph.

First observation based on Fig. 5.15 to Fig. 5.20 is that more earthquakes cause column failures in the bridge with  $R_x1$  abutments (superstructure ends are torsionally restrained) compared to the bridge with  $R_x0$  abutments (superstructure ends do not have torsional restraints). This is because the deformation demand for the bridge with  $R_x1$  abutments is more likely to exceed its deformation capacity compared to the bridge with  $R_x0$  abutments. The bridge with  $R_x1$  abutments has shorter period in the transverse direction of the bridge ( $T_1(R_x1) = 1.36$  sec) than the bridge with  $R_x0$  abutments ( $T_1(R_x0) = 1.70$  sec) due to the higher stiffness of that bridge system as a result of torsional restraints at the superstructure ends. It also has larger overall strength and 2.35 times smaller total displacement capacity in the transverse direction of the bridge than the bridge with the  $R_x0$  abutments (Fig. 5.21). As both bridges are in the displacement preserved range, based on analogy with an equivalent elastic SDOF system, an earthquake will induce (approximately  $T_1(R_x0)/T_1(R_x1) = 0.8$  times) smaller displacement demand on the bridge with the  $R_x1$  abutments than for the bridge with the  $R_x0$  abutments. Since displacement capacity of the bridge with  $R_x1$  abutments is much smaller than for the bridge with  $R_x0$  abutments, the bridge with  $R_x1$  abutments is likely to experience column failure prior to the bridge with  $R_x0$  abutments even though it is stronger.

Results presented in Fig. 5.15 to Fig. 5.20 suggest that the bridge is not safe for traffic after an earthquake if the abutments are not able to provide torsional restraints at the superstructure ends and if there is at least one failed column. In this case it is recommended to close the bridge no matter what is the maximum earthquake drift or residual drift. If after an earthquake abutments still provide torsional restraints at superstructure ends, the bridge may be used for emergency traffic immediately after the earthquake depending on the damage level of the columns. However, to accurately relate post-earthquake bridge truck load capacity to the damage level of bridge columns and degree of torsional restraints at the superstructure ends additional study is needed. Until then it is recommended to close the bridge if there is an indication of column failure.

In this study, column failure was determined on the basis of strains in column longitudinal reinforcement and column concrete core. Since the limit on longitudinal reinforcement strain was set conservatively at 6%, following Caltrans SDC recommendations (Caltrans, 2006a), failure of concrete core was rarely observed and column failure was governed by failure of longitudinal reinforcement bars. In practice, based on experimental observations, failure of longitudinal bars is often preceded by fracture of transverse spiral reinforcement. Therefore, assessment of column failure after an earthquake should be based on detection of fractures in both transverse spiral reinforcement and longitudinal column reinforcement.



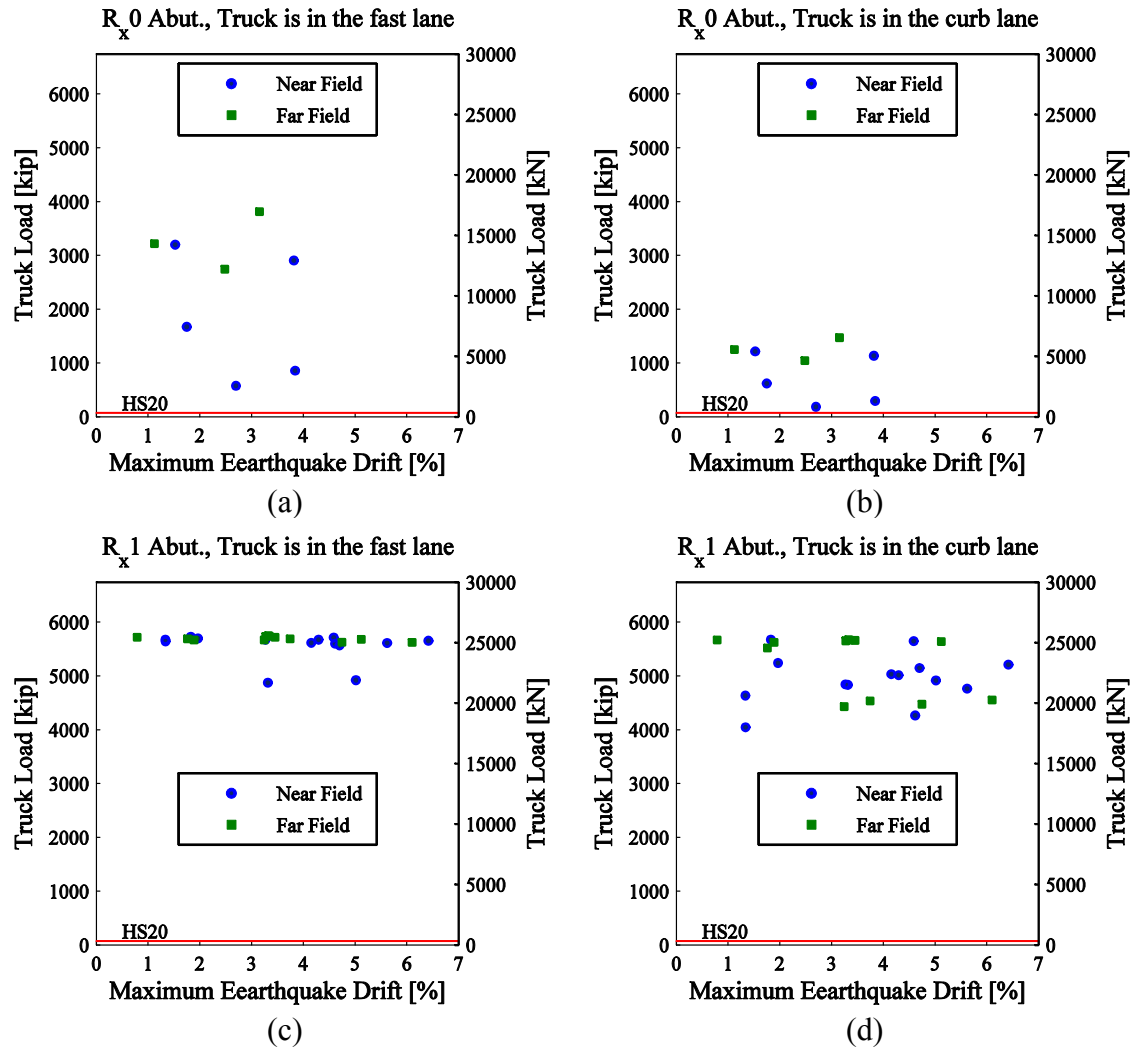


**Fig. 5.15 Post-earthquake bridge truck load capacity vs. maximum earthquake drift for the residual drift of 0.5% and the following cases: (a) Rx0 abutment, the truck is in the fast lane; (b) Rx0 abutment, the truck is in the curb lane; (c) Rx1 abutment, the truck is in the fast lane; (d) Rx1 abutment, the truck is in the curb**

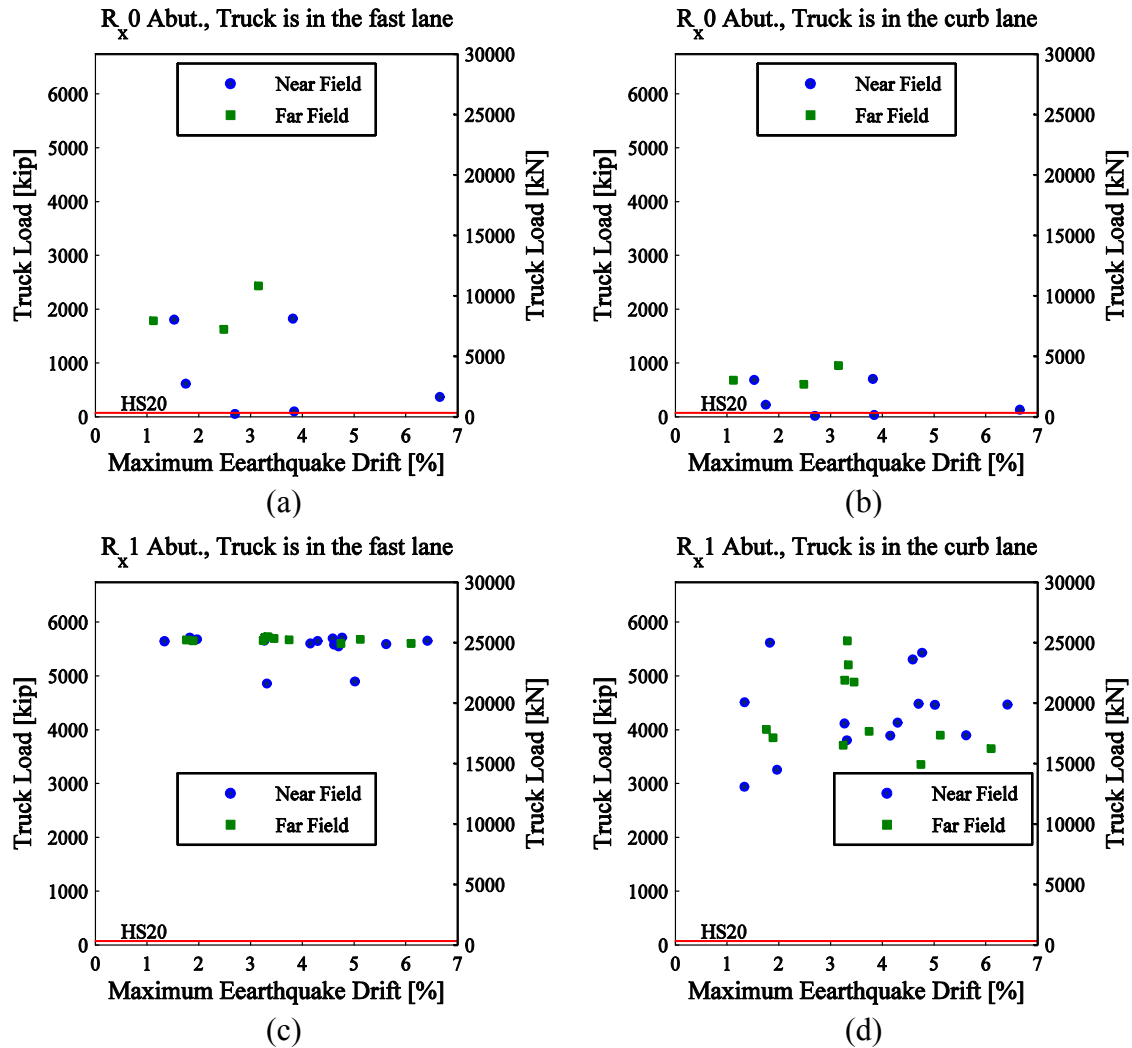


**Fig. 5.16 Post-earthquake bridge truck load capacity vs. maximum earthquake drift for the residual drift of 1.0% and the following cases: (a) Rx0 abutment, the truck is in the fast lane; (b) Rx0 abutment, the truck is in the curb lane; (c) Rx1 abutment, the truck is in the fast lane; (d) Rx1 abutment, the truck is in the curb**

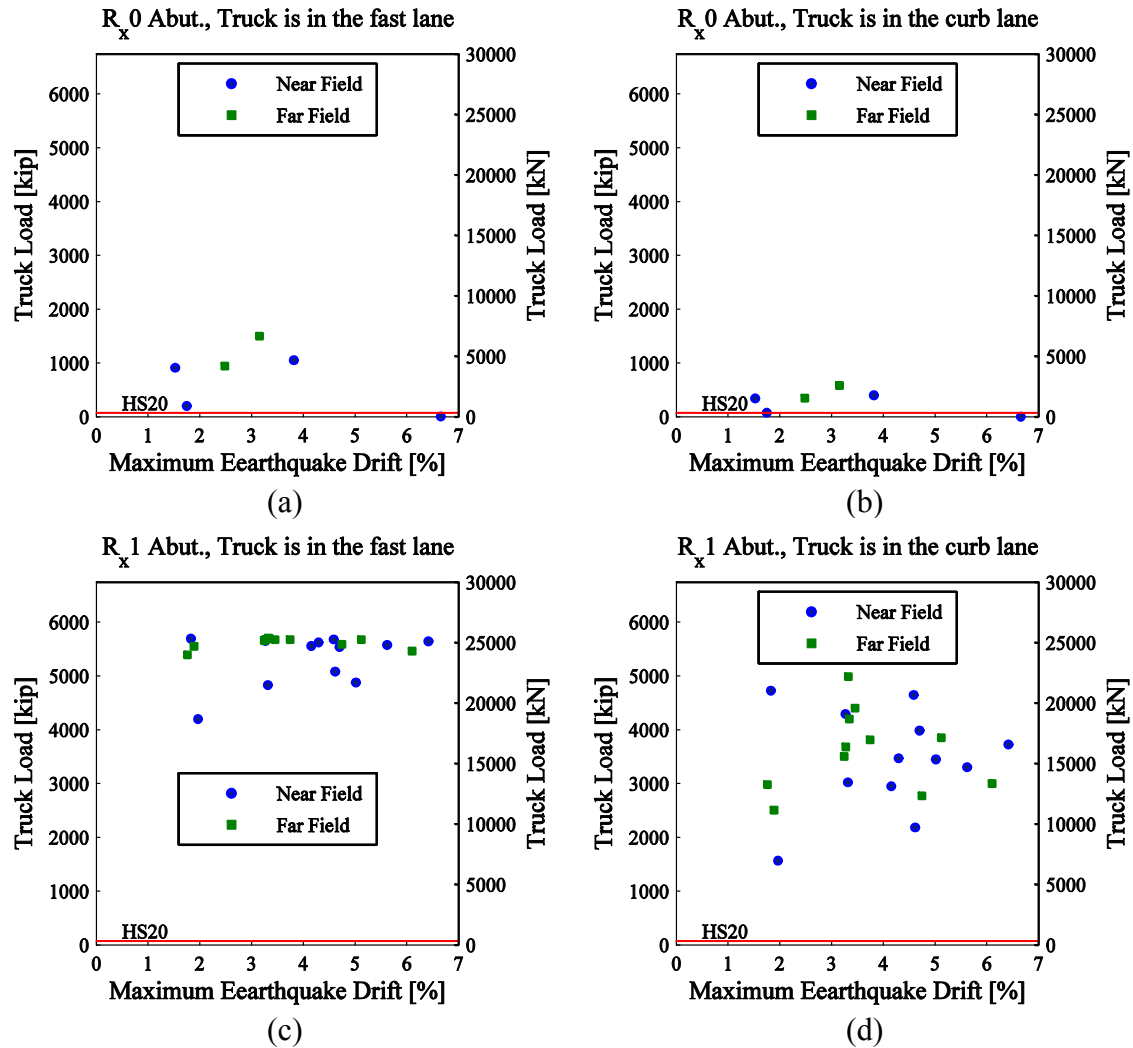


**Fig. 5.17 Post-earthquake bridge truck load capacity vs. maximum earthquake drift for the residual drift of 1.5% and the following cases: (a) Rx0 abutment, the truck is in the fast lane; (b) Rx0 abutment, the truck is in the curb lane; (c) Rx1 abutment, the truck is in the fast lane; (d) Rx1 abutment, the truck is in the curb**

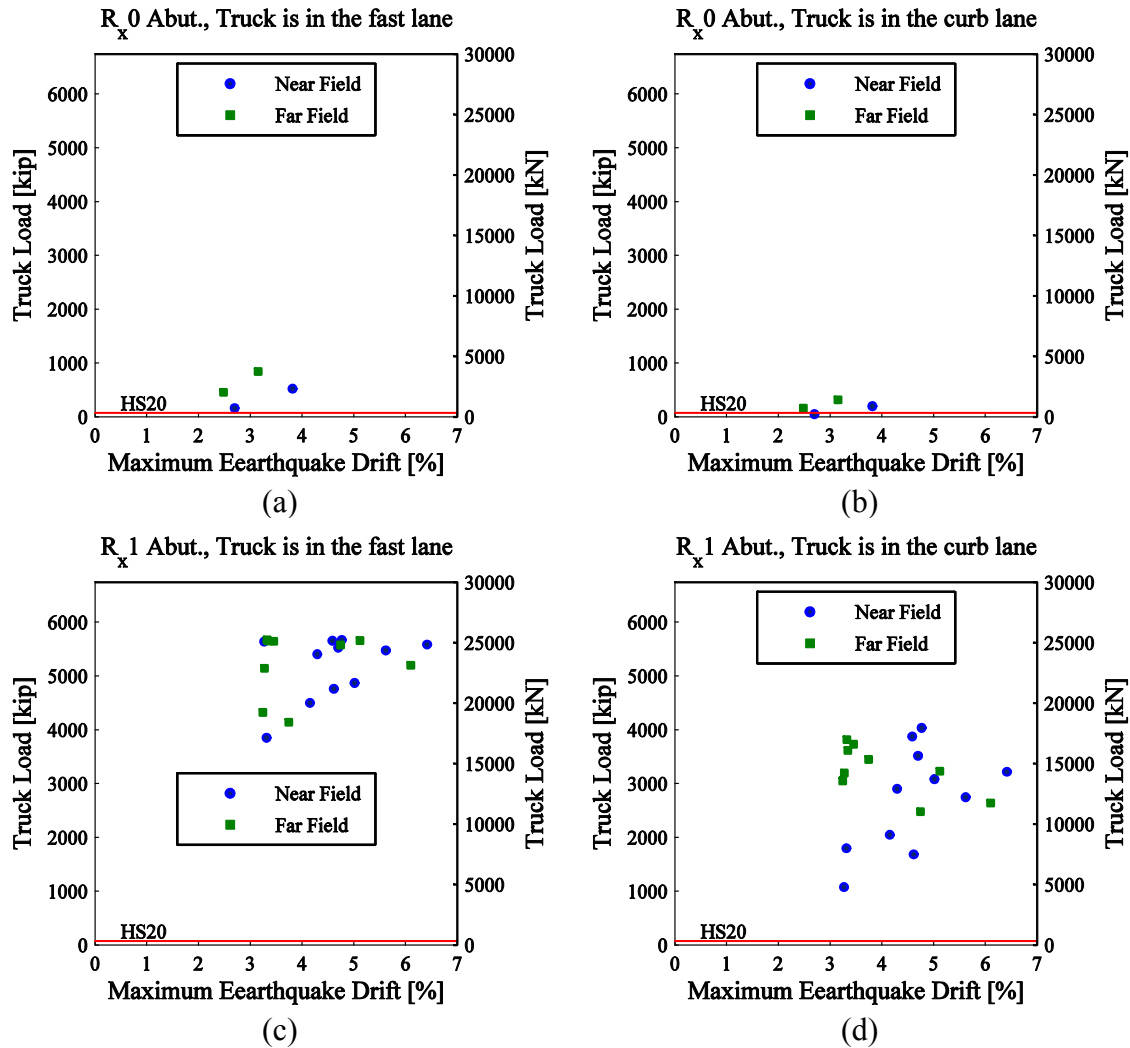


**Fig. 5.18 Post-earthquake bridge truck load capacity vs. maximum earthquake drift for the residual drift of 2.0% and the following cases: (a) Rx0 abutment, the truck is in the fast lane; (b) Rx0 abutment, the truck is in the curb lane; (c) Rx1 abutment, the truck is in the fast lane; (d) Rx1 abutment, the truck is in the curb**

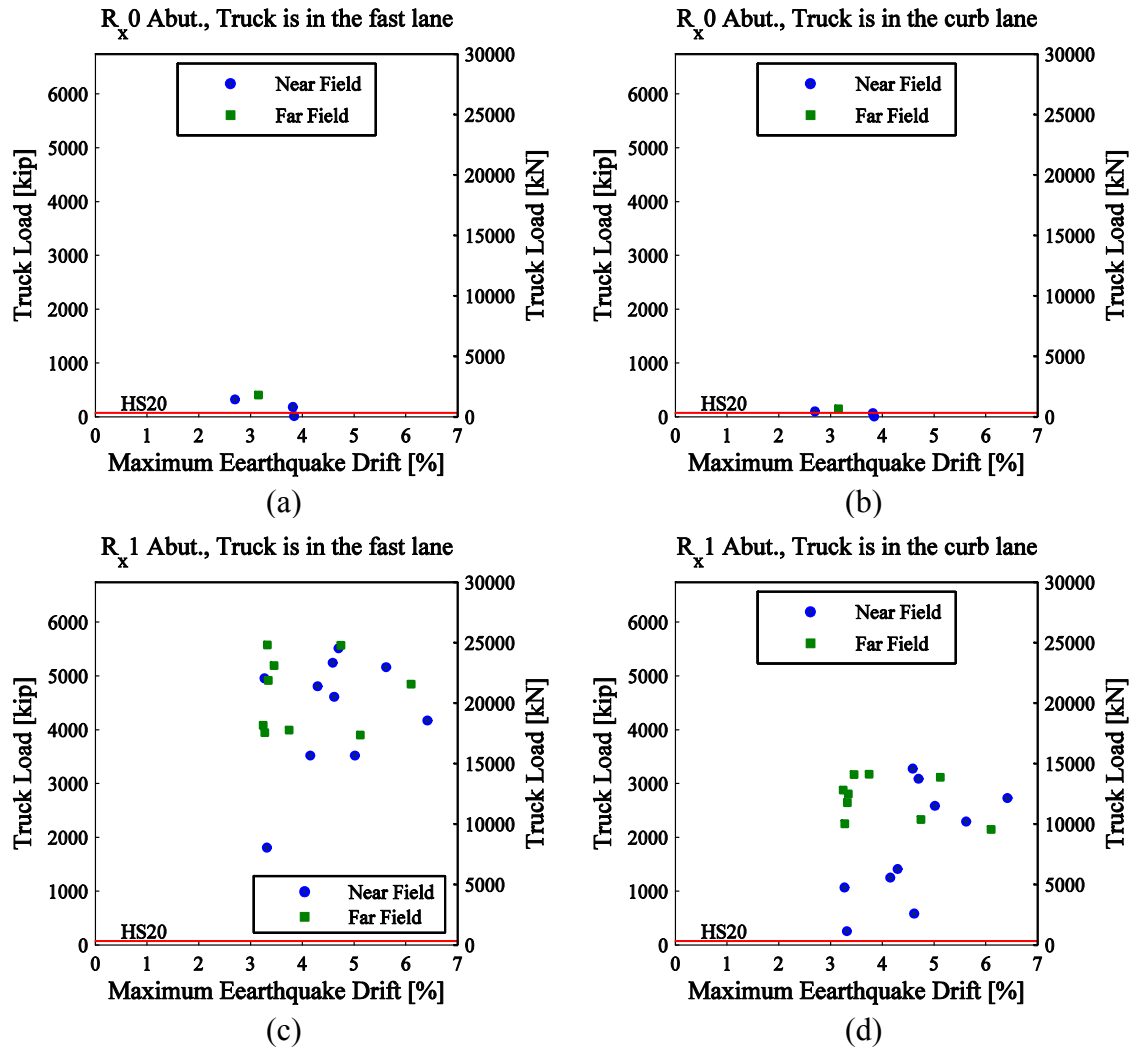


**Fig. 5.19 Post-earthquake bridge truck load capacity vs. maximum earthquake drift for the residual drift of 2.5% and the following cases: (a) Rx0 abutment, the truck is in the fast lane; (b) Rx0 abutment, the truck is in the curb lane; (c) Rx1 abutment, the truck is in the fast lane; (d) Rx1 abutment, the truck is in the curb**

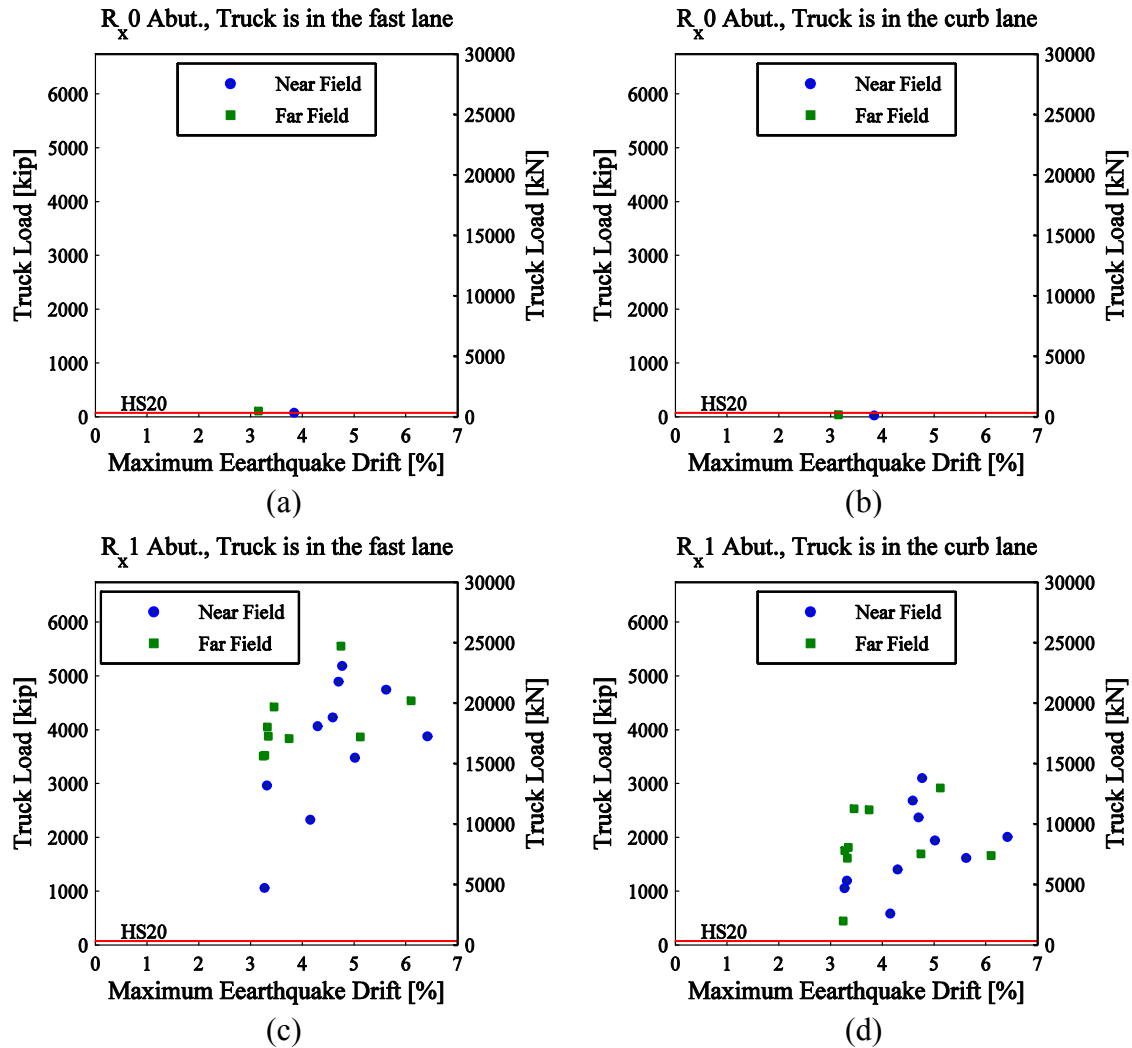


**Fig. 5.20 Post-earthquake bridge truck load capacity vs. maximum earthquake drift for the residual drift of 3.0% and the following cases: (a) Rx0 abutment, the truck is in the fast lane; (b) Rx0 abutment, the truck is in the curb lane; (c) Rx1 abutment, the truck is in the fast lane; (d) Rx1 abutment, the truck is in the curb**

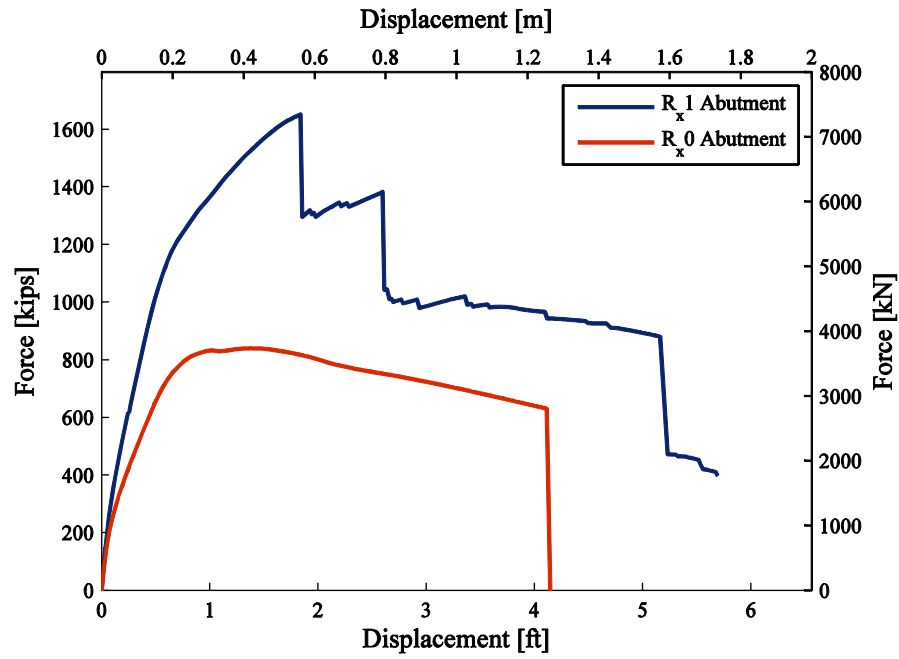


**Fig. 5.21 Pushover results for transverse bridge direction**

## **6 Conclusions and Future Work**

The main goal of this project was to develop analytical model of a bridge which can be used for evaluation of its post-earthquake traffic load capacity. The analytical model of a bridge will be then used in estimating the post-earthquake truck load capacities of a typical overpass bridge in California for a suite of ground motions and set of parameters that have a great influence on the truck load capacity. To achieve this, analytical and experimental investigations are combined. A chart in Fig. 1.1, repeated here as Fig 6.1 for convenience, shows the steps of the research program undertaken in this study.



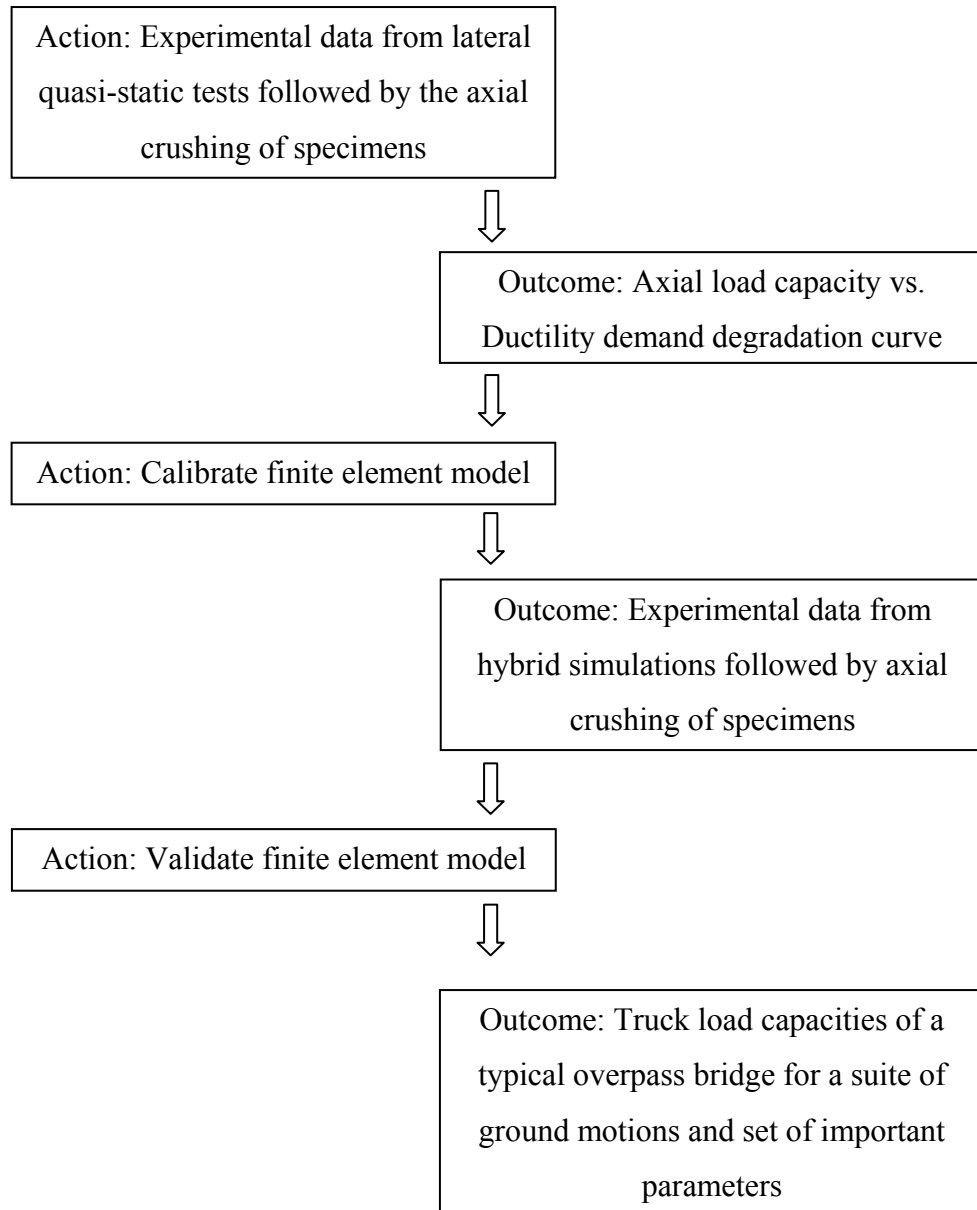


**Fig. 6.1 Methodology for evaluation of the remaining capacity of a bridge to carry traffic load after an earthquake event**

## 6.1 CONCLUSIONS

The post-earthquake axial capacities of single-bent overpass bridges in California were experimentally investigated first. Experiments performed on column specimens typical for tall overpass bridges indicated degradation of the residual axial strength with an increase in the amount of laterally induced damage. The loss of axial strength increases with increase of lateral deformation. The specimen loaded up to the displacement ductility level of 4.5 resulted in a loss of axial strength of approximately 20%. At the displacement ductility level of 4.5, the maximum ductility level the specimen was tested for, significant damage of concrete cover and core was observed. However, none of reinforcing bars or spiral fractured. Thus, it can be concluded that the bridge columns designed by Caltrans SDC will not experience a significant loss of nominal axial load carrying capacity after a design earthquake. This conclusion is limited to the bridge columns with no residual displacements after an earthquake. If the columns have residual displacement, they have to be analyzed as a part of the bridge structural system.

A reinforced concrete bridge column analytically modeled in OpenSees utilizing a fiber cross-section and force based beam-column element with distributed plasticity are capable of producing force-deformation response that matches the experimental result well. The cross-sections of the element are represented by assemblages of longitudinally oriented, unidirectional steel and concrete fibers where concrete is divided into unconfined cover and confined core areas. The reinforcing steel is modeled with a Steel02 material model. The concrete fibers are modeled with a Concrete01 material model using Mander's equations to calculate compressive and crushing strength of confined concrete.

Hybrid simulation tests on a typical modern overpass bridge in California demonstrated capability of a bridge to carry heavy truck load immediately after a very strong earthquake. The earthquake induced displacement ductility demands of 4.7 and 6.7 in the longitudinal and transverse direction of the bridge, respectively. Although the damage in the plastic hinge region of the column specimen (physical portion of the hybrid model) was pronounced, none of its reinforcing bars or its spiral fractured. This earthquake damaged bridge column with approximately zero tilt during the axial compression test had a loss of 15% of its axial strength.

Using the analytical model of a bridge developed and calibrated based on the quasi-static and hybrid simulation test data, it was shown that parameters that have a significant influence on the post-earthquake truck load capacity are: abutment type, residual drift of the bridge after an earthquake, position of the truck on the bridge relative to the superstructure centerline, and ultimate strain in column reinforcing bars. The post-earthquake truck load capacities of a typical modern overpass bridge in California were evaluated for a suite of ground motions and set of the important parameters with a purpose to show the trends of the post-earthquake truck load capacity with the change of significant parameters. As a function of residual drift, the truck load capacity of the bridge degrades faster for the bridge with no torsional restraints at the superstructure ends than for the bridge with torsional restraints at the superstructure ends. There is an additional reduction of the truck load capacity if the truck is located in the curb lane compared to the case when the truck is located in the fast lane. The analysis has also shown that it is unsafe to use the bridge after an earthquake if the abutments are not able to provide torsional restraints at the superstructure ends and at least one of the bridge columns has failed, meaning that at least one of its reinforcing bars fractured during the earthquake. In the case of the bridge that has damaged but not failed columns and abutments with no torsional restraints traffic restrictions (speed and weight) are necessary if residual drifts are bigger than 1.5%. If after an

earthquake abutments still provide torsional restraints at the superstructure ends and there are no broken reinforcing bars in any of the columns, the bridge may be open for traffic immediately after the earthquake.

## **6.2 FUTURE WORK**

The experiments and analyses of the post-earthquake bridge truck load capacities presented in this document are, to the best knowledge of the author, the first of their kind. Since this study is based on one specific bridge type, its main purpose is to show the trends of the post-earthquake truck load capacity of that bridge type with respect to variations of a number of significant parameters. Thus, the study can be further extended to include all bridge types that are present in the California highway traffic network, and broadened further to the bridge types in the US highway traffic network. Additional research is also needed to more precisely relate post-earthquake truck load capacity of the bridge to the damage level of bridge columns and degree of torsional restraints at the superstructure ends. The final aim would be a set of quantitative guidelines for estimating the remaining capacity of a bridge to carry traffic load after an earthquake based on observed residual deformation and damage state of the columns and the abutments. An attempt can also be made toward developing a simple model (for use in design offices and inclusion into Caltrans SDC) for evaluating the post-earthquake axial load capacity of individual bridge columns as function of their design parameters: however, caution should be exercised here because the bridge responds to traffic load as a system rather than as a set of individual columns. Such stand-alone column model would, therefore, have to be conservative and thus, may not be very useful. Instead, the analytical model developed and calibrated in this study should be used as the basis for developing bridge-level models to evaluate post-earthquake traffic load capacity.

The effect of the high cycle traffic load fatigue on the post-earthquake axial load-carrying capacity of the damaged bridge columns needs to be investigated. The effect of the high cycle fatigue is of concern for slightly damaged bridges that do not require a repair after an earthquake. Since the cracks are developed in the bridge columns under the earthquake load they may spread and enlarge under the service load, inducing larger strain cycles in already stretched reinforcing bars, and thus adversely affect the remaining axial load-carrying capacity of the bridge columns and thereby the remaining traffic load capacity of the bridge.

## REFERENCES

- ACI 318. 2005. *Building Code Requirements for Structural Concrete (ACI318-05) and Commentary (ACI318R-05)*. ACI Committee 318. American Concrete Institute, Detroit Michigan.
- ACI Committee 374. 2006. *Acceptance criteria for moment frames based on structural testing and commentary*. Report ACI 374.1-05. American Concrete Institute, Farmington Hills, Michigan.
- Arici, Y., and K. Mosalam. 2003. System identification of instrumented bridge systems. *Earthquake Engineering and Structural Dynamics* 32(7): 999-1020.
- Aviram, A., K. R. Mackie, and B. Stojadinovic. 2008. *Guidelines for nonlinear analysis of bridge structures in California*. Report PEER 2008/03. Berkeley, Calif.: Pacific Earthquake Engineering Research Center, University of California.
- Bollo, M. et al. 1990. *Observations and Implications of Tests on the Cypress Street Viaduct Test Structure*. Earthquake Engineering Research Center Report No. 1990/21.
- Brown, J., and S. Kunnath. 2000. *Low cycle fatigue behavior of longitudinal reinforcement in reinforced concrete bridge columns*. Report MCEER-00-0007.
- Caltrans. 2004. *Bridge Design Specifications*. State of California Department of Transportation.
- Caltrans. 2006a. *Seismic Design Criteria*. State of California Department of Transportation.
- Caltrans. 2006b. *Standard Specifications*. State of California Department of Transportation.
- Chang, G., and J. Mander. 1994. *Seismic energy based fatigue damage analysis of bridge columns: Part I – Evaluation of seismic capacity*. NCEER Technical Report 1994/0006. Department of Civil and Environmental Engineering, State University of New York at Buffalo, NY.
- Chopra, A.K. 2006. *Dynamics of Structures: Theory and Applications to Earthquake Engineering*. 3<sup>rd</sup> edition. Prentice Hall, New Jersey.
- Chung, Y. S., C. K. Park, B. G. Lee, and D. H. Lee. 2006. Cyclic response of RC column-bent piers subjected to bidirectional repeated loading. *Proceedings of the 8<sup>th</sup> U.S. National Conference on Earthquake Engineering, San Francisco, California, USA*, 761.
- Cornell, A., and H. Krawinkler. 2000. *Progress and Challenges in Seismic Performance Assessment*. PEER Center News 3(2): 1-2. Berkeley, Calif.: Pacific Earthquake Engineering Research Center, University of California.
- Dhacal, R. P., and K. Maekawa. 2002. Modeling for postyield buckling of reinforcement. *Journal of Structural Engineering* 128(9): 1139-1147.
- Eberhard, M., and M. Marsh. 1997a. Lateral-load response of a reinforced concrete bridge. *ASCE Journal of Structural Engineering* 123(4): 451-460.
- Eberhard, M., and M. Marsh. 1997b. Lateral-load response of a reinforced concrete bridge. *ASCE Journal of Structural Engineering* 123(4): 461-468.
- Elwood, K. J. 2002. *Shake table tests and analytical studies on the gravity load collapse of reinforced concrete frames*. PhD Dissertation, University of California, Berkeley.

- Elwood, K. J., and J. P. Moehle. 2005. Axial Capacity Model for Shear Damaged Columns. *ACI Structural Journal* 102(4): 578-587.
- Elwood, K. J., and J. P. Moehle. 2005. Drift capacity of reinforcement concrete columns with light transverse reinforcement. *Earthquake Spectra* 21(1): 71-89.
- Elwood, K. J., and J. P. Moehle. 2008. Dynamic collapse analysis for a reinforced concrete frame sustaining shear and axial failure. *Earthquake Engineering and Structural Dynamics* 37: 991-1012. John Wiley & Sons, Ltd.
- Fenves, G. L., and M. Ellery. 1998. *Behavior and failure analysis of a multiple-frame highway bridge in the 1994 Northridge earthquake*. Report PEER 98/08. Berkeley, Calif.: Pacific Earthquake Engineering Research Center, University of California.
- Gilani, A. S. et al. 1995. *Field Testing of Bridge Design and Retrofit Concepts: Part 1 of 2: Field Testing and Dynamic Analysis of a Four-Span Seismically Isolated Viaduct in Walnut Creek, California*. Earthquake Engineering Research Center Report No. 1995/14.
- Harris, H. G., and G. M. Sabins. 1999. *Structural modeling and experimental techniques*. Boca Raton, Fla.
- Jeong, H. I., J. Sakai, and S. A. Mahin. 2008. *Shaking table tests and numerical investigation of self-centering reinforced concrete bridge columns*. Report PEER 2008/06. Berkeley, Calif.: Pacific Earthquake Engineering Research Center, University of California.
- Karsan, I. D., and J. O. Jirsa. 1969. Behavior of concrete under compressive loading. *Journal of Structural Engineering*, 95(ST-12).
- Kato, D., and K. Ohnishi. 2002. *Axial load carrying capacity of reinforced concrete columns under lateral load reversals*. Report PEER 2002/02: 247-255. Berkeley, Calif.: Pacific Earthquake Engineering Research Center, University of California.
- Kawashima, K., H. Ogimoto, R. Hayakawa, and G. Watanabe. 2006. Effect of bilateral excitation on the seismic performance of reinforced concrete bridge columns. *Proceedings of the 8<sup>th</sup> U.S. National Conference on Earthquake Engineering, San Francisco, California, USA*, 567.
- Kawashima, K., et al. 2008. Seismic performance of a flexural failure type RC bridge column based on E-Defense excitation. *The 40<sup>th</sup> Joint Meeting on Panel on Wind and Seismic Effects, UJNR, Gaithersburg, Maryland, USA*.
- Kent, D. C., and R. Park. 1971. Flexural Members with Confined Concrete. *Journal of Structural Engineering*, 97(ST7): 1969-1990.
- Ketchum, M., V. Chang, and T. Shantz. 2004. *Influence of Design Ground Motion Level on Highway Bridge Costs*. Report PEER 6D01. Berkeley, Calif.: Pacific Earthquake Engineering Research Center, University of California.
- Krawinkler, H., A. Gupta, R. Medina, and N. Luco. 2000. *Loading histories for seismic performance testing SMRF components and assemblies*. SAC Joint Venture, Report No. SAC/BD-00/10.
- Krawinkler, H. 2005. *Van Nuys hotel building: Exercising seismic performance assessment*. Report PEER 2005/11. Berkeley, Calif.: Pacific Earthquake Engineering Research Center, University of California.

- Kunnath, S. K. 2006. *Application of the PEER PBEE Methodology to the I-880 Viaduct*. Report PEER 2006/10. Berkeley, Calif.: Pacific Earthquake Engineering Research Center, University of California.
- Lehman, D. E., and J. P. Moehle. 2000. *Seismic performance of well-confined concrete bridge columns*. Report PEER 1998/01. Berkeley, Calif.: Pacific Earthquake Engineering Research Center, University of California.
- Luco, N. 2001. *Probabilistic seismic demand analysis, SMRF connection fractures, and near source effects*. PhD Dissertation, Dept. of Civil and Environmental Engineering, Stanford University, California.
- MacGregor, J. G. and J. K. Wight. 2005. *Reinforced Concrete: Mechanics and Design*. 4<sup>th</sup> Edition, Prentice Hall, Upper Saddle River, New Jersey.
- Mackie, K. 2004. Degradation of reinforced concrete column axial strength. *The Fifth International Symposium in Civil Engineering, Delft, Netherlands*.
- Mackie, K., and B. Stojadinovic. 2005. *Fragility Basis for California Highway Overpass Bridge Decision Making*. Report PEER 2005/02. Berkeley, Calif.: Pacific Earthquake Engineering Research Center, University of California.
- Mander, J. B., M. J. N. Priestley, and R. Park. 1988. Theoretical Stress-Strain Model for Confined Concrete. *Journal of the Structural Engineering*, 114(ST8): 1804-1826.
- Marini, A., and E. Spacone. 2006. Analysis of reinforced concrete elements including shear effects. *ACI Structural Journal* 103(5): 645-655. American Concrete Institute.
- McKenna, F. T. 1997. *Object-oriented finite element programming: frameworks for analysis, algorithms and parallel computing*. PhD Dissertation, University of California, Berkeley.
- McKenna, F. T., and G. L. Fenves. 2000. An Object-Oriented Software Design for Parallel Structural Analysis. *Proceedings of the 2000 Structures Congress & Exposition: Advanced Technology in Structural Engineering, Philadelphia, Pennsylvania*.
- McKenna, F. T., G. L. Fenves, M. H. Scott, and B. Jeremic. 2000. *Open System for Earthquake Engineering Simulation*. <http://OpenSEES.berkeley.edu>.
- Medina, R., H. Krawinkler, and B. Alavi. 2001. Seismic Drift and Ductility Demands and their Dependence on Ground Motions. *Proceedings of the US-Japan Seminar on Advanced Stability and Seismicity Concepts for Performance-Based Design of Steel and Composite Structures, Kyoto, Japan*.
- Menegotto, M., and P. E. Pinto. 1973. Method of analysis for cyclically loaded R.C. plane frames including changes in geometry and nonelastic behaviour of elements under combined normal force and bending. *Proc., Symp. on the Resistance and Ultimate Deformability of Structures Acted on by Well Defined Repeated Loads*, International Association for Bridge and Structural Engineering, Zurich, Switzerland, 15–22.
- Nakashima, M., et al. 1988. Feasibility of pseudo dynamic test using substructuring techniques. *Proceedings, Ninth World Conference on Earthquake Engineering, Tokyo, Japan*.
- Neuenhofer, A., and F. C. Filippou. 1997. Evaluation of Nonlinear Frame Finite Element Models. *Journal of Structural Engineering*, 123(7): 958-966.
- Pantelides, C. et al. 2002. In-situ Tests at South Temple Bridge on Interstate 15. *Seventh National Conference on Earthquake Engineering, Boston, Massachusetts*.

- PEER Strong Motion Catalog. <http://peer.berkeley.edu/smcat>. Web page.
- Rodriguez, M. E., J. C. Botero, and J. Villa. 1999. Cyclic stress-strain behavior of reinforcing steel including effect of buckling. *Journal of Structural Engineering* 125(6): 605-612.
- Schoettler, M. J., J. I. Restrepo, F. Seible, and E. Matsuda. 2006. Bidirectional testing of a retrofitted bridge pier in BART's West Oakland aerial guideway. *Proceedings of the 8<sup>th</sup> U.S. National Conference on Earthquake Engineering, San Francisco, California, USA*, 1430.
- Scott, M. H., and G. L. Fenves. 2006. Plastic Hinge Integration Methods for Force-Based Beam-Column Elements. *Journal of Structural Engineering*, 132(2): 244-252.
- Scott, M. H., G. L. Fenves, F. T. McKenna, and F. C. Filippou. 2008. Software Patterns for Nonlinear Beam-Column Models. *Journal of Structural Engineering*, 134(4): 562-571.
- Schellenberg, A. H. 2008. *Advanced implementation of hybrid simulation*. PhD Dissertation, University of California, Berkeley.
- Shin, Y. B., and J. P. Moehle. 2002. *Quarter-scale reinforced concrete specimen test*. Internal technical report, University of California, Berkeley.
- Shome, N., C. A. Cornell, P. Bazzurro, and J. E. Carballo. 1998. Earthquakes, Records, and Nonlinear Responses. *Earthquake Spectra*, 14(3): 467-500.
- Spacone, E., V. Ciampi, and F. C. Filippou. 1996. Mixed Formulation of Nonlinear Beam Finite Element. *Computers and Structures*, 58(1): 71-83.
- Stojadinovic, B. 1995. *Seismic upgrading of bridge outrigger knee joint system*. PhD Dissertation, University of California, Berkeley.
- Tasai, A. 1999. *Residual axial capacity and restorability of reinforced concrete columns damaged due to earthquake*. Report PEER 1999/10. Berkeley, Calif.: Pacific Earthquake Engineering Research Center, University of California.
- Tasai, A. 2000. *Residual axial capacity of reinforced concrete columns during shear degradation*. Report PEER 2000/10. Berkeley, Calif.: Pacific Earthquake Engineering Research Center, University of California.
- Taucer, F. F., E. Spacone, and F. C. Filippou. 1991. *A fiber beam-column element for seismic response analysis of reinforced concrete structures*. Report No. UCB/EERC-91/17, Pacific Earthquake Engineering Research Center, University of California, Berkeley, CA.
- Terzic, V., K. Mackie, and B. Stojadinovic. 2006. Validation of finite element model ability to evaluate residual live load capacity of bridge columns. *5th National Seismic Conference on Bridges and Highways, San Mateo, California, USA*.
- Terzic, V., K. Mackie, and B. Stojadinovic. 2008. Experimental evaluation of the residual axial load capacity of circular bridge columns. *14th World Conference on Earthquake Engineering, Beijing, China*.
- Timoshenko, S. P., and J. N. Goodier. 1969. *Theory of Elasticity*. 3<sup>rd</sup> edition. McGraw-Hill, New York.
- Yoshimura, M., and T. Nakamura. 2002. *Axial collapse of reinforced concrete short columns*. Report PEER 2002/21. Berkeley, Calif.: Pacific Earthquake Engineering Research Center, University of California.

## **Appendix A: Materials and Construction**

### **A.1 MATERIALS**

Longitudinal steel reinforcement, spiral steel reinforcement, and plain concrete cylinders were tested to determine the stress-strain response. Steel and concrete modulus of elasticity together with stress and strain values that are used in the column modeling were based on the material testing.

#### **A.1.1 Longitudinal Reinforcement**

Longitudinal reinforcement (bar #4/13M) met the ASTM Designation A 706 requirements. The longitudinal reinforcement used for construction of the seven test specimens and for material testing was specified to be from a single batch of steel delivered in a single batch (to limit variation in steel properties). The reinforcing bars were tested using standard testing methods. A 20-inch bar length was cut and the center section was machined to localize bar yielding and permit precise measurement of the machined bar diameter. Four coupons were tested to obtain stress-strain response of the bar. The responses for the test specimens are shown in Figure A.1. The two tests, labeled as LB3 and LB4 in Figure A.1, were unsuccessful after the yielding of the specimen. The slippage of measuring instruments relative to the bar was observed. The steel had average yield strength of 70.7 ksi (487 MPa). The yield plateau extended from approximately 0.0025 in./in. to a strain of 0.01 in./in. The fracture strain was approximately 0.2 in./in. The average modulus of elasticity was approximately 29000 ksi.



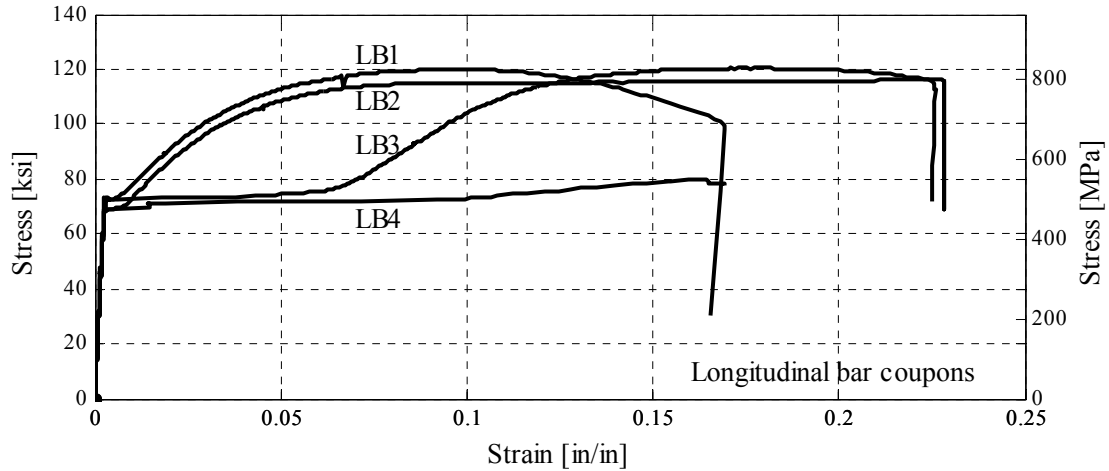


**Fig. A.1 Longitudinal reinforcement stress-strain response**

### A.1.2 Spiral Reinforcement

Steel wire (W3.5) with ASTM Designation A 82 was selected for the spiral reinforcement. The spiral reinforcement used for construction of all test specimens and for material testing was from the single batch of steel. Three coupons were tested to obtain the stress-strain response of the spiral. Figure A.2 shows the measured response. The yield strength corresponded to strain of 0.005 and was determined to be 95 ksi (655 MPa). The apparent fracture strain was 0.044 in./in. The ultimate strength of the steel was 106 ksi (731 MPa).

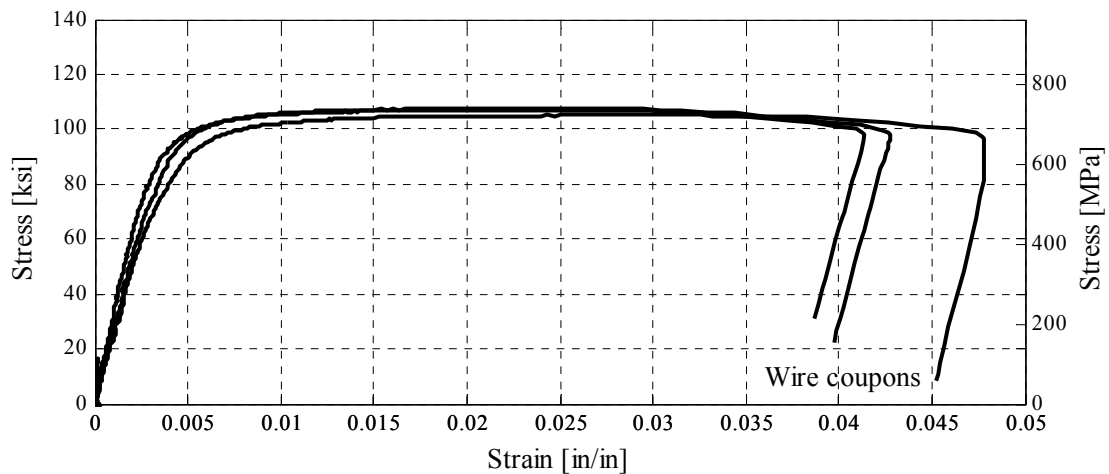


**Fig. A.2 Spiral reinforcement stress-strain response**

### A.1.3 Plain Concrete

The concrete mix was designed to approximate the prototype column mix, with 28-day target strength of 5 ksi. This target strength was selected to match the concrete strength data collected by Caltrans from constructed bridges. Table A.1 provides details of the mix. Another mix design

goal was to achieve the target strength of a period of about 60 days and to prevent significant change of concrete strength thereafter. Thus, the specimens tested over a period of approximately six months would have approximately the same strength at the day of testing. The seven columns (the four to be tested laterally in quasi-static manner and then crushed axially, one to be tested axially, and two to be tested using hybrid simulation technique and then crushed axially) were cast in two phases outside the laboratory facility. The seven anchor blocks were cast on May 18, 2007, from a single batch of concrete. The seven columns were cast on June 18, 2007, from a single batch of concrete.

**Table A.1 Concrete mix data**

Max. size Aggregate	28-Day Strength	Slump	W/C Ratio	Coarse Aggregate Weight	Fine Aggregate Weight	Cement	Fly ash	Water
[in]	[ksi]	[in]	[-]	[lb]	[lb]	[lb]	[lb]	[lb]
3/8	5.0	6	0.425	1000	1955	494	211	300

During each casting, a slump test was performed to ensure that the concrete slump was around 6 inches. The anchor block concrete had a slump of 5.75 inches, while the column concrete had a slump of 7 inches. Concrete cylinders, 12 inches in height and 6 inches in diameter, were cast with the anchor blocks and columns (Figure A.3). The cylinders were kept in the same location as the test specimens. The forms of the cylinders were removed when the column forms were removed. The cylinders from anchor block concrete were tested at 7 and 28 days while the cylinders from column concrete were tested at 7, 28, 35, 42, and 49 days to measure compressive strength. Three tests were performed on each test day. Table A.2 gives the average results for the tests.



(a) Casting concrete cylinders



(b) After casting concrete cylinders

**Fig. A.3 Casting concrete cylinders**

**Table A.2 Development of concrete strength**

Cylinders	7-Day	28-Day	35-Day	42-Day	49-Day
Anchor Blocks	3.26 ksi	5.39 ksi			
Columns	3.96 ksi	4.93 ksi	4.67 ksi	5.20 ksi	5.07 ksi

Additional material tests were performed on the day of the test. The tensile, compressive, and stress-strain responses of the anchor block and column concrete were measured; 3 splitting and 3 compressive tests were performed. The experimental setups for the two tests are shown in Figure A.4. Three tests were performed for each type of the test. Table A.3 gives the average results for the compressive strength ( $f_c$ ) and modulus of elasticity ( $E_c$ ) for both concrete batches. The average results for the tensile strength are presented in Table A.4. Figure A.5 and Figure A.6 show how the column and anchor block concrete strength, respectively, was developed with time. Figure A.7 through Figure A.13 give the measured stress-strain response for each column.



(a) Splitting test



(b) Compression test

**Fig. A.4 Experimental setups for concrete cylinder tests****Table A.3 Compressive strength and modulus of elasticity on or near day of test**

Test Designation	$f_{c,col}$ [ksi]	$f_{c,anc.bl}$ [ksi]	$E_{c,col}$ [ksi]	$E_{c,anc.bl}$ [ksi]
Base0	5.48	5.93	2998	3047
Base1.5	5.05	5.50	2829	2824
Base3	4.96	5.23	2861	2899
Base4.5	5.09	5.76	3067	3123
ShearShort4.5	6.34	6.56	3483	3322
BaseHST1	6.21	6.47	3645	3379
BaseHST2	6.39	6.69	3647	3519

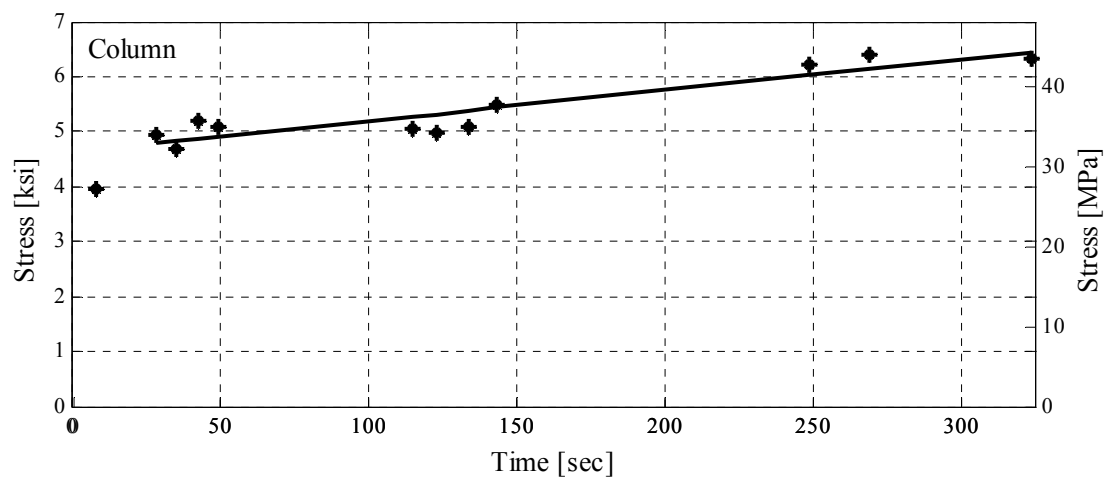


**Fig. A.5 Development of column concrete strength with time**

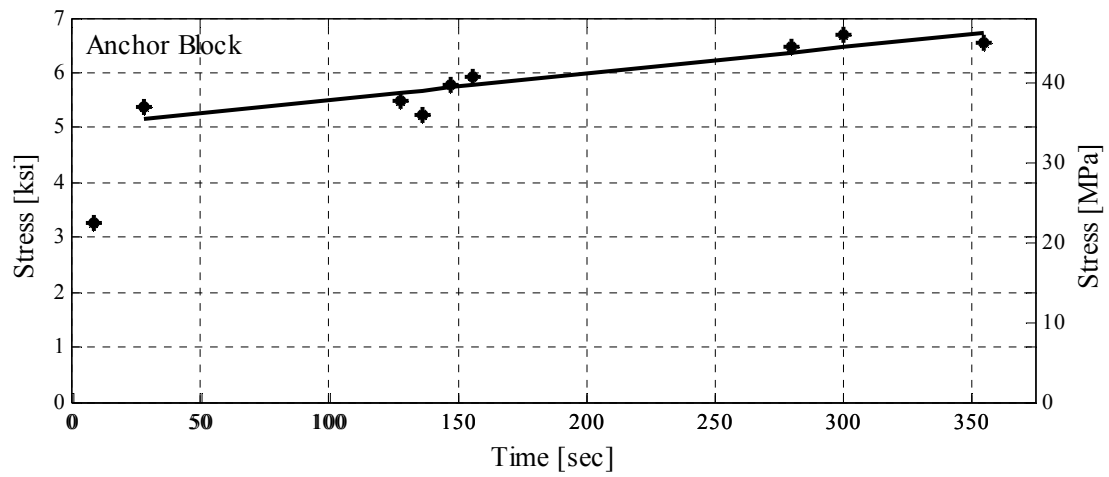


**Fig. A.6 Development of anchor block concrete strength with time**

**Table A. 4 Tensile strength on or near day of test**

Test Designation	Columns [ksi]	Anchor blocks [ksi]	Columns [%f <sub>c</sub> ]	Anchor blocks [%f <sub>c</sub> ]
Base0	0.40	0.45	7.3	7.6
Base1.5	0.41	0.45	8.0	8.3
Base3	0.35	0.41	7.1	7.9
Base4.5	0.43	0.39	8.5	6.8
ShearShort4.5	0.42	0.51	6.7	7.7
BaseHST1	0.43	0.48	7.0	7.5
BaseHST2	0.44	0.55	6.9	8.2

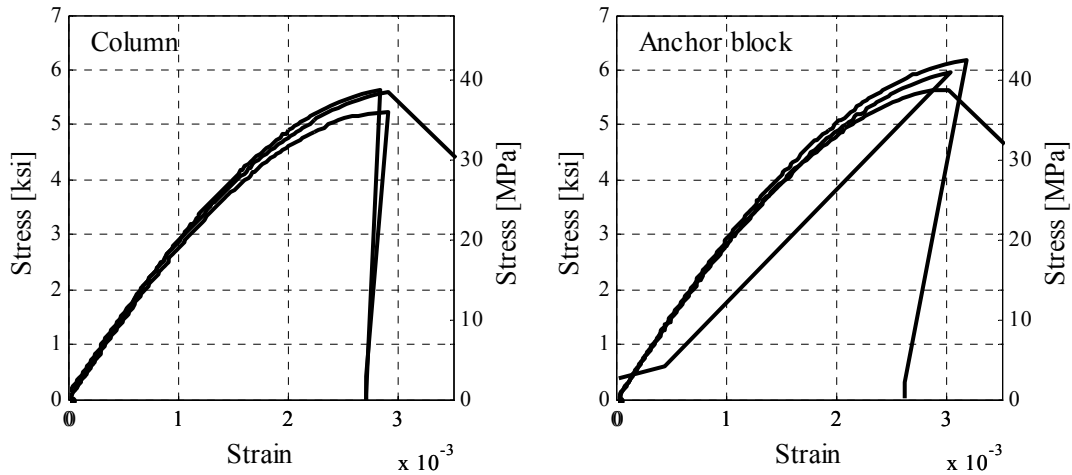


**Fig. A.7 Measured plain-concrete stress-strain response for test Base0**

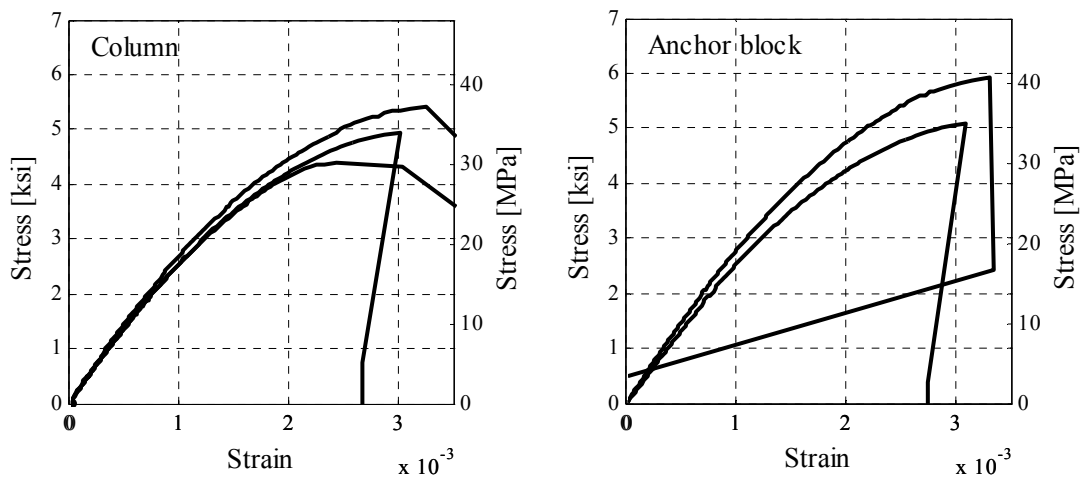


**Fig. A.8 Measured plain-concrete stress-strain response for test Base1.5**

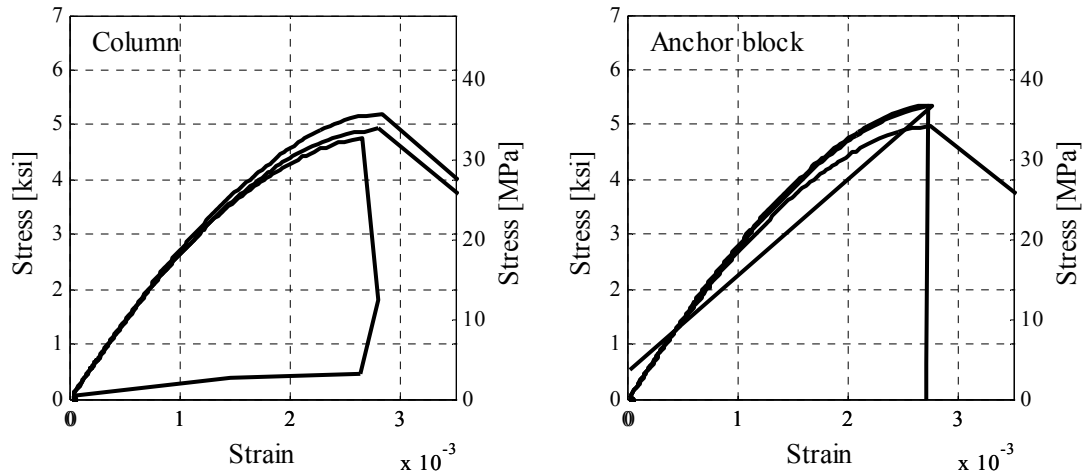


**Fig. A.9 Measured plain-concrete stress-strain response for test Base3**

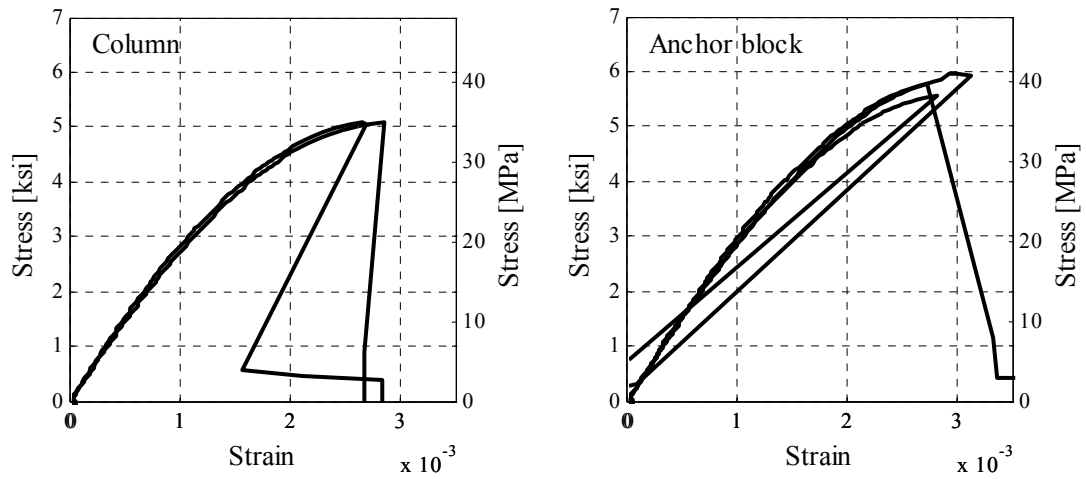


**Fig. A.10 Measured plain-concrete stress-strain response for test Base4.5**

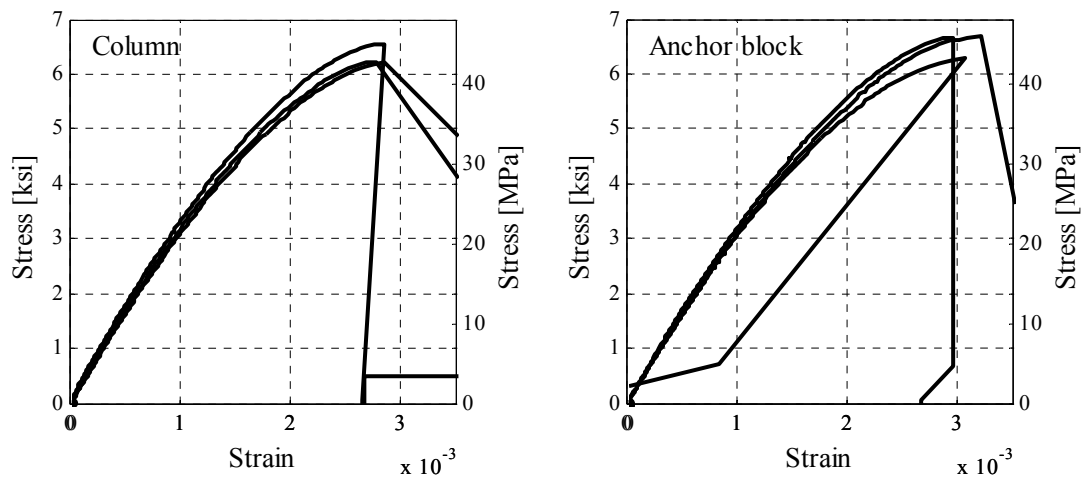


**Fig. A.11 Measured plain-concrete stress-strain response for test ShearShort4.5**

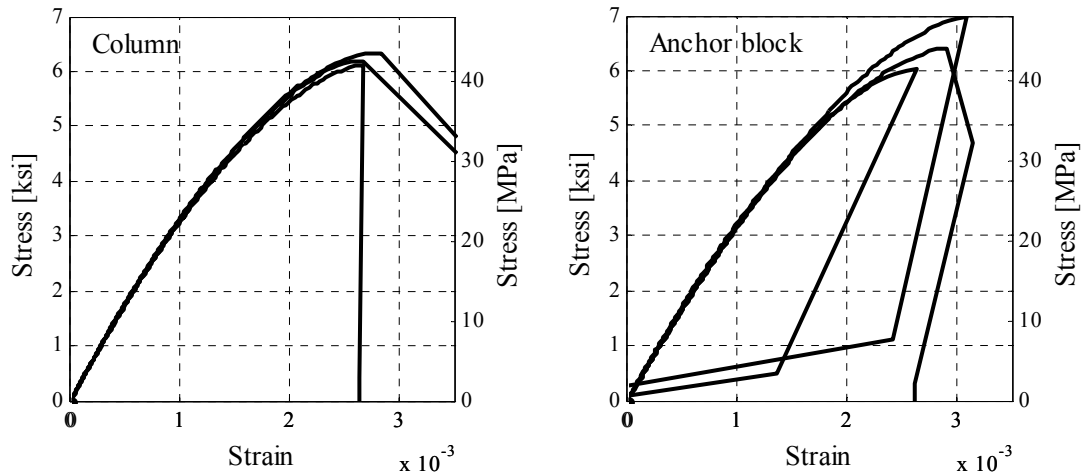


**Fig. A.12 Measured plain-concrete stress-strain response for test BaseHST1**

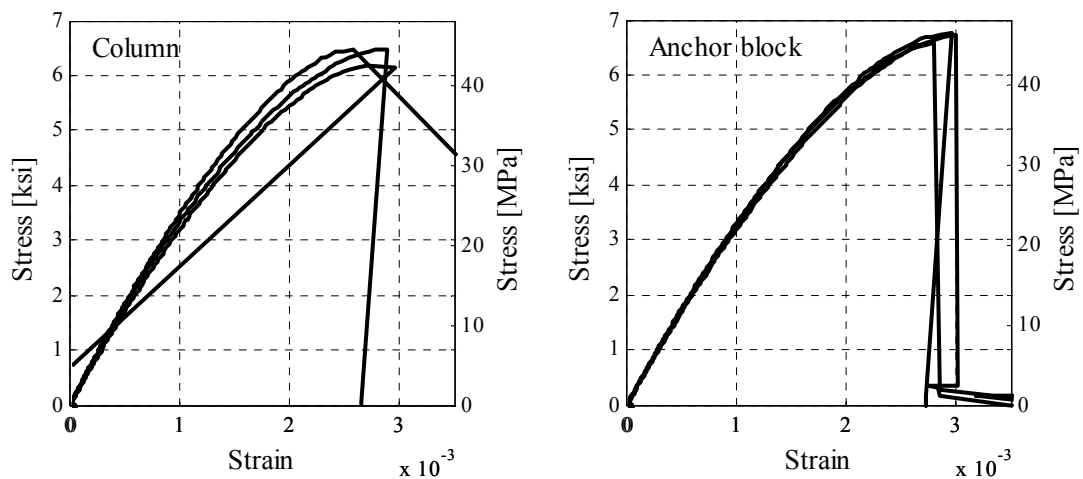


**Fig. A.13 Measured plain-concrete stress-strain response for test BaseHST2**

## A.2 CONSTRUCTION PROCEDURES

Procedures to construct the test specimens were established to mimic the construction sequence in the field. The construction process had four major phases: construction of the reinforcement cages, casting of the anchor blocks, preparation for column casting including plumbing the column reinforcement and forms and installation of the steel jackets at the top of the columns, and column casting.

The columns were constructed outside the structural laboratory at the Earthquake Engineering Research Center, Richmond Field Station, of the University of California. A local contractor constructed the specimens. The reinforcing steel was cut and bent off-site and delivered to the job site. The anchor block cages were constructed and placed inside the forms. The bottom portions of the anchor block cages were constructed first (Figure A.14). The longitudinal bars were placed in specified positions and secured (Figure A.15). The strain gages were attached to longitudinal steel prior to construction of the columns. The spiral reinforcement



was wound around longitudinal steel in the anchor block region of the column. The top portion of the anchor block cage was constructed. The anchor block ties were placed, completing the reinforcement cage construction. The cages were placed into the forms (Figure A.16).



**Fig. A.14 Bottom portion of the anchor block cage**



**Fig. A.15 Placement of longitudinal bars**





**Fig. A.16 Anchor block reinforcement cage**

Concrete from the shoot of the concrete truck was placed into the anchor block framework and vibrated (Figure A.17). The exposed surface was finished (Figure A.18) and wet cured by covering the surface with a thick nylon sheets. Spiral reinforcement was placed finishing the construction of the column cages (Figure A.19a). Strain gages were attached to column spiral. A heavy-wall Sonotube, half an inch thick, was placed over each column reinforcement cage to serve as formwork (Figure A.19b). Half an inch dobies (form spacers) were used to space the reinforcement cage and formwork. Strain gage wires were pulled out from the formwork and instrumentation rods were placed through holes in the formwork (Figure A.20). A wood structure for holding the steel jackets in place during casting of concrete was built. The steel jackets were placed in specified position and served as formwork for the top portions of columns (Figure A.21). Concrete was placed into the formwork. The exposed portion of the column was wet cured for a period of 7 days at which time the forms were stripped (Figure A.22).



**Figure A.17 Casting anchor block**



**Figure A.18 After casting the anchor blocks**

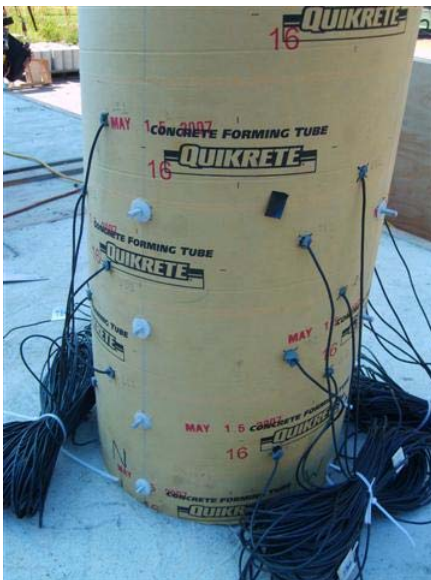


(a) After construction of the column cage



(b) After putting the Sonotube

**Figure A.19 Column cage and formwork**



(a)



(b)

**Fig. A.20 After placing the instrumentation rods**





**Figure A.21 Installation of steel jackets**



**Figure A.22 After stripping the forms**

## Appendix B: Selection of Loading Pattern for Quasi-Static Tests

In order to define the most suitable pattern of loading for bilateral quasi-static tests, nonlinear time history analyses were performed. The two existing single-column-bent overpass bridges, designated as MGR and W180 (Aviram et al., 2008), were considered in analysis. Columns of the bridges were slightly modified to match the geometry and reinforcement of the prototype column for the base column specimen (refer to Table 2.5). Geometry of the analyzed bridges is given in Table B.1.

**Table B.1 Geometry of the bridges**

Bridge type	No. spans	Outer spans	Inner spans	Deck width	Deck height	No. Cols	Col. Diam.	Col. Height
MGR	3	109.7 ft	146.3 ft	42.3 ft	6.23 ft	2	6.25 ft	50 ft
		33.45 m	44.60 m	12.90 m	1.90 m		1.91 m	15.24 m
W180	4	142.6 ft	193.6 ft	41.2 ft	7.74 ft	3	6.25 ft	50 ft
		43.47 m	59.00 m	12.57 m	2.36 m		1.91 m	15.24 m

Two suites of ground motions (20 records per suite) representing the two types of earthquakes with respect to different rupture mechanisms were considered: strike-slip and thrust fault earthquakes. The strike-slip earthquakes with the two components of motion: normal and parallel to the fault, were near field earthquakes with a distance from a fault less than 10 km. The thrust fault earthquakes were far field earthquakes.

To model the bridges, a three-dimensional nonlinear finite element models were developed in OpenSees (<http://opensees.berkeley.edu>). A finite element model is a spine model of the bridge structure with line elements located at the centroid of the cross section following the alignment of the bridge. Three-dimensional nonlinear beam-column elements with corresponding cross-sectional properties were used to model the columns. The nonlinear beam-column elements are based on force formulation and consider the spread of plasticity along the element. The parameters that define nonlinear reinforced concrete columns were calibrated based on Lehman's test (Lehman, 2000) and are given in Section 4.2 of this document. The superstructure was modeled using elastic beam elements. All six degrees of freedom were restrained at the base of the columns. Single point constraints against displacement in vertical direction (vertical support) were defined at the superstructure ends.

Displacement ductilities at the top of the columns were traced and the most representative responses of all are selected to be shown. Fig. B.1 shows displacement ductility orbits at the top of the column for the strike-slip earthquake where component of the motion normal to the fault is aligned with the transverse direction of the bridge. For the same type of the earthquake and the case where component of the motion parallel to the fault is aligned with the transverse direction of the bridge, results are shown in Fig. B.2. Results related to the thrust fault earthquakes are shown in Fig. B.3. On the plots in Fig. B.1, Fig. B.2, and Fig. B.3, X axes correspond to displacement ductility in longitudinal bridge direction and Y axes correspond to displacement ductility in transverse bridge direction.

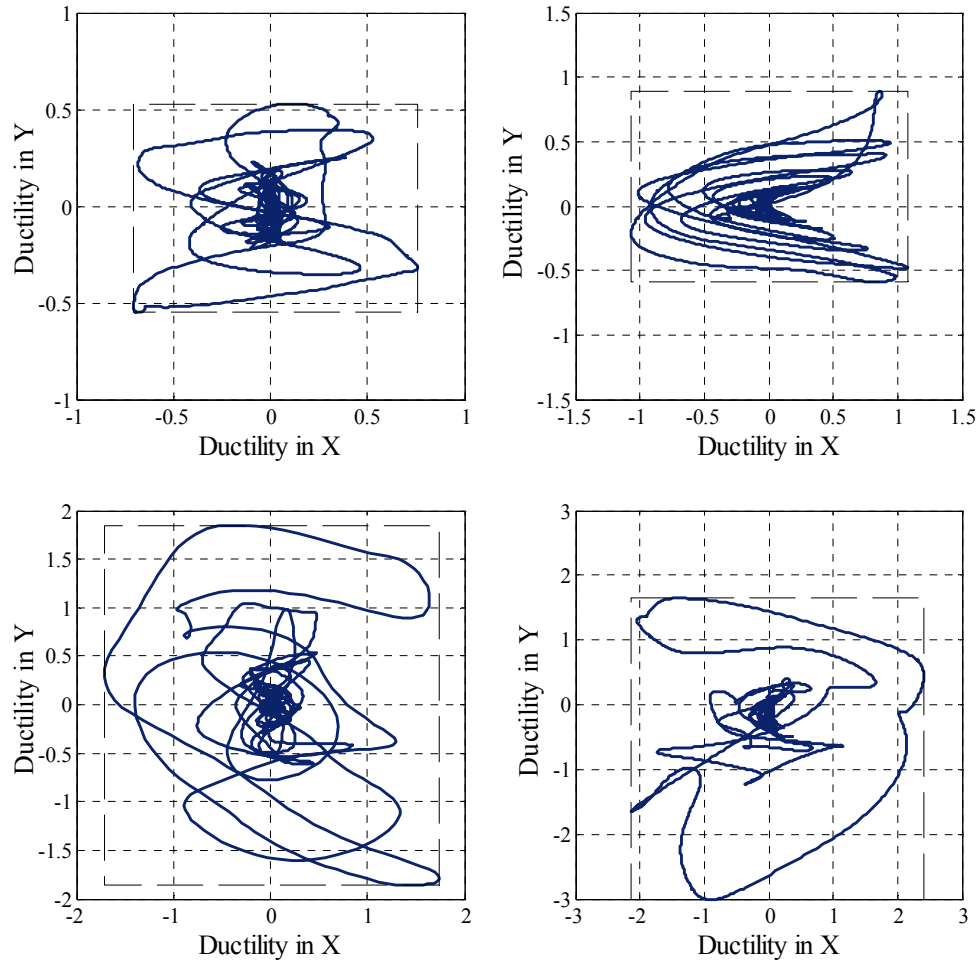


**Fig. B.1 Displacement orbits at the top of the column for the strike-slip earthquake; component of motion normal to the fault is aligned with the transverse direction of the bridge**

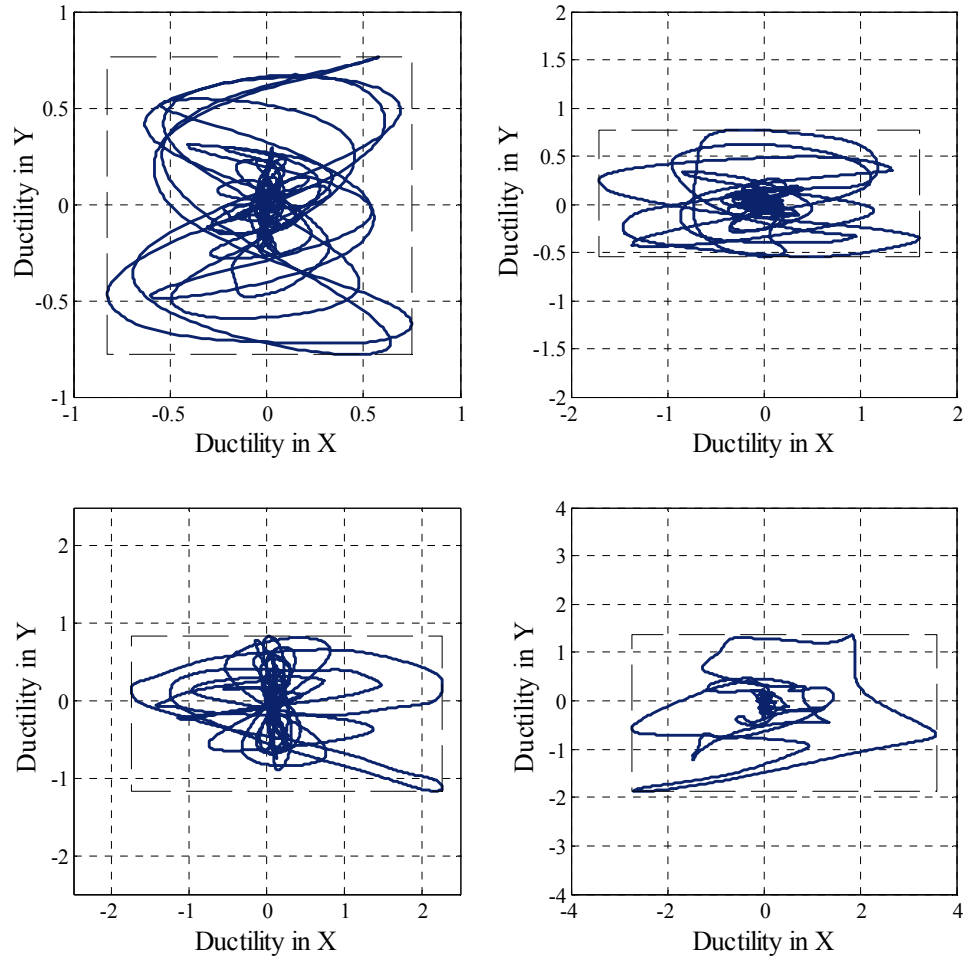


**Fig. B.2 Displacement orbits at the top of the column for the strike-slip earthquake; component of motion parallel to the fault is aligned with the transverse direction of the bridge**

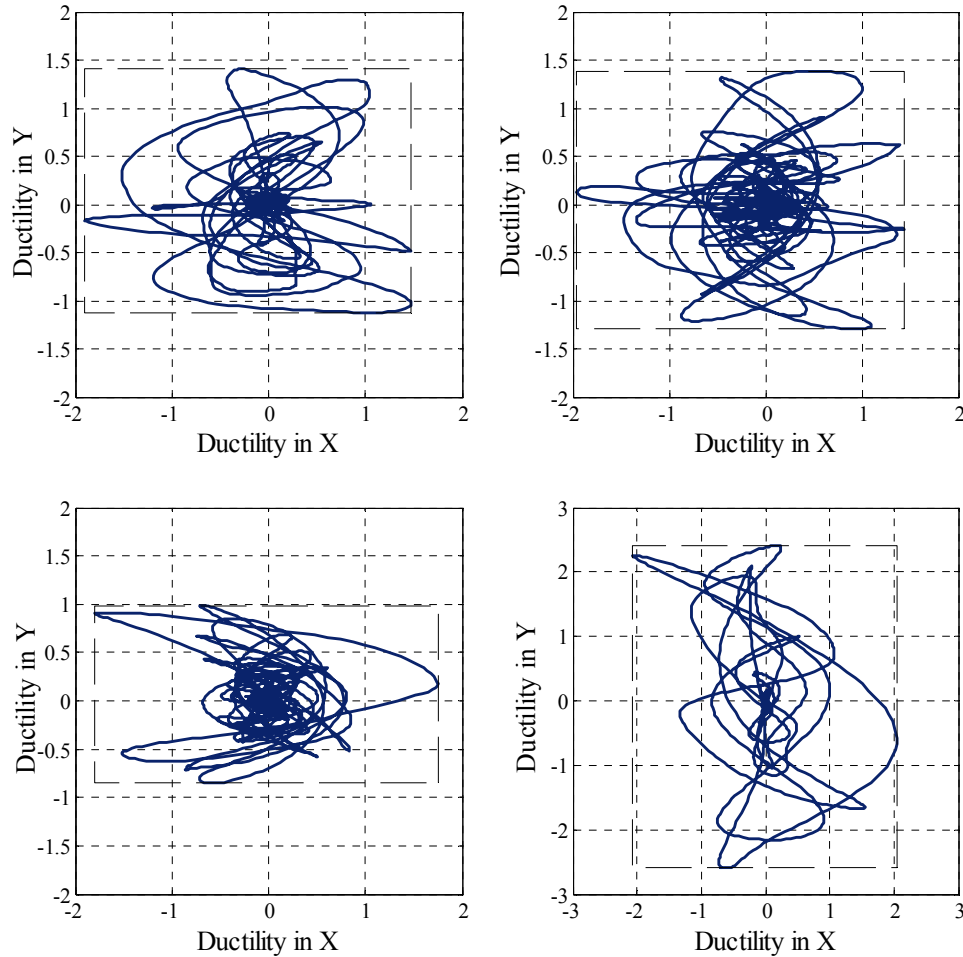


**Fig. B.3 Displacement orbits at the top of the column for the trust fault earthquake**

From the results shown in Fig. B.1, Fig. B.2, and Fig. B.3, it can be observed that the bridge columns have proportional responses in X and Y directions for most of the ground motions. Excluding the responses from the near field earthquakes with a pronounced impulse, all the other responses are a combination of dumbbell like patterns and ‘C’ like patterns. Thus, from all the loading patterns shown in Figure 2.5, it can be concluded that the circular loading pattern can best envelope typical bridge responses.

The two loading patterns with the circular orbits were considered (Fig. B.4). The first loading pattern (Loading Pattern I), schematically shown in Fig. B.4a, is defined by two cycles at each displacement level. In the first cycle, starting from the initial position O the specimen is displaced toward the position A, after which the circular pattern of displacement in clockwise direction follows until the end of the circle, point B. The specimen is then moved back to the initial position O (red line in Fig. B.4a). In the second cycle the path O-C-D-O is followed with the circular path C-D in the counterclockwise direction (blue line in Fig. B.4a). On the other hand, the second loading pattern (Loading Pattern II), schematically shown in Fig. B.4b, is defined by one cycle at each displacement level. At the current level of displacement the specimen follows the path O-A-B-O with the circular path A-B in the clockwise direction (red line in Fig. B.4b), while at the subsequent level of displacement the specimen follows the path



O-D-C-O with the circular path C-D in the counterclockwise direction (blue line in Fig. B.4b). In developing the loading patterns care was taken not to induce torsion in the column considering that there is unavoidable small eccentricity inherent to the actuator mounts.

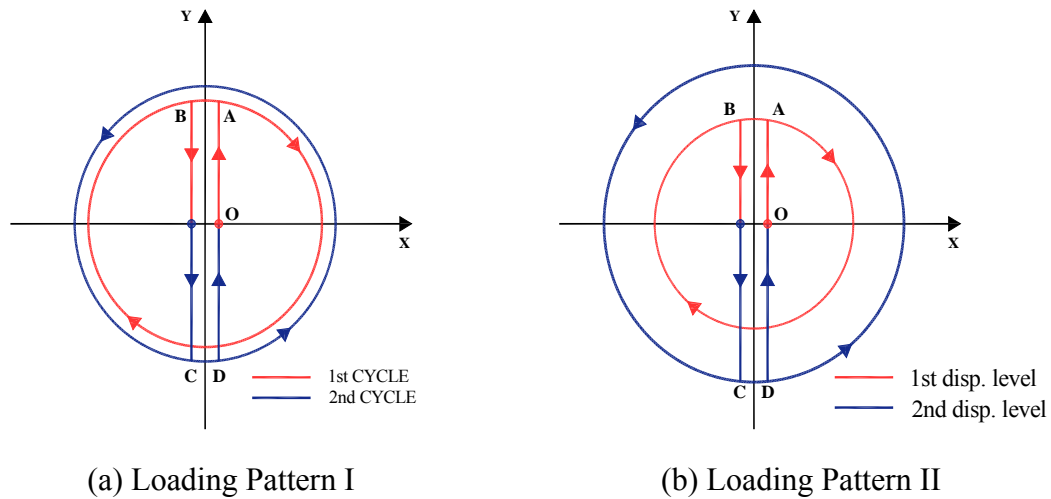
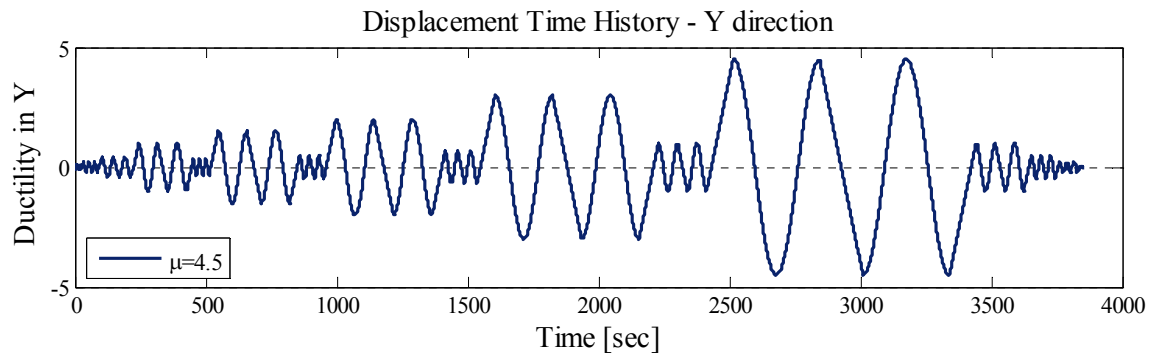
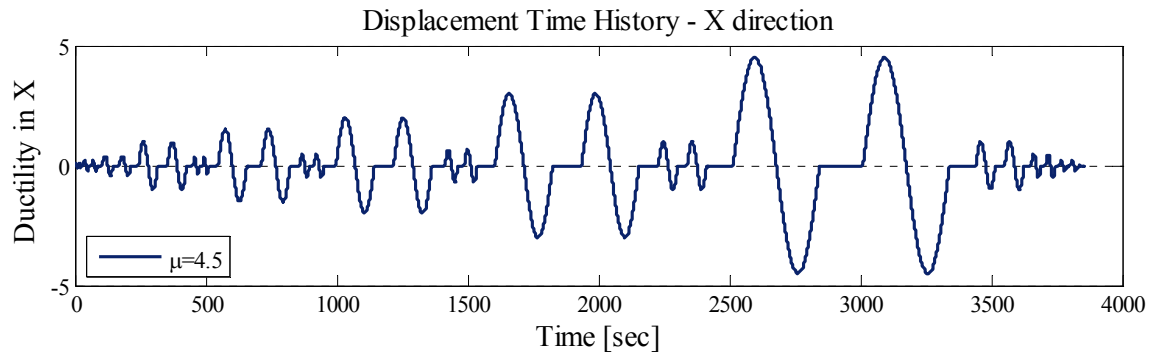
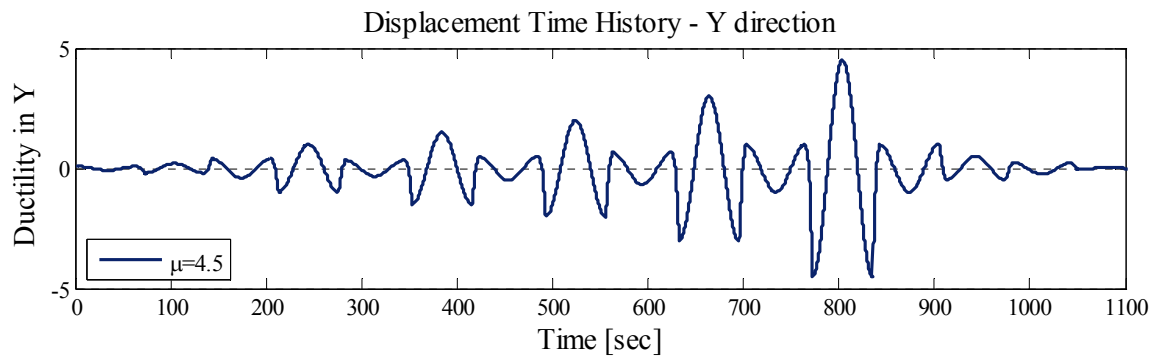
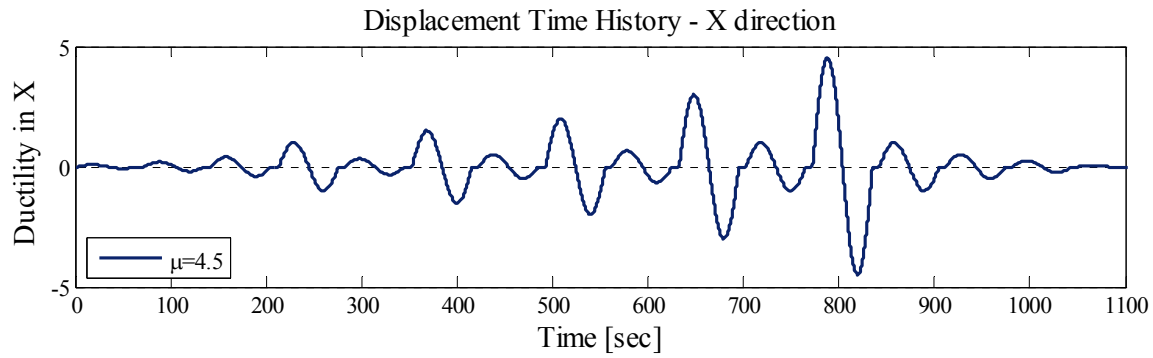


**Fig. B.4 Two loading patterns considered for quasi-static tests**

The displacement histories of the two loading patterns are shown in Fig. B.5. The Loading Pattern I was chosen to be used in the quasi-static tests as it does not induce any bias in lateral deformation of the column. Moreover, the Loading Pattern I with the two cycles at each displacement level provides an indication of the degradation characteristics of the column at the same displacement level and is more demanding in terms of low-cycle fatigue.



(a) Displacement time history following Loading Pattern I



(b) Displacement time history following Loading Pattern II

**Fig. B.5 Displacement histories for the two considered loading patterns**

## Appendix C: Experimental Setup and Instrumentation

### C.1 EXPERIMENTAL SETUP: QUASI-STATIC LATERAL TESTS

The experimental portion of the research program was designed to characterize the cyclic response of circular bridge columns subjected to bidirectional lateral loading. The prototype column is modeled as cantilever column representing the bottom half of a bridge column that is fully fixed into the foundation (shaded region in Fig. C.1). The test specimen was constructed to model the column only; the influence of the pile response or soil-structure interaction was not modeled.

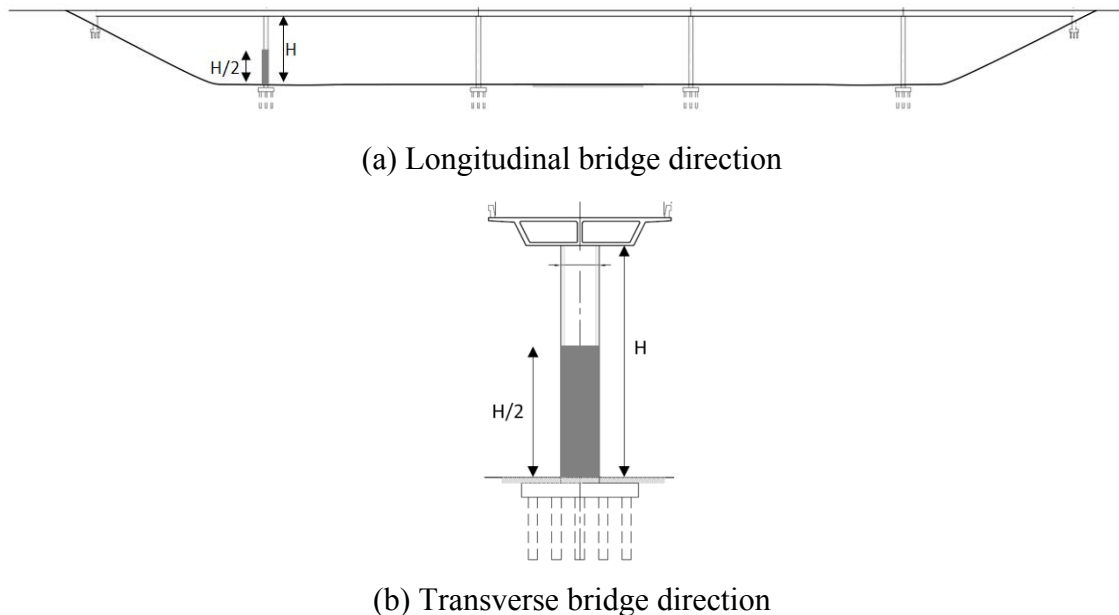


**Fig. C.1 Modeled section of prototype system column**

The specimens were modeled and tested in the upright position. Prior to testing, the columns were moved into position in the laboratory. The setup procedure in the laboratory consisted of placing the specimen, placing hydrostone and prestressing the anchor block to the laboratory floor, attaching horizontal actuators and attaching the axial load set up. The following paragraphs summarize the procedure used to place the specimen in the laboratory.

The specimens were tested in the NEES Laboratory at the Richmond Field Station at the University of California, Berkeley. The plan and elevation views of the specimen in position in the laboratory are shown in Fig. C.2 and Fig. C.3.

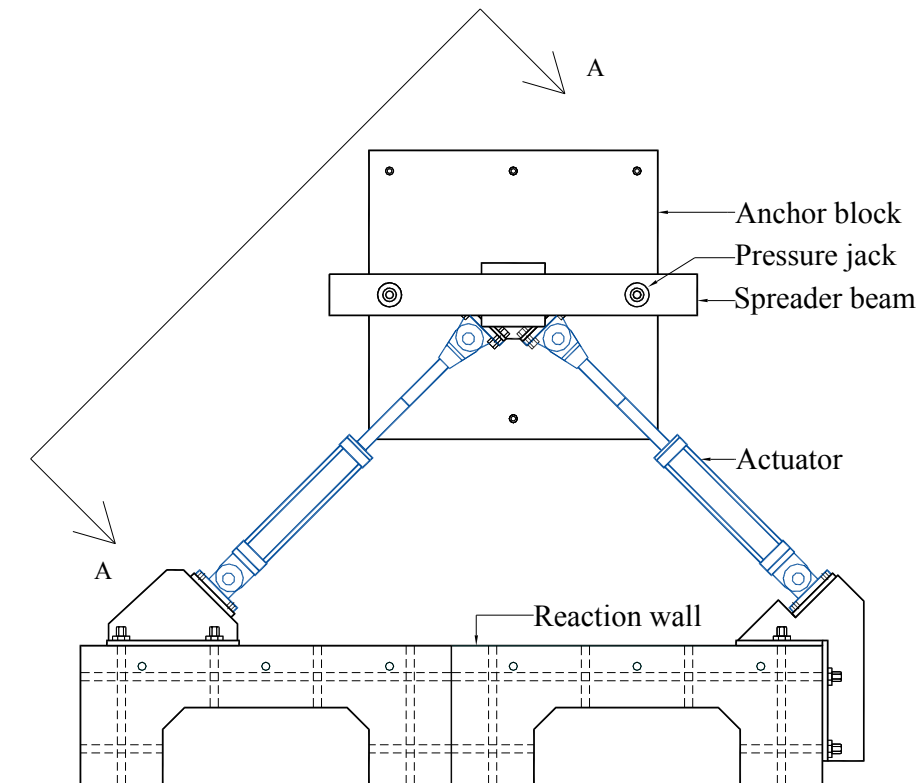


**Fig. C.2 Plan view of the experimental setup**

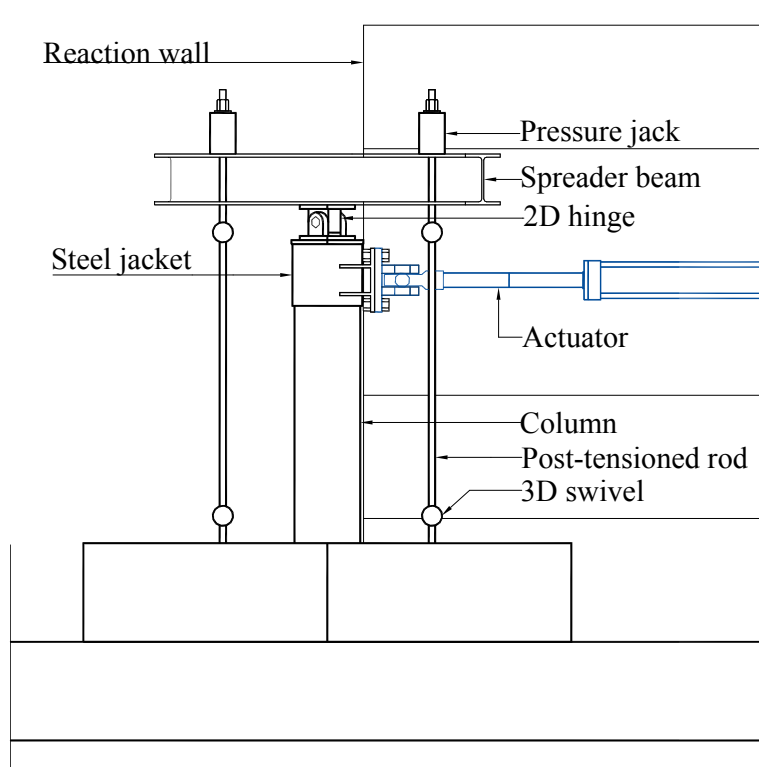


**Fig. C.3 Elevation (A-A) of the experimental setup**

The column was placed approximately 8.5 feet from the reaction wall and the anchor block was centered on holes in the floor. Holes in the laboratory floor are spaced at 3 feet on center. The anchor block was placed on ½-inch thick steel spacers. The hydrostone was poured through the holes of the anchor block, to fill the gap between the anchor block and the floor. The holes were constructed by placing PVC pipe in the anchor block prior to casting the concrete. There were eight holes placed at the perimeter of each anchor block. Two holes were used for post-tensioning of the bottom clevises of the threaded rods that are part of the axial load setup to the laboratory floor. Another six holes were for post-tensioning of the anchor block of the specimen to the laboratory floor.

The hydrostone was allowed to cure for 24 hours. Then the anchor block was post-tensioned to the laboratory floor with six high-strength rods, as indicated in Fig. C.4. The rods were post-tensioned to a force of 100 kips apiece to restrain rotation of the anchor block and prevent sliding of the specimen during the lateral test. To define the required prestressing force to restrain the rotation of the anchor block in any direction,  $P_{r,max}$ , the following three cases of the lateral load orientation were considered: (i) Case I – the lateral force is aligned with the diagonal of the anchor block, (ii) Case II – the force is aligned with the horizontal X axis of the anchor block, and (iii) Case III – the force is aligned with the vertical Y axis of the anchor block (Fig. C.4). The prestressing force that is developed in the rods for the three considered cases can be calculated from Eq. C.1, Eq. C.2, and Eq. C.3 as

$$P_{r,max,Case I} = \frac{V_{max} \cdot H + P \cdot \frac{L}{2} \cdot \sqrt{2}}{1.25 \cdot L \cdot \sqrt{2}}, \quad (C.1)$$

$$P_{r, \max, \text{Case II}} = \frac{V_{\max} \cdot H + P \cdot \frac{L}{2}}{2 \cdot L}, \quad (\text{C.2})$$

$$P_{r, \max, \text{Case III}} = \frac{V_{\max} \cdot H + P \cdot \frac{L}{2}}{3 \cdot L}, \quad (\text{C.3})$$

where  $V_{\max}$  is the shear capacity of the column,  $P$  is the axial load applied during the lateral test,  $H$  is the height of the specimen and  $L$  is the distance of post-tensioned rods along vertical Z axis of the anchor block. Fig. C.5a and Fig. C.5b show equilibrium of the laboratory configuration for the Case I and the Case II.

In addition to restricting specimen rotation, the prestressing force was required to prevent sliding of the test specimen. Hydrostone was placed between the specimen and laboratory floor to provide a reliable shear transfer mechanism. Assuming a hydrostone friction coefficient of 0.2, the force in each rod is:

$$P_{r, \max, sl} = \frac{V_{\max} - 0.2 \cdot P}{0.2 \cdot 6}. \quad (\text{C.4})$$

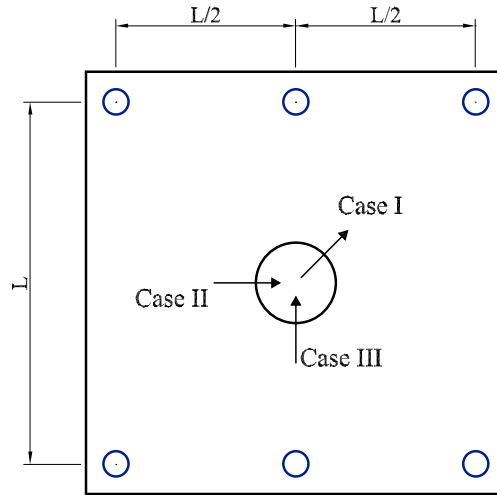


**Fig. C.4 Layout of rods**

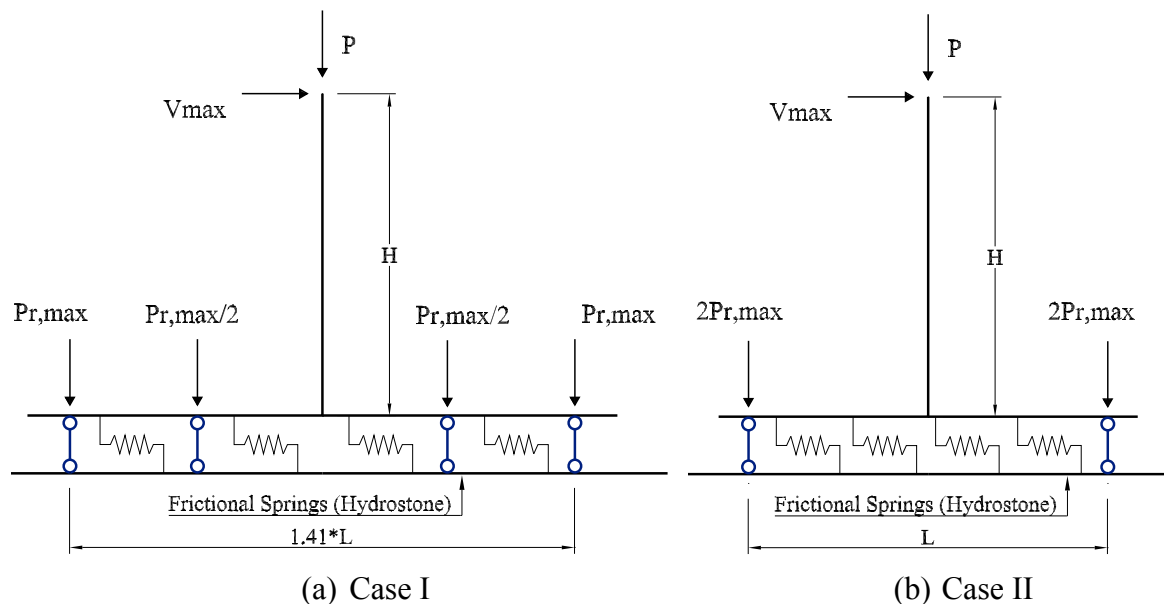


**Fig. C.5 Equilibrium of laboratory configuration**

The maximum forces that can be developed in a rod for the three lateral load cases are tabulated for the base and shear-short column specimens in Table C.1. Given that the maximum possible force in a rod of 65 kips, prestressing force of 100 kips per rod provides adequate attachment of the anchor block to the laboratory floor.

**Table C.1 Forces in the post-tensioned rod**

Prestressing force	Base spec.	Shear-short spec.
$P_{r,max,Case\ I}$	53 kips	65 kips
$P_{r,max,Case\ II}$	36 kips	44 kips
$P_{r,max,Case\ III}$	24 kips	29 kips
$P_{r,max,sl}$	4 kips	12 kips

Each column was subjected to a constant axial load and a cyclic bidirectional lateral load. The axial load was applied by prestressing two rods, one on each side of the specimen, using manually controlled jacks. The axial load was transferred from the rods to the column by a spreader beam. An axial load approximately equal to 10% of the column's nominal axial load capacity was maintained during the lateral test. This load varies with the strength of concrete of the specimen, obtained by testing concrete cylinders at the day of the test. The axial loads for all quasi static tests are given in Table C.2.

**Table C.2 Axial load matrix**

Test	Axial load
Base15	100 kips
	445 kN
Base3	100 kips
	445 kN
Base45	100 kN
	445 kN
ShearShort45	130 kips
	578 kN

The axial load setup consisted of a 2D hinge, a spreader beam, two prestressing jacks and two threaded rods with the clevises at the ends of each rod containing spherical swivels (Fig. C.6). The bottom clevises were positioned above appropriate holes on the anchor block and prestressed to the laboratory floor by two high-strength rods (Fig. C.7b). Hydrostone was placed between the lower clevis and the anchor block. The top clevises were connected to the pressure jacks and the spreader beam by short treaded rods. The main treaded rods were treaded into sleeves of the top end bottom spherical swivels (Fig. C.7a). Spherical hinges (swivels) were provided at both ends of the rods in order to avoid bending of the rods during bi-directional displacements of the column. A 2D hinge (Fig. C.8) connected spreader beam to the column maintaining horizontal position of the beam in the plane of the rods during the lateral displacements of the column. In this way, buckling of the rods was avoided.

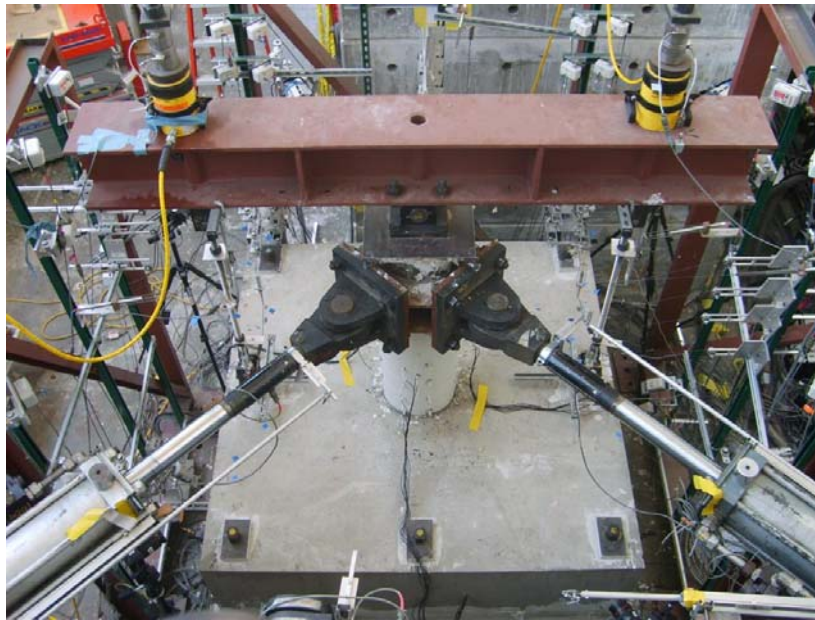


**Fig. C.6 Experimental setup**

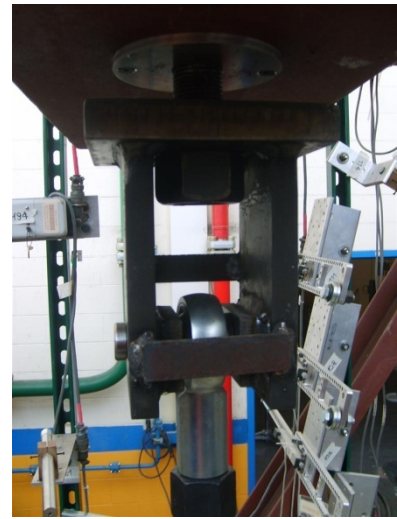




(a) Post-tensioned rod



(b) Bottom clevis



(c) Top clevis

**Fig. C.7 Post-tensioned rod details**



**Fig. C.8 2D hinge**

The bidirectional lateral load was applied using the two servo-controlled hydraulic actuators. The actuators applied the force to the top of the column and reacted against the reaction frame, as shown in Fig. C.2 and Fig. C.6. The actuators had 120 kips load and 36 inches stroke capacities. To attach the actuators at the top of the column, a 0.5 inch (1.27 cm) thick steel jacket was placed at the top of the reinforced concrete column during construction. The steel jacket (Fig. C.9) had two vertical plates to provide attachment for the actuators and two horizontal plates to provide load transfer from the actuators to the column.



**Fig. C.9 Attachment of actuators to the column**

The tested system consisted of the column and the axial load setup. To displace the top of the column laterally, stiffness of the whole system was engaged. Thus, the lateral forces measured by the load cells of the actuators during the quasi-static test originated from two sources: (i) the column and (ii) the axial load setup. While the column experienced plastic deformations during the tests, all elements of the axial load setup behaved elastically. Therefore, the lateral force originating from the axial load setup could be easily extracted from the total force.

The lateral forces originating from the axial load setup are the horizontal components of the tension forces in the post-tensioned rods. As the top of the column is displacing during a bilateral quasi-static test, the post-tensioned rods tilt. Thus, the tension forces in the rods have three components of load in the global coordinate system:  $P_x$ ,  $P_y$ , and  $P_z$ . The axes of the global coordinate system are chosen to follow the right-hand rule where X axis is aligned with the spreader beam and Z axis is aligned with the column pointing upward. The vertical component of the load (the axial force for the column),  $P_z$ , and horizontal components (lateral forces for the column),  $P_x$  and  $P_y$ , can be expressed as:

$$P_z = 2 \cdot P \cdot \cos(\varphi_x), \quad (C.5)$$

$$P_x = 2 \cdot P \cdot \cos(\varphi_x) \cdot \frac{u_x}{L_{rod}}, \quad (C.6)$$

$$P_y = -2 \cdot P \cdot \sin(\varphi_x), \quad (C.7)$$

where  $P$  is the force applied on the spreader beam by the pressure jack,  $\varphi_x$  is a rotation of the spreader beam around X axis (its only axis of rotation),  $u_x$  is a displacement of the spreader beam in X direction and  $L_{rod}$  is the length of the post-tensioned rod (pin-to-pin distance). Fig. C.10 identifies parameters that enter into Equations C.5, C.6, and C.7 by showing the deformed configuration of the axial load setup in X and Y direction.

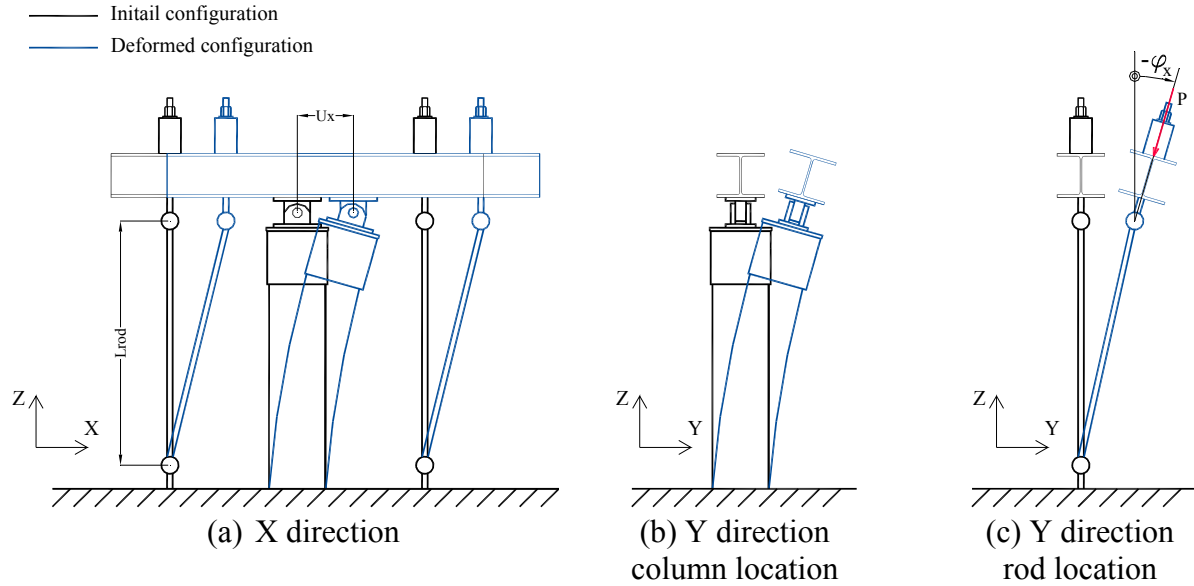


**Fig. C.10 Initial vs. deformed configuration of the axial test setup in X and Y direction**

## C.2 INSTRUMENTATION

To monitor displacements, rotations and curvature along the height of the column the columns were instrumented externally using displacement potentiometers at several levels along the height of the column. Three points at each level (referred as target points, Fig. 2.11b) were instrumented with three displacement potentiometers per point (Fig. 2.11). The instruments were connected to the target points of the column by piano wires. All instruments were attached to the instrumentation frames located on three sides of the specimen (Fig. 2.12). The displacements of any target point at any level of the column were measured in three arbitrary spatial directions and mathematically transformed to displacements of the point in global XYZ system. The axes of the global coordinate system are chosen to follow the right-hand rule where X axis is parallel with the spreader beam and Z axis is parallel with the column.

Fig. C.11 shows the sketch of instrumentation for a target point P whose displacements are traced during the test. Three instruments whose locations are designated as points 1, 2, and 3 are connected to the target point P by piano wires and measure displacements of the target point P in directions of the piano wires. The points 1, 2, 3, and P form a pyramid where the point P is the apex of the pyramid. When viewed from the apex of the pyramid, the points 1, 2, and 3 have counter-clock-wise orientation.

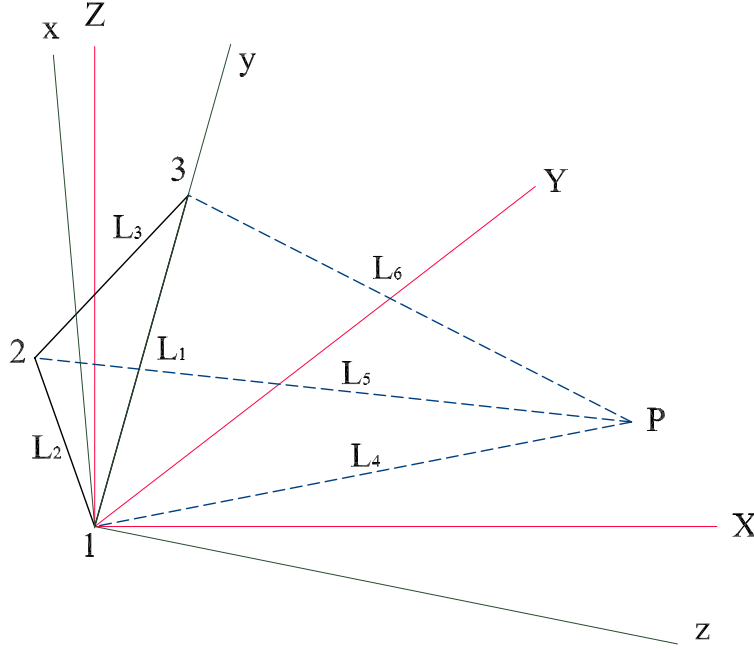


**Fig. C.11 Sketch of instrumentation for a target point P**

Positions of the instruments as well as the initial position of the target point P are defined in the global coordinate system (XYZ) whose origin is located at the point 1. Thus, the position of the instrument 1 in the global coordinate system (GCS) is  $[0, 0, 0]$ , the position of the instrument 2 in the GCS is  $[X_2, Y_2, Z_2]$ , the position of the instrument 3 in the GCS is  $[X_3, Y_3, Z_3]$ , and the initial position of the target point P in the GCS is  $[X_{P,in}, Y_{P,in}, Z_{P,in}]$ . Therefore, the distances among the instruments designated as  $L_1$ ,  $L_2$  and  $L_3$  can be calculated as follows:

$$L_1 = \text{norm}(X_3, Y_3, Z_3), \quad (\text{C.8})$$

$$L_2 = \text{norm}(X_2, Y_2, Z_2), \quad (\text{C.9})$$

$$L_3 = \text{norm}(X_3 - X_2, Y_3 - Y_2, Z_3 - Z_2), \quad (\text{C.10})$$

where *norm* is a function that assigns length to a vector. For instance, the norm of a vector (X, Y, Z) is:

$$\text{norm}(X, Y, Z) = \sqrt{X^2 + Y^2 + Z^2}. \quad (\text{C.11})$$

The distances from the instrument locations 1, 2, and 3 to the target point P (including the instrument reading), designated as  $L_4$ ,  $L_5$  and  $L_6$  can be calculated as follows:

$$L_4 = \text{norm}(X_{P,in} - X_1, Y_{P,in} - Y_1, Z_{P,in} - Z_1) + IR_1, \quad (\text{C.12})$$

$$L_5 = \text{norm}(X_{P,in} - X_2, Y_{P,in} - Y_2, Z_{P,in} - Z_2) + IR_2, \quad (\text{C.13})$$

$$L_6 = \text{norm}(X_{P,in} - X_3, Y_{P,in} - Y_3, Z_{P,in} - Z_3) + IR_3, \quad (\text{C.14})$$

where  $IR_1$ ,  $IR_2$ , and  $IR_3$  are the readings of the instruments 1, 2, and 3.

Since instrument measurements do not coincide with the global coordinate axis, local right-hand coordinate system (xyz) is established to trace the displacements of the target point P.

The origin of the local coordinate system (LCS) coincides with the origin of the global coordinate system (point 1). The local y-axis passes through the point 3 and the local x-axis is chosen such that the base of the pyramid lies in x-y plane.

Positions of instruments 2 and 3 in the LCS are  $[x_2, y_2, 0]$  and  $[0, y_3, 0]$  and can be calculated as follows:

$$x_2 = L_2 \cdot \sin(\alpha), \quad (C.15)$$

$$y_2 = L_2 \cdot \cos(\alpha), \quad (C.16)$$

$$y_3 = L_1, \quad (C.17)$$

where  $\alpha$  is the internal angle of the base of the pyramid between sides 12 and 13 and can be calculated using Equation C.18.

$$\alpha = \cos^{-1} \left( \frac{L_3^2 - L_2^2 - L_1^2}{-2 \cdot L_1 \cdot L_2} \right) \quad (C.18)$$

The position of the point P in the local coordinate system is  $[x, y, z]$  and can be calculated using Equations C.19, C.20, and C.21.

$$x = \frac{x_2^2 y_3 - y_2 y_3^2 - y_2 L_4^2 + y_2 L_6^2 + y_3 y_2^2 + y_3 L_4^2 - y_3 L_5^2}{-2 \cdot x_2 \cdot y_3} \quad (C.19)$$

$$y = \frac{L_6^2 - L_4^2 - y_3^2}{-2 \cdot y_3} \quad (C.20)$$

$$z = \sqrt{L_4^2 - x^2 - y^2} \quad (C.21)$$

Finally, the position of the point P in the GCS can be calculated using transformation matrix  $M$  whose columns are unit vectors along the local axes x, y, and z, expressed by the vectors in the GCS. For example, the second column of the matrix  $M$  is the unit vector along the local y-axis expressed as follows:

$$M_2 = \begin{bmatrix} \frac{X_3}{\text{norm}(X_3, Y_3, Z_3)} \\ \frac{Y_3}{\text{norm}(X_3, Y_3, Z_3)} \\ \frac{Z_3}{\text{norm}(X_3, Y_3, Z_3)} \end{bmatrix}. \quad (C.22)$$

After the transformation matrix is formed, the coordinates of the point P in the global coordinate system  $[X, Y, Z]$  can be calculated using Eq. C.23.

$$[X \ Y \ Z] = [x \ y \ z] \cdot M^T \quad (C.23)$$

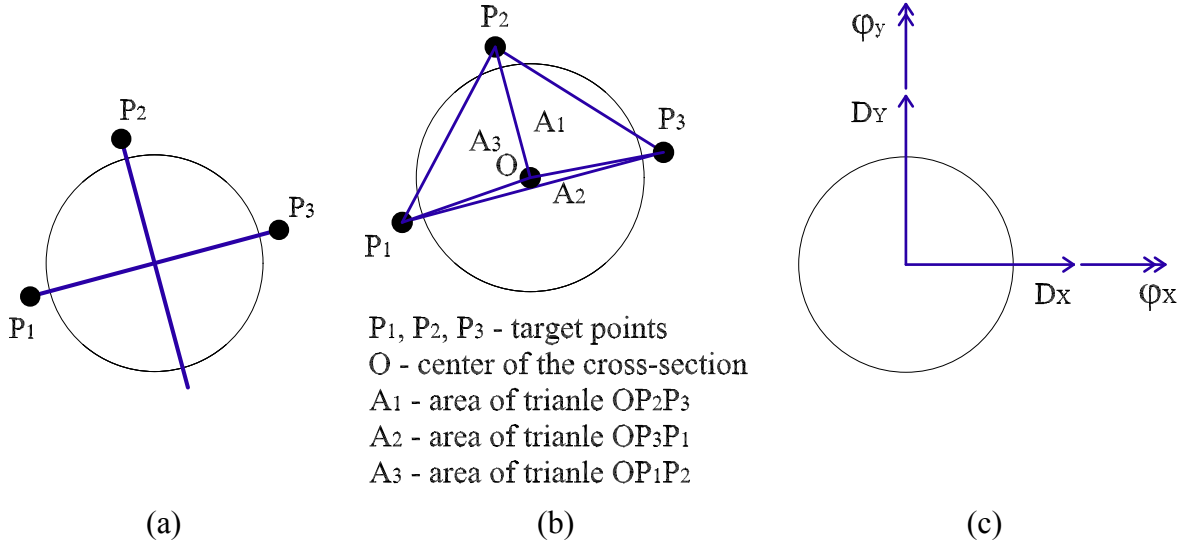


**Fig. C.12 Transformation of displacements at target points to displacements and rotations at the centroid of the column's cross-section that the plane defined by points  $P_1$ ,  $P_2$ , and  $P_3$  intersects**

Consider a plane defined by three target points  $P_1$ ,  $P_2$ , and  $P_3$  (Fig. C.12a). Since the three components of displacements of the target points can be traced during the test, they will be used to calculate three displacements and three rotations at the centroid of a column's cross-section that the plane defined by points  $P_1$ ,  $P_2$ , and  $P_3$  intersects. If the origin of the GCS is positioned at the centroid of the section, then the coordinates of the points  $P_1$ ,  $P_2$ , and  $P_3$  in GCS are defined as  $[X_1, Y_1, Z_1]$ ,  $[X_2, Y_2, Z_2]$ , and  $[X_3, Y_3, Z_3]$ . Collect the coordinates of the three target points in the matrix  $T$  as shown:

$$T = \begin{bmatrix} X_1 & Y_1 & Z_1 \\ X_2 & Y_2 & Z_2 \\ X_3 & Y_3 & Z_3 \end{bmatrix}. \quad (C.24)$$

The plane formed by the points  $P_1$ ,  $P_2$ , and  $P_3$  can be defined by Equation C.25, where coefficients  $A$ ,  $B$ ,  $C$ , and  $D$  are given by Equations C.26-C.29.

$$A \cdot X + B \cdot Y + C \cdot Z + D = 0 \quad (C.25)$$

$$A = \begin{vmatrix} 1 & Y_1 & Z_1 \\ 1 & Y_2 & Z_2 \\ 1 & Y_3 & Z_3 \end{vmatrix} \quad (C.26)$$

$$B = \begin{vmatrix} X_1 & 1 & Z_1 \\ X_2 & 1 & Z_2 \\ X_3 & 1 & Z_3 \end{vmatrix} \quad (C.27)$$

$$C = \begin{vmatrix} X_1 & Y_1 & 1 \\ X_2 & Y_2 & 1 \\ X_3 & Y_3 & 1 \end{vmatrix} \quad (C.28)$$

$$D = - \begin{vmatrix} X_1 & Y_1 & Z_1 \\ X_2 & Y_2 & Z_2 \\ X_3 & Y_3 & Z_3 \end{vmatrix} \quad (C.29)$$

Assuming that the distances between the points  $P_1$ ,  $P_2$ , and  $P_3$  do not change during the test the displacements of the centroid of the cross-section can be traced during the test if the ratios of the areas  $A_1/A_T$ ,  $A_2/A_T$  and  $A_3/A_T$  are known (Fig. C.12b). The area of the triangle formed by the points  $P_1$ ,  $P_2$ , and  $P_3$  is designated as  $A_T$ . Forming a row vector  $V$  consisting of the area ratios as shown in Equation C.30, the displacements of the centroid of the considered cross-section can be calculated using Equation C.31.

$$V = \left[ \frac{A_1}{A_T} \quad \frac{A_2}{A_T} \quad \frac{A_3}{A_T} \right] \quad (C.30)$$

$$D = [D_X \quad D_Y \quad D_Z] = V \cdot T \quad (C.31)$$

Neglecting the rotation around Z axis (torsional rotation), rotations of the plane defined by the points  $P_1$ ,  $P_2$ , and  $P_3$  around X and Y axis are calculated using the Equations C.32 and C.33 where coefficient  $A$ ,  $B$  and  $C$  are defined by Equations C.26-C.28.

$$\varphi_X = -a \tan\left(\frac{B}{C}\right) \quad (C.32)$$

$$\varphi_Y = a \tan\left(\frac{A}{C}\right) \quad (C.33)$$

Since the initial plane that points  $P_1$ ,  $P_2$ , and  $P_3$  define does not coincide with the X-Y plane, initial rotations  $\varphi_X$  and  $\varphi_Y$  have to be calculated and subtracted from the rotations calculated for any instant in time during the test to get the rotations of the X-Y plane. Fig. C.12c shows the sign convention for displacements and rotations of the centroid of the cross-section.

After the rotations are calculated at the discrete points along the height of the column the average curvatures of the segments between the points with known rotations can be calculated as follows:

$$\kappa_{Xi}^{avg} = \frac{1}{H_i} \cdot (\varphi_{Y,i+1} - \varphi_{Y,i}) \quad (C.34)$$

$$\kappa_{Yi}^{avg} = \frac{1}{H_i} \cdot (\varphi_{X,i+1} - \varphi_{X,i}) \quad (C.35)$$

where  $\kappa_{Xi}$  and  $\kappa_{Yi}$  are the average curvatures in X and Y direction of the  $i^{\text{th}}$  segment that is bounded by the instrumented sections  $i$  and  $i+1$  (numbering goes from the bottom to the top of the column),  $H_i$  is the height of the  $i^{\text{th}}$  segment,  $\varphi_{X,i+1}$  and  $\varphi_{Y,i+1}$  are the rotations of the  $i+1^{\text{st}}$  section and  $\varphi_{X,i}$  and  $\varphi_{Y,i}$  are the rotations of the  $i^{\text{th}}$  section in X and Y direction.

The average curvatures of the segments calculated based on the rotations of the sections can be compared with the average curvatures calculated using the readings of the strain gages attached on the longitudinal bars. Based on the strain gage readings, the curvatures at the  $i^{\text{th}}$  section can be calculated as follows:

$$\kappa_{Xi} = \frac{1}{h} \cdot (\varepsilon_{L,i} - \varepsilon_{R,i}) \quad (\text{C.36})$$

$$\kappa_{Yi} = \frac{1}{h} \cdot (\varepsilon_{T,i} - \varepsilon_{B,i}) \quad (\text{C.37})$$

where  $\kappa_{Xi}$  and  $\kappa_{Yi}$  are the curvatures in X and Y direction of the  $i^{\text{th}}$  section,  $h$  is the distance between the strain gages in X or Y direction, and  $\varepsilon_{T,i}$ ,  $\varepsilon_{B,i}$ ,  $\varepsilon_{L,i}$ , and  $\varepsilon_{R,i}$  are the readings of the strain gages located in the  $i^{\text{th}}$  section. The positions of the strain gages in the section are designated with letters: L, B, R, and T (Fig. C.13).

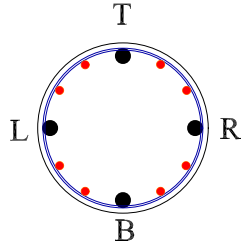


**Fig. C.13 Positions of the strain gages in a section**

Replacing the index  $i$  with the index  $i+1$  in Equations C.36 and C.37, the curvatures at the  $i+1^{\text{st}}$  section can be calculated. The average curvatures of the  $i^{\text{th}}$  segment bounded by the  $i^{\text{th}}$  and  $i+1^{\text{st}}$  sections are:

$$\kappa_{Xi}^{avg} = \frac{1}{2} \cdot (\kappa_{Xi} + \kappa_{Xi+1}) \quad (\text{C.38})$$

$$\kappa_{Yi}^{avg} = \frac{1}{2} \cdot (\kappa_{Yi} + \kappa_{Yi+1}) \quad (\text{C.39})$$



## **Appendix D: Ground Motion Records**

Specific information detailing all the ground motion records used to study post-earthquake traffic capacity of the bridge is contained in the tables of this Appendix. The records were obtained from the PEER Center ground motion database available on <http://peer.berkeley.edu/>. The tables are separated according to bin. In the tables, designation M stands for the moment magnitude and designation R stands for the closest distance to the fault rupture.

**Table D.1 Record bin LMSR (Large Magnitude, Small Distance)**

Record ID	Event	Year	M	R (km)	Station	Soil	Mechanism
AGW	Loma Prieta	1989	6.9	28.2	Agnews State Hospital	D	reverse-oblique
CAP	Loma Prieta	1989	6.9	14.5	Capitola	D	reverse-oblique
G03	Loma Prieta	1989	6.9	14.4	Gilroy Array #3	D	reverse-oblique
G04	Loma Prieta	1989	6.9	16.1	Gilroy Array #4	D	reverse-oblique
GMR	Loma Prieta	1989	6.9	24.2	Gilroy Array #7	D	reverse-oblique
HCH	Loma Prieta	1989	6.9	28.2	Hollister City Hall	D	reverse-oblique
HDA	Loma Prieta	1989	6.9	25.8	Hollister Differential Array	D	reverse-oblique
SVL	Loma Prieta	1989	6.9	28.8	Sunnyvale - Colton Ave.	D	reverse-oblique
CNP	Northridge	1994	6.7	15.8	Canoga Park - Topanga Can.	D	reverse-slip
FAR	Northridge	1994	6.7	23.9	LA - N Faring Rd.	D	reverse-slip
FLE	Northridge	1994	6.7	29.5	LA - Fletcher Dr.	D	reverse-slip
GLP	Northridge	1994	6.7	25.4	Glendale - Las Palmas	D	reverse-slip
HOL	Northridge	1994	6.7	25.5	LA - Hollywood Stor FF	D	reverse-slip
NYA	Northridge	1994	6.7	22.3	La Crescenta-New York	D	reverse-slip
LOS	Northridge	1994	6.7	13.0	Canyon Country - W Lost Cany	D	reverse-slip
RO3	Northridge	1994	6.7	12.3	Sun Valley - Roscoe Blvd	D	reverse-slip
PEL	San Fernando	1971	6.6	21.2	LA - Hollywood Stor Lot	D	reverse-slip
B-ICC	Superstition Hills	1987	6.7	13.9	El Centro Imp. Co. Cent	D	strike-slip
B-IVW	Superstition Hills	1987	6.7	24.4	Wildlife Liquef. Array	D	strike-slip
B-WSM	Superstition Hills	1987	6.7	13.3	Westmorland Fire Station	D	strike-slip

**Table D.2 Record bin LMLR (Large Magnitude, Large Distance)**

Record ID	Event	Year	M	R (km)	Station	Soil	Mechanism
A-ELC	Borrego Mountain	1968	6.8	46.0	El Centro Array #9	D	strike-slip
A2E	Loma Prieta	1989	6.9	57.4	APEEL 2E Hayward Muir Sch.	D	reverse-oblique
FMS	Loma Prieta	1989	6.9	43.4	Fremont - Emerson Court	D	reverse-oblique
HVR	Loma Prieta	1989	6.9	31.6	Halls Valley	D	reverse-oblique
SJW	Loma Prieta	1989	6.9	32.6	Salinas - John & Work	D	reverse-oblique
SLC	Loma Prieta	1989	6.9	36.3	Palo Alto - SLAC Lab.	D	reverse-oblique
BAD	Northridge	1994	6.7	56.1	Covina - W. Badillo	D	reverse-slip
CAS	Northridge	1994	6.7	49.6	Compton - Castlegate St.	D	reverse-slip
CEN	Northridge	1994	6.7	30.9	LA - Centinela St.	D	reverse-slip
DEL	Northridge	1994	6.7	59.3	Lakewood - Del Amo Blvd.	D	reverse-slip
DWN	Northridge	1994	6.7	47.6	Downey - Co. Maint. Bldg.	D	reverse-slip
JAB	Northridge	1994	6.7	46.6	Bell Gardens - Jaboneria	D	reverse-slip
LH1	Northridge	1994	6.7	36.3	Lake Hughes #1	D	reverse-slip
LOA	Northridge	1994	6.7	42.4	Lawndale - Osage Ave.	D	reverse-slip
LV2	Northridge	1994	6.7	37.7	Leona Valley #2	D	reverse-slip
PHP	Northridge	1994	6.7	43.6	Palmdale - Hwy 14 & Palmdale	D	reverse-slip
PIC	Northridge	1994	6.7	32.7	LA - Pico & Sentous	D	reverse-slip
SOR	Northridge	1994	6.7	54.1	West Covina - S. Orange Ave.	D	reverse-slip
SSE	Northridge	1994	6.7	60.0	Terminal Island - S. Seaside	D	reverse-slip
VER	Northridge	1994	6.7	39.3	LA - E Vernon Ave.	D	reverse-slip

**Table D.3 Record bin SMSR (Small Magnitude, Small Distance)**

Record ID	Event	Year	M	R (km)	Station	Soil	Mechanism
H-CAL	Imperial Valley	1979	6.5	23.8	Calipatria Fire Station	D	strike-slip
H-CHI	Imperial Valley	1979	6.5	28.7	Chihuahua	D	strike-slip
H-E01	Imperial Valley	1979	6.5	15.5	El Centro Array #1	D	strike-slip
H-E12	Imperial Valley	1979	6.5	18.2	El Centro Array #12	D	strike-slip
H-E13	Imperial Valley	1979	6.5	21.9	El Centro Array #13	D	strike-slip
H-WSM	Imperial Valley	1979	6.5	15.1	Westmorland Fire Station	D	strike-slip
A-SRM	Livermore	1980	5.8	21.7	San Ramon Fire Station	D	strike-slip
A-KOD	Livermore	1980	5.8	17.6	San Ramon - Eastman Kodak	D	strike-slip
M-AGW	Morgan Hill	1984	6.2	29.4	Agnews State Hospital	D	strike-slip
M-G02	Morgan Hill	1984	6.2	15.1	Gilroy Array #2	D	strike-slip
M-G03	Morgan Hill	1984	6.2	14.6	Gilroy Array #3	D	strike-slip
M-GMR	Morgan Hill	1984	6.2	14.0	Gilroy Array #7	D	strike-slip
PHN	Point Mugu	1973	5.8	25.0	Port Hueneme	D	reverse-slip
BRA	Westmorland	1981	5.8	22.0	5060 Brawley Airport	D	strike-slip
NIL	Westmorland	1981	5.8	19.4	724 Niland Fire Station	D	strike-slip
A-CAS	Whittier Narrows	1987	6.0	16.9	Compton - Castlegate St.	D	reverse
A-CAT	Whittier Narrows	1987	6.0	28.1	Carson - Catskill Ave.	D	reverse
A-DWN	Whittier Narrows	1987	6.0	18.3	14368 Downey - Co Maint Bldg	D	reverse
A-W70	Whittier Narrows	1987	6.0	16.3	LA - W 70th St.	D	reverse
A-WAT	Whittier Narrows	1987	6.0	24.5	Carson - Water St.	D	reverse

Distance R marked red indicates hypocentral distance

**Table D.4 Record bin SMLR (Small Magnitude, Large Distance)**

Record ID	Event	Year	M	R (km)	Station	Soil	Mechanism
B-ELC	Borrego	1942	6.5	49.0	El Centro Array #9	D	unknown
H-C05	Coalinga	1983	6.4	47.3	Parkfield - Cholame 5W	D	reverse-oblique
H-C08	Coalinga	1983	6.4	50.7	Parkfield - Cholame 8W	D	reverse-oblique
H-CC4	Imperial Valley	1979	6.5	49.3	Coachella Canal #4	D	strike-slip
H-CMP	Imperial Valley	1979	6.5	32.6	Compuertas	D	strike-slip
H-DLT	Imperial Valley	1979	6.5	43.6	Delta	D	strike-slip
H-NIL	Imperial Valley	1979	6.5	35.9	Niland Fire Station	D	strike-slip
H-PLS	Imperial Valley	1979	6.5	31.7	Plaster City	D	strike-slip
H-VCT	Imperial Valley	1979	6.5	54.1	Victoria	D	strike-slip
A-STP	Livermore	1980	5.8	37.3	Tracy - Sewage Treatment Plant	D	strike-slip
M-CAP	Morgan Hill	1984	6.2	38.1	Capitola	D	strike-slip
M-HCH	Morgan Hill	1984	6.2	32.5	Hollister City Hall	D	strike-slip
M-SJB	Morgan Hill	1984	6.2	30.3	San Juan Bautista	C	strike-slip
H06	N. Palm Springs	1986	6.0	39.6	San Jacinto Valley Cemetery	D	strike-slip
INO	N. Palm Springs	1986	6.0	39.6	Indio	D	strike-slip
A-BIR	Whittier Narrows	1987	6.0	56.8	Downey - Birchdale	D	reverse
A-CTS	Whittier Narrows	1987	6.0	31.3	LA - Century City CC South	D	reverse
A-HAR	Whittier Narrows	1987	6.0	34.2	LB - Harbor Admin FF	D	reverse
A-SSE	Whittier Narrows	1987	6.0	35.7	Terminal Island - S. Seaside	D	reverse
A-STC	Whittier Narrows	1987	6.0	39.8	Northridge - Saticoy St.	D	reverse

Distance R marked red indicates hypocentral distance

**Table D.5 Record bin VN (Van Nuys)**

Record ID	Event	Year	M	R (km)	Station	Soil	Mechanism
plma	North Palm Springs	1986	6.0	9.6	Palm Springs Airport	D	reverse-oblique
plmb	North Palm Springs	1986	6.0	9.6	Palm Springs Airport, reversed components	D	reverse-oblique
env1	Northridge	1994	6.7	17.7	Encino, Ventura Blvd. #1	D	reverse
env9	Northridge	1994	6.7	17.9	Encino, Ventura Blvd. #9	D	reverse
nhl2	Northridge	1994	6.7	18.4	North Hollywood, Lankershim Blvd. #1	D	reverse
vns1	Northridge	1994	6.7	12.8	Van Nuys, Sherman Way #1	D	reverse
vnscl	Northridge	1994	6.7	12.8	Van Nuys - Sherman Circle #1	D	reverse
whox	Northridge	1994	6.7	20.0	Woodland Hills, Oxnard Street #4	D	reverse
cnpk	Northridge	1994	6.7	17.7	Canoga Park, Topanga Canyon Blvd.	D	reverse
spva	Northridge	1994	6.7	9.2	Sepulveda VA Hospital - ground	D	reverse
vnuy	Northridge	1994	6.7	11.3	Van Nuys - 7-Story Hotel	D	reverse
nord	Northridge	1994	6.7	9.4	Arleta, Nordhoff Fire Station	D	reverse
nrr1	Northridge	1994	6.7	13.7	Northridge, Roscoe #1	D	reverse
rosc	Northridge	1994	6.7	10.8	Sun Valley, 13248 Roscoe Blvd.	D	reverse
sf253	San Fernando	1971	6.6	16.3	Los Angeles, 14724 Ventura Blvd.	D	reverse
sf461	San Fernando	1971	6.6	16.2	Los Angeles, 15910 Ventura Blvd.	D	reverse
sf466	San Fernando	1971	6.6	16.4	Los Angeles, 15250 Ventura Blvd.	D	reverse
glen	San Fernando	1971	6.6	18.8	Glendale, Muni. Bldg., 633 E. Broadway	D	reverse
vvnuy	Whittier Narrows	1987	6.0	9.5	Van Nuys - 7-Story Hotel	D	reverse
athl	Whittier Narrows	1987	6.0	16.6	Cal Tech, Brown Athletic Building	D	reverse

**Table D.6 Record bin I-880 (Nearby-Field)**

Record ID	Event	Year	M	R (km)	Station	Soil	Mechanism
cclyd	Coyote Lake	1979	5.7	4.0	Coyote Lake Dam abutment	C	strike-slip
gil6	Coyote Lake	1979	5.7	1.2	Gilroy #6	C	strike-slip
temb	Parkfield	1966	6.0	4.4	Temblor	C	strike-slip
cs05	Parkfield	1966	6.0	3.7	Array #5	D	strike-slip
cs08	Parkfield	1966	6.0	8.0	Array #8	D	strike-slip
fgnr	Livermore	1980	5.5	4.1	Fagundes Ranch	D	strike-slip
mgnp	Livermore	1980	5.5	8.1	Morgan Territory Park	C	strike-slip
clyd	Morgan Hill	1984	6.2	0.1	Coyote Lake Dam abutment	C	strike-slip
andd	Morgan Hill	1984	6.2	4.5	Anderson Dam Downstream	C	strike-slip
hall	Morgan Hill	1984	6.2	2.5	Halls Valley	C	strike-slip
lgpc	Loma Prieta	1989	6.9	3.5	Los Gatos Presentation Center	C	reverse-oblique
srtg	Loma Prieta	1989	6.9	8.3	Saratoga Aloha Ave	C	reverse-oblique
cor	Loma Prieta	1989	6.9	3.4	Corralitos	C	reverse-oblique
gav	Loma Prieta	1989	6.9	9.5	Gavilan College	C	reverse-oblique
gilb	Loma Prieta	1989	6.9	11.0	Gilroy historic	C	reverse-oblique
lex1	Loma Prieta	1989	6.9	6.3	Lexington Dam abutment	C	reverse-oblique
kobj	Kobe, Japan	1995	6.9	0.5	Kobe JMA	C	strike-slip
ttr007	Tottori, Japan	2000	6.6	10.0	Kofu	C	strike-slip
ttrh02	Tottori, Japan	2000	6.6	1.0	Hino	C	strike-slip
erzi	Erzincan, Turkey	1992	6.7	1.8	Erzincan	C	strike-slip

**Table D.7 Record bin Near (Nearby-Field)**

Record ID	Event	Year	M	R (km)	Station	Soil	Mechanism
I-ELC	Imperial Valley	1940	7.0	8.3	El Centro Array #9	D	strike-slip
C08	Parkfield	1966	6.1	5.3	Cholame #8	D	strike-slip
H-AEP	Imperial Valley	1979	6.5	8.5	Aeropuerto Mexicali	D	strike-slip
H-BCR	Imperial Valley	1979	6.5	2.5	Bonds Corner	D	strike-slip
H-CXO	Imperial Valley	1979	6.5	10.6	Calexico Fire Station	D	strike-slip
H-ECC	Imperial Valley	1979	6.5	7.6	EC County Center FF	D	strike-slip
H-E05	Imperial Valley	1979	6.5	1.0	El Centro Array #5	D	strike-slip
H-SHP	Imperial Valley	1979	6.5	11.1	SAHOP Casa Flores	D	strike-slip
H-PVP	Coalinga	1983	6.4	8.5	Pleasant Valley P.P. - bldg	D	reverse-oblique
M-HVR	Morgan Hill	1984	6.2	3.4	Halls Valley	D	strike-slip
A-JAB	Whittier Narrows	1987	6.0	9.8	Bell Gardens - Jaboneria	D	reverse-slip
A-SOR	Whittier Narrows	1987	6.0	10.5	West Covina - S. Orange Ave.	D	reverse-slip
GOF	Loma Prieta	1989	6.9	12.7	Gilroy - Historic Bldg.	D	reverse-oblique
G02	Loma Prieta	1989	6.9	12.7	Gilroy Array #2	D	reverse-oblique
JEN	Northridge	1994	6.7	6.2	Jensen Filter Plant	D	reverse-slip
NWH	Northridge	1994	6.7	7.1	Newhall - Fire Station	D	reverse-slip
RRS	Northridge	1994	6.7	7.1	Rinaldi Receiving Station	D	reverse-slip
SPV	Northridge	1994	6.7	8.9	Sepulveda VA	D	reverse-slip
SCS	Northridge	1994	6.7	6.2	Sylmar - Converter Station	D	reverse-slip
SYL	Northridge	1994	6.7	6.4	Sylmar - Olive View Med FF	D	reverse-slip